2020

Composition, Encapsulation, and Dimensionality: A Study of the Photophysics Brought on by Synthetic Changes in Perovskite Materials

Andrew Towers
University of Central Florida

STARS Citation

Towers, Andrew, "Composition, Encapsulation, and Dimensionality: A Study of the Photophysics Brought on by Synthetic Changes in Perovskite Materials" (2020). *Electronic Theses and Dissertations, 2020-*. 459.
https://stars.library.ucf.edu/etd2020/459

COMPOSISTION, ENCAPSULATION, AND DIMENSIONALITY: A STUDY OF THE PHOTOPHYSICS BROUGHT ON BY SYNTHETIC CHANGES IN PEROVSKITE MATERIALS

by

ANDREW C TOWERS
B.S. University of Central Florida, 2013
M.S. University of Central Florida, 2015

A dissertation submitted in partial fulfillment of the requirements
for the degree of Doctor of Philosophy
in the Department of Chemistry
in the College of Sciences
at the University of Central Florida
Orlando, Florida

Spring Term
2020

Major Professor: Andre Gesquiere

ABSTRACT

Perovskite materials are currently being explored as a candidate for a wide variety of optoelectronic applications with a focus on active materials for solar cell and an array of lighting applications. To optimize perovskites for optoelectronic applications, a myriad synthetic and processing techniques are used to overcome limitations in the raw materials. Presently, perovskite materials have demonstrated vast improvements as candidates for solar cell and lighting applications, though the fundamental photophysical characteristics resulting from the rapid succession of synthetic developments require further investigation. Further comprehension of the basic photophysical processes being altered by synthetic and processing changes must be achieved to continue the advancement of perovskite materials.

Here, we employ imaging and molecular spectroscopy techniques to explore photophysical changes brought on by synthetic modifications to perovskite materials. We hypothesized that the excited state lifetimes could be used as an indicator to probe the stability of perovskite materials, which was investigated for encapsulated perovskite samples. For 0D nanoparticles an improvement was observed for average photoluminescence lifetimes for and overall structural order with reduced Urbach energy values for encapsulated samples. These findings indicate a surface defect passivation effect from the polymer matrix and imply the emissive nature of these materials proceeds by either bimolecular or trap-assisted recombination events. It was also hypothesized that 1D encapsulated nanorod structures, when mechanically aligned, were capable of emitting polarized light. In addition to emitting polarized light (P=0.4), the encapsulated nanorods were found to display similar photophysical pathways for their emissive processes to that of the encapsulated 0D nanoparticles. Finally, we hypothesized by further reducing 2D Ruddlesden-Popper hybrid perovskite films to quantum dots and nanoplatelets would further increase already prominent quantum confinement effects. The 2D Ruddlesden-Popper perovskite quantum dots and nanoplatelets show strong absorption and emission in the UV region as well as short average photoluminescence decay lifetimes. The outcome of these optical properties can be attributed to the strong quantum and dielectric confinement brought on by the unique quantum well structure adopted by 2D perovskite materials, specifically lattice vibration effects (exciton-polaron interactions) and a mixed layered material ($n = 2$ or 3). These findings indicate three possible mechanistic emissive processes in these 2D Ruddlesden-Popper perovskites: free exciton, intrinsically trapped, and defect trapped recombination.

The results obtained in these studies demonstrate alterations in fundamental photophysical processes as perovskite materials are tailored for various optoelectronic applications.

To my mom. You may not be here now, but I made it.

ACKNOWLEDGEMENTS

I would like to thank Dr. Andre Gesquiere for giving me the opportunity to work in his group. He gave me the freedom to tinker and explore, which helped me to find my passions in the research I was fortunate to conduct. Thank you to Dr. Yaije Dong for your help and guidance, especially in our collaborative works. To that extent I would also like to thank my work wife Juan He (Rachel), I wouldn't have been able to carry out all these elaborate studies without your help and patience.

A big thanks goes out to Dr. Matthew Rex; you've been a great mentor in everything from teaching to handling specific problems in research. Your advice and stories always helped keep me levelheaded even when the apocalypse seemed imminent. I'd also like to thank the rest of my doctoral committee: Dr. Eloy Hernandez and Dr. Shengli Zou for their support throughout the PhD process.

A special thank you to Dr. Alison Tamasi, without your guidance in both the academic and professional world, I don't think I'd be where I am today. I will never forget my experiences working alongside you and all of the glitter that came with it.

I'd also like to thank the NSTC and Chemistry department staff for all their hard work supporting our research goals and aiding in any way they can. Specifically, I'd like to thank both Ernie Gemeinhart and Ted Molina for the countless hours of help fixing any and everything that went down. I'd also like to thank Dr. Jayan Thomas and his lab group for the opportunity to work on some truly interesting projects and all of their collaborative efforts.

I would also like to acknowledge my fellow lab mates and graduate students in the NSTC and chemistry departments. The countless lunches and coffee runs made any and all research possible.

Finally, I would also like to thank the one person that has stuck by me and at this point has literally pushed me over the finish line, Ajani Gibson. I don’t know how I would have made it here without you and I thank you from the bottom of my heart for all you’ve put up with up to this point. Also, my best of friends Jessica Powell and Adrienne Showman thank you for your continued support right up until the end, it means the world to me. Thank you to my parents, grandparents, sister, and brother for their constant support and encouragement over all these years, I am eternally grateful for all your help.

TABLE OF CONTENTS

LIST OF FIGURES

LIST OF TABLES

LIST OF ABBREVIATIONS

ABS – Acrylonitrile-butadiene-styrene

Abs – Absorbance

BU – Bottom-up

BS – Beam splitter

CA – Cellulose acetate

CB – Conduction band

CBM – Conduction band minimum

CVD – Chemical vapor deposition

DLS – Defect level state

DMF – Dimethylformamide

FC – Free carriers

FE – Free excitons

GS – Ground state

HI – Hydroiodic acid

IF – Interference filter

LED – Light emitting diode

LP – Long-pass filter

MA – Methylammonium

NA – Numerical aperture

ND – Neutral density filter

NP – Nanoparticle

NR – Nanorods

OIP – Organic-inorganic perovskite

PBS – Polarizing beam splitter

PL – Photoluminescence

PLQY – Photoluminescence quantum yield

PC – Polycarbonate

PMMA – Polymethylmethacrylate

PS – Polystyrene

PVC – Polyvinyl chloride

QD – Quantum dot

QW – Quarter wave plate

RP – Ruddlesden-Popper

RPM – Rotations per minute

SEM – Scanning electron microscopy

STE – Self-trapping exciton

TCSPC – Time-correlated single photon counting

TD – Top-down

TEM – Transmission electron microscopy

UV-Vis – Ultraviolet-Visible

VB – Valance band

VBM – Valance band maximum

WD – Working distance

XRD – X-ray diffraction

CHAPTER 1: INTRODUCTION

Perovskite Background Information

While the focus of this dissertation is on the photophysical changes of perovskite materials, it is impossible to solely do so without a brief introduction to their structural properties and their effects on the optics and photophysics of perovskites. The term perovskite is used to describe a crystallographic group with the general structural formula ABX_3, where A is a monovalent cation (methylammonium (MA) or Cs), B is a divalent cation (typically Pb) and X is a halogen (Cl, Br, or I) [1].Originally, perovskite materials were discovered in 1839 as the naturally forming compound $CaTiO_3$ and modified half a century later to create the man-made variation $CsPbX_3$ [2]. While the $CsPbX_3$ iteration of perovskite materials is sensitive to ambient conditions, they exhibit desired semiconductor properties and are a current interest as an active material in optoelectronic devices.

Perovskite materials can be divided up in to five major types with regards to their structure and dimensionality [3]: polycrystalline films [4], super lattice/crystals [5], single or polycrystalline nanoplatelets/disks [6/7], single or polycrystalline nanospheres/nanocubes (quantum dots/nanoparticles) [8], and single or polycrystalline nanowires/nanorods [9/10]. Regardless of their dimensionality, all perovskite materials share the common unit cell with regards to their crystal structure: a Pb ion is located at the center of the unit cell with halogens occupying the face centers and a cation occupying the vertices, which creates an infinite array of corner sharing PbX_6 octahedra with the cation occupying the space between each unit cell (Figure 1.1). This structure plays an important role in the optical and photophysical properties of perovskites in that the electronic band gap for these materials is composed of a conduction band comprised of the p-orbitals of lead and a valance band made up from hybridized orbitals: a p-orbital of the halogen element and an s-orbital of the lead element [11]. Thus, the unique photophysical and optical characteristics originate from small changes to the Pb-X lattice structure instigated by concomitants (the monovalent cation, organic spacers, etc.) or defects (halogen rich sites, dimers, vacancies, uncapped surface charges, etc.) [12,13]. Subsequently, the unique and tunable structural and optical properties have propelled these materials into the spotlight for optoelectronic applications including: solar cell [1,14-18], lighting and display [1, 19-24], lasing [1, 25-31], photodetection [1, 32-38], and many other applications [1, 39-44].

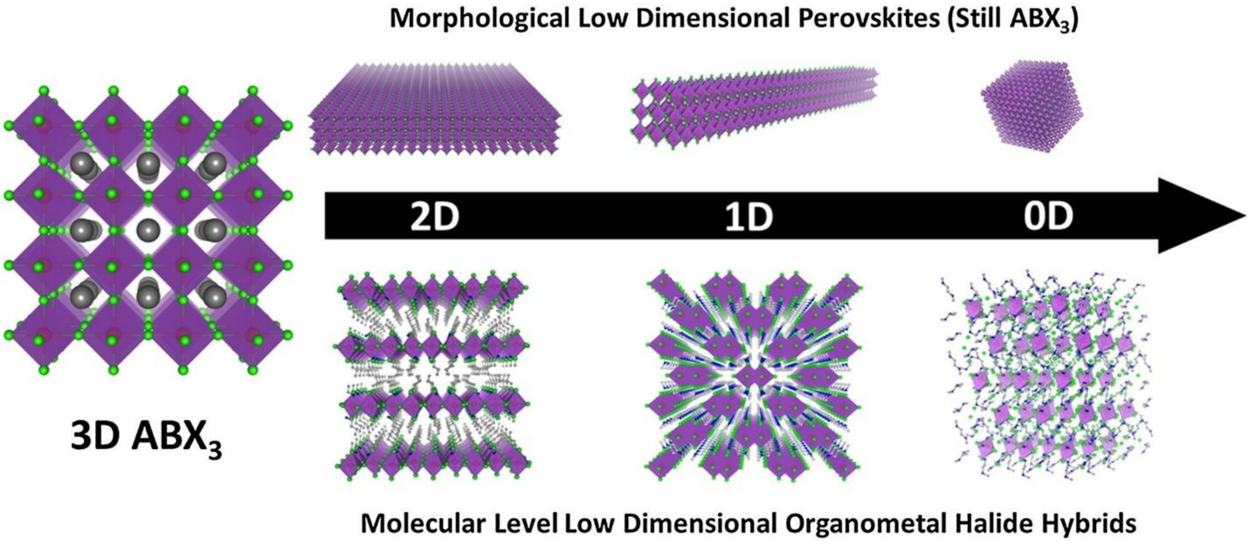

Figure 1.1: Perovskite unit cell (ABX_3) and arrangement in different morphologies and dimensions. Adapted with permission from reference [80].

Photophysical Properties of Perovskite Materials

Structural Impact

Revisiting the ABX_3 structure that constitutes the unit cell of perovskite materials, the orientation of perovskite unit cells greatly effects the overall electronic structure of the material. Depending on the cation (A site), the halogen(s) (X site) used, or even additives to achieve lower ordered structures (organic spacers), perovskites can take on one of five phases: cubic, orthorhombic, tetragonal, monoclinic, and rhombohedral [45]. The cubic phase typically will only occur at elevated temperatures and represents the “most ordered” phase the perovskite material can achieve. As the temperature decreases the PbX_6 octahedra will begin to tilt and give rise to the other lower order phases listed above. These phase transitions occur due to the doubly-bridged halide ion (X-B-X), which is what gives rise to the electronic structure in perovskites and thus impacts their optical and photophysical properties [46,47]. As an example of this, consider iodide perovskites: it was found that as temperature is lowered and the phase shifts to one of lower order, there is a decrease in charge transport across the inorganic framework of the material [48]. This implies that these slight modifications to the I-Pb-I bond angle greatly effects the charge transport properties in the material and based on the valance and conduction band in these materials (Figure 1.4) the band gap is directly influenced by the B site and halide composition [49].

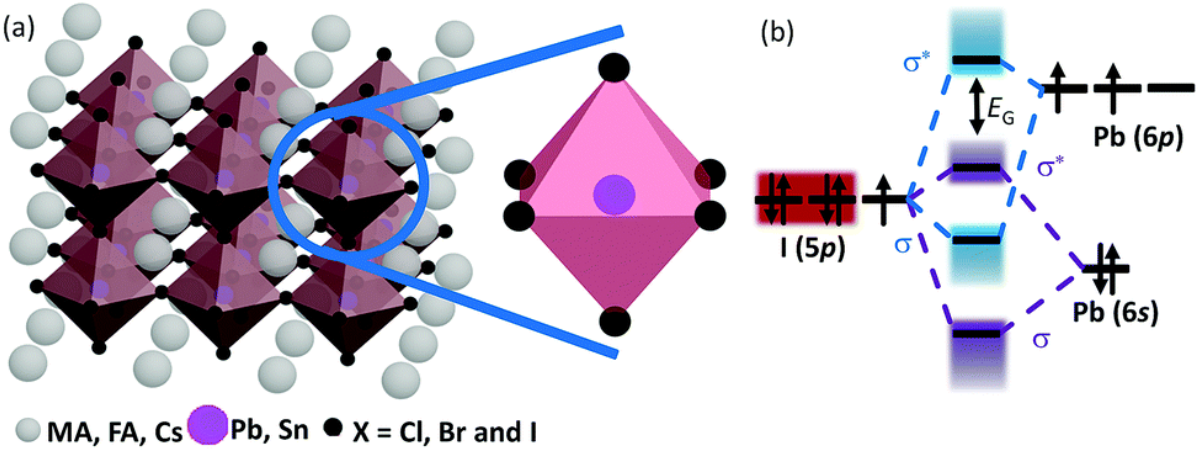

Figure 1.2: (a) Perovskite crystal structure. (b) Bonding (σ) and anti-bonding (σ*) orbital interactions in $MAPbI_3$. Reproduced with permission from reference [50] - Published by The Royal Society of Chemistry.

Further evidence of the structural impact on charge transport properties can be observed in any metal halide perovskite’s energy band gap [50,51]. *Goesten and Hoffmann* have recently published a detailed account on the chemical bonding interaction in metal halide perovskites through the ADF BAND package, at the ZORA-SCAN/TZ2P level of theory. The computational method probes the valance and conduction band for all-inorganic ($CsPbBr_3$) perovskites in a cubic (Pm$\bar{3}$m) crystal structure and establishes a mirrored effect in both the valance and conduction bands created through the interactions between bonding and antibonding orbitals of lead (6s) and bromine (4p). The same treatment was done with the hybrid perovskite analog ($MAPbBr_3$) which, showed the mirror effect persisted when the A site was replaced (Cs → MA) and the interaction between the bonding and antibonding orbitals of lead and bromine persisted with similar bandgaps (2.1 vs 2.2 eV) (Figure 1.3).

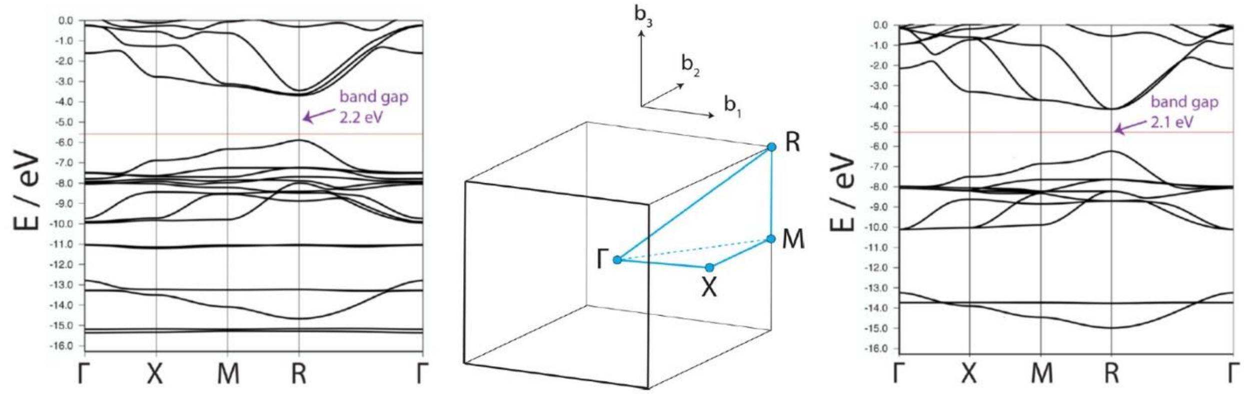

Figure 1.3: Band structure of $CsPbBr_3$, computed at SCAN/TZ2P (left), Brillouin zone for a simple cubic lattice (center), and the band structure of $MAPbBr_3$ (right). Adapted with permission from (M. G. Goesten, R. Hoffmann, Journal of the American Chemical Society (2018) 140 (40), 12996-13010.) Copyright 2019 American Chemical Society.

Similar simulations were conducted for substitution of the B site (Pb → Ge → Sn), which is popular when considering the interest in producing lead free active materials for optoelectronic devices. Conditions for varying the B site cation kept the halide ligand constant (Br) and found that in this case the energy from the s orbital of the B site metal ion will set the energy value for the valance band maximum (VBM) at R (the point where the energy band gap value is smallest). This relationship of the metal s orbital energy to the Br 4p orbital suggests the closer these energy values lie, the wider the band gap mirror and the more the σ* component of that mirror will be displaced to higher energies [51]. As a consequence of the bandgap mirror shift, the valance band is shifted to higher energies closer to that of the conduction band, which results in a narrower bandgap (Figure 1.4) [51].

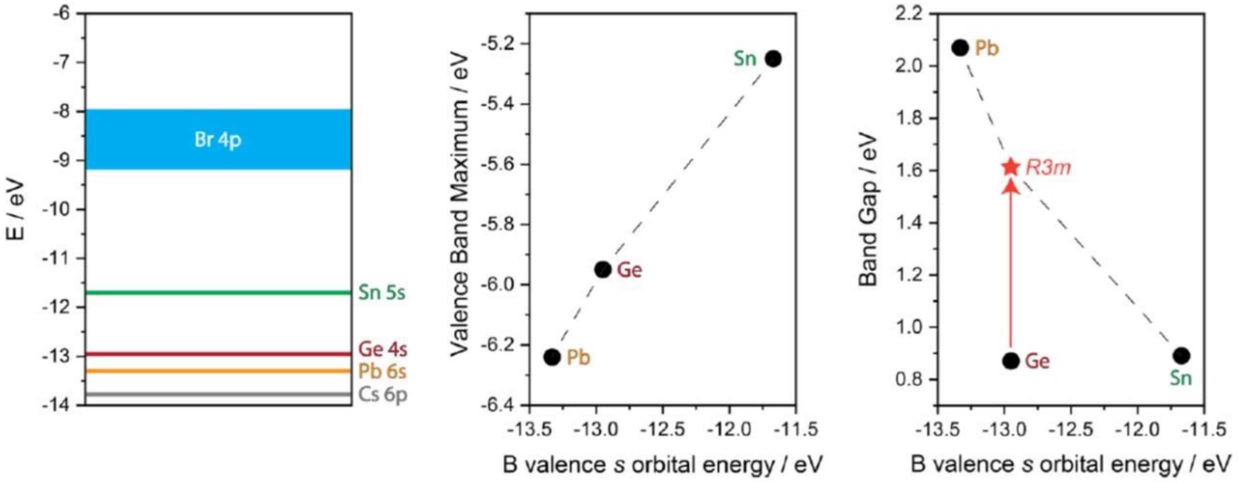

Figure 1.4: Schematic representation of the Br 4p and metal valance s energy levels with the Cs 6p reference band (left). Correlation between B metal valance s energy, VBM (middle), and band gap (right). Adapted with permission from (M. G. Goesten, R. Hoffmann, Journal of the American Chemical Society (2018) 140 (40), 12996-13010.). Copyright 2019 American Chemical Society.

Finally, when the halide site (X) is substituted (I → Br → Cl → F), significant changes occur in the energy bandgap (Figure 1.5), which can be correlated to their valance p orbital energies [51]. Altering the halide composition of both $MAPbX_3$ and $CsPbX_3$ perovskites is known to cause distortions in their crystal lattice at room temperature ($Pm\overline{3}m$ → Pnma) but at the time of writing, no simple explanation relating band gap energies to structural geometry exists for halide substitutions and surmise the bandwidth is dictated entirely by the difference in energy levels between the halide p and lead 6s [51]. Currently, the general consensus is that halide-based perovskites electronic properties emerge from interactions between their atomic orbitals where their energy differences set the bandgap. From this understanding, considerable changes to the electronic band structure are induced by varying the elemental composition of the ABX_3 structure with an emphasis on the B and X sites [51].

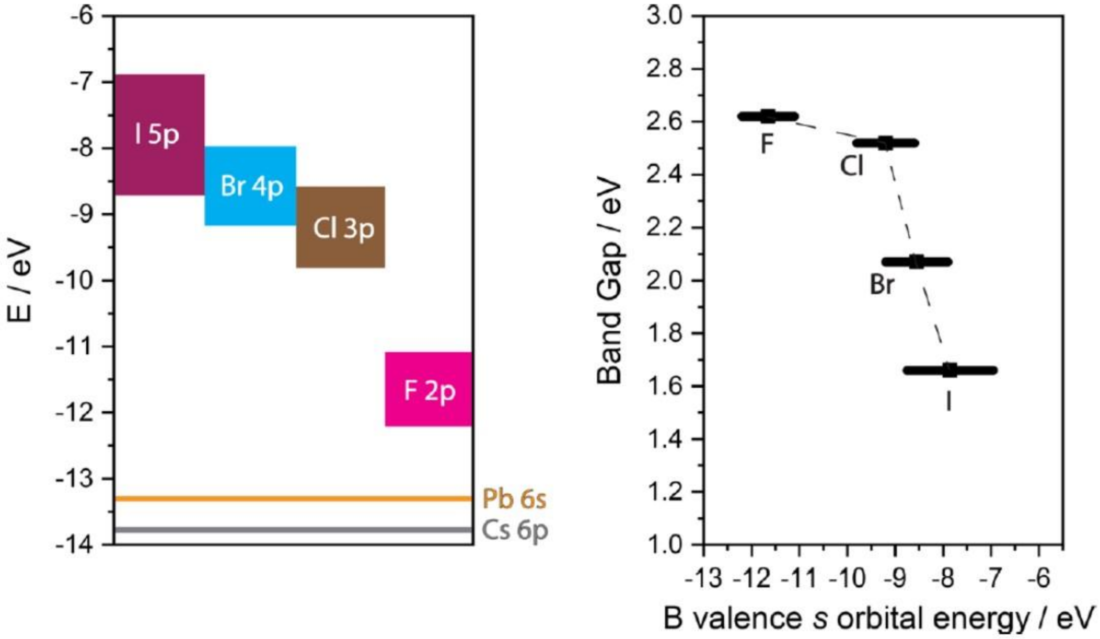

Figure 1.5: Schematic representation of the halide p and Pb 6s energy levels (left), and the correlation between halide p energy and the band gap (right). Adapted with permission from (M. G. Goesten, R. Hoffmann, Journal of the American Chemical Society (2018) 140 (40), 12996-13010.). Copyright 2019 American Chemical Society.

Carrier Relaxation Processes in Perovskite Materials

As discussed above, the electronic band structure of both hybrid and inorganic perovskites around the band edges is dominated by the lead and halide orbital interactions. Initial generation of photoexcited species perovskite materials results in a large population of free carriers (electrons and holes) along with a small population of weakly bound Wannier-Mott type excitons due to their low exciton binding energies ($E_B \leq k_BT$) at room temperature for 3D perovskite films [52]. However, in lower ordered materials (XD, where $0 \leq X \leq 2$) the photoexcited species tend to shift more to lattice bound excitons rather than free carriers ($E_B > k_BT$) due to quantum confinement effects, creating photophysical interactions and pathways currently under investigation [52]. Following the initial excitation and generation of excited state species, fast relaxation processes occur in order to generate the band edge excited species responsible for photon generation. These ultra-fast relaxation processes, such as hot carrier cooling, typically result from carrier-carrier or carrier-phonon interactions dissipating excess energy, which brings carriers to a band-edge state [52, 55]. From the band edge state, three primary processes are responsible for excited species relaxation in perovskite materials: monomolecular charge recombination, bimolecular electron-hole recombination, and Auger recombination (Figure 1.6**)** [52–56].

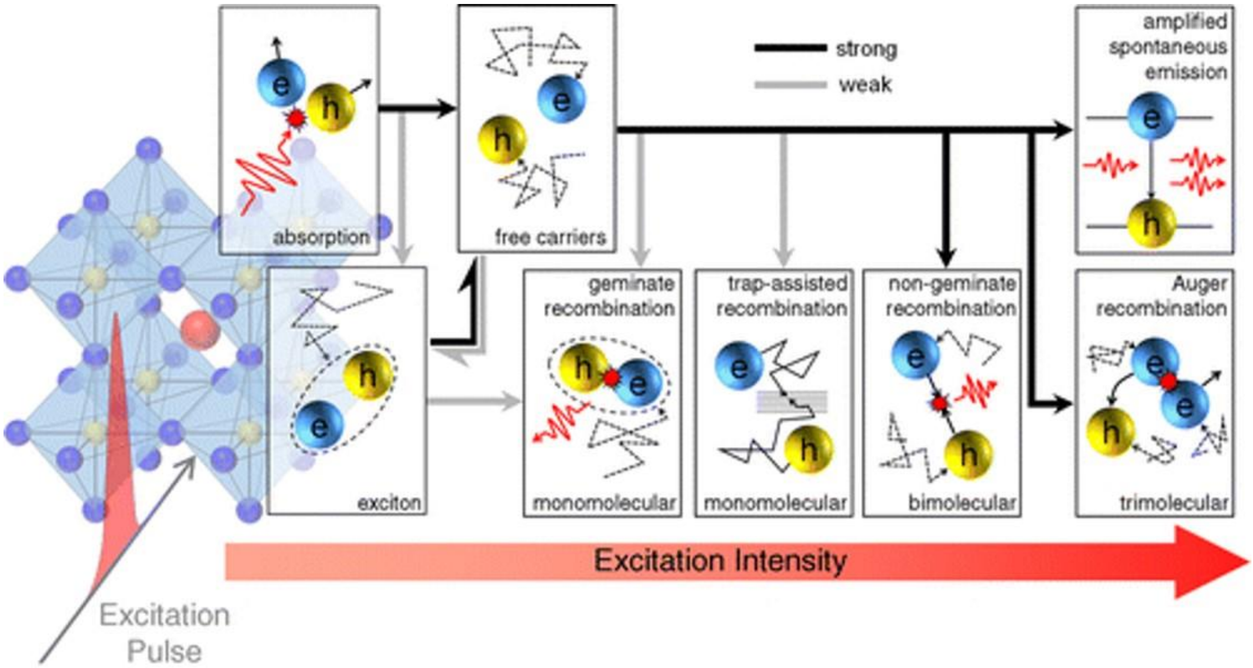

Figure 1.6: Possible photophysical processes and recombination events in perovskite materials. Adapted with permission from (T. C. Sum, N. Mathews, G. Xing, S. S. Lim, W. K. Chong, D. Giovanni, H. A. Dewi, Accounts of Chemical Research (2016) 49 (2), 294-302.). Copyright 2016 American Chemical Society.

Monomolecular recombination, by definition, is a process involving one "particle", which could comprise a valance-band hole, a conduction-band electron, or an exciton containing an already bound electron-hole pair. Due to the types of carriers typically present as discussed above, the monomolecular recombination event is attributed to trap-assisted recombination, which is dependent on several different factors including: trap cross section, energetic depth for the trap, and distribution of traps within a given area all of which are dependent on sample processing conditions [54-56]. Monomolecular recombination processes have been found to be weaker in perovskite materials with low first order recombination coefficients, which indicates lower trap densities or shallow trap states within the material [56]. Discussing trap-assisted recombination in perovskite materials requires a different approach when considering other semiconductor materials due their intrinsic defect tolerance brought on from their band structure discussed in the next section.

The direct reverse for the light absorption process in perovskite semiconductor materials is the bimolecular recombination processes between electrons and holes, which results in direct release of a photon. Bimolecular recombination events, unlike trap-assisted recombination events, are minimally dependent on material processing techniques and thus are intrinsic to the material. Compositional changes, such as those to the Pb or halide site have shown to alter the bimolecular recombination rate with increases being attributed to lighter metals/halide materials [52,54,56]. This phenomenon has been noted in perovskite materials using larger concentrations of Br in X sites, which is attributed to enhancements in exciton binding energies that lead to changes in the continuum absorption near the band-edges [52-54, 56].

The final recombination event is a multi-body process, which involves the recombination of an electron with a hole that coincides with an energy transfer all while maintaining the conservation of momentum to a separate electron or hole [56-90]. This type of recombination event is Auger recombination and with its described mode of energy transfer along with momentum conservation is highly dependent on the electronic band structure of the material [56,58]. The difficulty in achieving efficient Auger recombination events extends from obtaining simultaneous energy and wavevector conservation from a two-band system (conduction and valance). Thus, this implies there are additional bands at play in this system such as split-off bands stemming from spin-orbital coupling and may also be encouraged by phonons either accepting or donating momentum to achieve this form of recombination event [56,57]. While this type of recombination pathway is of little consequence for photovoltaic applications, further investigation into bandgap tuning through synthetic modifications (doping, processing, etc.) is requires for light emitting applications, such as lasing and LED lighting to better control or eliminate this recombination pathway [56].

Emissive processes involving charge carrier recombination in perovskite materials can be divided into two major categories: bimolecular recombination events involving the emission of light from the recombination of non-geminate electron hole pairs or excitonic recombination events involving a bound exciton confined to the material's lattice. Typically, bimolecular recombination events are found in 3D perovskite materials with low exciton binding energies and excitonic mechanics are more prominent in low-dimensionality perovskites with higher electron binding energies [59]. Considering the case of a free carrier system for light emission applications, the radiative recombination from a population of unbound electrons and holes (proportional to n^2 based on the general kinetics model for charge transfer in perovskites) must surpass non-radiative trap-mediated recombination (proportional to n) in order to achieve the desired high quantum yields, which would require high carrier densities in the material. However, looking at this same situation for the standpoint of excitonic radiative processes, if the radiative recombination process were to occur through a populace of bound excitons (proportional to n), lower carrier densities would achieve the desired PLQY due to the nature of the trapped species [59].

Charge transfer kinetic models used to describe perovskite excited state dynamics highlights two classes of non-radiative processes: trap-assisted and Auger recombination. However, at low fluences of power (typical working power and carrier densities for devices: 10^{13}-10^{15} cm^{-3}) Auger recombination is considered negligible [59] and the low abundance of trap-states gives rise to the radiative processes occurring due to biexponential (biexciton) recombination (k_2n^2). A simplified Jablonski diagram (Figure 1.7) highlights these fundamental processes below.

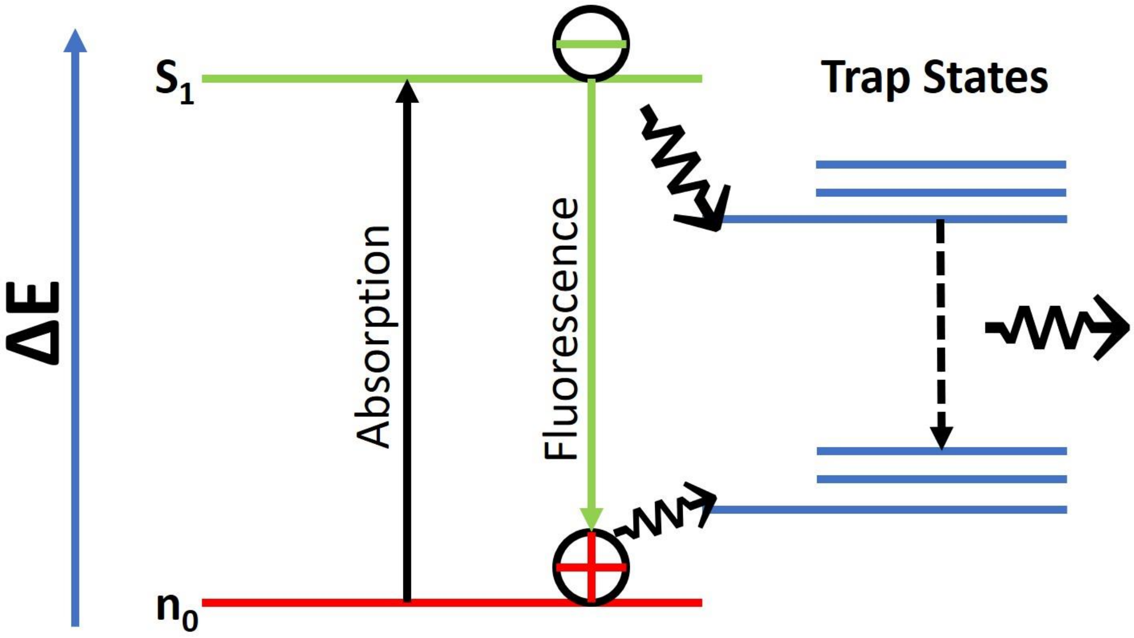

Figure 1.7: Simplified Jablonski diagram outlining the major radiative processes occurring in free carrier perovskite materials.

Defect Influences on Photophysical Processes

Defect tolerance is one of the defining features in perovskite materials and is integral to the overall better performance seen in most perovskite semiconductor materials. This defect tolerant property arises from the unique band structure and can be better understood by considering a local picture of the defect-localized state (DLS) Defects can be generalized into two different categories: shallow defects, which occur when the DLS is situated at or near the valance band maximum (VBM) and deep defects, which are a result of the DLS occurring within the actual band gap of the material. Continuing with the $MAPbI_3$ example from above, the top of the VBM is created through the s-p anti-bonding interaction of I with Pb and the bottom of the

CBM is created through the coupling of empty p-orbitals. This indicates the VBM is higher than the p-orbital of I and the CBM is lower than the atomic Pb orbitals. Because the energies of the possible defects are much higher than that of the CBM or much lower than that of the VBM, these all result in defects outside of the band gap of the material and thus the defects are shallow [60].

Because of this high tolerance to defect states, even polycrystalline halide perovskite materials tend to exhibit superb optical properties. This comes from the generally accepted kinetic model for charge transport in perovskite materials:

$$-\frac{dn}{dt} = k_1 n + k_2 n^2 + k_3 n^3 \tag{1.1}$$

Where n represents the carrier density, k_1 is the defect trapping rate constant, k_2 is the free carrier/exciton recombination constant, and k_3 is the Auger non-radiative rate constant [61]. Both the free carrier recombination constant and Auger non-radiative rate constant are material dependent, which insinuates these two values cannot be improved on through synthetic modifications. However, the trap-dependent rate constant is not an intrinsic property of the material and can be modified through alterations in synthetic approaches [61,62]. Even with their high defect tolerance, elimination of defect states stands as a primary source of interest for the improvement of optical and photophysical properties in perovskite materials with modifications to perovskite synthesis standing at the precipice of change [63-72]. Synthetic modifications to perovskite materials range from altering the ABX_3 composition [73,74] to changing synthetic conditions [75,76] and adding frameworks to stabilize material composition for environmental concerns [68, 77-80]. Further discussion regarding synthetic modification to perovskite materials and their optical/photophysical impact is presented in subsequent sections in this chapter.

Optical and Photophysical Properties of Perovskite Materials: Conclusions

The fundamental optical and photophysical properties are better understood for simplified models of 3D perovskite materials where free charge carriers are assumed to be the dominant species of radiative recombination. These models do not extend to lower-ordered perovskite structures where quantum confinement effects increase exciton binding energies and locally trap excitons within the lattice of the material. Furthermore, constant synthetic modifications are being made to decrease the formation of defects within the perovskite crystal structure, which in turn will lead to new photophysical pathways being accessed by the material itself or changes to existing pathways in order to accommodate lower defect densities within the material. Consistent monitoring of new materials and complete photophysical understanding of existing perovskite materials is paramount towards creating more efficient perovskite materials for eventual commercialized optoelectronic applications.

Perovskite Synthetic Techniques

General Overview

Extraordinary effort has been directed to the endeavors of creating reliable and straightforward methods for synthesizing high quality and size-controlled perovskite materials. The overall flow of these methods can be classified into two broad categories: either top-down methods, where the starting materials are further broken down into lower ordered materials through mechanical (eg. ball milling [79]) or chemical methods (eg. chemical exfoliation [80]), or bottom-down methods, where the materials begin on a molecular level (molecules/ion) and are built up to higher ordered structures through gas or liquid-phase chemical reactions (eg. hot injection [81] or ligand-assisted reprecipitation [82]). Further classification of perovskite material synthesis can be achieved based on the morphology produced by the chosen method

(Nanoparticles, quantum dots, nanoplatelets, nanorods/nanowires, etc.). The subsequent sections on perovskite synthesis in this chapter will provide a brief review of methods employed for the synthesis of perovskite materials based on the resulting morphology of the materials.

Perovskite Quantum Dot Synthesis

The first instance of perovskite colloidal nanoparticles was accomplished by *Schmidt, et al*, through a simple reaction of CH_3NH_3Br and $PbBr_2$ in DMF followed by precipitation in an acetone solution with long-chain alkylammonium bromides, all under ambient atmospheric conditions [83]. After reaction optimization, the final product produced were perovskite quantum dots of about 5nm in diameter with a high quantum yield (83%), though low ambient stability (only stable in aprotic organic solvents). Afterwards, similar methods were used with a mixed halide strategy (varied Br/I and Br/Cl ratios), which demonstrated the ability to tune the emission properties though at a cost of PLQY (50% – 70%) and smaller quantum dot diameter (3.3 nm) [84]. Further investigation of this reprecipitation method prompted another group to change the precursor solution to include both DMF and γ-butrolacetone in the solvent but remove one of the original alkylammonium chains [85]. This synthetic modification resulted in an amorphous layer of nanoparticles and precursor materials as the nanoparticles aggregated due to the solvent system used.

Following the success of methylammonium (MA) based perovskite quantum dots, $CsPbX_3$ (X = Cl, Br, I and mixed systems of Cl/Br and Br/I) based quantum dot systems were developed beginning with work reported by *Protesescu et al.* [86], where a hot injection method was used to synthesize quantum dots by injecting the precursor solution containing Cs-oleate into a PbX_2 solution containing various alkylammonium length chains. This synthetic pathway resulted in colloidal quantum dots exhibiting a cubic-like shape, narrow emission spectra tuned through the visible region, and relatively high quantum yields (50% - 90%) Expanding on this, this group was able to accomplish a wide emissive display gambit in $CsPbX_3$ quantum by adjusting the halogen ratios and using lower temperatures [87].

In addition to the above methods, supersaturated recrystallization techniques have been used to synthesize both MA and Cs based perovskite quantum dots [88,89], which shows excellent PLQY (70%-90%) even after being recrystallized under atmospheric conditions as well as narrow emission spectra (FWHM < 38 nm for highest value) and an average nanoparticle size ≈10 - 14 nm (Figure 1.2). Finally, an ambient-state cubic-phase quantum dot of $CsPbI_3$ was synthesized by *Swarnkar et al.* [90], by simply changing their washing protocol to use methyl acetate to dispose of unreacted precursor materials. This resulted in a stable form of these quantum dots that was previously though to only exist at elevated temperatures.

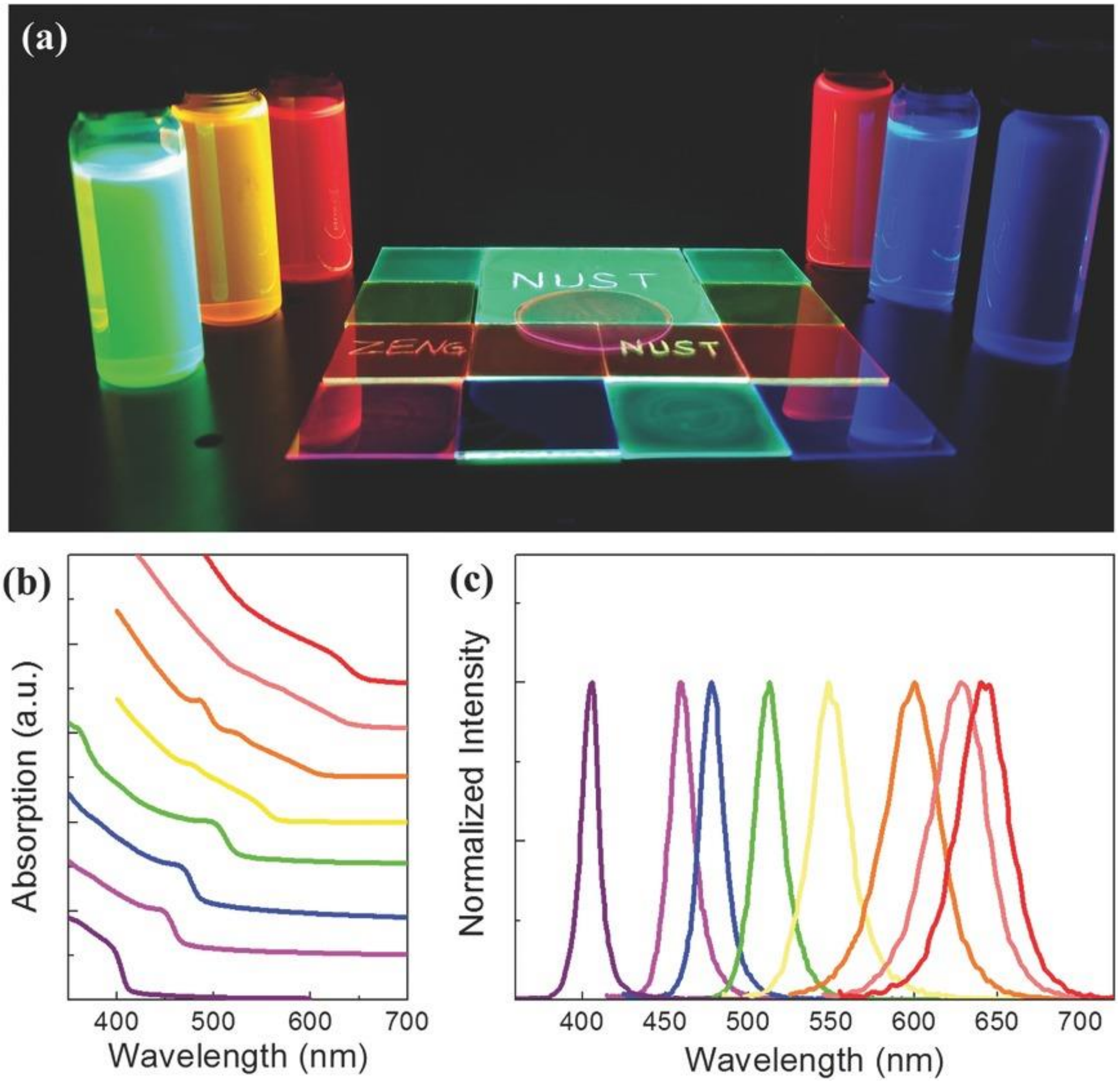

Figure 1.8: (a) $CsPbX_3$ Quantum dots produced from supersaturation recrystallization at room temperature along with their corresponding optical absorbance (b) and photoluminescence (c). Reproduced with permission from reference [85].

Perovskite Nanowire/Nanorod Synthesis

As with the inspiration of many perovskite material synthetic approaches, perovskite nanowire/rod synthesis originally began under a method typically used in creating II-VI and III-V semiconductor nanowires: chemical vapor deposition (CVD) [91,92]. However, the CVD method has been largely phased out in regard to perovskite materials due to the lower formation temperature for creating perovskite structures when compared to other semiconductor materials [92]. Due to the difficulties with CVD methods and a more attractive lower cost, the synthetic approach for perovskite nanowires/rods has shifted to more solution-based methods.

Beginning in 2014, *Horvath, et al.* developed a synthetic method for $MAPbI_3$ nanowires through a low-temperature solution crystallization involving a slip-coating process, which produced nanowires between 50 -200 nm [93]. These wires exhibited charge transfer mechanics over as-synthesized quantum dots [94] however, this slip-coating procedure made control of nanowire length impossible. A two-step spin-coating method was later developed by *Park, et al.* to prepare uniformly sized $MAPbI_3$ nanowires by first loading a PbI_2 solution onto a TiO_2/FTO/glass substrate and afterwards a solution of MAI in isopropanol and DMF was loaded onto the PbI_2 loaded substrate. Rather than forming cubic shaped nanoparticles, 100 nm diameter nanorods were formed instead due to the presence of added DMF in the second loading step [95]. In 2015, *Yang, et al.* achieved synthesis of both MA and Cs based perovskite nanorods through a saturated solution spin-coating technique followed by anion exchange through heating under $MANH_3I$ or $CsNH_3I$ vapor with no discernable changes to rod morphology [96-98].

Hot injection methods have also been used for the synthesis of perovskite nanowire/rod morphologies. This approach was first reported in 2015 by *Yang, et al.* where the cesium precursor was injected into a PbX_2 (X = Br or I) solution with added long chain organic spacer ligands at elevated temperatures (≈ 250 °C) [65]. After this, a period of investigation into hot-injection methods for colloidal perovskite nanowires ensued [80]. This investigation proved fruitful with discoveries such as changes in nanowire length, composition, and shifting the absorption and photoluminescence spectra (Figure 1.9) through merely adding hydrohalic acids (HX, X = Cl, Br, I) [100].In addition to the use of hydrohalic acids employing microwaves was also found as a suitable alternative to synthesize $CsPbBr_3$ nanorods with shorter lengths and red shifting in absorbance onset, which indicates alterations to the bandgap structure [101].

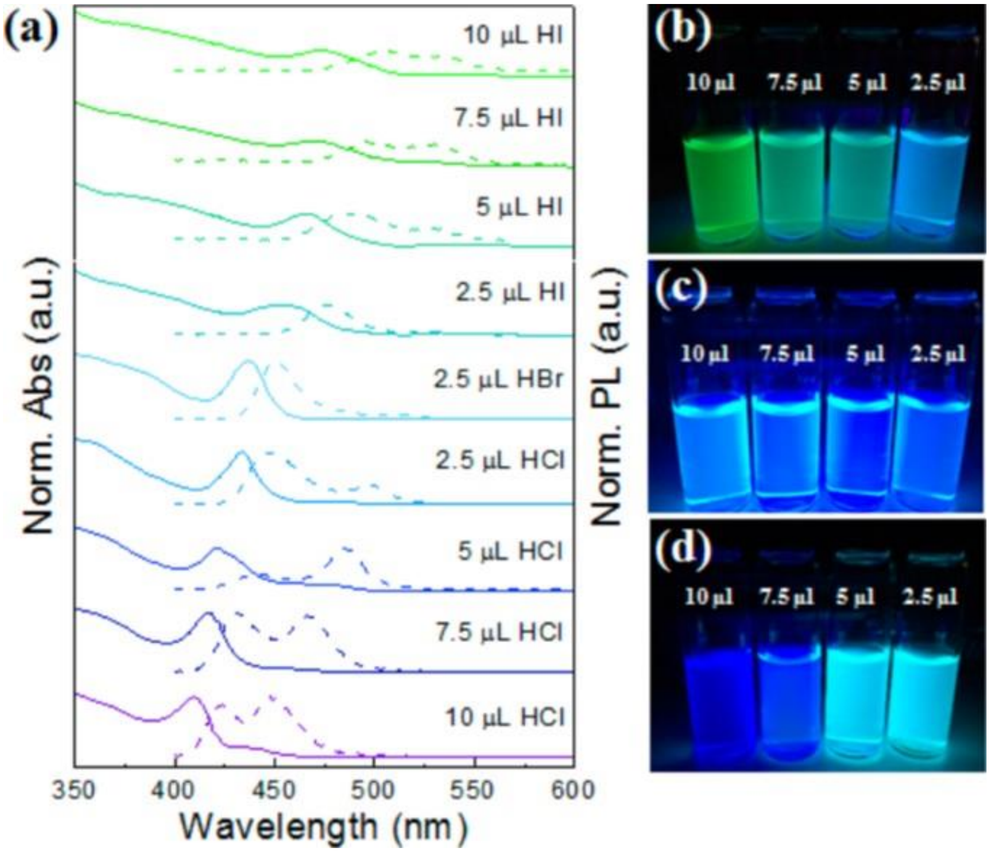

Figure 1.9: (a) Normalized absorption and normalized photoluminescence (PL) spectra of the various sample of CsPbX3 NWs. The solid lines refer to absorption spectra, and dashed lines refer to PL spectra. Panels b, c, and d present photographs of the synthesized NWs with addition of HI, HBr, and HCl acids, respectively, under UV light (λ = 365 nm). Reproduced with permission from (D. Amgar, A. Stern, D. Rotem, D. Porath, L. Etgar. Nano Letters (2017) 17 (2), 1007-1013.). Copyright 2016 American Chemical Society.

Nanowires/nanorods have also been synthesized through template assisted methods, where templates of exact size and shape are used to tune perovskite nanowires/rods to controlled specifications. An effective strategy for employing a template assisted growth scheme is the use of anodized aluminum oxide scaffolds containing specifically oriented nanopores to achieve a controlled nanorod growth [102]. While these scaffolds can help with consistency with nanowire growth and formation, they became a permanent fixture in the nanowire system and removing them is extremely difficult, if not impossible, due perovskite's susceptibility to etchants [80]. Control of nanowire dimensions has also been observed by *He*, *et al.* by a swelling-deswelling microencapsulation method in a polystyrene matrix. In this study, rod size and shape were controlled through precursor concentration and spin speeds when spin-coating the $CsPbBr_3$-PS composites [68]. The nanorods produced in this study exhibited lower PLQY when compared to nanoparticle of encapsulated $MAPbBr_3$-PS composites (27% < 34%) but emitted polarized light when the rods were mechanically aligned through gentle heating.

Perovskite Nanoplatelet Synthesis

One of the first reports of perovskite nanoplatelet synthesis involved the use of the CVD method. This was achieved by depositing lead halide crystals with an epitaxial growth mechanism on a muscovite mica substrate followed by introducing the lead halide crystals to methylammonium halides in a vapor deposition chamber [103]. A similar approach to this was also used by *Liu, et al.* where a precursor solution of aqueous PbI_2 was hot casted on a SiO_2 substrate and subsequently exposed to methylammonium halide CVD [104]. The methods described above show promise for creating 2D perovskite nanoplatelet structures, however the optical properties are varied between the two methods. The first study, using the CVD approach, generates nanoplatelet layers with steeper absorption band onset and red shifted photoluminescence spectra. The second study, using a hot casting method, generates similar absorption bands albeit with different absorption onsets also exhibits differences in their photoluminescence spectra with the onset of broad and unsymmetrical photoluminescence spectra. Considering the optical characteristic differences in both the absorption and photoluminescence spectra between the methods it could indicate different confinement properties between the two methods as well as structural and bandgap variations [56,58,59]. While both methods serve to produce pure perovskite nanoplatelets, its application on a large-scale scheme would prove too costly for commercial applications.

The most common approach seen in the literature is the use of long chained organic surfactants to act as a restraint in directional growth and creating 2D nanoplatelet structures. Nanoplatelets of $CsPbBr_3$ were synthesized through this method using long chained carboxylic acids (oleic acid) in tandem with long chained alkylamines (oleylamine and dodecylamine) and carboxylates of cesium (rather than CsX) as the precursor materials [105,106] (Figure1.10). While this serves as a more precise method for perovskite nanoplatelets, there are still discrepancies in their optical properties from sample to sample. Again, the most noticeable variation from the two different studies is the onset of the absorption band for their samples. The method carried out by *Sun, et al.* produces a nanoplatelet material (n = 4) with a band onset at 510 nm. *Kumar, et al* uses a very similar approach and creates a nanoplatelet material (n = 5) with an absorption band onset at 475 nm. This is an interesting phenomenon due to the notion that adding more layers in 2D nanoplatelet systems tends to red shift the absorption band onset, however the opposite is observed when comparing these two studies. This is a clear indication in a band structure alteration and may be further influenced by quantum confinement effects generated from spacer materials or even the introduction of sub-bandgap layers alongside electron-phonon or phonon-phonon interactions from the lattice [56-59]. These divergences from one method to another warrant further investigation in the underlying photophysical processes governing 2D perovskite materials in order to enhance understanding of a new material as well as to better predict the outcome of optical properties in novel 2D perovskite materials post synthetic modification.

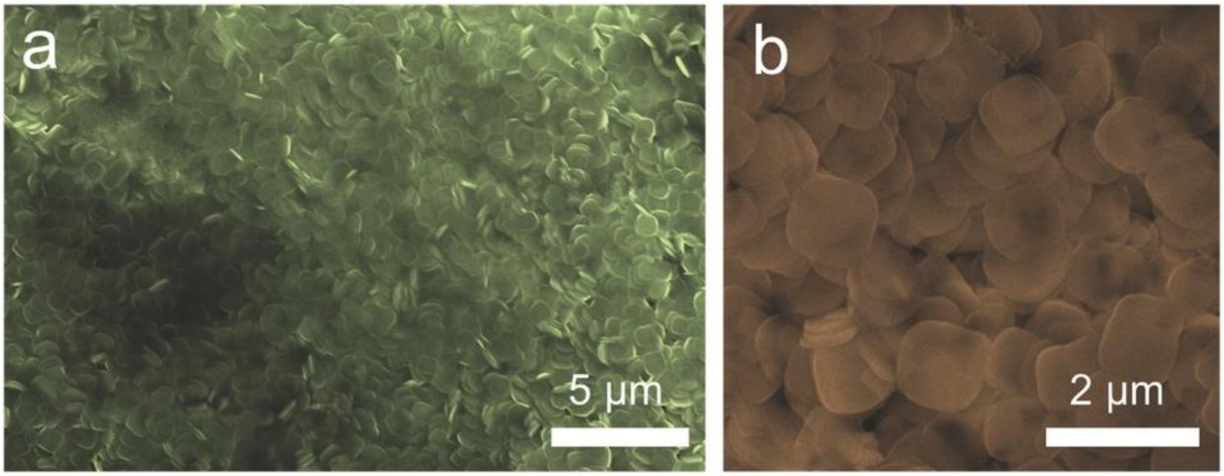

Figure 1.10: 2D ultrathin $CsPbBr_3$ nanoplatelets at (a) low magnification (sample overview) and (b) high magnification (individual nanoplatelet view) SEM images. Reproduced with permission from reference [105].

Perovskite Materials Synthetic Methods: Conclusion

While the development of new synthetic methods for perovskite materials has seen exponential growth over the last decade, there is still a lack of understanding of material outcome when modifying the synthetic methods for perovskite materials. An obvious indication of this are the inconsistent optical and photophysical properties seen from method to method even within the same category of techniques (eg. multiple hot injection methods produce materials with vastly different PLQY). In order to develop more precise synthetic methods for perovskite materials a better understanding of the factors that affect the optical and photophysical processes is required in addition to the main processes that govern the optoelectronic properties of perovskite materials.

Objectives of the Dissertation

The objective of my dissertation work was to probe the optical and photophysical characteristics of novel perovskite materials to facilitate an understanding of their fundamental emissive processes in relation to their synthetic pathways. The first study involved the investigation of $MAPbBr_3$ perovskite nanoparticles embedded into a variety of polymer substrates through swelling-deswelling microencapsulation method. The objectives of this study were to determine if the polymer substrates had any effect on the optical and photophysical properties of the embedded perovskite nanoparticles, assess the prominent photophysical pathways of the material composite, and to determine this strategy's viability as an encapsulation method for perovskite materials. The second study was a continued investigation using the simple microencapsulation swelling-deswelling strategy but with varied precursor concentrations and spin-coating speeds and a different A site cation (Cs), which produced a nanorod like structure. The objectives of this study were to examine the fundamental photophysical processes of this material, while investigating the hypothesis of polarized emission from this sample. The final study investigated the further reduction of dimensionality in 2D Ruddlesden-Popper perovskite materials to quantum dots and nanoplatelets. This study involved three different synthetic pathways to creates 2D-Ruddlesden-Popper perovskite quantum dots and nanoplatelets. Each were investigated spectroscopically to determine the effects of each synthetic pathway on the photophysical properties of the produced materials. The research conducted in these studies is expected to aid in the design of new synthetic approaches in perovskite material synthesis as well as add to a lacking understanding of photophysical properties in novel perovskite materials.

References

[1] J. S. Manser, J. A. Christians, K. V. Prashant. Chemical Reviews (2016) 116 (21), 12956-13008.

[2] H. L. Wells, D. Über. Zeitschrift fü r Anorg. Chemie (1893) 3, 195−210.

[3] S.-T. Ha, R. Su, J. Xing, Q. Zhang, Q. Xiong. *Chem. Sci.*, (2017) 8, 2522-2536.

[4] Y. Cao, N. Wang, H. Tian, J. Guo, Y. Wei, H. Chen, Y. Miao, W. Zou, K. Pan, Y. He, H. Cao, Y. Ke, M. Xu, Y. Wang, M. Yang, K. Du, Z. Fu, D. Kong, D. Dai, Y. Jin, G. Li, H. Li, Q. Peng, J. Wang, W. Huang, Nature, (2018) 562, 249-253.

[5] Y. Tong, E.-P. Yao, A. Manzi, E. Bladt, K. Wang, M. Döblinger, S. Bals, P. Müller-Buschbaum, A. S. Urban, L. Polavarapu, J. Feldmann. Adv. Mater., (2018) 30, 1801117.

[6] Y. Ling, Z. Yuan, Y. Tian, X. Wang, J. C. Wang, Y. Xin, K. Hanson, B. Ma, H. Gao. Adv. Mater., (2016) 28, 305-311.

[7] Q. Liao, K. Hu, H. Zhang, X. Wang, J. Yao, H. Fu. Adv. Mater., (2015) 27, 3405-3410.

[8] Z. Shi, Y. Li, Y. Zhang, Y. Chen, X. Li, D. Wu, T. Xu, C. Shan, G. Du. Nano Lett. (2017) 17, 313-321

[9] A. B. Wong, M. Lai, S. W. Eaton, Y. Yu, E. Lin, L. Dou, A. Fu, P. Yang. Nano Lett. (2015) 15, 5519-5524.

[10] Y. Liu, M. Guo, S. Dong, X. Jiao, T. Wang, D. Chen. J. Mater. Chem. *C*, (2018) 6, 7797-7802.

[11] F. Brivio, A. B. Walker, A. Walsh. APL Mater. (2013) 1, 042111.

[12] A. R. Srimath Kandada, A. Petrozza. Accounts of Chemical Research (2016) 49 (3), 536-544.

[13] C Zhou, H. Lin, Q. He, L. Xu, M. Worku, M. Chaaban, S. Lee, X. Shi, M.-H. Du, B. Ma. Materials Science and Engineering: R: Reports (2019) 137, 38-65.

[14] M. A. Green, A. Ho-Baillie, H. J. Snaith. Nature Photonics (2014) 8, 506.

[15] N. J. Jeon, J. H. Noh, W. S. Yang, Y. C. Kim S. Ryu, J. Seo. S. I. Seok. Nature (2015) 517, 476.

[16] Q. Lin, A. Armin, R. C. R. Nagiri, P. L. Burn, P. Meredith, Nature Photonics (2014) 9, 106.

[17] N.-G. Park. Materials Today (2015) 18 (2), 65-72.

[18] H. Tsai, W. Nie, J.-C. Blancon, C. C. Stoumpos, R. Asadpour, B. Harutyunyan, A. J. Neukirch, R. Verduzco, J. J. Crochet, S. Tretiak, L. Pedesseau, J. Even, M. A. Alam, G. Gupta, J. Lou, P. M. Ajayan, M. J. Bedzyk, M. G. Kanatzidis, A. D. Mohite, Nature (2016) 536, 312.

[19] Q. Zhou, Z. Bai, W. Lu, Y. Wang, B. Zou, H. Zhong, Adv. Mater. (2016) 28: 9163-9168.

[20] H.-C. Wang, S.-Y. Lin, A.-C. Tang, B. P. Singh, H.-C. Tong, C.-Y. Chen, Y.-C. Lee, T.-L. Tsai, R.-S. Liu. Angew. Chem. Int. Ed. (2016) 55, 7924.

[21] Z. Bai, H. Zhong. Science Bulletin (2015) 60 (18), 1622-1624.

[22] G.-L. Yang, H.-Z. Zhong. Chinese Chemical Letters (2016) 27 (8), 1124-1130.

[23] Y. Gao, C. Huang, C. Hao, S. Sun, L. Zhang, C. Zhang, Z. Duan, K. Wang, Z. Jin, N Zhang, A. V. Kildishev, C.-W. Qiu, Q. Song, S. Xiao. ACS Nano (2018) 12 (9), 8847-8854.

[24] M. B. Teunis, K. N. Lawrence, P. Dutta, A. P. Siegel, R. Sardar. Nanoscale (2016) 8 (40), 17433-17439.

[25] G Xing, N. Mathews, S. S. Lim, N. Yantara, X. Liu, D. Sabba, M. Grätzel, S. Mhaisalkar, T. C. Sum. Nature Materials (2014) 13, 476.

[26] H. Zhu, Y. Fu, F. Meng, X. Wu, Z. Gong, Q. Ding, M. V. Gustafsson, M. T. Trinh, S. Jin, X. Y. Zhu. Nature Materials (2015) 14, 636.

[27] F. Deschler, M. Price, S. Pathak, L. E. Klintberg, D.-D. Jarausch, R. Higler, S. Hüttner, T. Leijtens, S. D. Stranks, H. J. Snaith, M. Atatüre, R. T. Phillips, R. H. Friend. The Journal of Physical Chemistry Letters (2014) 5 (8), 1421-1426.

[28] S. W. Eaton, M. Lai, N. A. Gibson, A. B. Wong, L. Dou, J. Ma, L.-W. Wang, S. R. Leone, P. Yang. Proceedings of the National Academy of Sciences 2016, 113 (8), 1993.

[29] S. Yakunin, L. Protesescu, F. Krieg, M. I. Bodnarchuk, G. Nedelcu, M. Humer, G. De Luca, M. Fiebig, W. Heiss, M. V. Kovalenko. Nature Communications (2015) 6 (1), 8056.

[30] Y. Wang, X. Li, J. Song, L. Xiao, H. Zeng, H. Sun, Adv. Mater. (2015) 27: 7101-7108.

[31] Y. Jia, R. A. Kerner, A. J. Grede, B. P. Rand, N. C. Giebink. Nature Photonics (2017) 11 (12), 784-788.

[32] C. Li, C. Han, Y. Zhang, Z. Zang, M. Wang, X. Tang, J. Du. Solar Energy Materials and Solar Cells (2017) 172, 341-346.

[33] L. Dou, Y. Yang, J. You Z. Hong W.-H. Chang, G. Li, Y. Yang. Nature Communications (2014) 5, 5404.

[34] H. Lu, W. Tian, F. Cao, Y. Ma, B. Gu, L. Li, Adv. Funct. Mater. (2016) 26: 1296-1302.

[35] Y. Lee, J. Kwon, E. Hwang, C. Ra, W. J. Yoo, J. Ahn, J. H. Park, J. H. Cho, Adv. Mater. (2015) 27: 41-46.

[36] L. Shen, Y. Fang, D. Wang, Y. Bai, Y. Deng, M. Wang, Y. Lu, J. Huang. Adv. Mater. (2016) 28: 10794-10800.

[37] Y. Fang, Q. Dong, Y. Shao, Y. Yuan, J. Huang. Nature Photonics (2015) 9, 679.

[38] H. Sun, T. Lei, W Tian, F. Cao, J. Xiong, L. Li. Small (2017) 13, 1701042.

[39] X. Y. Chin, D. Cortecchia, J. Yin, A. Bruno, C. Soci. Nature Communications (2015) 6 (1), 7383.

[40] D. B. Mitzi, C. D. Dimitrakopoulos, L. L. Kosbar. Chemistry of Materials (2001) 13 (10), 3728-3740.

[41] T. Matsushima, S. Hwang, A. S. Sandanayaka, C. Qin, S. Terakawa, T. Fujihara, M. Yahiro, C. Adachi. Adv. Mater. (2016) 28: 10275-10281.

[42] C. Pan, T. Takata, M. Nakabayashi, T. Matsumoto, N. Shibata, Y. Ikuhara, K. Domen. Angew. Chem. Int. Ed. (2015) 54: 2955-2959.

[43] Y. L. Zhu, W. Zhou, Y. J. Zhong, Y. F.Bu, X. Y. Chen, Q. Zhong, M. L. Liu, Z. P. Shao. Adv. Energy Mater. (2017) 7, 1602122.

[44] B. R. Sutherland, E. H. Sargent. Nature Photonics (2016) 10, 295.

[45] K. Chen, S. Schünemann, S. Song, H. Tüysüz. Chemical Society Reviews (2018) 47 (18), 7045-7077.

[46] R. X. Yang, J. M. Skelton, E. L. da Silva, J. M. Frost, A. Walsh. J. Phys. Chem. Lett. (2017) 8, 4720-4726.

[47] C. C. Stoumpos, M. G. Kanatzidis, Acc. Chem. Res. (2015) 48, 2791-2802.

[48] C. C. Stoumpos, C. D. Malliakas, M. G. Kanatzidis. Inorg. *Chem.*, (2013) 52, 9019-9038.

[49] L. Protesescu, S. Yakunin, M. I. Bodnarchuk, F. Krieg, R. Caputo, C. H. Hendon, R. X. Yang, A. Walsh, M. V. Kovalenko. Nano Lett. (2015) 15 , 3692-3696.

[50] S. Kumar, J. Jagielski, S. Yakunin, P. Rice, Y.-C. Chiu, M. Wang, G. Nedelcu, Y. Kim, S. Lin, E. J. G. Santos, M. V. Kovalenko, C.-J. Shih. ACS Nano (2016) 10 (10), 9720-9729.

[51] M. G. Goesten, R. Hoffmann, Journal of the American Chemical Society (2018) 140 (40), 12996-13010.

[52] T. C. Sum, N. Mathews, G. Xing, S. S. Lim, W. K. Chong, D. Giovanni, H. A. Dewi, Accounts of Chemical Research (2016) 49 (2), 294-302.

[53] N. Mondal, A. De, S. Das, S. Paul, A. Samanta, Nanoscale (2019) 11 (20), 9796-9818.

[54] D.W. deQuilettes, K. Frohna, D. Emin, T. Kirchartz, V. Bulovic, D. S. Ginger, S. D. Stranks, Chemical Reviews (2019) 119 (20), 11007-11019.

[55] L. M. Herz, Annual Review of Physical Chemistry (2016) 67 (1), 65-89.

[56] M. B. Johnston, L. M. Herz, Accounts of Chemical Research (2016) 49 (1), 146-154.

[57] A. R. Beattie, P. T. Landsberg, Proc. R. Soc. London, Ser. A (1959) 249, 16– 29.

[58] A. Haug, Journal of Physics C: Solid State Physics (1983) 16 (21), 4159-4172.

[59] Y. Jiang, X. Wang, A. Pan. Adv. Mater. (2019) 1806671.

[60] J. Kang, L.-W. Wang. The Journal of Physical Chemistry Letters (2017) 8 (2), 489-493.

[61] M. B. Johnston, L. M. Herz. Accounts of Chemical Research (2016) 49 (1), 146-154.

[62] J. S. Manser, J. A. Christians, P. V. Kamat. Chemical Reviews (2016) 116 (21), 12956-13008.

[63] S. D. Stranks, ACS Energy Letters (2017) 2 (7), 1515-1525.

[64] T. Zhao, C.-C. Chueh, Q. Chen, A. Rajagopal, A.K.Y. Jen, ACS Energy Letters (2016) 1 (4), 757-763.

[65] X. Zheng, B. Chen, J. Dai, Y. Fang, Y. Bai, Y. Lin, Y. Wei, H. Zeng, C. Xiao, J. Huang, Nature Energy (2017) 2 (7), 17102.

[66] F. Wang, S. Bai, W. Tress, A. Hagfeldt, F. Gao, npj Flexible Electronics 2018, 2 (1), 22.

[67] N. K. Noel, A. Abate, S. D. Stranks, E. S. Parrott, V. M. Burlakov, A. Goriely, H. J. Snaith, ACS Nano 2014, 8 (10), 9815-9821.

[68] J. He, A. Towers, Y. Wang, P. Yuan, Z. Jiang, J. Chen, A. J. Gesquiere, S.-T. Wu, Y. Dong. Nanoscale 2018**,** *10* (33), 15436-15441.

[69] W. Xu, Q. Hu, S. Bai, C. Bao, Y. Miao, Z. Yuan, T. Borzda, A. J. Barker, E. Tyukalova, Z. Hu, M. Kawecki, H. Wang, Z. Yan, X. Liu, X. Shi, K. Uvdal, M. Fahlman, W. Zhang, M. Duchamp, J.-M. Liu, A. Petrozza, J. Wang, W. Huang, F. Gao, Nature Photonics (2019) 13 (6), 418-424.

[70] S. Singh, B. Sharma, G. Banappanavar, A. Dey, S. Chakraborty, K. L. Narasimhan, P. Bhargava, D. Kabra, ACS Applied Energy Materials (2018) 1 (5), 1870-1877.

[71] S. Lee, J. H. Park, B. R. Lee, E. D. Jung, J. C. Yu, D. Di Nuzzo, R. H. Friend, M. H. Song, The Journal of Physical Chemistry Letters (2017) 8 (8), 1784-1792.

[72] S. Colella, E. Mosconi, P. Fedeli, A. Listorti, F. Gazza, F. Orlandi, P. Ferro, T. Besagni, A. Rizzo, G. Calestani, G. Gigli, F. De Angelis, R. Mosca, Chemistry of Materials 2013, 25 (22), 4613-4618.

[73] A. J. Barker, A. Sadhanala, F. Deschler, M. Gandini, S. P. Senanayak, P. M. Pearce, E. Mosconi, A. J. Pearson, Y. Wu, A. R. Srimath Kandada, T. Leijtens, F. De Angelis, S. E. Dutton, A. Petrozza, R. H. Friend, ACS Energy Letters (2017) 2 (6), 1416-1424.

[74] M. P. U, Haris, R. Bakthavatsalam, S. Shaikh, B. P. Kore, D. Moghe, R. G. Gonnade, D. D. Sarma, D. Kabra, J. Kundu, Inorganic Chemistry (2018) 57 (21), 13443-13452.

[75] S. T. Williams, A. Rajagopal, S. B. Jo, C. C. Chueh, T. F. L. Tang, A. Kraeger, A. K. Y. Jen, Journal of Materials Chemistry A (2017) 5 (21), 10640-10650.

[76] J. Ren, T. Li, X. Zhou, X. Dong, A. V. Shorokhov, M. B. Semenov, V. D. Krevchik, Y. Wang, Chemical Engineering Journal (2019) 358, 30-39.

[77] D. Zhang, W. Zhou, Q. Liu, Z. Xia, ACS Applied Materials & Interfaces (2018) 10 (33), 27875-27884.

[78] H.-C. Wang, S.-Y. Lin, A.-C. Tang, B. P. Singh, H.-C. Tong, C.-Y. Chen, Y.-C. Lee, T.-L. Tsai, R.-S. Liu, Angew. Chem. Int. Ed. (2016) 55, 7924.

[79] Z.-Y. Zhu, Q.-Q. Yang, L.-F. Gao, L. Zhang, A.-Y. Shi, C.-L. Sun, Q. Wang, H.-L. Zhang. The Journal of Physical Chemistry Letters (2017) 8 (7), 1610-1614.

[80] V. A. Hintermayr, A. F. Richter, F. Ehrat, M. Döblinger, W. Vanderlinden, J. A. Sichert, Y. Tong, L. Polavarapu, J Feldmann, A. S. Urban. Adv. Mater. (2016) 28, 9478-9485.

[81] N. Wang, W. Liu, Q. Zhang. Small Methods (2018) 2, 1700380.

[82] C. de Weerd, T. Gregorkiewicz, L. Gomez. Adv. Opt. Mater. (2018) 6, 1800289.

[83] L. C. Schmidt, A. Pertegás, S. González-Carrero, O. Malinkiewicz, S. Agouram, G. Mínguez Espallargas, H. J. Bolink, R. E. Galian, J. Pérez-Prieto. Journal of the American Chemical Society (2014) 136 (3), 850-853.

[84] F. Zhang, H. Zhong, C. Chen, X.-G. Wu, X. Hu, H. Huang, J. Han, B. Zou, Y. Dong, Y. ACS Nano (2015) 9 (4), 4533-4542.

[85] J. Xing, F. Yan, Y. Zhao, S. Chen, H. Yu, Q. Zhang, R. Zeng, H. V. Demir, X. Sun, A. Huan, Q. Xiong. ACS Nano (2016) 10 (7), 6623-6630.

[86] L. Protesescu, S. Yakunin, O. Nazarenko, D. N. Dirin, M. V. Kovalenko. ACS Appl. Nano Mater. (2018) 1, 1300-1308.

[87] G. Nedelcu, L. Protesescu, S. Yakunin, M. I. Bodnarchuk, M. J. Grotevent, M. V. Kovalenko. Nano Letters (2015) 15 (8), 5635-5640.

[88] P. K. Nayak, D. T. Moore, B. Wenger, S. Nayak, A. A. Haghighirad, A. Fineberg, N. K. Noel, O. G. Reid, G. Rumbles, P Kukura, P. K. A. Vincent, H. J. Snaith. Nature Communications (2016) 7 (1), 13303.

[89] X. Li, Y. Wu, S. Zhang, B. Cai, Y. Gu, J. Song, H. Zeng. Adv. Funct. Mater. (2016) 26: 2435-2445.

[90] A. Swarnkar, A. R. Marshall, E. M. Sanehira, B. D. Chernomordik, D. T. Moore, J. A. Christians, T. Chakrabarti, J. M. Luther. Science (2016) 354 (6308), 92-95.

[91] F. Vietmeyer, P. A. Frantsuzov, B. Janko, M. Kuno. Phys. Rev. B: Condens. Matter Mater. Phys., (2011) 83, 115319.

[92] S.-T. Ha, R. Su, J. Xing, Q. Zhang, Q. Xiong. Chemical Science (2017) 8 (4), 2522-2536.

[93] E. Horváth, M. Spina, Z. Szekrényes, K. Kamarás, R. Gaal, D. Gachet, L. Forró. Nano Letters (2014) 14 (12), 6761-6766.

[94] M. Spina, M. Lehmann, B. Náfrádi, L. Bernard, E. Bonvin, R. Gaál, A. Magrez, L. Forró, E. Horváth, Small (2015) 11: 4824-4828.

[95] J.-H, Im, J. Luo, M. Franckevičius, N. Pellet, P. Gao, T. Moehl, S. M. Zakeeruddin, M. K. Nazeeruddin, M. Grätzel, N.-G. Park. (2015) 15 (3), 2120-2126.

[96] A. B. Wong, M. Lai, S. W. Eaton, Y. Yu, E. Lin, L. Dou, A. Fu, P. Yang. Nano Letters (2015) 15 (8), 5519-5524.

[97] S. W. Eaton, M. Lai, N. A. Gibson, A. B. Wong, L. Dou, J. Ma, L. W. Wang, S. R. Leone, P. Yang. Proceedings of the National Academy of Sciences (2016) 113 (8), 1993-1998.

[98] L. Dou, M. Lai, C. S. Kley, Y. Yang, C. G. Bischak, D. Zhang, S. W. Eaton, N. S. Ginsberg, P. Yang. Proceedings of the National Academy of Sciences (2017) 114 (28), 7216-7221.

[99] D. Zhang, S. W. Eaton, Y. Yu, L. Dou, P. Yang. Journal of the American Chemical Society (2015) 137 (29), 9230-9233.

[100] D. Amgar, A. Stern, D. Rotem, D. Porath, L. Etgar. Nano Letters (2017) 17 (2), 1007-1013.

[101] W. Liu, J. Zheng, S. Cao, L. Wang, F. Gao, K.-C. Chou, X. Hou, W. Yang. Inorganic Chemistry (2018) 57 (3), 1598-1603.

[102] H.-C. Kwon, W. Yang, D. Lee, J. Ahn, E. Lee, S. Ma, K. Kim, S.-C. Yun, J. Moon. ACS Nano (2018) 12 (5), 4233-4245.

[103] S. T. Ha, X. Liu, Q. Zhang, D. Giovanni, T. C. Sum, Q. Xiong. Advanced Optical Materials (2014) 2: 838-844.

[104] J Liu, Y. Xue, Z. Wang, Z.-Q. Xu, C. Zheng, B. Weber, J. Song, Y. Wang, Y. Lu, Y. Zhang, Q. Bao. ACS Nano (2016) 10 (3), 3536-3542.

[105] J Song, L. Xu, J. Li, J. Xue, Y. Dong, X. Li, H. Zeng. Adv. Mater. (2016) 28: 4861-4869.

[106] S. B. Sun, D. Yuan, Y. Xu, A. F. Wang, Z. T. Deng. ACS Nano (2016) 10, 3648.

CHAPTER 2: SPECTROSCOPIC METHODS AND INSTRUMENTAL THEORY

Overview

Photoluminescent spectroscopic techniques can readily be divided into two categories: steady-state and time-resolved measurements. Even with the capabilities of time-resolved techniques being able to probe the photophysical processes occurring over time scales ranging from femtoseconds to milliseconds, steady-state measurements are often required to verify time resolved data and compliment findings. To perform steady-state measurements a continuous excitation source is required along with a spectrometer containing a detector in order to analyze transmitted or emitted light. Steady state measurements also require a state of equilibrium to be established between excitation and emissive processes along with relaxation of various vibrational modes. Conversely, time-resolved measurements capture information about the analyte of interest while in the excited state to probe various transient phenomenon such as: energy transfer, proton transfer, electronic relaxation, and charge transfer. Though in order to accomplish time-resolved measurements, a much more sophisticated set-up is required. The key differences between the set-up for steady-state and time-resolved measurements are the required pulsed excitation source and a detector able to process time resolved events at a faster pace than the scale of the process under investigation. [1-8]

This chapter is a general overview of the instrumentation being used for steady-state and time resolved spectroscopic measurements. This chapter will also serve as an introduction the general theory and set-up being utilized in this dissertation.

UV-Vis Absorption Spectroscopy Theory

Absorption spectroscopy measures the amount of incident light transmitted through a sample compared to the light absorbed by the sample. Specifically, absorption measurements are compiled from the ultraviolet (UV) and visible (Vis) regions of the electromagnetic spectrum, which in the case of semiconductor materials are very important as they correlate with the band-gap edge(s) of a given material. The wavelength range capable of these instruments is typically from 200 – 1100 nm based on the excitation sources usually present. In order for an absorption process to take place, the wavelength of light being absorbed much match the difference in energy levels for the transition. The following equation relates the energy transition to incident wavelength of light:

$$\Delta E = {}^{hc}/_{\lambda} \tag{2.1}$$

Where $\Delta E = E_2 - E_1$, which corresponds to the difference in energy between the excited state to the ground state [9], h is Plank's constant, c is the speed of light, and λ is the wavelength of the incident light absorbed. Overlap between the states and population of the molecules along with specific selection rules govern the resulting intensity of observed transition [10]. As a form of molecular spectroscopy, absorption spectra typically consist of one or more broad peaks representing both the electronic and vibrionic transitions available to the molecule of interest.

Intensity of the absorption process as it relates to the material of interest is quantified through the Beer-Lambert law [11]. The following equation can be used to describe monochromatic light of intensity I_0 incident of a sample of thickness L, traveling along an infinite path (dL) and experiencing a reduction of intensity (dI):

$$dI = -I\sigma\mathrm{N}\, dL \tag{2.2}$$

Where σ is the effective cross-section of absorption and N is the density of molecules. Thus, the number of photons absorbed is proportional to the density of molecules present as well as the photon density. Integration of the above equation yields [10]:

$$I = I_0 e^{-\sigma N L} \tag{2.3}$$

This equation can be expressed as its more popular form:

$$A(\lambda) = \varepsilon(\lambda) c L \tag{2.4}$$

Where A is the absorbance at a wavelength (λ) and provided by $\log_{10}(I_0/I)$, c is the molar concentration of the analyte of interest expressed in units of mol/dm^3 and related to the species density by $N = N_A c(10^{-3})$, and ε(λ) is the molar extinction coefficient expressed in units of mol^{-1} cm^{-1} dm^3 at a wavelength (λ) and related to the optical absorbance cross-section through $\sigma = 3.81 \times 10^{-19}\varepsilon$. The typically pathlength of the sample is dictated by the cell length of the sample holder, in which most cases are 1 cm.

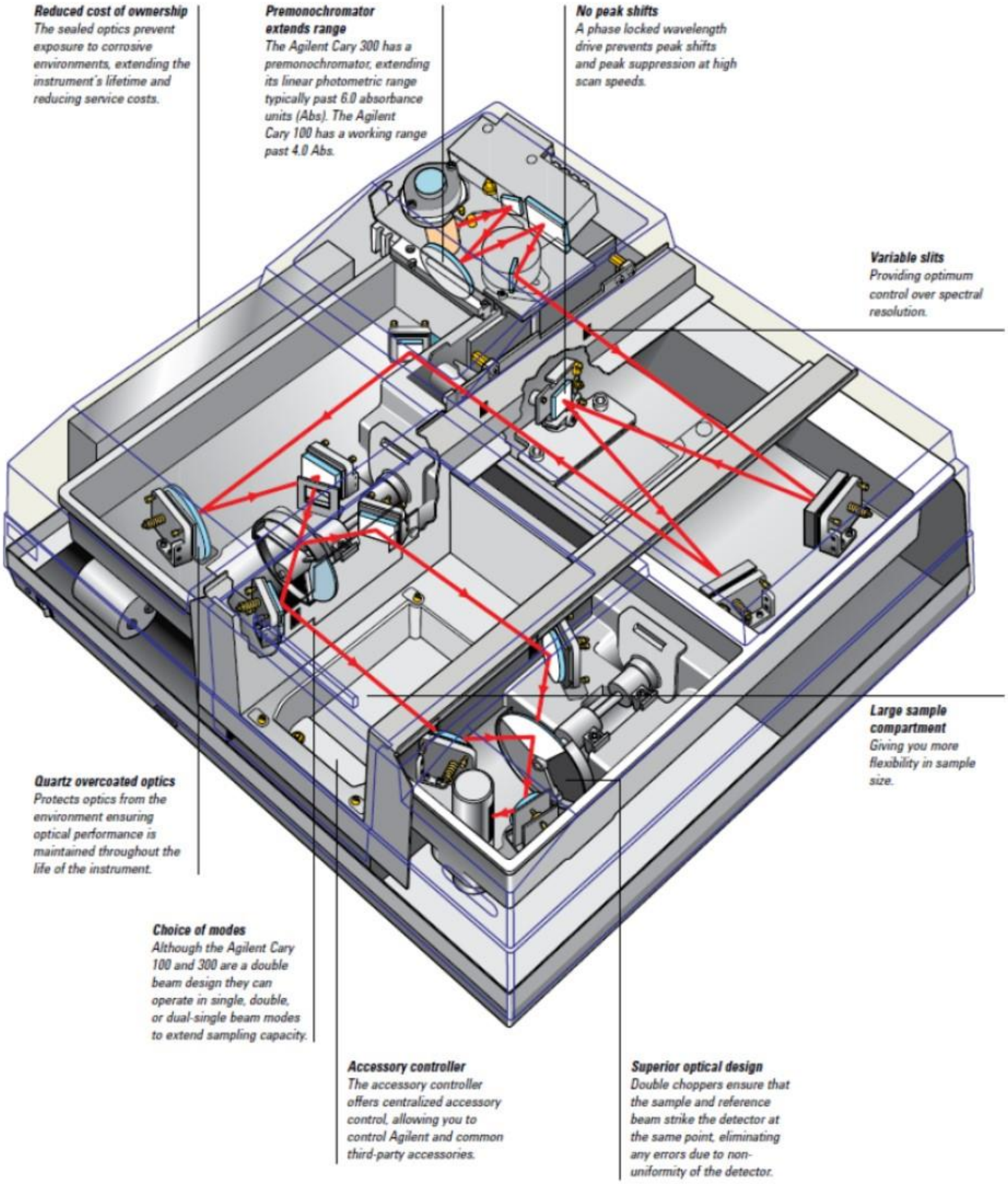

Figure 2.1: Schematic and optical pathways for Cary 300 UV-Vis spectrometer [12].

UV-Vis Absorbance Spectroscopy Methods

The instrument used for absorption spectrum measurements was a Cary 300 UV-Vis spectrometer (Figure 2.1). This is a dual beam, dual chopper, monochromator UV-vis spectrometer, centrally controlled via PC. The spectrometer was equipped with two excitation sources, a deuterium lamp for UV excitation (190 – 400 nm) and a tungsten-halogen lamp with quartz window for Vis excitation (400-900 nm). The grating used is a 30 x 35mm, 1200 lines/mm, blaze angle 8.6° at 240nm grating and the detector used is an R928 PMT, which provide 0.189 nm of spectral resolution [12]. All samples were examined in ambient conditions with no further preparation work and temperature adjustments.

Fluorescence Spectroscopy Theory

Subsequently after absorbing a photon a radiative transition occurs moving the excited state species from a higher energy level back to the ground state via a radiative or nonradiative process [10,11]. A radiative transition and the spontaneous emission of light responsible for fluorescence typically occurs from the vibrational levels of the first exited singlet state (S_1) to the vibrational levels of the ground state (η_0). This type of transition typically mirrors the excitation pathways and is the reason for the presence of a stokes shift form the absorbance spectrum [10]. Besides fluorescence there are other radiative pathways such as phosphorescence, which is the result of a spin forbidden transition occurring from the triplet excited state (T_1) to the vibrational levels of the ground state (η_0). In addition to radiative pathways, non-radiative pathways can also be utilized through a process like intersystem crossing (ISC) which is the spin forbidden transition from the first excited singlet state (S_1) to the vibrational levels of the triplet excited state (T_1) (Figure 2.2).

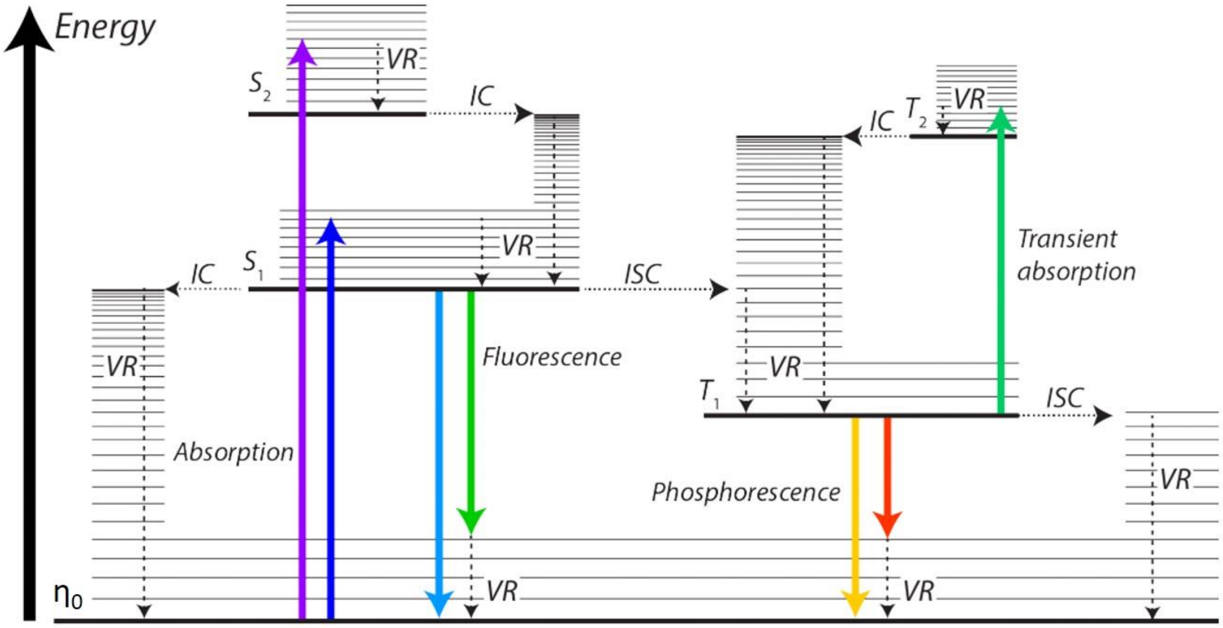

Figure 2.2: Jablonski Diagram. The thicker horizontal lines depict the electronic singlet (S_n) and triplet (T_n) states. The thin horizonal lines represent the vibrational level. ISC is intersystem crossing, IC is internal conversion, and VR is vibrational relaxation.

The radiative any non-radiative pathways can be directly to the fluorescence quantum yield (ϕ) through the rate constants k_r (radiative) and k_{nr} (non-radiative). The lifetime of an excited species is the average time the molecule occupies the excited state before electronic transition to a lower energy state. The simplest manner to describe this electronic process is through first-order reaction kinetics where we let N_t represent the number of excited state species present at a time t. Considering a case with no external quenchers, the radiative and non-radiative rate constants can be related to a change in excited state population by [10]:

$$-\frac{dN_t}{dt} = (k_r + k_{nr})N_t \tag{2.5}$$

This equation can be rewritten as:

$$N_t = N_0 e^{-(k_r+k_{nr})t} \tag{2.6}$$

Where we define N_0 as the number of molecules existing in the excited state at a time t = 0. The average lifetime of an excited state species is:

$$\tau_{avg} = \frac{1}{k_r + k_{nr}} \tag{2.7}$$

The fluorescence quantum yield is defined as a ratio of the number of photons emitted as part of a decay process to the number of photons absorbed by the molecules [11]:

$$\phi = \frac{N_{em}}{N_{abs}} \tag{2.8}$$

Solely considering processes that produce radiative emission:

$$\frac{dN_{r,t}}{dt} = k_r N_t \tag{2.9}$$

Where $N_{r,t}$ is defined as the number of emitted photons at a time t. Combining with equation (2.6) yields:

$$\frac{dN_{r,t}}{dt} = k_r N_0 e^{-(k_r + k_{nr})} \tag{2.10}$$

Integration of equation (2.10) yields:

$$\Delta N_r = k_r N_0 \frac{1}{k_r + k_{nr}} \tag{2.11}$$

Where ΔN_r is the total number of photons that were emitted after the initial excitation, meaning $N_{em} = \Delta N_r$. Conversely, this implies N_0 is the total number of molecules in the excited state immediately following excitation (t = 0), which insinuates the number of photons absorbed are $N_{abs} = N_0$ (for this case we assume there is no instance of multiphotonic absorption).By combining equations (2.2) and (2.8) we arrive at the relationship between quantum yield and the radiative and non-radiative rate constants:

$$\phi = \frac{k_r}{k_r + k_{nr}} \tag{2.12}$$

Equations (2.7) and (2.12) can be used in conjunction to obtain the values for k_r and k_{nr}:

$$k_r = \frac{\phi}{\tau_{avg}} \qquad ; \qquad k_{nr} = \frac{1 - \phi}{\tau_{avg}} \tag{2.13}$$

The average fluorescence lifetime can be measured through time-resolved techniques such as time correlated single photon counting (TCSPC) methods, which will be discussed in the next section.

Fluorescence quantum yield is determined through a relative measurement technique using a standard of known and similar absorbance and emission properties to the analyte of interest [15]. The relative quantum yield can then be determined based on the absorption and emission spectra alone. Considering the instrument being used is coupled with a PMT detector, then the total number of photons emitted by the analyte of interest is proportional to the area under the obtained fluorescence spectra (the integrated fluorescence spectra):

$$N_{em} \propto \int F(\lambda_{em})\, d\lambda_{em} \tag{2.14}$$

Where $F(\lambda_{em})$ and $A(\lambda_{ex})$ represent an instrument-corrected fluorescence spectrum and the absorbance spectrum of the analyte of interest. For this method, the fluorescence photon flux at the detector is directly affected by the refractive index (n) of the medium and thus, inversely proportional to n^2. As a result, a correction must be done to account for the change in flux at the medium interface for the detector to calculate total number of photons present:

$$N_{em} \propto \left(\int F(\lambda_{em})\, d\lambda_{em}\right) n^2 \tag{2.15}$$

The number of photons being absorbed by the analyte of interest will be proportional to the decrease in intensity observed as light travels through the sample. Using the definition of absorbance established in the previous section ($A(\lambda_{ex}) = \log_{10}(I_0/I)$), the number of photons being absorbed by the analyte can be calculated:

$$N_{abs} \propto \Delta I = (I_0 - I) = I_0(1 - 10^{-A(\lambda_{ex})}) \tag{2.16}$$

With this definition for absorbance, we can combine it with equation (8) to define quantum yield as:

$$\phi \propto \frac{(\int F(\lambda_{em}) d\lambda_{em}) n^2}{I_0\left(1 - 10^{-A(\lambda_{ex})}\right)} \tag{2.17}$$

The relative quantum yield can then be defined as:

$$\frac{\phi_A}{\phi_R} = \frac{(\int F_A(\lambda_{em}) d\lambda_{em})}{(\int F_R(\lambda_{em}) d\lambda_{em})} \frac{1 - 10^{-A_A(\lambda_{ex})}}{1 - 10^{-A_R(\lambda_{ex})}} \frac{n_A^2}{n_R^2} \tag{2.18}$$

Where F_A and F_R are the instrument corrected fluorescence spectra for the analyte and reference, respectively. A_A and A_R are the absorbance spectra for the analyte and reference, respectively. For this instance, by using the same substrate, the corrective term for refractive index can be eliminated and the resulting terms can be measured through spectroscopic means. Because all terms can be derived spectroscopically, if the ϕ_R is known, the ϕ_A can be determined.

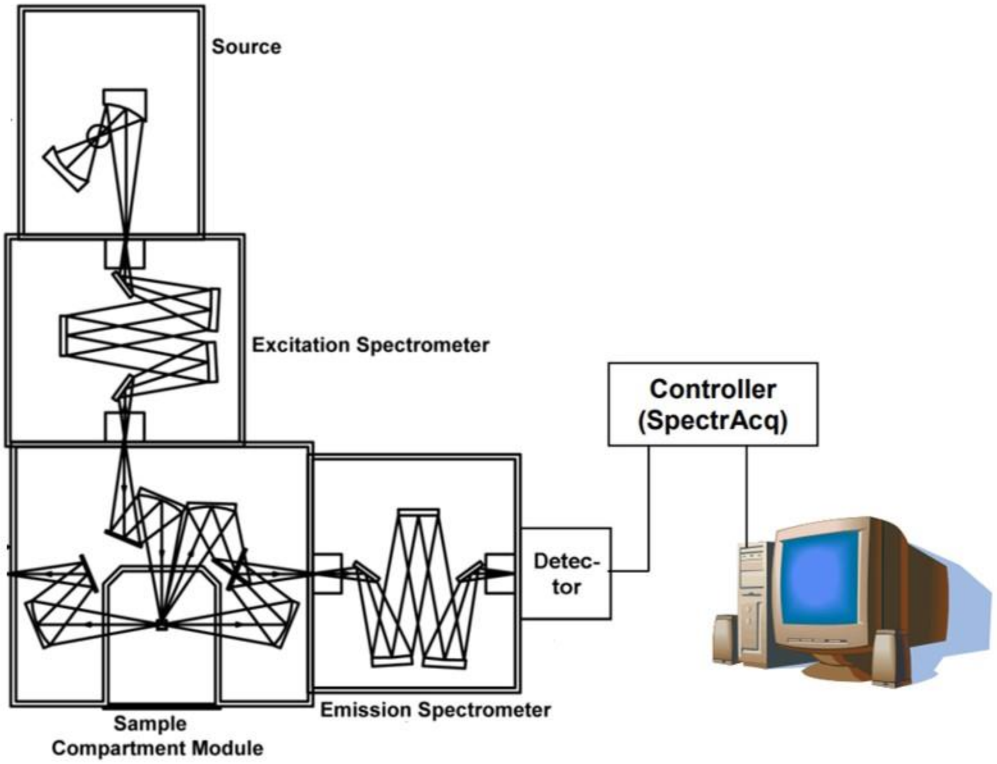

Figure 2.3: General schematic representation of the Horiba nanolog spectrofluorometer [14].

Steady-State Fluorescence Spectroscopy and Imaging Methods

In chapters 1&3 of this dissertation, steady-state photoluminescence spectroscopy measurements are carried out using a Horiba Nanolog spectrofluorometer. To acquire fluorescence spectra, the sample is excited at an angle perpendicular to the excitation source in order to reduce interference of the light source with the detector [13]. The major components that constitute this instrument is a 450 W continuous wavelength (CW) xenon (Xe) arc-lamp (230-1100 nm), both an excitation and emission monochromator to allow for excitation and emission spectra to be acquired, a sample compartment with an allowed 90° geometry set-up, a photomultiplier tube (PMT) to detect the fluorescence signal, and a program system controller that supplies data to the readout system. Because the spectrofluorometer is equipped with two scanning monochromators, the excitation spectra can be obtained by holding the emission monochromator at a fixed wavelength and scanning along the desired wavelength range. Conversely, the same can be done to collect emission spectra by holding the excitation monochromator at a fixed wavelength and scanning along a desired wavelength range with the emission monochromator. This fluorescence spectrometer is also equipped with adjustable slit widths in order to adjust the resolution of the obtained spectrum. The excitation and emission monochromators are routinely calibrated with respect to the excitation spectra provided by the Xe arc-lamp at 467 nm and the Raman water scattering peak at 397 nm for the primary excitation wavelength of the Xe arc-lamp. A general schematic is provided above in Figure 2.3.

In chapter 2 of this dissertation, steady state photoluminescence measurements were preformed using an ocean optics 2000 USB spectrometer. The excitation source used was a 457nm continuous wavelength laser (Argon laser: Stellar-Pro Select 150). The sample compartment is fiber coupled to the ocean optics 2000 USB spectrometer, which contains: a 1200 grooves/mm grating, a f/4 focal length with 42 mm input and 68 mm output and has a spectral range from 200-1100nm. The detector used in the spectrometer is a Sony ILX511 2048-element linear silicon CCD array.

Chapter 2 of this dissertation also employs macroscale photoluminescence microscopy through use of an Olympus BX51 fluorescence microscope. This microscope produces fluorescence illumination through episcopic optical pathways and has a xenon lamp excitation source for both UV and visible light excitation. The housing includes a turret of “cubes,” which contain a barrier filter, a dichroic mirror, and an excitation filter. Light being emitted from the episcopic lamp housing passes through a collector lens followed by the field and aperture diaphragms before passing through the first interference filter in the cube set, the emission filter. The emitted light is then directed through the objective lens and onto the sample by a dichroic mirror. Secondary fluorescence being emitted will travel back through the objective lens and dichroic mirror before passing through the barrier filter and into the camera setup (Figure 2.4).

Finally, chapters 1&2 of this dissertation rely on an integrating sphere method to determine PLQY for perovskite samples. An integrating sphere is used for these types of measurements due to their ability to remove ambiguities due to angular dependencies as well as keeping samples oriented and aligned in a similar manner when alternating do different samples. A Quanta-φ integrating sphere with Fluorolog-3 package was incorporated into the Horiba nanolog spectrometer to take PLQY measurements.

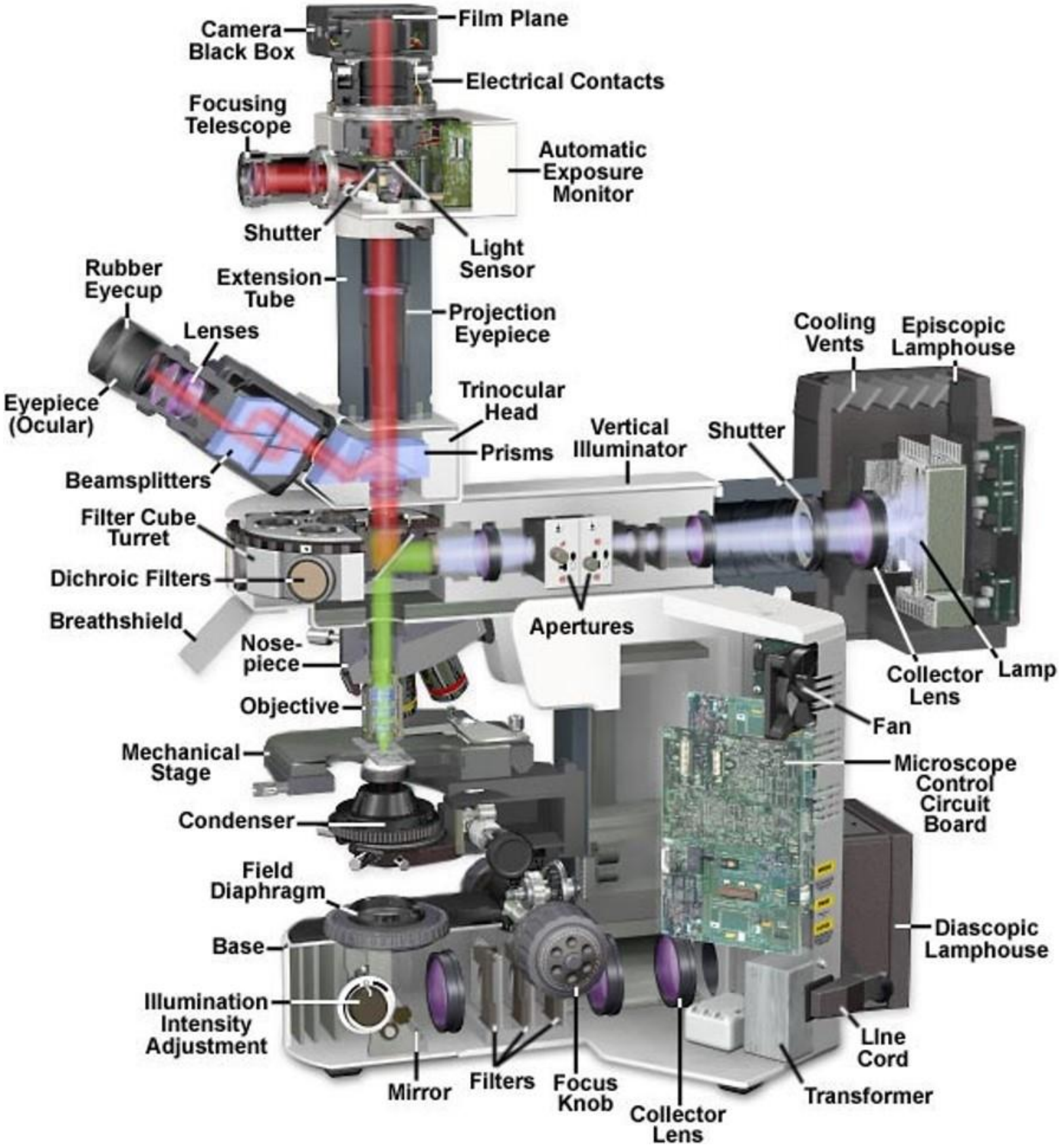

Figure 2.4: Cutaway diagram of an Olympus BX51 fluorescence microscope equipped for episcopic fluorescence imaging [16].

Time Correlated Single Photon Counting (TCSPC) Theory

TCSPC is presently one of the most important tools for studying the excited state dynamics of semiconductor materials and is used extensively throughout out this dissertation. TCSPC is applied in time-resolved photoluminescence spectroscopies for the collection of photon arrival times. Due to the nature of this technique (ie. time-resolved) it requires the utilization of a pulsed excitation source. The emission of light from the excited state is a spontaneous event, which implies only estimations of the probability that a single molecule will emit a photon during a certain time interval is possible. From the equations above, we can see the number of molecules in the excited state after a time (t) is derived from equation (2.6), while the average photoluminescence lifetime of the analyte in the excited state is given by equation (2.7). Emission intensity for a given photoluminescent molecule is usually proportional to the number of molecules contained within the excited state, which indicates for a single photoluminescent molecule [17]:

$$P(t) \propto e^{-\frac{t}{\tau}} \tag{2.19}$$

From experimental data the excited state decay function can be experimentally acquired by collecting a population of single photon events, which can be correlated to the time intervals occurring amid the excitation and emission processes rather than solely collecting the intensity after an individual pulse [17].

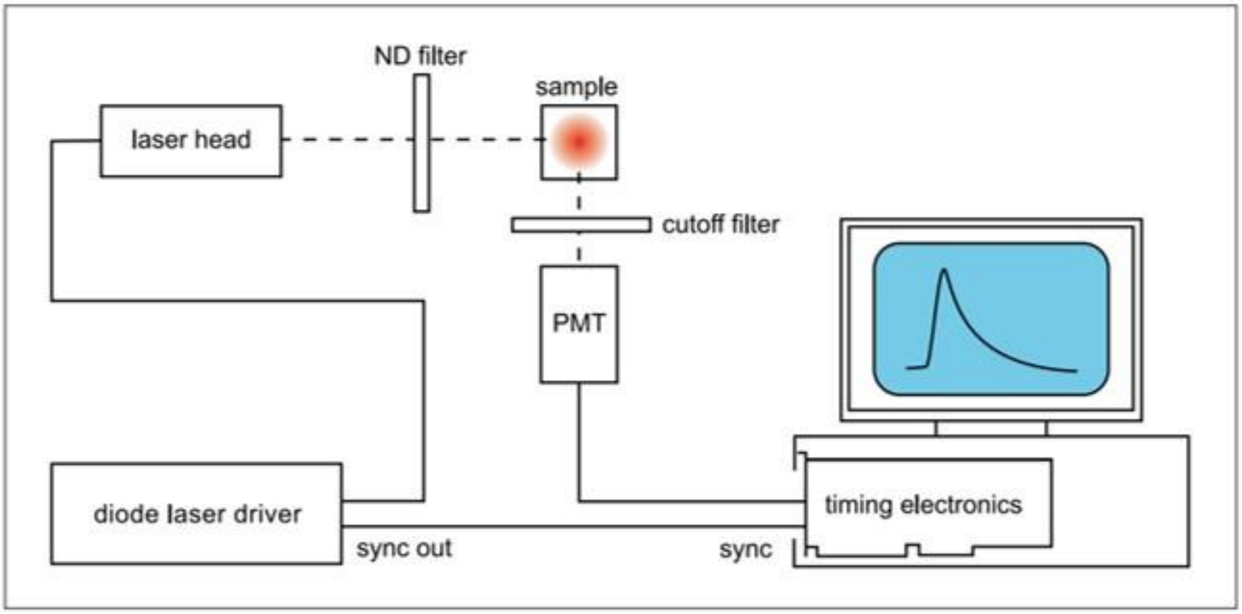

Figure 2.5: Simple diagram of a TCSPC experimental set-up [18]

A diagram containing a simple experimental set-up for time-resolved photoluminescence decay measurements has been provided in Figure 2.4 [18]. To explain the process of recording photoluminescence decay using TCSPC, it all begins at the diode laser driver, which is responsible for both firing the laser at a specific pulse frequency (laser repetition rate) and communicating to the timing electronics when to start the countdown until the first photon arrives. In the case of perovskite samples, the laser pulse will excite the sample and produce excited state charge carriers, which will proceed down some form of radiative recombination pathway and eventually release photons, which are timed and recorded. This important function is accomplished through a time-to-amplitude (TAC) converter and a detector, which will ensure the first arriving photon is the only recorded photon in the designated time interval between laser pulses. The TAC itself is one of the most crucial components to the TCSPC system as it acts like an ultra-fast stopwatch. This stopwatch function of the TAC is accomplished by recording the START pulse and STOP pulse and measuring the time delay between these two events. The

START pulse is recorded as the initiation of the laser pulse to the sample and the STOP pulse is recorded as the first arriving photon at the detector (Figure 2.5) [18]. The TAC provides an output of digital numbers, which are stored using an analog-to-digital converter (ACD), where photon arrival times are stored in specific “time channels.” This process is then repeated multiple times under the preset collection window time, where the sample is excited multiple times by the pulsed laser source and arrival times are collected. After the sample collection window has expired, the arrival times are binned into a histogram depending on photon arrival times at the detector and these are used to build a photoluminescence decay curve (Figure 2.6).

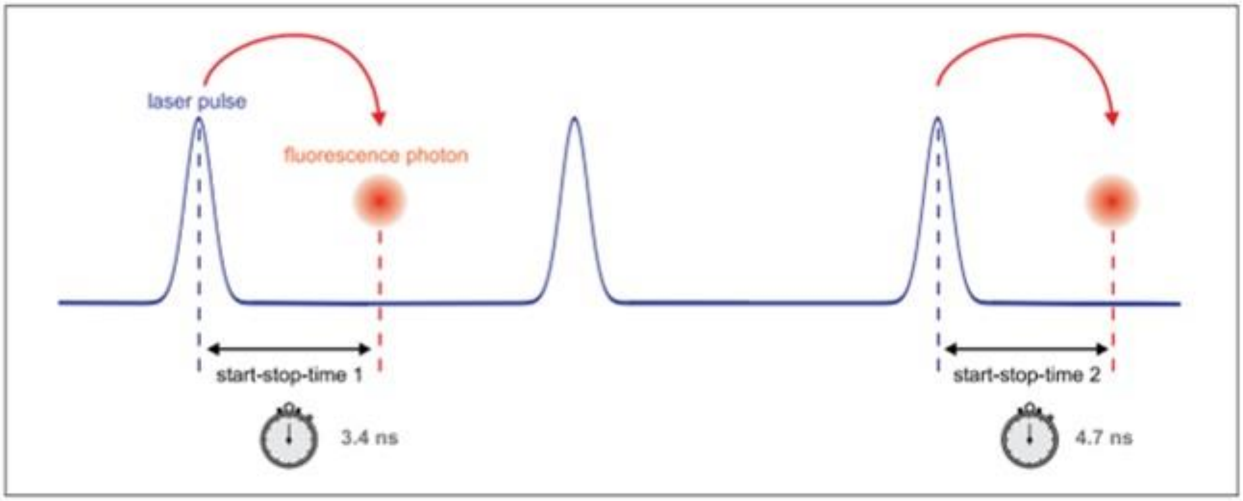

Figure 2.6: Schematic representation of TSCPC collection of START and STOP pulse events [18].

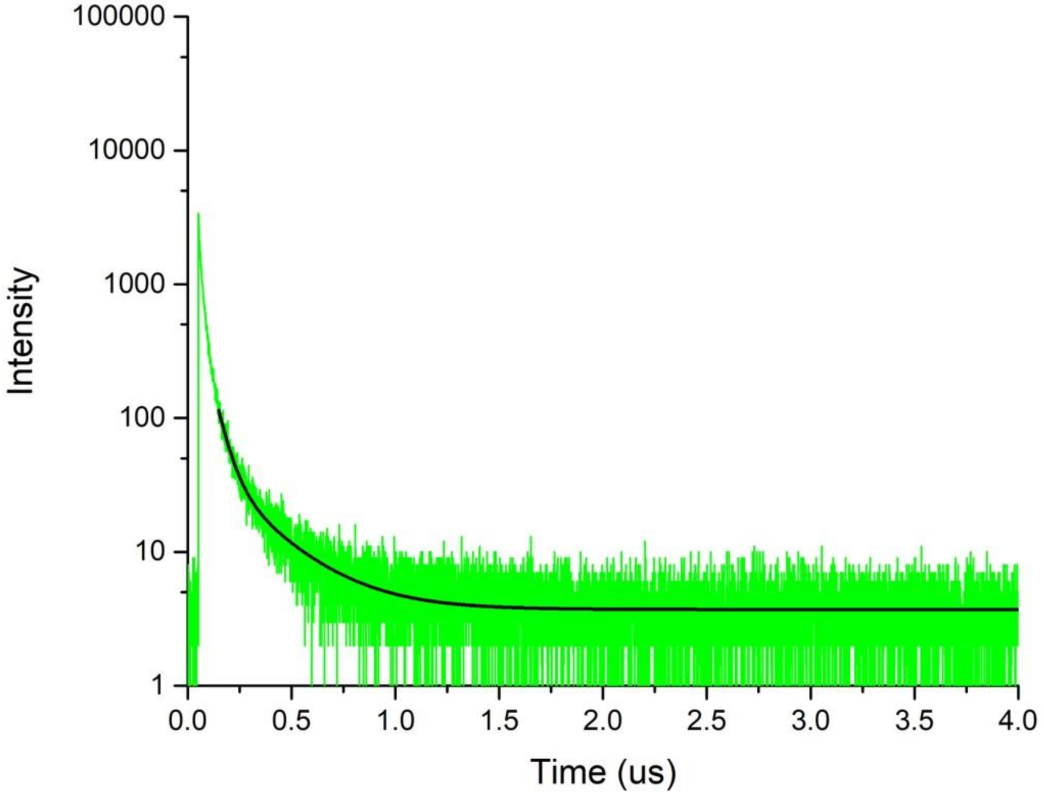

Figure 2.7: Time-resolved photoluminescence spectrum of $MAPbBr_3$ nanoparticles encapsulated in a polystyrene substrate.

The experimental set-up used in this dissertation is home-built and divided into excitation and emission sides. The excitation side of the set-up consists of pulsed laser sources (Picoquant LDH-P-C-470 and LDH-P-C-375), which pass through ND filters (reduce intensity) and an IF (interference filter) to promote spectral purity of the beam. The beam then passes through telescopic arrangement of lenses to adjust the size of the beam by a factor of five to fill the optics in the microscope. The light enters the back of the confocal microscope and passes through a dichroic mirror (excitation source dependent) and is focused down to a spot-size of 300 nm (Zeiss 100x Fluar objective lens: NA = 1.3 and WD = 0.17 mm). The samples can be scanned statically, or raster scanned using a Mad City Labs piezoelectric stage (Nano-LP100). The emission from the sample then enter the emission side of the set-up where it first passes through a long pass (LP) filter to filter out the excitation source. The emission light can then interact with the detector (Picoquant Micro Photon Devices, PDM series) where timing effects can be recorded. The photon timing is measured using a pulsed laser driver (PDL 800-D), which provides the timing to a Picoharp 300 TCSPC module in combination with a detector router (PHR 800).

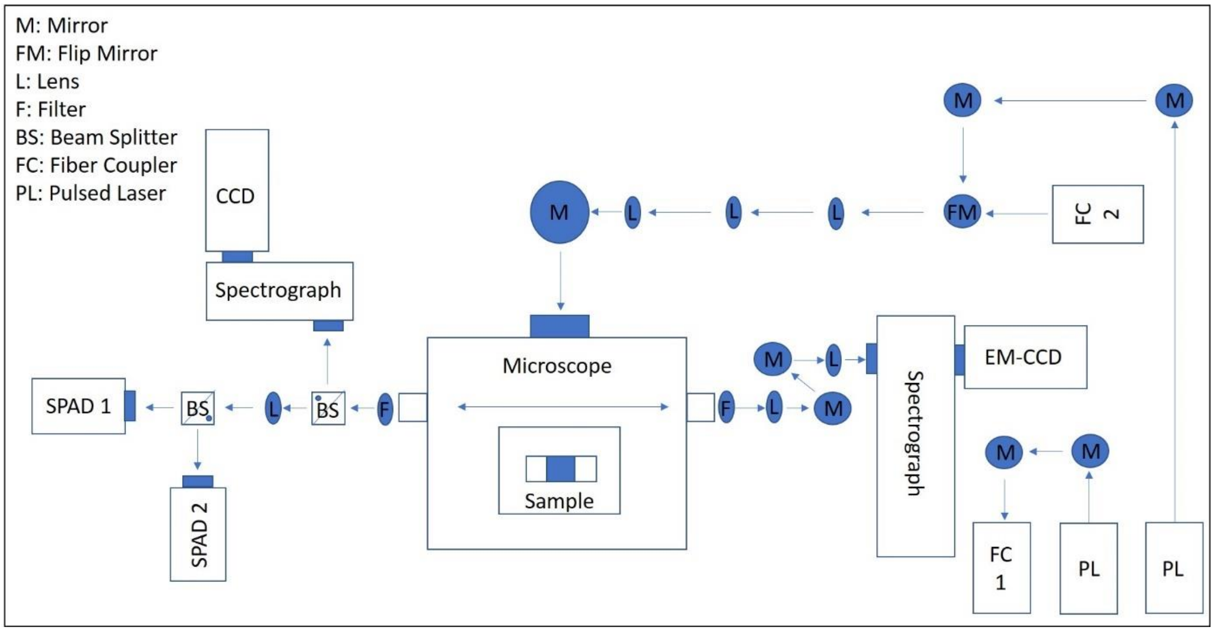

Figure 2.8: General optical table set-up for TCSPC measurements.

References

[1] D. English, W. Zhang, G. A. Kraus, J. W. Petrich. J. Am. Chem. Soc. (1997) 119 (13), 2980-2986.

[2] K. Das, A. V. Smirnov, J. Wen, P. Miskovsky, J. W. Petrich. Photochem. Photobiol. (1999) 69 (6), 633-645.

[3] J.W. Petrich, G. R. Fleming. Photochem. Photobiol. (1984) 40 (6), 775-780. 66

[4] P. K. Chowdhury, M. Halder, L. Sanders, T. Calhoun, J. L. Anderson, D. W. Armstrong, X. Song, J. W. Petrich. J. Phys. Chem. B. (2004) 108 (29), 10245-10255.

[5] M. Nisoli, P. Decleva, F. Calegari, A. Palacios, F. Martín. Chem. Rev. (2017) 117 (16), 10760-10825.

[6] M. Cho, S. J. Rosenthal, N. F. Scherer, L. D. Ziegler, G. R. Fleming. J. Chem. Phys. (1992) 96 (7), 5033-5038.

[7] D. Laage, T. Elsaesser, J. T. Hynes. Chem. Rev. (2017) 117 (16), 10694-10725.

[8] D. English, K. Das, K. Ashby, J. Park, J. W. Petrich, E. Castner. J. Am. Chem. Soc. (1997) 119 (48), 11585-11590.

[9] D. C. Harris, M. D. Bertolucci, Symmetry and Spectroscopy: An Introduction to Vibrational and Electronic Spectroscopy Courier Corporation: 1978.

[10] J. B. Birks. Photophysics of Aromatic Molecules Wiley-Interscience: London, New York, 1970.

[11] J. R. Lakowicz. Principles of Fluorescence Spectroscopy, 3rd ed.; Springer: 2011.

[12] Cary 300 UV-Visible Spectroscopy System: Operator's Manual 2013.

[13] W. Melhuish. J. Res. Nat. Bur. Stand. USA. (1972) 76 (6), 547- 560.

[14] Horiba nanolog SPEX Spectrofluorometer Owner’s Manual 2013.

[15] C. Würth, M. Grabolle, J. Pauli, M. Spieles, U. Resch-Genger. Nat. Protoc. (2013) 8 (8), 1535.

[16] Olympus BX51 fluorescence microscope informational brochure 2015.

[17] D. V. O'Connor, D. Phillips, Time Correlated Single Photon Counting Academic Press Inc.: London, 1984.

[18] M. Wahl. Time-Correlated Single Photon Counting. Technical Note, PicoQuant. 2014.

CHAPTER 3: PHOTOPHYSICAL MODIFICATIONS BROUGHT ON BY POLYMERIC ENCAPSULATION OF MAPbBr$_3$ NANOPARTICLES

Adapted with permission from: Wang, Y., He, J., Chen, H., Chen, J., Zhu, R., Ma, P., Towers, A., Lin, Y., Gesquiere, A. J., Wu, S. and Dong, Y. (**2016**), Ultrastable, Highly Luminescent Organic–Inorganic Perovskite–Polymer Composite Films. Adv. Mater., 28: 10710-10717.

Introduction

Over the past decade, organic-inorganic perovskites (OIP) have demonstrated continuous growth in efficiency for solar cell photovoltaics [1-3]. In addition to the growth in solar cell applications, OIP have also displayed superb promise in light emission applications with their high efficiency and tunable color purity [4,5]. However, one of the most prominent concerns with these materials is their stability under external stressors, mainly high temperatures and atmospheric conditions, before they can be considered for commercial lighting and photovoltaic applications [6-8]. To enhance these materials for their desired low-cost and high performance photovoltaic or light emitting applications, we report a simple synthetic microencapsulation process for achieving ultrastable and highly luminescent $CH_3NH_3PbBr_3$ (MAPbBr$_3$) OIP-polymer composite film along with the synthetic strategy's overall effects on the OIP's photophysical properties. To investigate and validate improvements to the stability of the OIP nanoparticles post encapsulation, a spectroscopic study utilizing both steady-state and time-resolved measurements was completed.

Numerous studies link changes in light absorption and emission properties in perovskite materials to material integrity and overall stability [9]. As a semiconductor, Perovskites have a key spectral feature in their absorption spectra: a peak followed by a sharp sloping effect into higher wavelength values. This characteristic peak is a result of the band gap energy for the material, with the definition of this peak is a good indicator of the material's overall order and by extension it's stability. Another key characteristic seen in pristine or well-ordered perovskite materials are longer photoluminescence lifetimes [24]. Longer photoluminescence lifetimes in perovskite materials are correlated to a decrease in trap states within the material, which indicates: consistency in the material’s crystal structure within the lattice, efficient excited state carrier processes, and overall brighter material luminescence: all of which indicate better material stability [12].

Understanding the effects novel synthetic techniques have on the underlying photophysics and overall optical properties is paramount to the continued growth of OIP materials. New processing and synthetic techniques are being developed for perovskites to combat material instability issues and improve the overall material’s efficiency for eventual commercialization applications. The instability of OIP’s originates from the material’s overall anionic framework and low formation energy (≈0.1-0.3 eV). The anionic framework makes the OIP material more susceptible to environmental factors such as water and molecular oxygen, which cause material break down or defect sites to form in perovskite materials [10]. The formation energy of a material is also a good indicator of material stability where higher values tend to correlate to more stable materials, as an example the formation energy of graphene is almost 1 eV [11]. This makes OIPs prime candidates for solution processing techniques but as a trade-off leaves them highly susceptible to external stressors, including light, moisture, heat, or electric fields [6-8]. Even under atmospheric storage conditions with relative humidity levels of 50%-60%, OIP crystal growth has been observed but with an added cost of increased defect density throughout the material along with reported shorter carrier lifetimes [12].

The understanding behind the formation for defect states and how to passivate them in any semiconductor material is integral for their market growth as they assume a prominent role in the optoelectronic and photophysical properties exhibited by the material [54]. Defects in OIP structure tend to be classified into two broad categories: point defects within the crystal structure and multi-charged surface defects able to interact with the environment. Point defects found in OIP are attributed to vacancies within the crystal lattice or the intercalation of molecules/atoms detrimental to the carrier dynamics in the OIP (ie. water, repeating atoms, halide and lead dimer formation etc.). Fortunately, a defining attribute of OIPs are their ability to tolerate high defect densities within the materials and even those that do form tend to be easily overcome shallow level defects. Surface defects found in OIP result from exposed, charged terminations (Pb^{2+}, MA^+, Br^-) that are susceptible to unfavorable environmental interactions.

Many surface modification and defect passivation strategies involving the use of organic ligands are currently being explored in order to innately passivate surface defects found in OIP materials. While major improvements to OIP material stability and their optical properties are seen from the implementation of these strategies, there are still aspects to these methods that still need further investigation. First, a better understanding of ligand interactions on the surface of perovskite crystals is necessary in order to achieve precise control of film or QD morphology [13,14]. Secondly, if efficient surface binding, defect recovery, and carrier transport are the desired outcome from utilizing surface passivation techniques then and in-depth understanding of the interactions of the ligands with different functional groups and the perovskite crystal surface is essential [13,14].

Attempts at stabilizing and passivating OIP nanoparticles have led to the development of three major techniques, though each expresses limited success. The first common approach is the use of a pre-formed inorganic matrix, which is used as a template where the OIP nanoparticle film is formed through the impregnation of and pore-filling of the matrix. For this technique, commonly used inorganic matrices include Al_2O_3 [16] and TiO_2 [15] matrices. However, the biggest drawback to this technique is that after solvent evaporation the perovskite materials are often left exposed. This unwanted exposure results from the solvent evaporation step occurring after the matrix is already pre-formed. Because the matrix is already formed and static at this point, it cannot flex to incorporate the perovskite materials, which causes aggregation at the surface of the material. It was even noted in some instances that decomposition began to occur during the annealing of OIP materials on porous TiO_2 at 85 °C within an inert environment [17]. Beyond the inorganic scaffolding discussed above, carbon nanotube/polymer composites have shown promise in creating noteworthy “water resistant” devices, [18] though the macroscale passivation utilized in this instance leaves OIPs susceptible to potential degradation through film leakages.

The second strategy to come of research into OIP material passivation involves a solution-based synthesis of surfactant-protected OIP nanoparticles. This technique allows for the passivation of individual nanocrystals and has achieved colloidal OIPs with both enhanced stability alongside increases in PLQY [19-21]. However, the average yield in these types of reactions involving OIP nanoparticles remains low and suffer from critically reduced PLQY (0.025-13%) and photoluminescence lifetimes (30-60 ns) brought on by quenching effects from spontaneous particle aggregations [22].

The third technique is comprised of depositing composite films from a mixture of OIP precursors with some form of protecting media (small molecules, polymers [23], inorganic molecules [24]). While this approach is inherently simple in theory, it often results in extreme phase separation between the OIP nanoparticles/films and the material providing environmental protection. Because of this, these materials tend to suffer from larger OIP grain size variations, broad photoluminescence spectra, and an overall lower PLQY with subpar protection.

Here, we report spectroscopic methodologies to corroborate added stability as a result of encapsulation of OIP nanoparticles in six different polymer matrices. Steady-state UV-Visible absorption spectroscopy is utilized to probe the band to band transitions in semiconductors as well as to gauge order in the crystal structure of the material [25]. Perovskites exhibit an absorption onset within the 400-600 nm with a steep offset, which gives an approximation of the band gap energy for the material along with insight into the disorder of the crystal structure depending on the tail produced from this peak [26]. Steady-state photoluminescence spectroscopy is another tool to support band to band transitions in semiconductor materials in addition to a method to examine overall structural order [27]. By examining the full width half maxima (FWHM) of the emissive peak produced, insight into crystallinity of the material can be gained with narrow and symmetrical peaks indicating higher orders of crystallinity in a material [27]. Finally, time-resolved photoluminescence measurements provide direct insight into the radiative and non-radiative pathways being utilized by a material. This information can be exploited to explore possible photophysical pathways being utilized by perovskite materials in addition to guidance for designing methodologies for optimizing synthetic production of perovskite materials. We hypothesize OIP nanoparticles encapsulated in polymeric materials will exhibit distinct spectral properties indicative of perovskite materials with fewer defect states, a higher ordered crystal lattice, and overall brighter photoluminescence. These distinct spectral improvements will include: a distinct absorption band with minimal tailing effects, narrow photoluminescence peaks, and longer photoluminescence lifetimes. All of these indicators will serve as a basis to qualify a global improvement to stability in OIP nanoparticles embedded in a polymer matrix.

In addition to the spectroscopic approach described above we report a swelling-deswelling microencapsulation synthetic strategy to achieve both dispersed and intimately passivated OIP nanoparticles inside six polymer matrices: Polycarbonate (PC), acrylonitrile–butadiene–styrene (ABS), cellulose acetate (CA), polyvinyl chloride (PVC), polymethylmethacrylate (PMMA), and Polystyrene (PS) and investigate the photophysical and optical modifications resulting from each polymer used in the microencapsulation process through a spectroscopic study. Different solvents and solutes can be introduced into a polymer matrix by treating the polymer with a “good solvent.” A good solvent will allow polymer chains to swell and expand, which typically can be reversed through a deswelling process brought on by the evaporation of the good solvent. We hypothesize here that through the dynamic polymer swelling-deswelling processes the OIP precursors can be fully embedded within the various polymer matrices. Through this solvent-induced polymer swelling process, OIP precursors can be introduced into the different polymers as solvent. Afterwards, the solvent can be driven out of the polymer matrix with heat, which allows for the OIP precursors to react to form not only well disbursed but exceptional quality OIP nanoparticles embedded and secured throughout the desired polymer matrix [28].

The synthesis for the composite OIP-polymer materials takes advantage of a simple swelling-deswelling process that allows microencapsulation of IOP material with overall excellent distribution within the polymer matrix and crystallinity. In addition to this, these OIP-polymer composites exhibit high photoluminescence quantum yields (PLQY) of up to 48%, exceptional color purity with full width at half maxima (FWHM) at narrow emissions as low as 18 nm, and long average fluorescent lifetimes (τ_{avg}) as high as 502 ns. The overall synthetic goal was to provide a sound shield for the OIP nanoparticles from detrimental environmental factors known to plague OIP nanoparticles such as: external sources of heat, water, and oxygen. In doing so, the polymer matrix shield can provide a sort of surface defect passivation for the OIP nanoparticles, which allow for increases in the number of radiative pathways available and thus brighter nanoparticles. Surface passivation in perovskite materials takes advantage of ligands (typically organic) with functional groups containing positive or negative valance (NH_3^+, COO^-, and halogen ions (X^-). Rather than adding specific organic ligands, the terminal ends of the polymer matrix can achieve a similar effect and decrease the density of surface traps on the OIP nanoparticles. To better understand the photophysics behind the encapsulation method, photoluminescence lifetimes are acquired in order to investigate the excited state dynamics within the polymer encapsulated OIP nanoparticles in addition to steady-state absorbance and photoluminescence spectra.

Experimental

Materials

Polycarbonate (PC) films, acrylonitrile–butadiene–styrene (ABS) films, cellulose acetate (CA) films, polyvinyl chloride (PVC) films, and polymethylmethacrylate (PMMA) sheets were purchased from McMaster-Carr. Polystyrene (PS) substrates and HPLC grade acetone (omnisolv) were purchased from VWR International, Inc. CH_3NH_3Br (CH_3NH_3 = MA) was purchased from Luminescence Technology Corp. PbBr2 (99%), *N*,*N*-dimethylformamide (extra dry, 99%), and sodium hydroxide pellets were purchased from Sigma-Aldrich, coverslips (22x22-1) were purchased from Fisher Scientific (Catalog No. 12-544-10).. Unless stated otherwise, all materials were used as received.

Synthesis

Perovskite–polymer composite films, MABr and $PbBr_2$ (3:1 molar ratio) with overall concentration of 100 mg mL^{-1} were prepared in DMF while stirring overnight before use. To achieve varying concentrations of 2, 5, 10, 20 and 50 mg mL^{-1}, the solution was further diluted in DMF. Cotton swab painting or spin coating at 2000-4000 rpm was used to process the $MAPbBr_3$ solutions onto different polymer film substrates. A baking period of 2-8 hours was then applied to polymer film substrates at 20-80 °C inside a glovebox. Control samples on glass were also processed using the MABr and $PbBr_2$ (3:1 molar ratio) with an overall concentration of 100 mg mL^{-1} in DMF. Control samples were spin coated on glass substrates at 3000 rpm and dried overnight at room temperature in a glovebox. PS and PC were both dissolved in chloroform at a concentration of 100 mg mL^{-1}. To create control samples, polymer substrates were spin coated at 3000 rpm on top of deposited perovskite layers on glass substrate. Following spin coating, control samples were baked at 60 °C for 30 minutes and allowed to cool to room temperature in a glovebox.

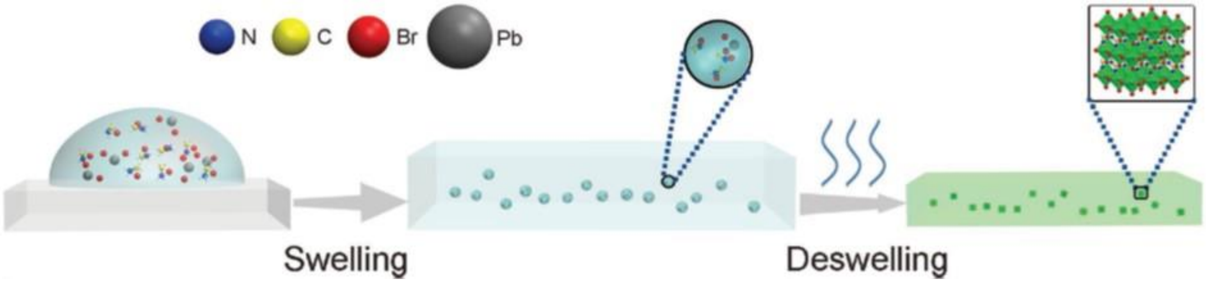

Figure 3.1: Microencapsulation swelling-deswelling synthetic strategy scheme of $MAPbBr_3$-polymer composite film formation. Based on figure from reference [43].

Scanning Electron Microscopy (SEM)

All samples were coated with gold for one minute before scanning electron microscopy measurements were taken. Scanning electron microscopy measurements were then carried out with the use of a high-resolution field-emission SEM (Philips-FEI XL30-SFEG) operating at 15-25 kV with typical beam currents 0.15-2.5 nA.

Transmission Electron Microscopy (TEM)

Cross sectioned samples were first prepared using a FEI 200 TEM focused-ion-beam instrument before analysis operating at 4 kV and 1 mA beam current. Afterwards, all TEM measurements were completed using a FEI Tecnai F30 TEM operating at 200 kV for cross-sectioned $MAPbBr_3$-polymer composite films.

UV-Vis Spectroscopy (UV-Vis)

Absorption spectra were measured using a CARY 300 Bio spectrophotometer in room temperature conditions.

Photoluminescence Spectroscopy

The steady-state photoluminescence of the $MAPbBr_3$-polymer composite films was measured using a Horiba Nanolog Spectrofluorometer at an excitation wavelength of 467nm.

Coverslip Cleaning and Preparation for TCSPC Measurements

The coverslips (22 x 22-1) are used for samples in the custom-built sample holder used for microscope stage. The coverslips are first rinsed with nanopure water and sonicated in HPLC grade acetone (Omnisolv) for twenty minutes. The coverslips are then rinsed with nanopure water and sonicated in a 10 %wt sodium hydroxide solution for twenty minutes. Finally, the coverslips are rinsed with nanopure water and put through two more rounds of sonication in nanopure water for twenty minutes each time. After the subsequent washes, the coverslips are dried with N_2 and processed in a UV-Ozone chamber for 15 minutes.

Photoluminescence Imaging and Time Correlated Single Photon Counting (TCSPC)

Photoluminescence images and time correlated single photon counting measurements were acquired using a home-built sample-scanning confocal microscope. A 466 nm pulsed laser was used as the excitation source (Picoquant LDH-P-C-470) for all $MAPbBr_3$-polymer composite samples. The excitation side before the sample includes the following filters and optical elements: A gradient ND filter, 2.0 ND filter, 466/5 IF, and a dichroic mirror for 466 nm. The emission side after the sample includes the following optical elements: 470 nm LP filter, 45/45/10 beam splitter, and an achromatic lens (FL = 100 mm). The laser was focused down to a spot size of ~300nm using a Zeiss 100x Fluar objective lens (NA 1.3, WD 0.17mm). To create a fluorescence image of the scanned area, the $MAPbBr_3$ samples were raster scanned across the focused laser beam using a Mad City Labs piezoelectric stage (Nano-LP100). Fluorescence from single particles was collected using a fast, single photon counting detector (Picoquant, Micro Photon Devices, PDM series). Images were collected using the following scan parameters: dwell time of 5 ms, a laser repetition rate of 125 kHz, a scanning range of 10 x 10 μm^2 – 100 x 100 μm^2, and a laser power registering <1 nW.

Using the same set-up as described above, TCSPC excited state lifetime studies were completed by parking an area of interest of the samples over the focused pulsed laser beam (Picoquant LDH-P-C-470) and collecting photons with a fast, single photon counting detector (Picoquant, Micro Photon Devices, PDM series). The photon timing was measured using a pulsed laser driver (PDL 800-D), which provided the timing signal to a PicoHarp 300 TCSPC module in combination with a detector router (PHR 800), all from Picoquant.

TCSPC Data Fitting

The time-resolved PL decay curves were fit to a biexponential function of time (t):

$$F\ (t) = f_1 e^{-t/\tau_1} + \ f_2 e^{-t/\tau_2} \tag{3.1}$$

Where f_1 and f_2 are prefactors containing the amplitude information for the i^{th} component of the decay curve, and τ_1 and τ_2 are the time constants. All decay curves were fitted using the FluoFit® Pro software (Picoquant). Photoluminescence decay curve fitting is done through a tail-fitting method to account for the instrument response function (IRF). Average recombination lifetimes are estimated with the use of the f and τ values obtained from the fitted curve data according to the following equation:

$$\tau_{avg} = \ f_1\tau_1 + \ f_2\tau_2 \tag{3.2}$$

Results and Discussion

MAPbBr$_3$-Polymer Composite Design

The MAPbBr$_3$-polymer composites are a polymer matrix containing dispersed OIP nanoparticles introduced through a polymer swelling-deswelling protocol. Dynamic polymer swelling-deswelling strategies have already been applied to the medical industry with successful encapsulation and controlled release of bioactive pharmaceuticals from within a polymer matrix [29]. The different polymers used in this study were chosen for their optical transparency in addition to their physical properties pertaining to heat resistance and ease of use in the chosen solvent for the OIP nanoparticle incorporation process. The solvent, dimethylformamide (DMF), is ideal for this investigation due to its suitability as a solvent for the OIP nanoparticle precursors as well as its ability to initiate the swelling processes when applied to the selected polymers for this study.

As discussed in Chapter 1, there are a multitude of synthetic approaches employed to create MAPbBr$_3$ OIP nanoparticles. However, the swelling-deswelling strategy implemented in this study aims to remove unfavorable and/or superfluous processing conditions such as: templates, additional organic ligands, high processing temperatures, and multiple solvent fronts to name a few to not only create OIP nanoparticles but within a coherently shielded and favored environment for optimal nanoparticle formation. Through the swelling-deswelling method, MAPbBr$_3$ OIP nanoparticles can be formed through stoichiometric control of the OIP nanoparticle precursors (3:1 MABr and PbBr$_2$) and low-temperature baking (60 °C).

The fabrication process for the MAPbBr$_3$ OIP nanoparticles was found to be extremely robust and allows for a high tolerance to variable synthetic conditions (annealing temperatures and times as well as spin-coating speeds) to an extent. This was demonstrated through both simple cotton-swab painting and spin-coating application methods with each of the polymer substrates, each resulting in the anticipated swelling effect as soon as the precursor solution was brought into contact with the polymers. Afterwards, the annealing of each substrate would bring on a visible change to the polymer either transparent (most polymers) or semiclear (ABS) to a light green color. This visible color change is a direct result of three different desired effects: 1) $MAPbBr_3$ OIP nanoparticle formation, 2) solvent evaporation from the polymer matrix, and 3) A deswelling of the polymer.

In addition to providing an optimal synthetic route for encapsulated OIP nanoparticles, the swelling-deswelling strategy addresses a major concern in perovskite materials: their overall stability with heat, moisture, and atmospheric conditions. With glass transitions temperatures above 100 °C, all the polymers chosen for encapsulation of perovskite OIP nanoparticles: Polycarbonate (PC: 147 °C), acrylonitrile–butadiene–styrene (ABS: 105 °C), cellulose acetate (CA: 175 °C), polyvinyl chloride (PVC: 100 °C), polymethylmethacrylate (PMMA: 105 °C), and Polystyrene (PS: 110 °C), will greatly increase heat resistance. Another promising aspect of the polymers chosen for this study are their high permeability values regarding oxygen and water, which will prevent access to material decomposition pathways initiated by radical oxygen species and hydrolysis. Finally, added stability is added to heat and moisture resistance simply by using higher density polymers due to their higher orders of crystallinity and lower formations of branching polymer chains. This swelling-deswelling strategy not only provides a simple method for synthesizing OIP nanoparticles but tackles the pertinent concern with perovskite materials in general: a straightforward way of improving material stability for eventual commercial use in optoelectronic devices.

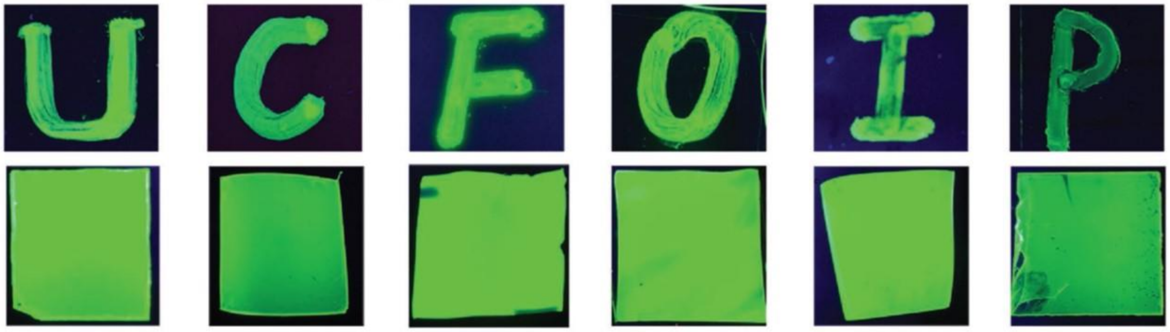

Figure 3.2: Cotton swab painting and spin coated samples with UV excitation (365 nm). Samples displayed from left to right are: $MAPbBr_3$-PS, $MAPbBr_3$-PC, $MAPbBr_3$-ABS, $MAPbBr_3$-CA, $MAPbBr_3$-PVC, and $MAPbBr_3$-PMMA. Figure adapted from reference [43].

Results: Concentration Dependence

Achieving the emissive green color from the polymer substrate signaled the successful synthesis of $MAPbBr_3$ OIP nanoparticles though with differing photoluminescence quantum yields (PLQY) (Table 3.3). Differing concentrations of the precursors used (2, 5, 10, 20, and 50 mg mL^{-1}) had a direct effect on the steady-state photoluminescence spectra for each polymer substrate (Table 3.1, Table 3.2, & Figure 3.3). The steady-state photoluminescence spectra show a slight redshift and dimming in each sample as the concentration is increased (5 mg mL^{-1} → 50 mg mL^{-1}), which indicates levels of concentration quenching occurring in the samples as the precursor concentration increases from 5 mg mL^{-1} (Table 3.1). In each case however, using an overall concentration of 5mg mL^{-1} produced samples with peak PLQY for each polymer substrate. This was realized through decreasing the overall precursor concentration and observing a systematic increase of PLQY, which could be brought on by a reduction of concentration quenching [30]. In fact, with an extraordinary high PLQY ≈48%, the $MAPbBr_3$-ABS composite films (5 mg•mL^{-1}) have obtained a record high PLQY value for $MAPbBr_3$ solid composite films (Table 3.4) [4, 24]. For this reason, photophysical characterization is further carried out on $MAPbBr_3$-polymer composites using 5 mg•mL^{-1} precursor concentrations.

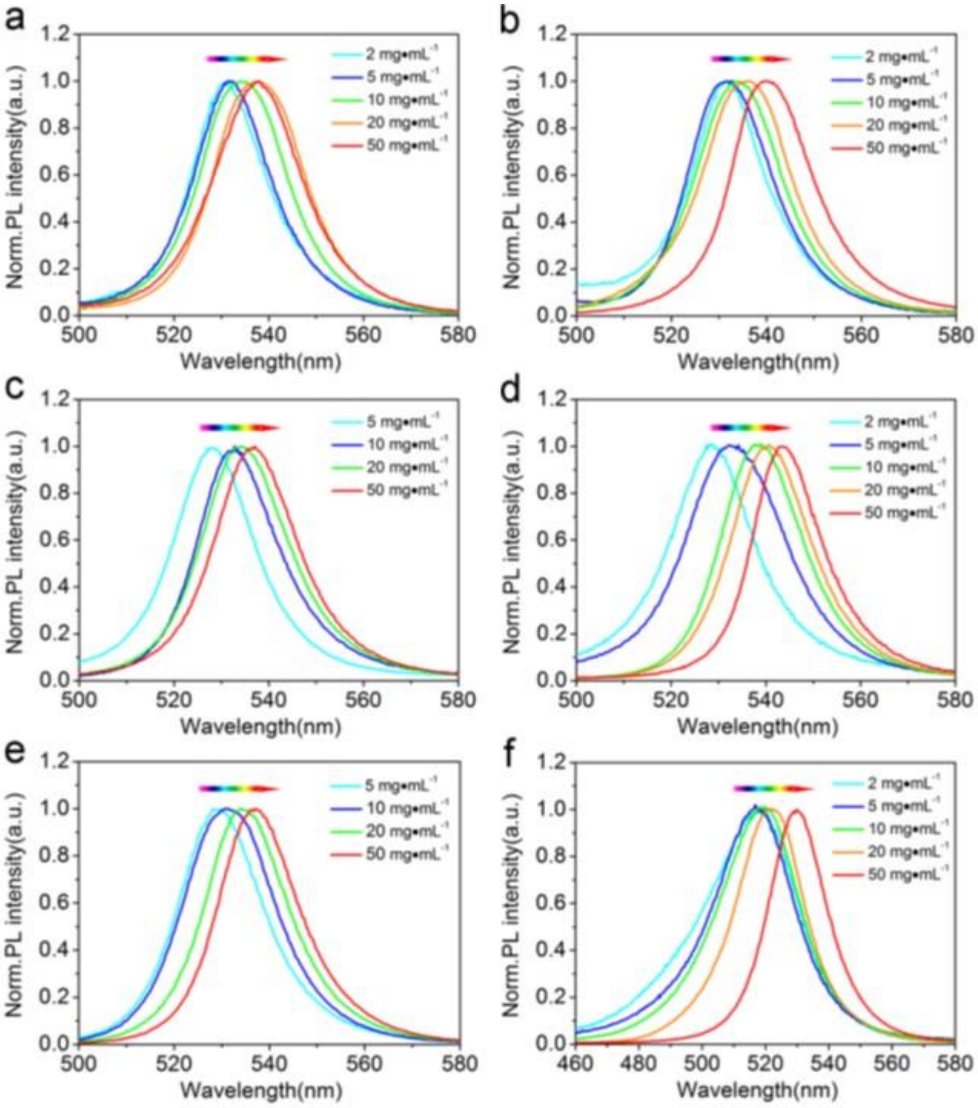

Figure 3.3: Concentration-dependent photoluminescence spectra of $MAPbBr_3$-polymer composite samples. a) $MAPbBr_3$-PS. b) $MAPbBr_3$-PC. c) $MAPbBr_3$-ABS. d) $MAPbBr_3$-CA. e) $MAPbBr_3$-PVC. f) $MAPbBr_3$-PMMA. Adapted from reference [43].

Table 3.1: Peak wavelength of photoluminescence spectra for concentration dependence in $MAPbBr_3$-polymer composite samples. Adapted from reference [43].

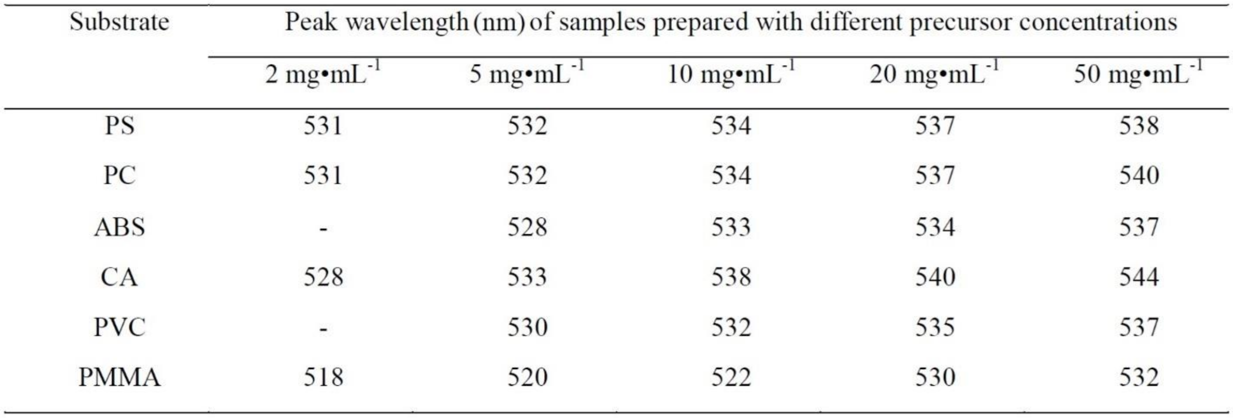

Substrate	Peak wavelength (nm) of samples prepared with different precursor concentrations				
	2 mg•mL^{-1}	5 mg•mL^{-1}	10 mg•mL^{-1}	20 mg•mL^{-1}	50 mg•mL^{-1}
PS	531	532	534	537	538
PC	531	532	534	537	540
ABS	-	528	533	534	537
CA	528	533	538	540	544
PVC	-	530	532	535	537
PMMA	518	520	522	530	532

Table 3.2: Full width at half maximum (FWHM) of photoluminescence spectra for concentration-dependence in $MAPbBr_3$-polymer composite samples. Adapted from reference [43].

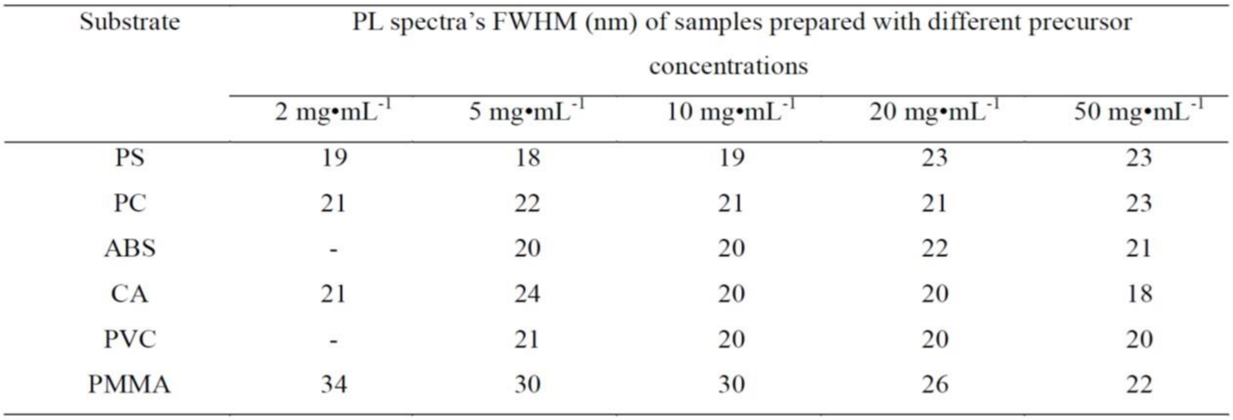

Substrate	PL spectra's FWHM (nm) of samples prepared with different precursor concentrations				
	2 mg•mL^{-1}	5 mg•mL^{-1}	10 mg•mL^{-1}	20 mg•mL^{-1}	50 mg•mL^{-1}
PS	19	18	19	23	23
PC	21	22	21	21	23
ABS	-	20	20	22	21
CA	21	24	20	20	18
PVC	-	21	20	20	20
PMMA	34	30	30	26	22

$MAPbBr_3$-Polymer Composite Characterization

SEM was used in order to (1) confirm the stemming $MAPbBr_3$-Polymer OIP composites had allowed for the uptake of IOP nanoparticle precursors and (2) resulting $MAPbBr_3$ OIP nanoparticles were disbursed throughout the polymer rather than solely on the surface. The SEM images show the surface of the polymer both with and without the $MAPbBr_3$ OIP nanoparticle incorporation. Before the nanoparticles are embedded, four of the polymers show a smooth surface (PS, PC, CA, and PVC) and two of the polymers display a cracked or grainy surface (ABS and PMMA). After spin-coating, embedded OIP nanoparticles were observed for $MAPbBr_3$-PS, $MAPbBr_3$-PC, $MAPbBr_3$-CA, $MAPbBr_3$-PVC, and $MAPbBr_3$-ABS polymer composites (Figure 3.4). Though originally displaying a grainy surface, the $MAPbBr_3$-ABS polymer composite shows a smoothed-out surface after spin-coating was performed (Figure 3.4). The $MAPbBr_3$-PMMA polymer composite was the only sample where nanoparticles can be observed on the surface of the polymer, which indicates a lower swelling ability of PMMA polymer in DMF (Figure 3.4)

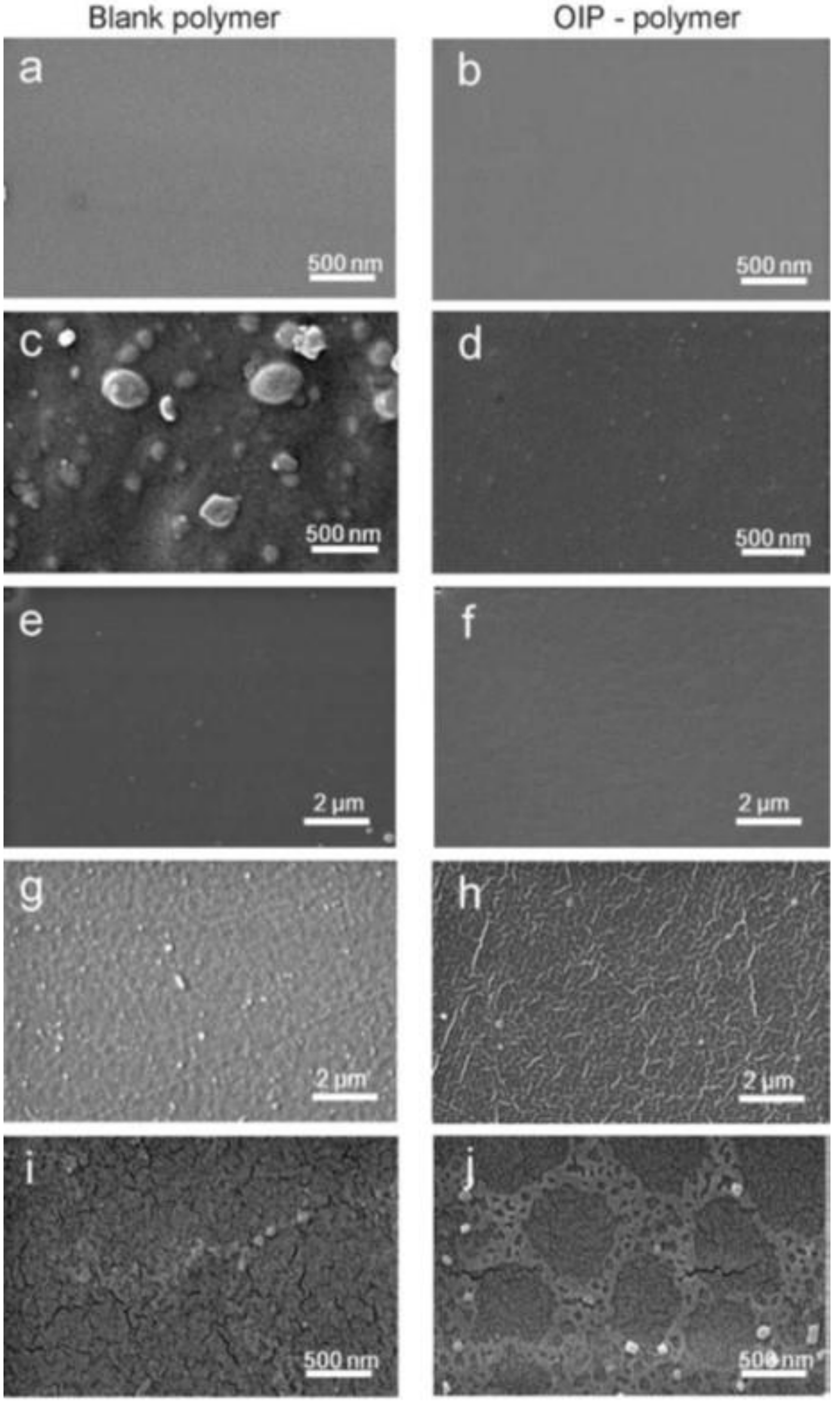

Figure 3.4: Top down view of SEM images for blank polymer substrates before OIP nanoparticle embedding and $MAPbBr_3$-polymer composite samples (5 mg mL^{-1} precursor concentration). a) PC. b) MAPbBr3-PC. c) ABS. d) MAPbBr3-ABS. e) CA. f) MAPbBr3-CA. g) PVC. h) MAPbBr3-PVC. i) PMMA. j) MAPbBr3-PMMA. Based on figure from reference [43].

Cross-sectional TEM images were also obtained using the $MAPbBr_3$-PS polymer composite sample to ensure nanoparticle dispersion throughout the polymer matrix as well as the average size of the $MAPbBr_3$ nanoparticles. The TEM images not only indicate $MAPbBr_3$ nanoparticles dispersed within the polymer matrix but also that they are intimately passivated and crystalline as well. In addition, the nanoparticles also display a clear correlation between their size and the depth in which they are found. At a depth of approximately 1 μm with respect to the sample surface, the nanoparticles have an average size of <10nm and are more densely gathered, however, as we probe further into the polymer substrate ≈5-6 μm the average size of the nanoparticles increase to >60nm but with a decrease in nanoparticle density (Figure 3.5 g-k). Further investigation with high resolution transmission electron microscopy (HRTEM) and Fast Fourier Transformation (FFT) allowed for the identification of two recognized crystal faces of $MAPbBr_3$ perovskites (110 and 200) by measuring the interplanar distances within the image (2.9 and 4.1 Å, respectively) (Figure 3.5 j & l). The TEM images not only provided evidence of well dispersed and crystalline nanoparticles within the polymer substrate but indicated their formation is happening simultaneously during the spin-coating, baking assisted swelling-deswelling process.

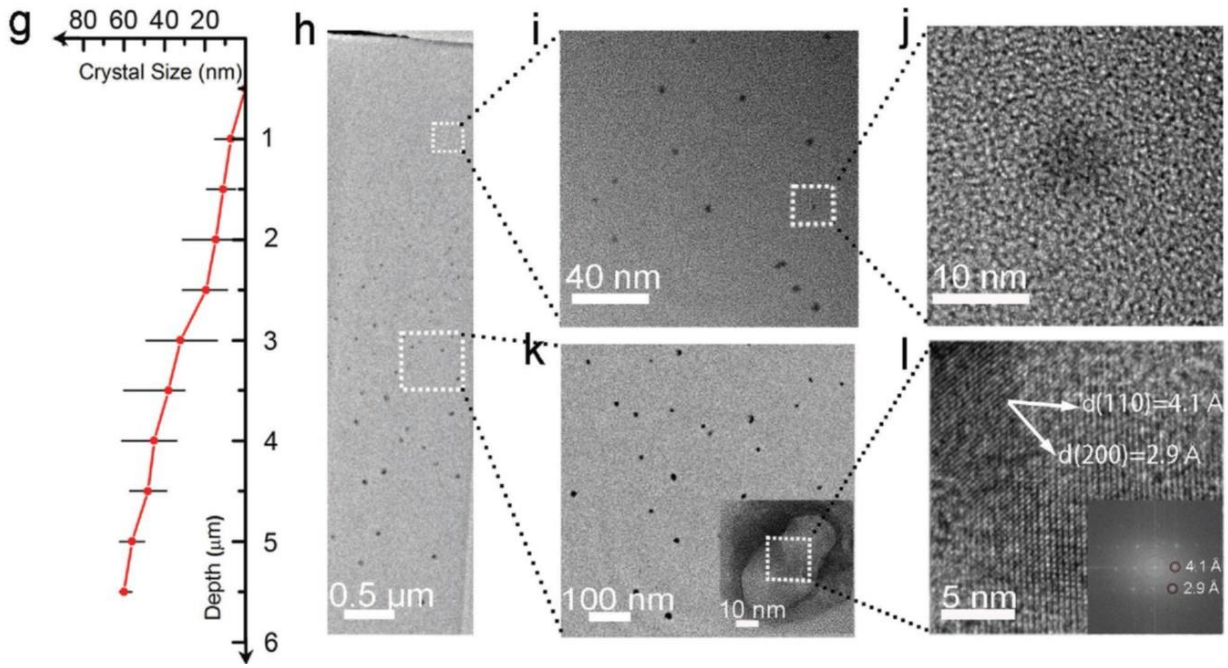

Figure 3.5: TEM cross sectional images: g) Depth of polymer substrate from the surface and average OIP crystal size along with distribution. h) TEM cross section image of $MAPbBr_3$-PS film to demonstrate depth-dependence and size-variability for $MAPbBr_3$ nanoparticles embedded in PS. Distribution of $MAPbBr_3$ nanoparticles in PS at i) 1 μm and k) 3.5 μm depths, respectively. Inset of (k) HRTEM of an individual $MAPbBr_3$ embedded nanoparticle. j) HRTEM image of emphasized area in (i). l) HRTEM image of emphasized area in (k). Inset: fast FFT of (l). All precursor concentrations were prepared at 5 mg mL^{-1}. Based on figure from reference [43].

UV-Vis, photoluminescence, and photoluminescence decay spectroscopies were used in order to investigate the optical and photophysical properties of $MAPbBr_3$-Polymer composites. UV-Vis spectroscopy indicates an overall absorption in the UV and visible up to ~550 nm where it then tapers off. Each sample also possess a noticeable absorption band ~530 nm, which is known to be another clear indicator of the formation of a bromine perovskite structure due to its direct bandgap at 2.3 eV. The wide absorption spectra of $MAPbBr_3$ perovskites can typically be divided up into three different zones: (a) band to band absorption in the UV, (b) an excitonic peak indicating the band edge (2.3 eV or 530 nm in this case), and (c) a tailing after the band edge absorption peak, referred to as Urbach tailing.

The optical absorption spectrum for semiconductor materials are closely related to the magnitude of exciton binding energy, which is what gives the absorption spectrum its step like absorption onset seen in OIP nanoparticles. These excitons can absorb light and undergo a resonance effect which can be magnified when exciton mobility is decreased and absorption cross-section grows stronger, which is proportional to the probability of electron-hole pairs being found in the same position [49]. In the absorption spectra for the encapsulated OIP nanoparticles, distinct differences can be seen in shape and intensity of the band-edge absorption at 530 nm. These changes in intensity and peak shape suggest exciton confinement is enhanced when certain polymers are chosen for encapsulation, which can be further investigated through examination of excited state dynamic using photoluminescence lifetime measurements.

Optical absorptions for electronic transitions near the band edge in disordered materials can be categorized into three well-defined regions: the strong absorption region (A), the lower absorption region (B), and the residual absorption region (C) (Figure 3.6). The absorption occurring in region A originates from one of two absorption events: either a band to band or band to edge transition, which could also be considered extended to extended states or extended to localized states transitions, respectively. The absorption in region B represents the energy or width of localized tail states and is known as the Urbach energy. The Urbach energy is almost temperature independent at room temperature, which indicates the tailing effect is produced by disorder-inducing band tailings [58]. Finally, the absorption found from area C is still not completely understood but is thought to be derived from the width of defect states [58]. In an ideally crystalline material, the slope of the band edges diverges at the bottom of the conduction band and at the top of the valance band, which gives rise to the boundaries of the energy band gap for the material. However, as crystalline order decreases and gives rise to a lack of periodicity (long-range order), as seen in less ordered and amorphous materials, localized states (defect states) begin to blur the band gap edges and display a tailing effect that encroaches into the forbidden band gap (Figure 3.7)

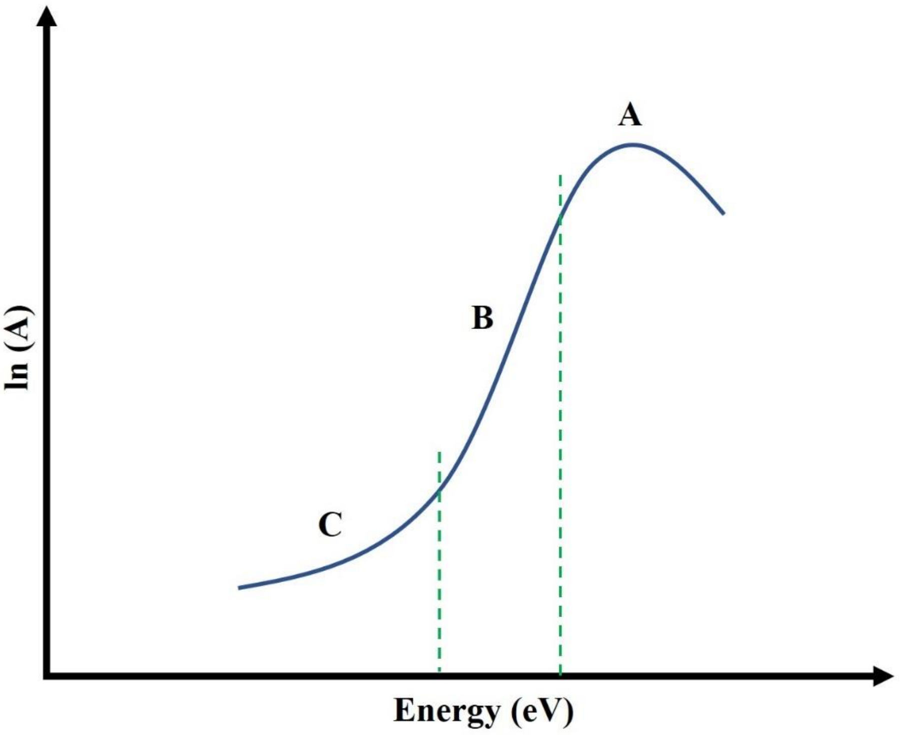

Figure 3.6: Regions of optical absorbance for disordered materials: (A) strong absorption region, (B) lower absorption region (Urbach region), (C) residual absorption region.

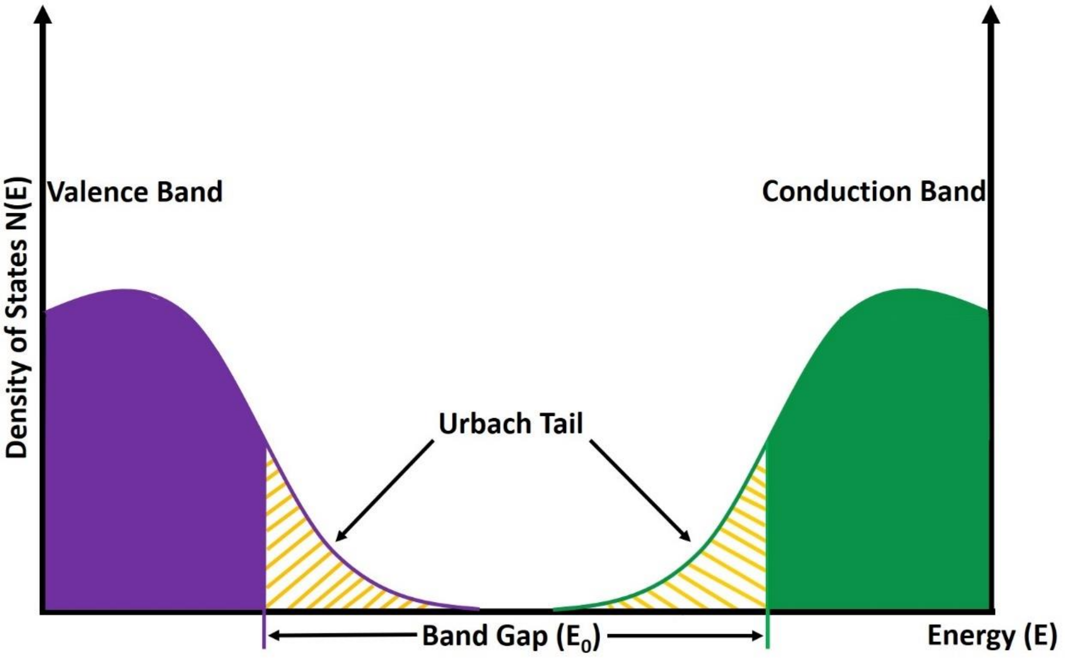

Figure 3.7: Electronic density of states (DOS) for a semiconductor material displaying disorder effects in its crystal structure.

Urbach tailing is a phenomenon occurring in semiconductor materials where there is a continuation of the absorption spectrum after the band edge, which signifies distortion/defect states prevalent in the material [51]. In low photon energy ranges, the spectral dependence of the absorption coefficient (α) and photon energy (hν) is known as the Urbach empirical rule and is given by the following equation:

$$\alpha = \alpha_0 e^{h\nu/E_U} \tag{3.3}$$

Where α_0 is a material dependent constant and E_U denotes the energy of the band tail, which is also referred to as the Urbach energy. The Urbach energy value is weakly dependent on temperature and is often associated with the width of the band tail due to localized energy states within the energy band gap due to low crystallinity or structural disorder brought on by trap states within the semiconductor material. To determine the Urbach energy of a material, the natural log of the Urbach empirical rule equation (above) must be taken resulting in the equation:

$$\ln \alpha = \ln \alpha_0 + (h\nu/E_U) \tag{3.4}$$

This form of the Urbach equation (equation 3.4) allows for the determination of the Urbach energy from the reciprocal of the slope of the resulting straight line by plotting ln (α) against energy (E). Because the absorption coefficient (α) is proportional to absorbance, ln (abs) is plotted against energy (E) to obtain the Urbach energy values for encapsulated OIP-polymer substrates [52] (Figure 3.8).

Urbach energies for $MAPbBr_3$-PS, $MAPbBr_3$-ABS, $MAPbBr_3$-PVC, and $MAPbBr_3$-CA are lower (67.51, 44.54, 86.04 and 77.74 meV, respectively) than the Urbach energies for $MAPbBr_3$-PC and $MAPbBr_3$-PMMA (126.06 and 147.02 meV, respectively) (Table 3.3), which indicates more ordered crystalline structures in the samples encapsulated with PS, ABS, PVC, and CA polymers. From the obtained values for the $MAPbBr_3$-polymer substrates, Urbach tailing is most prominent in two of the samples: MAPbBr$_3$-PC, MAPbBr$_3$-PC, and MAPbBr$_3$-PMMA from their higher Urbach energy values and visual Urbach tailing on their respective absorption spectra. This observation is sensible for the MAPbBr$_3$-PMMA sample due to the presence of OIP nanoparticles on the surface of the polymer, though in the case of MAPbBr$_3$-PC it points to disorder in the OIP nanoparticle crystal structure even though they are embedded within the polymer substrate. Further investigation into the excited state properties of the MAPbBr$_3$-polymer composites is required to completely understand that absorption spectra and Urbach energies obtained.

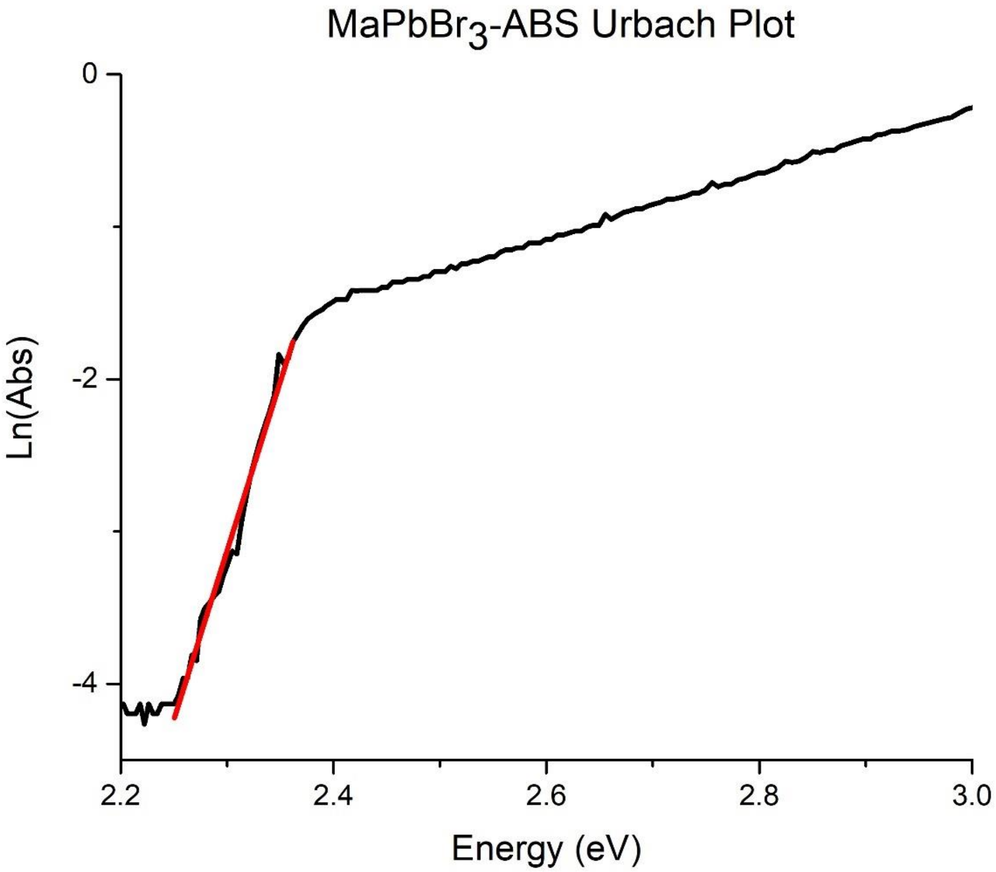

Figure 3.8: Absorbance spectrum of MAPbBr$_3$-ABS replotted at ln(abs) vs energy (eV). The red line represents the fitting of the Urbach tail and the reciprocal of the slope of this line is the Urbach energy for the material.

Table 3.3: Urbach energy values for $MAPbBr_3$-polymer composites with OIP nanoparticle concentration of 5 mg•mL^{-1}.

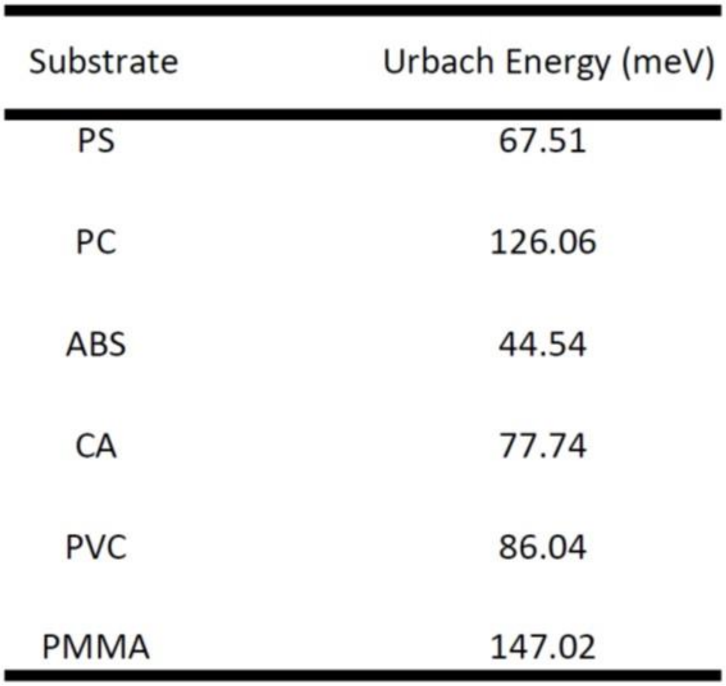

Substrate	Urbach Energy (meV)
PS	67.51
PC	126.06
ABS	44.54
CA	77.74
PVC	86.04
PMMA	147.02

The photoluminescence spectra obtained for each $MAPbBr_3$-Polymer substrate, excluding $MAPbBr_3$-PMMA shows a similar peak wavelength centered ~530 nm. Due to the nanoparticles appearing primarily on the surface of the $MAPbBr_3$-PMMA sample, degradation due to environmental factors may have caused the blue shifting that is observed in this sample (520 nm). In addition, a similar trend is observed when examining the full width half maximum (FWHM) obtained for each photoluminescence spectrum. The FWHM for each sample, excluding the $MAPbBr_3$-PMMA sample, is ~20 nm (Figure 3.9) Not only does this point to improved color purity for these samples, it also indicates uniformity to the size and composition of the OIP nanoparticles. As for the $MAPbBr_3$-PMMA sample, the FWHM was found to be ~30nm. While broadening of the photoluminescence spectrum in this case suggests a less pure color emission as more wavelengths are emitted from the sample, this is still much lower than previously reported $MAPbBr_3$ OIP nanoparticles [36].

Beyond the static photoluminescence and UV-vis measurements, time-resolved photoluminescence lifetimes are taken as a hallmark of perovskite film quality [40]. Higher performing materials are typically shown to have longer decay lifetimes, which signals more ordered crystallinity within the material or passivation of trap states within the material. For both perovskite/metal mixed solid based films [48] and colloidal nanoparticles [36] of $MAPbBr_3$, the average photoluminescence lifetime (τ_{avg}) is usually within 10-100 ns. Astonishingly, most $MAPbBr_3$-polymer composites in this study showed long τ_{avg} ranging from 130 ns ($MAPbBr_3$-PS) to 502 ns ($MAPbBr_3$-ABS), the only exception being the $MAPbBr_3$-PMMA sample with a τ_{avg} of ≈15 ns. The low τ_{avg} has been attributed to the OIP nanoparticles being primarily on the surface of the PMMA substrate and through exposure to unfavorable environmental factors, has caused degradation effects leading to a lower τ_{avg}.

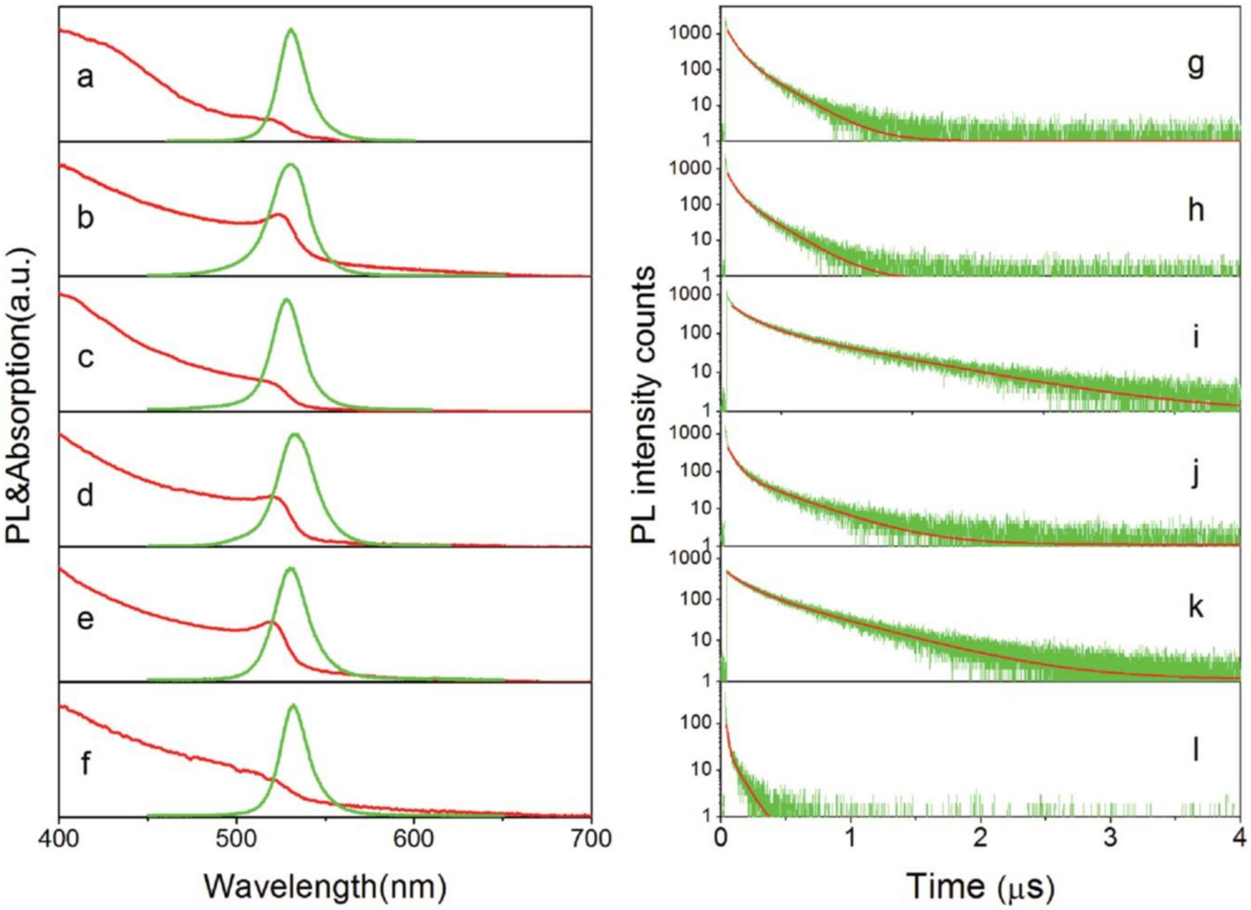

Figure 3.9: Optical properties of $MAPbBr_3$-polymer composites. a–f) UV–vis absorption (red) and PL emission (green) spectra. g–l) PL decay (green) and fitting curves (red) for excitation at 467 nm and emission at ≈530 nm of various MAPbBr3–polymer composite films. The samples from top to bottom are a,g) MAPbBr3–PS, b,h) MAPbBr3–PC, c,i) MAPbBr3–ABS, d,j) MAPbBr3–CA, e,k) MAPbBr3–PVC, and f,l) MAPbBr3–PMMA. All samples were prepared with precursor concentration of 5 mg mL^{-1}. Based on figure from reference [43].

Table 3.4: Photoluminescence lifetime (τ_1, τ_2, τ_{avg}) of $MAPbBr_3$-polymer composites (5 mg mL^{-1} precursor concentration). Based on figure from reference [43].

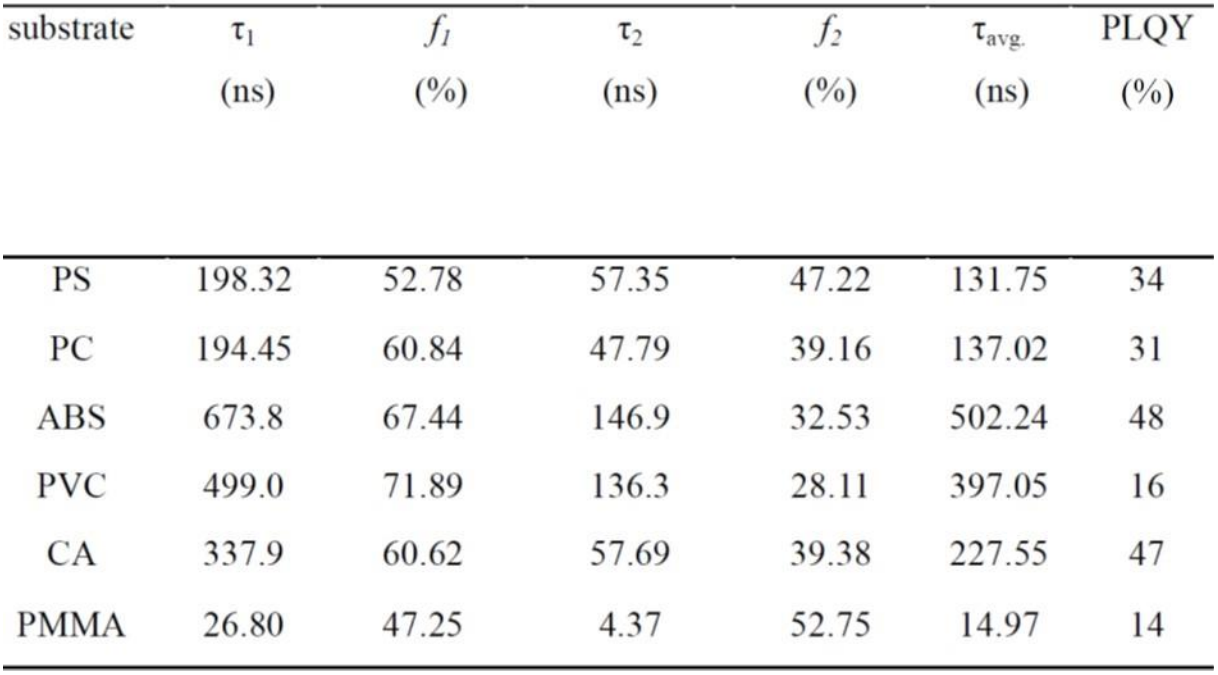

substrate	τ_1 (ns)	f_1 (%)	τ_2 (ns)	f_2 (%)	$\tau_{avg.}$ (ns)	PLQY (%)
PS	198.32	52.78	57.35	47.22	131.75	34
PC	194.45	60.84	47.79	39.16	137.02	31
ABS	673.8	67.44	146.9	32.53	502.24	48
PVC	499.0	71.89	136.3	28.11	397.05	16
CA	337.9	60.62	57.69	39.38	227.55	47
PMMA	26.80	47.25	4.37	52.75	14.97	14

Photoluminescence Lifetime and Photophysics Analysis of $MAPbBr_3$-Polymer Composites

Probing the excited state dynamics of materials intended for light harvesting or emission applications is integral to understanding the fundamental processes and characteristics behind their operation. TCSPC data elucidates how many excited state processes are occurring in the material and can also provide valuable information behind the mechanisms at play in photoluminescent materials. $MAPbBr_3$ OIP materials are widely accepted to display a biexponential decay, which highlights two major processes generating excited state carriers: short-lived trap-mediated short states (τ_1) and longer-lived excited states (τ_2) [56]

In the case of all $MAPbBr_3$-Polymer composite samples investigated in this study, a biexponential decay was observed for all samples. However, the biexponential decays can be further investigated by examining the individual lifetime components (τ_1 & τ_2) and their overall contribution to the average lifetime (τ_{avg}) in each $MAPbBr_3$-polymer composite. Beginning with $MAPbBr_3$-PMMA $\left(\tau_{avg} \approx 15\ ns\right)$, this sample had both a short τ_1 & τ_2 component (4 & 27 ns, respectively) and close to equal contribution from each component ($f_1 \approx 53\%$ & $f_2 \approx 47\%$). The low overall average photoluminescence lifetime is attributed to the incomplete encapsulation of OIP nanoparticles within the PMMA matrix. With the nanoparticles exposed to the environment, premature decomposition of OIP nanoparticles will cause a breakdown in available radiative pathways/processes through an over abundant generation of surface trap states.

Both the $MAPbBr_3$-PS and $MAPbBr_3$-PC samples exhibit similar average photoluminescent lifetimes and lifetime components (Table 3.4) but the contribution of each component to the overall average photoluminescent lifetime is slightly different, with the $MAPbBr_3$-PS sample favoring the shorter lifetime component (τ_1) and the $MAPbBr_3$-PC sample favoring the longer lifetime component (τ_2). This is an indication the polymer substrate itself may be providing more than just a coherent barrier to the outside world in the form of surface defect passivation. Chain terminations in polycarbonate polymers can result in carboxylic acids due to their derivation from carbonic acids and bisphenol [50], which could aid in the passivation of Pb^{2+} or MA^+ defects found on the surface of the OIP nanoparticles [46]. This same phenomenon can be seen in the $MAPbBr_3$-CA, $MAPbBr_3$-PVC, and $MAPbBr_3$-ABS samples, where there is a drastic increase in overall average photoluminescence decay due to the larger τ_2 lifetime components (338, 499, and 674 ns, respectively) as well as their overall higher contribution (61%, 72% and 67%, respectively). In each case there is the possibility for a charged termination in the polymer or charged functional groups within the polymer matrix, which provide surface defect passivation to either Pb^{2+} and/or Br^{-1} defects [46]. Overall, this agrees with studies suggesting that by either increasing the exciton binding energy or reducing the defect density one can achieve PL enhancements (ie. longer average PL lifetimes) in $MAPbBr_3$ nanoparticles [55].

Further investigation of the photophysical characteristics in each polymer matrix can be accomplished by deriving the radiative (k_r) and non-radiative (k_{nr}) rate constants, which give insight to the photophysical pathways being utilized in the material. The rate constants for each $MAPbBr_3$-polymer composite can be calculated through the following equations:

$$\tau_{avg} = \frac{1}{k_r + k_{nr}} \tag{3.5}$$

$$\phi = \frac{k_r}{k_r + k_{nr}} \tag{3.6}$$

$$k_r = \frac{\phi}{\tau_{avg}} \tag{3.7}$$

$$k_{nr} = \frac{1 - \phi}{\tau_{avg}} \tag{3.8}$$

where the PLQY (ϕ) and average photoluminescence lifetime (τ_{avg}) can be used to derive the individual rate constants (k_r and k_{nr}) (Table 3.5). For each of the $MAPbBr_3$-Polymer composites $k_{nr} > k_r$, which signifies there are more non-radiative decay pathways utilized than the radiative pathways available. However, half of the samples ($MAPbBr_3$-PS, $MAPBBr_3$-ABS and $MAPbBr_3$-CA) display k_r and k_{nr} constants with similar values, which indicates more radiative pathways are being utilized in these samples. This claim is further supported by the reduction of Urbach tailing in their absorption spectra and lower Urbach energy values, which indicates higher orders of crystallinity and a smaller density of trap states. With fewer trap states in the material this allows for longer average photoluminescence lifetimes with a higher contribution from the τ_2 component or smaller contributions from the τ_1 value, and higher PLQY values. The other samples ($MAPbBr_3$-PC, $MAPbBr_3$-PVC, and $MAPbBr_3$-PMMA) have significantly higher contributions from non-radiative decay pathways, display increased Urbach tailing with higher Urbach energies in their absorption spectra, and in the cases of the $MAPbBr_3$-PVC and $MAPbBr_3$PMMA samples have considerably lower PLQY. This is to be expected with the $MAPbBr_3$-PMMA sample due to the exposed nanoparticles on the surface, however the PVC polymer may not be able to provide the same level of passivation as ABS and CA due to the low-lateral symmetry of polyvinyl chloride, which makes it somewhat susceptible to moisture and oxygen permeability [53]. The following reactions are considered to be the major pathways of decomposition by water and oxygen:

$$CH_3NH_3PbX_3 \xrightarrow{H_2O} CH_3NH_2 + PbX_2 + HX$$

$$2CH_3NH_3X + \frac{1}{2}O_2 \xrightarrow{hv} 2CH_3NH_2 + I_2 + \ O_2$$

where X is the substituted halogen (I, Br, or Cl). The products of these reactions continue to further collapse and decompose the perovskite material into its precursor components [54, 55]. While this could explain the low PLQY, it doesn’t address the long average photoluminescence lifetime decay seen in the $MAPbBr_3$-PVC polymer composite sample. To understand how it is possible for a sample to have both a low PLQY and high average photoluminescence lifetime, further insight into the photophysical pathways is required.

To further discuss specific photophysical pathways, a basic description of possible radiative and non-radiative pathways is required. As stated in Chapter 1 of this thesis, charge transfer processes in $MAPbBr_3$ nanoparticles can be classified into three major contributing factors: (A) defect mediated recombination, (B) free carrier or exciton recombination, and (C) Auger recombination:

$$-\frac{dn}{dt} = k_1 n + k_2 n^2 + k_3 n^3 \tag{3.9}$$

Where n represents the carrier density, k_1 is the defect trapping rate constant, k_2 is the free carrier recombination constant, and k_3 is the Auger non-radiative rate constant. For $MAPbBr_3$ nanoparticles, the auger recombination is so small it is considered negligible in low power density illumination [57]. That leaves defect mediated recombination events and free carrier/exciton recombination as the primary photoluminescent pathways available as no dark state transitions have been discovered in perovskite nanoparticles as of yet [56]. In some instances, trap states can be further distinguished into surface traps and volume related traps, where surface trap states result in extremely low photoluminescence lifetimes and volume trap states result in much longer photoluminescence lifetimes. This instance of volume related trap states could offer an explanation to the relatively long average photoluminescence lifetime and low PLQY of $MAPbBr_3$-PVC composite samples where there is a constant trap filling of charges which extends the average photoluminescence decay [56]. Verification of this instance would require further investigation through transient spectroscopic means, either with terahertz spectroscopies or transient absorption measurements.

Due to their size, the $MAPbBr_3$-polymer composite nanoparticles propagate most of their defect states at the surface (high surface area combined with small volume), which is why the polymer passivation is successful in most of the cases for this study. The photophysical pathways, specifically the biexponential or trap-mediated monoexponential, then allow for luminescence from $S_0 \rightarrow S_1 \rightarrow S_0$ transitions (the longer lifetime observed) or from $S_0 \rightarrow S_1 \rightarrow$ Trap sites $\rightarrow S_0$ (Figure 3.10). The transition from $S_1 \rightarrow$ trap sites continue until there reaches a saturation point where the trap site(s) are filled and the transition from trap site $\rightarrow S_0$ is allowed. However, the transitions from $S_1 \rightarrow$ trap sites and from trap sites $\rightarrow S_0$ are significantly shorter, which lowers the overall average photoluminescent lifetime, decreases quantum yield, and drives up the rate constant for k_{nr}.

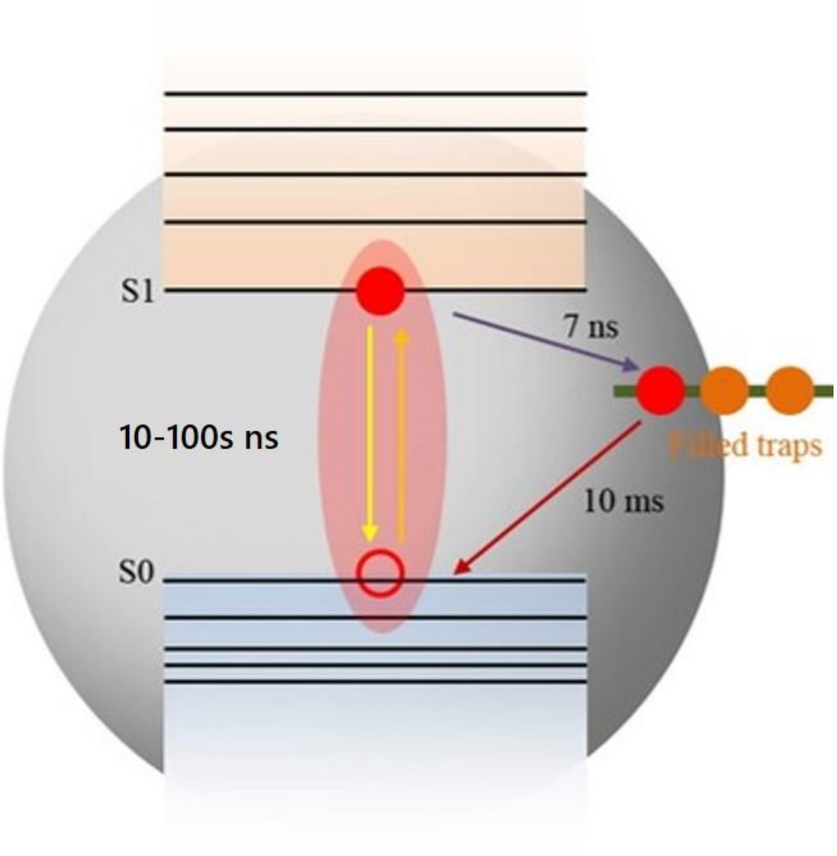

Figure 3.10: Schematics of the trap-mediated charge recombination in NPs. Purple arrow denotes the surface trapping process, and the yellow arrow is the radiative recombination of the exciton. Adapted with permission from Reference [56]. Copyright 2016 American Chemical Society.

Table 3.5: Substrate dependent radiative (k_r) and non-radiative (k_{nr}) rate constants. Average photoluminescence decay lifetime and PLQY used to calculate rate constants are relisted here as well.

Substrate	τ_{avg} (ns)	PLQY (%)	k_r (s^{-1})	k_{nr} (s^{-1})
PS	131.75	34	2.58×10^6	5.01×10^6
PC	137.02	31	2.26×10^6	5.04×10^6
ABS	502.24	48	9.56×10^5	1.04×10^6
PVC	397.05	16	4.03×10^5	2.12×10^6
CA	227.55	47	2.07×10^6	2.33×10^6
PMMA	14.97	14	9.35×10^6	5.74×10^7

It is widely accepted that the size of OIP nanoparticles play an integral role in their fundamental photophysical processes. In cases where the surface to volume ratio of the OIP nanoparticles is very high (ie. when nanoparticles are extremely small) the presence of surface defects greatly increases due to high surface lattice distortion, which in turn enhances the possibility of nonradiative processes occurring [45, 47, 48]. The TEM images confirm the average $MAPbBr_3$ crystal size increases as the depth from the top surface of polymer substrate increases with an average size near the top is still >10nm. Combining this with the excited state dynamics observed from the TCSPC data ($\tau_2 > \tau_1$ contribution to overall τ_{avg} for most samples) the swelling-deswelling encapsulation method could provide further optimization to not only crystal size control but a passivation method to increase radiative pathways available for possible exciton recombination events [46].

Because of the global applications possible from the swelling-deswelling microencapsulation strategy, we believe this could be applicable to other OIP nanoparticles (eg, $MAPbCl_3$, $MAPBI_3$, etc.) along with different polymers and applicable solvent systems. Further investigation of the swelling-deswelling microencapsulation synthetic strategy could either enable or improve on other highly stable OIP nanoparticle systems. Provided the electrical transport properties of the OIP nanoparticle-polymer system can be further enhanced, either through doping with conductive nanoparticles or exploring other conductive materials to be blended with the polymer matrix itself, these materials could become critical components for numerous photovoltaic devices (lasers [42], light emitting devices [41], solar cells, etc).

Conclusions

This spectroscopic study has demonstrated an overall increase to the stability of $MAPbBr_3$ nanoparticles when encapsulated in a polymeric matrix. Microscopy techniques (SEM and TEM) show encapsulation of $MAPbBr_3$ nanoparticles in all polymer substrates studied, excluding samples prepared with PMMA. Absorption spectroscopy revealed an overall higher order of crystallinity for most $MAPbBr_3$-polymer composites with low Urbach energies, which indicates a decrease in the density of trap states present. The photoluminescence spectroscopies showed improved PLQY and color purity in all samples (FWHM < 30nm) compared to current $MAPbBr_3$ nanoparticle synthetic routes. Finally, photoluminescence lifetime measurements indicate two primary photophysical pathways involved in light emission: defect mediated and free carrier/exciton recombination. Higher radiative rate constants (k_r) provide indications of surface defect passivation in all samples, again excluding those made with PMMA. These spectroscopic methods indicate the swelling-deswelling microencapsulation method should be further investigated not only as a method for synthesizing OIP nanoparticles but a means to increase their overall stability.

References

[1] a) J. Berry, T. Buonassisi, D. A. Egger, G. Hodes, L. Kronik, Y. L. Loo,I. Lubomirsky, S. R. Marder, Y. Mastai, J. S. Miller, D. B. Mitzi, Y. Pas,A. M. Rappe, I. Riess, B. Rybtchinski, O. Stafsudd, V. Stevanovic, M. F. Toney, D. Zitoun, A. Kahn, D. Ginley, D. Cahen, Adv. Mater. 2015, 27, 5102; b) H. J. Snaith, J. Phys. Chem. Lett. 2013, 4, 3623; c) M. A Green, A. Ho-Baillie, H. J. Snaith, Nat. Photonics (2014) 8, 506.

[2] a) A. Kojima, K. Teshima, Y. Shirai, T. Miyasaka, J. Am. Chem. Soc. (2009) 131, 6050; b) M. Lee, J. Teuscher, T. Miyasaka, T. Murakami, H. J. Snaith, Science (2012) 338, 643; c) M. Liu, M. B. Johnston, H. J. Snaith, Nature (2013) 501, 395; d) J. Burschka, N. Pellet, S. J. Moon, R. Humphry-Baker, P. Gao, M. K. Nazeeruddin, M. Grätzel, Nature (2013) 499, 316.

[3] a) H. Zhou, Q. Chen, G. Li, S. Luo, T.-b. Song, H.-S. Duan, Z. Hong, J. You, Y. Liu, Y. Yang, Science (2014) 345, 542; b) N. J. Jeon, J. H. Noh, Y. C. Kim, W. S. Yang, S. Ryu, S. Seok, Nat. Mater. (2014) 13, 897; c) W. S. Yang, J. H. Noh, N. J. Jeon, Y. C. Kim, S. Ryu, J. Seo, S. I. Seok, Science (2015) 348, 1234; d) W. Y. Nie, H. Tsai, R. Asadpour, J. C. Blancon, A. J. Neukirch, G. Gupta, J. J. Crochet, M. Chhowalla, S. Tretiak, Science (2015) 347, 522; e) X. Li, D. Bi, C. Yi, J. D. Décoppet, J. Luo, S. M. Zakeeruddin, A. Hagfeldt, M. Grätzel, Science (2016) 353, 58.

[4] a) S. D. Stranks, H. J. Snaith, Nat. Nano (2015) 10, 391; b) S. Gonzalez-Carrero, R. E. Galian, J. Perez-Prieto, Opt. Express (2016) 24, A285; c) Y. Zhao, K. Zhu, Chem. Soc. Rev. (2016) 45, 655; d) S. A. Veldhuis, P. P. Boix, N. Yantara, M. Li, T. C. Sum, N. Mathews, S. G. Mhaisalkar, Adv. Mater. (2016) 28, 6804.

[5] a) S. Pathak, N. Sakai, F. Wisnivesky Rocca Rivarola, S. D. Stranks, J. Liu, G. E. Eperon, C. Ducati, K. Wojciechowski, J. T. Griffiths, A. A. Haghighirad, A. Pellaroque, R. H. Friend, H. J. Snaith, Chem. Mater. (2015) 27, 8066; b) F. Deschler, M. Price, S. Pathak, L. E. Klintberg, D. D. Jarausch, R. Higler, S. Hüttner, T. Leijtens, S. D. Stranks, H. J. Snaith, M. Atatüre, R. T. Phillips, R. H. Friend J. Phys. Chem. Lett. (2014) 5, 1421; c) Z. Ning, X. Gong, R. Comin, G. Walters, F. Fan, O. Voznyy, E. Yassitepe, A. Buin, S. Hoogland, E. H. Sargent, Nature (2015) 523, 324.

[6] a) E. von Hauff, M. Lira-Cantu, T. M. Brown, H. Hoppe, Adv. Energy Mater. (2015) 5, 1501924; b) T. Leijtens, G. E. Eperon, N. K. Noel, S. N. Habisreutinger, A. Petrozza, H. J. Snaith, Adv. Energy Mater. (2015) 5, 1500963; c) L. Loo, P. Patel, MRS Bull. (2015) 40, 636.

[7] G. Niu, X. Guo, L. Wang, J. Mater. Chem. A (2015) 3, 8970.

[8] a) T. A. Berhe, W. N. Su, C. H. Chen, C. J. Pan, J. H. Cheng, H. M. Chen, M. C. Tsai, L. Y. Chen, A. A. Dubale, B. J. Hwang, Energy Environ. Sci. 2016, 9, 323; b) M. Shahbazi, H. Wang, Solar Energy (2016) 123, 74.

[9] L. Zhang, M. Zhou, Z. Zhang, J. Yuan, B. Li, W. Wen, J. Tian, Journal of Materials Chemistry A (2019) 7 (39), 22229-22234.

[10] Y. Wei, Z. Cheng, J. Lin, Chemical Society Reviews (2019) 48 (1), 310-350.

[11] Y. Fujimoto, Advances in Condensed Matter Physics, (2015) 571490.

[12] R. Sheng, X. Wen, S. Huang, X. Hao, S. Chen, Y. Jiang, X. Deng, M. Green, A. Ho-Baillie, Nanoscale (2016) 8, 1926.

[13] S. Bonabi Naghadeh, B. Luo, G. Abdelmageed, Y.-C. Pu, C. Zhang, J. Z. Zhang, The Journal of Physical Chemistry C (2018) 122 (28), 15799-15818.

[14] B. Chen, P. N. Rudd, S. Yang, Y. Yuan, J. Huang, Chemical Society Reviews (2019) 48 (14), 3842-3867.

[15] T. Leijtens, B. Lauber, G. E. Eperon, S. D. Stranks, H. J. Snaith, J. Phys. Chem. Lett. (2014) 5, 1096.

[16] S. Guarnera, A. Abate, W. Zhang, J. M. Foster, G. Richardson, A. Petrozza, H. J. Snaith, J. Phys. Chem. Lett. (2015) 6, 432.

[17] B. Conings, J. Drijkoningen, N. Gauquelin, A. Babayigit, J. D'Haen, L. D'Olieslaeger, A. Ethirajan, J. Verbeeck, J. Manca, E. Mosconi, Adv. Energy Mater. (2015) 5, 1500477.

[18] S. N. Habisreutinger, T. Leijtens, G. E. Eperon, S. D. Stranks, R. J. Nicholas, H. J. Snaith, Nano Lett. (2014) 14, 5561.

[19] a) L. C. Schmidt, A. Pertegás, S. González-Carrero, O. Malinkiewicz, S. Agouram, G. Mínguez Espallargas, H. J. Bolink, R. E. Galian, J. Pérez-Prieto, J. Am. Chem. Soc. (2014) 136, 850; b) B. Luo, Y. Pu, Y. Yang, S. Lindley, G. Abdelmageed, H. Ashry, Y. Li, X. Li, J. Zhang, J. Phys. Chem. C (2015) 119, 26672; c) P. Tyagi, S. M. Arveson, W. A. Tisdale. J. Phys. Chem. Lett. (2015) 6, 1911; d) H. Huang, A. S. Susha, S. V. Kershaw, T. F. Hung, A. L. Rogach, J. Adv. Sci. (2015) 2, 1500194.

[20] a) F. Zhang, H. Zhong, C. Chen, X.-G. Wu, X. Hu, H. Huang, J. Han, B. Zou, Y. Dong, ACS Nano (2015) 9, 4533; b) O. Vybornyi, S. Yakunina, M. V. Kovalenko, Nanoscale (2016) 8, 6278.

[21] L. Protesescu, S. Yakumin, M. I. Bodnarchuk, F. Krieg, R. Caputo, C. H. Hendon, R. X. Yang, A. Walsh, M. C. Kovalenko, Nano Lett. (2015) 15, 3692.

[22] F. Zhu, L. Men, Y. Guo, Q. Zhu, U. Bhattacharjee, P. M. Goodwin, J. W. Petrich, E. A. Smith, J. Vela, ACS Nano (2015) 9, 2948.

[23] D. Di, K. P. Musselman, G. Li, A. Sadhanala, Y. Ievskaya, Q. Song, Z.-K. Tan, M. L. Lai, J. L. MacManus-Driscoll, N. C. Greenham, R. H. Friend, J. Phys. Chem. Lett. (2015) 6, 446.

[24] G. Longo, A. Pertegás, L. Martínez-Sarti, M. Sessolo, H. J. Bolink, J. Mater. Chem. C (2015) 3, 11286.

[25] f Zanatta, A. R., Scientific Reports (2019) 9 (1), 11225.

[26] S. D. Stranks, R. L. Z. Hoye, D. Di, R. H. Friend, F. Deschler, Advanced Materials (2019) 31 (47), 1803336.

[27] H. Huang, M. I. Bodnarchuk, S. V. Kershaw, M. V. Kovalenko, A. L. Rogach, ACS Energy Letters (2017) 2 (9), 2071-2083.

[28] B. Erman, P. Flory, Macromolecules (1986) 19, 2342.

[29] a) S. Freitas, H. P. Merkle, B. Gander. J. Controlled Release 2005, 102, 313; b) M. Li, O. Rouaud, D. Poncelet, Int. J. Pharm. (2008) 363, 26.

[30] D. Dexter, J. H. Schulman, J. Chem. Phys. (1954) 22, 1063.

[31] Y. H. Kim, H. Cho, J. H. Heo, T. S. Kim, N. Myoung, C. L. Lee, S. H. Im, T. W. Lee, Adv. Mater. (2015) 27, 1248.

[32] D. W. deQuilettes, S. M. Vorpahl, S. D. Stranks, H. Nagaoka, G. E. Eperon, M. E. Ziffer, H. J. Snaith, D. S. Ginger, Science (2015) 348, 683.

[33] L. W. McKeen, Permeability Properties of Plastics and Elastomers. William Andrew, Elsevier, Amsterdam, The Netherlands, (2011).

[34] N. Grassie, G. Scott, Polymer Degradation and Stabilisation. Cambridge University Press, Cambridge (1985)

[35] C. Carrillo-Carrión, S. Cárdenas, B. M. Simonet, M. Valcárcel, Chem. Commun. (2009), 5214.

[36] Y. Tian, A. Merdasa, E. Unger, M. Abdellah, K. Zheng, S. McKibbin, A. Mikkelsen, T. Pullerits, A. Yartsev, V. Sundström, I. G. Scheblykin, J. Phys. Chem. Lett. (2015), 6, 4171.

[37] a) Z. Chen, C. Yu, K. Shum, J. J. Wang, W. Pfenninger, N. Vockic, J. Midgley, J. T. Kenney, J. Lumin. (2012), 132, 345; b) K. Wu, A. Bera, C. Ma, Y. M. Du, Y. Yang, L. Li, T. Wu, Phys. Chem. Chem. Phys. (2014) 16, 22476.

[38] S. D. Stranks, V. M. Burlakov, T. Leijtens, J. M. Ball, A. Goriely, H. J. Snaith, Phys. Rev. Appl. (2014), 2, 034007.

[39] a) Z. Luo, D. Xu, S.-T. Wu, J. Display Technol. 2014, 10, 526; b) R. Zhu, Z. Luo, H. Chen, Y. Dong, S.-T. Wu, Opt. Express (2015), 23, 23680.

[40] a) J. Chen, S. Gensler, J. Hartlove, J. Yurek, E. Lee, J. Thielen, J. Van Derlofske, J. Hillis, G. Benoit, J. Tibbits, SID Int. Symp. Dig. Tech. Pap. (2015), 46, 173; b) J. S. Steckel, J. Ho, C. Hamilton, J. Xi, C. Breen, W. Liu, P. Allen, S. Coe-Sullivan, J. Soc. Inf. Disp. (2015), 23, 294.

[41] a) Z.-K. Tan, R. S. Moghaddam, M. L. Lai, P. Docampo, R. Higler, F. Deschler, M. Price, A. Sadhanala, L. M. Pazos, D. Credgington, F. Hanusch, T. Bein, H. J. Snaith, R. H. Friend, Nat. Nano (2014), 9, 687; b) H. Cho, S.-H. Jeong, M.-H. Park, Y.-H. Kim, C. Wolf, C.-L. Lee, J. H. Heo, A. Sadhanala, N. Myoung, S. Yoo, Science (2015), 350, 1222.

[42] a) G. Xing, N. Mathews, S. S. Lim, N. Yantara, X. Liu, D. Sabba, M. Grätzel, S. Mhaisalkar, T. C. Sum, Nat. Mater. (2014), 13, 476; b) S. W. Eaton, M. Lai, N. Gibson, A. B. Wong, L. Dou, J. Ma, L. Wang, S. R. Leone, P. Yang, Proc. Natl. Acad. Sci. USA 2016, 113, (1993); c) H. M. Zhu, Y. P. Fu, F. Meng, X. X. Wu, Z. Z. Gong, Q. Ding, M. V. Gustafsson, M. T. Trinh, S. Jin, X. Y. Zhu, Nat. Mater. (2015), 14, 636; d) Q. Zhang, S. T. Ha, X. F. Liu, T. C. Sum, Q. H. Xiong, Nano Lett. (2014), 14, 5995.

[43] Y. Wang, J. He, H. Chen, J. Chen, R. Zhu, P. Ma, A. Towers, Y. Lin, A. J. Gesquiere, S. Wu, and Y. Dong, Adv. Mater., (2016), 28: 10710-10717.

[44] K. Zheng, K. Žídek, M. Abdellah, M. E. Messing, M. J. Al-Marri, T. Pullerits, The Journal of Physical Chemistry C (2016), 120 (5), 3077-3084.

[45] Ananthakumar, S. Moorthy Babu, Synthetic Metals, (2018), 246, 64-95.

[46] B. Luo, S. B. Naghadeh, A'L. Allen, X. Li, J. Z. Zhang, Adv. Funct. Mater. (2017), 27, 1604018.

[47] D. M. Jang, K. Park, D.H. Kim, J. Park, F. Shojaei, H. S. Kang, J.-P. Ahn, J. W. Lee, J. K. Song, Nano Letters (2015), 15 (8), 5191-5199.

[48] M. Anaya, A. Rubino, T. C. Rojas, J. F. Galisteo-López, M. E. Calvo, H, Míguez, Advanced Optical Materials (2017), 5, 1601087.

[49] D. Marongiu, M. Saba, F. Quochi, A. Mura, G. Bongiovanni, Journal of Materials Chemistry C (2019) 7 (39), 12006-12018.

[50] D. C. Clagett, S. J. Shafer, G. Allen, J. C. Bevington, Eds. Pergamon: Amsterdam, (1989); pp 345-356.

[51] M. Roy Vikram, S. Banerjee, A. Mitra, A. Alam, M. Aslam, Chem. Eur. J. (2019) 25, 9892.

[52] V. R. Akshay, B. Arun, G. Mandal, M. Vasundhara, Physical Chemistry Chemical Physics (2019) 21 (24), 12991-13004.

[53] P. W. Morgan. Ind. Eng. Chem. (1953) 45, 2296–2306.

[54] J. M. Frost, K. T. Butler, F. Brivio, C. H. Hendon, M. van Schilfgaarde, A. Walsh. Nano Lett., (2014) 14, 2584–2590.

[55] N. Sultana, N. J. Demarais, D. Shevchenko. P. J. Derrick. Sol. RRL, (2018), 2, 9.

[56] K. Zheng, K. K. Žídek, M. Abdellah, M. E. Messing, M. J. Al-Marri, T. Pullerits. The Journal of Physical Chemistry C (2016) 120 (5), 3077-3084.

[57] M. T. Trinh, X. Wu D. Niesner, X. Y. Zhu. Journal of Materials Chemistry A (2015) 3 (17), 9285-9290.

[58] J. Singh and K. Shimakawa, Advances in Amorphous Semiconductors. Taylor & Francis, New York, NY (2003).

CHAPTER 4: IN SITU SYNTHESIS AND MACROSCALE ALIGNMENT OF $CsPbBr_3$ PEROVSKITE NANORODS IN A POLYMER MATRIX

Adapted from reference [67] with permission from The Royal Society of Chemistry

Introduction

One dimensional (1D) materials have long been considered a fundamental building block in regard to nanoscience and the technologies entwined with it. Specifically, 1D semiconductor nanowires [1-5] and nanorods [6,7] are of particular interest due to their potential use as functional materials in growing technology fields such as photonics [3] and optoelectronics [2,4,8-10]. Specifically, finding low cost solutions to polarized emission sources is exceedingly coveted in the display industries. A recent influx of proposals for aligned cadmium selenide (CdSe) nanorods for polarized light sources [11-18] influences these interests due to their applicability for use in liquid crystal display (LCD) backlighting [19-21] to drive up optical efficiency. Nonetheless, the suggested CdSe nanorods require a relatively complex synthetic process along with high production costs. Furthermore, processes for their macroscale alignment must be improved to eventually realize their desire to adapt them for display industry applications [22,23].

Metal halide perovskites with the general formula ABX_3, have become a matter of interest in regard to a low cost, high performance light emitting or photovoltaic material [24-33]. An advantage to perovskite materials is their appeal as a versatile material, in that multiple substitutions can be made to their general ABX_3 formula to modify their optical properties. The A site can be used to make the material itself either completely inorganic with cesium (Cs) or a hybrid material by using organic components such as formamidinium (FA) or methylammonium (MA). The B sites are a divalent cation and the X sites are a halogen, typically Pb^{2+} or Sn^{2+} and Cl^-, Br^-, or I^-, respectively. Purely inorganic perovskite materials, specifically $CsPbBr_3$, have garnered interest due to their increased stability over their hybrid counterparts [33-36].

In the inorganic perovskite materials class, $CsPbBr_3$ has shown great promise in particular due to its overall high color purity and emission efficiency [33,36,37] combined with its recently achieved polarized emission as a 1D nanostructured material [38-40]. Perovskite nanowires/nanorods have been achieved now through various synthetic methods involving either solid phase [41-50] or vapor phase methods [51]. These investigations have led to nanowires/nanorods of considerable size, shape, and sometimes local alignment [38] but still suffer from difficulties in achieving a macroscale alignment of the nanowires/nanorods. This is a direct result of an inherent challenge with all perovskite materials, their inherent susceptibility to heat and moisture [38]. Beyond the stability issues facing these materials, challenges still arise with nanowires/nanorods coming into contact during the synthetic process and aggregating into bulk structures [48].

Unlike their 2D and 3D counterparts, the design and understanding of 1D perovskite materials is lackluster and continues to lag behind. A majority of low dimensional (1D/0D) perovskite materials have been prepared on a trial and error basis and an understanding of their optical and photophysical properties beyond photovoltaics is scarce [63]. This could be attributed to the low number of systematic and reliable theories for a controlled growth of low dimensional perovskite nanostructures.

Here we report a spectroscopic investigation of 1D $CsPbBr_3$ nanorods embedded in a polymer matrix synthesized through an *in-situ*, catalyst free method. This strategy affords high stability to the perovskite nanorods, while affording a macroscale alignment without a luminescence degradation cost. Furthermore, optical and photophysical characterization is carried out to elucidate fundamental photophysical properties, such as: optical absorption, photoluminescence emission, and the excited state pathways of the 1D nanorods created through this technique.

The synthetic strategy employed in this instance takes advantage of a simple swelling-deswelling microencapsulation processes demonstrated in chapter one of this thesis [52]. The $CsPbBr_3$ perovskite precursor solution was introduced into a polymer matrix (polystyrene (PS), polycarbonate (PC), and acrylonitrile-butadiene- styrene (ABS)) through a solvent-induced swelling process and distributed in-between the swollen polymer chains as horizontally elongated droplets. Afterwards, the solvent is driven out through a heat induced annealing process, which initiates the perovskite nanocrystal nucleation process. The polymer chain clusters surrounding the supersaturated perovskite droplets then act as a growth template and allow for perovskite nanorod formation. Alongside the nanorod growth, a deswelling process occurs, which shrinks the polymer matrix and provides both protection from the external environment and passivation.

Optical and photophysical characterization was carried out through UV-Vis, photoluminescence, and time resolved photoluminescence spectroscopies. In addition to this, polarization imaging was completed in conjunction with fluorescence imaging due to the unique properties brought on by the macroscale alignment of the perovskite nanorods. Spectroscopic investigation of encapsulated $CsPbBr_3$ perovskite nanorods offers insight into optimization strategies for further synthetic developments as well as delving into optical and photophysical properties for a fundamental material with promise in optoelectronic and photonic applications. We hypothesize the encapsulated $CsPbBr_3$ nanorods will display improved optical and spectral characteristics such as narrower FWHM photoluminescence spectra, a distinct band to band transition peak with minimal Urbach tailing in the absorption spectra, longer photoluminescent lifetimes with a higher number of radiative pathways utilized ($k_r > k_{nr}$), and a higher polarization ratio for emitted light compared to previously synthesized $CsPbBr_3$ perovskite nanorods. These optical enhancements will be achieved by applying the swelling-deswelling synthetic technique with precursor concentration control and spin-coating to achieve encapsulated $CsPbBr_3$ nanorods along with heating and stretching to mechanically align the resulting nanorods.

Experimental

Materials

Polystyrene (PS) substrates were purchased from VWR International, Inc, and polycarbonate (PC) films, acrylonitrile–butadiene–styrene (ABS) films were purchased from McMaster-Carr. CsBr (99.999%), PbBr2 (99.999%) N,N-dimethylformamide (extra dry, 99%), and sodium hydroxide pellets were purchased from Sigma-Aldrich, HPLC grade acetone (omnisolv) was purchased from VWR International, and coverslips (22x22-1) were purchased from Fisher Scientific (Catalog No. 12-544-10). All substrates and materials were used as received.

Synthesis

The perovskite precursors, CsBr and $PbBr_2$, were dissolved in dimethylformamide (DMF) solvent and mixed in a stoichiometric molar ratio of 1:1 with a resulting concentration of 30 mg mL^{-1}. The resulting precursor solution was allowed to stir at room temperature overnight and diluted into different concentrations (12, 15, and 20 mg mL^{-1}) with DMF. The resulting precursor solutions were processed onto a polymer substrate through spin coating at various spin speeds (1000, 2000, and 3000 rpm) inside a N_2 filled glovebox. The samples were then annealed at one of three annealing temperatures and times: 25 °C/8hr, 40 °C/4hr, or 80 °C/2hr on a hotplate. A schematic of the synthetic process can be found in Figure 4.1. Each annealing temperature/time combination produced no visible changes to brightness or morphology in any of the nanorod/polymer composite samples produced.

Figure 4.1: *in situ* synthesis of encapsulated $CsPbBr_3$ nanorods. Reproduced from Ref. 67 with permission from The Royal Society of Chemistry.

Macroscale Alignment of $CsPbBr_3$ Nanorods

$CsPbBr_3$-PS composite samples were used the macroscale alignment testing. Each sample was placed on a mechanical stage under a heat gun in atmospheric conditions and stretched until it had grown 8x in length (Figure 3.2).

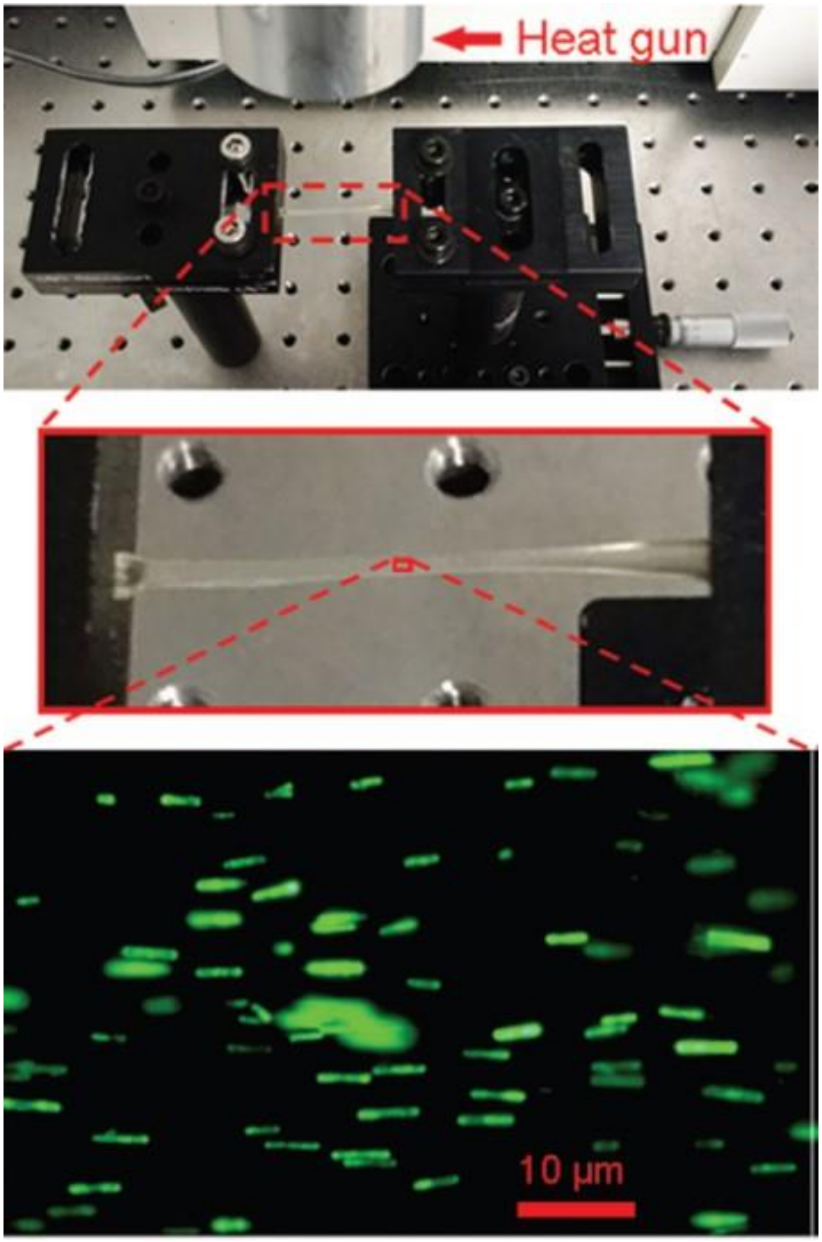

Figure 4.2: Mechanical stretching alignment of a $CsPbBr_3$-PS composite sample. Top: Mechanical stretching set-up for $CsPbBr_3$-PS nanocomposites. Middle: Enlarged image of a stretched $CsPbBr_3$-PS sample. Bottom: fluorescence microscopy image of aligned $CsPbBr_3$ nanorods. Reproduced from Ref. [67] with permission from The Royal Society of Chemistry.

Macroscale Fluorescence Microscopy

Fluorescence microscopy images were taken using an Olympus BX51 microscope. Excitation of the samples was achieved with a 450-480 nm light source.

UV-Vis Spectroscopy

All UV-Vis absorption spectra were collected using a Varian Cary 500 spectrometer at room temperature.

Steady-State Photoluminescence Spectroscopy

All steady-state photoluminescence spectra were obtained using an Ocean optics USB2000 spectrometer with an excitation wavelength at 460nm.

Photoluminescence Quantum Yield (PLQY)

All PLQY measurements were carried out using an integrating sphere method with an intensity modulated 409 nm laser beam used for the excitation source. All measurements were carried out at room temperature in atmospheric conditions.

Coverslip Preparation for TCSPC Measurements

The coverslips (22 x 22-1) are used for samples in the custom-built sample holder used for microscope stage. The coverslips are first rinsed with nanopure water and sonicated in HPLC grade acetone (Omnisolv) for twenty minutes. The coverslips are then rinsed with nanopure water and sonicated in a 10 %wt sodium hydroxide solution for twenty minutes. Finally, the coverslips are rinsed with nanopure water and put through two more rounds of sonication in nanopure water for twenty minutes each time. After the subsequent washes, the coverslips are dried with N_2 and processed in a UV-Ozone chamber for 15 minutes.

Photoluminescence Imaging

Photoluminescence images were acquired using a home-built sample-scanning confocal microscope. A 466 nm pulsed laser was used as the excitation source (Picoquant LDH-P-C-470) for all $CsPbBr_3$-polymer composite samples. The excitation side before the sample includes the following filters and optical elements: A gradient ND filter, 2.0 ND filter, 466/5 IF, and a dichroic mirror for 466 nm. The emission side after the sample includes the following optical elements: 470 nm LP filter, 45/45/10 beam splitter, and an achromatic lens (FL = 100 mm). The laser was focused down to a spot size of ~300nm using a Zeiss 100x Fluar objective lens (NA 1.3, WD 0.17mm). To create a photoluminescence image of the scanned area, the $CsPbBr_3$ samples were raster scanned across the focused laser beam using a Mad City Labs piezoelectric stage (Nano-LP100). Fluorescence from single particles was collected using a fast, single photon counting detector (Picoquant, Micro Photon Devices, PDM series). Images were collected using the following scan parameters: dwell time of 5 ms, a laser repetition rate of 125 kHz, a scanning range of 10 x 10 μm^2 – 100 x 100 μm^2, and a laser power registering <1nW.

Photoluminescence Spectroscopy

Using the table setup described above, single particle photoluminescence spectra were obtained by a spectrograph with the grating (150 g/mm blaze: 500 nm) centered at 680 nm (PI Acton SP-2156) which was coupled to a thermoelectrically cooled Electron Multiplying Charge Coupled

Device (EM-CCD, Andor iXon EM+ DU-897 BI). Each fluorescence spectrum was collected with five second exposure times with three consecutive exposures and then averaged.

Time Correlated Single Photon Counting

Using the same set-up as described above, TCSPC excited state lifetime studies were completed by parking an area of interest of the samples over the focused pulsed laser beam (Picoquant LDH-P-C-470) and collecting photons with a fast, single photon counting detector (Picoquant, Micro Photon Devices, PDM series). The photon timing was measured using a pulsed laser driver (PDL 800-D), which provided the timing signal to a PicoHarp 300 TCSPC module in combination with a detector router (PHR 800), all from Picoquant. The following parameters were used in each decay curve acquisition: 125kHz repetition rate, 512ps resolution, 120 second collection time, laser power intensity >1nw for excitation, and counts recorded kept at ~3000 cts for all samples.

Individual Nanorod Photoluminescence Polarization Imaging

Individual nanorod polarization imaging is achieved using the same custom, home-built set up described in the photoluminescence imaging section above. The addition of a $\frac{\lambda}{4}$ waveplate on the excitation side is implemented to ensure circular polarized light emission from the laser source (Picoquant LDH-P-C-470). Adjustments to the detector set-up include the use of two separate single photon avalanching diodes (SPAD) (Picoquant, Micro Photon Devices, PDM series), simultaneously and orthogonal to one another, to acquire two separate polarization images (X and Y). The detectors have a polarization beam splitter placed in front of them to separate any parallel and perpendicularly polarized light emitted by the sample (Figure 3.3)

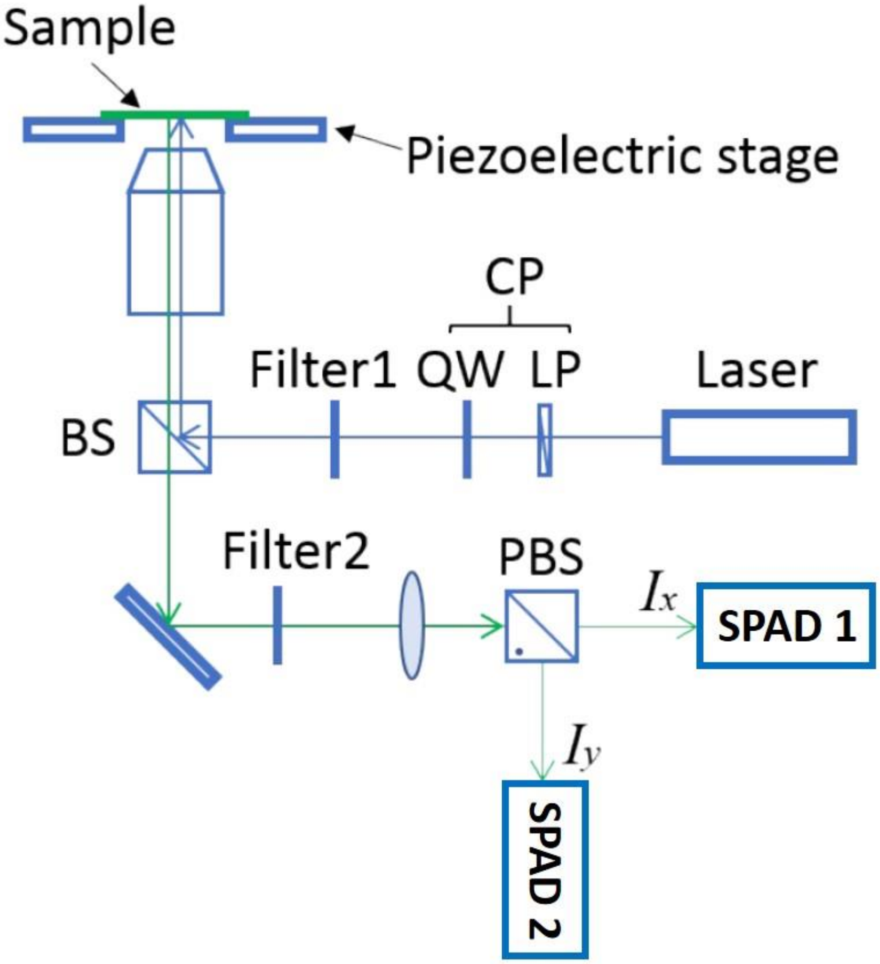

Figure 4.3: Optical measurement schematic of the polarization imaging set-up. SPAD: Single photon avalanching diode; CP: circular polarizer; QW: Quarter-wave plate; PBS: polarizing beam splitter; BS: beam splitter. Reproduced from Ref. 67 with permission from The Royal Society of Chemistry.

TCSPC Data Fitting

The time-resolved PL decay curves were fit to a biexponential function of time (t):

$$F\ (t) = A_1 e^{-t/\tau_1} + \ A_2 e^{-t/\tau_2} \tag{4.1}$$

Where A_1 and A_2 are the amplitudes each time constant makes to the overall lifetime and τ_1 and τ_2 are the time constants. All decay curves were fitted using the FluoFit® Pro software (Picoquant). Photoluminescence decay curve fitting is done through a tail-fitting method to account for the instrument response function (IRF). Average recombination lifetimes are estimated with the use of the A and τ values obtained from the fitted curve data according to the following equation:

$$\tau_{avg} = \frac{\{\Sigma_i\ (\mathrm{A}_i\ x\ \tau_i)^2\}}{\{\Sigma_i\ (\mathrm{A}_i\ x\ \tau_i)\}} \tag{4.2}$$

Where $A_i$is the amplitude of the *ith* lifetime component and τ_i is the respective lifetime component.

Polarization Imaging Processing

The sets of images obtained from polarization imaging were processed in a custom created application using MatLab. The simultaneously images obtained were averaged together, pixel by pixel, to create a resulting polarization image using the following equation:

$$P = \frac{(I_y - I_x)}{(I_y + I_x)} \tag{4.3}$$

Where P is the overall polarization for the resulting image, and $I_y$and I_x are the resulting intensities of the two perpendicular polarized photoluminescence signals.

Calculation of Theoretical 1D nanostructure Polarization

Due to the cylindrical shape of 1D nanorods, there is no reduction in electric field along the long axis and the electric field perpendicular to the long axis is attenuated. The ratio of the two can be calculated with the following equation:

$$\frac{E_{\perp}}{E_{\parallel}} = \frac{2\varepsilon_0}{\varepsilon + \varepsilon_0} \tag{4.4}$$

Where ε or ε_0 is the dielectric constant of the cylindrical material or the environmental material, respectively. The dielectric constant for $CsPbBr_3$ is estimated to be 6.35 and the dielectric constant for PS is 2.6. Therefore, the ratio between the electric fields is of two polarizations is calculated to be ≈0.6, which results in a theoretical polarization (P) ≈0.47.

Results and Discussion

$CsPbBr_3$-Polymer Composite Design and Characterization

The swelling-deswelling synthetic strategy was found to have a direct impact on nanorod size through varying the precursor concentration deposited in each drop on the polymer substrate. Because the precursor concentration exhibited such a drastic effect on the nanorod formation, exact control and distribution of the precursor solution (concentration and total volume) was regulated to ensure control of nanorod size. To control nanorod size two different strategies were used: the first involving precursor concentration and the second pertaining to spin-coating speed modulation. Considering the kinetics behind precursor distribution in a polymer matrix, lowering the precursor concentrations will lead to a lower overall solution viscosity, which in turn should enable the formation of smaller nanorods because of a higher particle diffusion rate within the polymer matrix [81]. Increasing the spin-coating speed can also produce smaller nanorods. The increased rotational speed would lead to a more dynamic distribution of deposited precursor solution, which would result in smaller nanorods because of an increased diffusion rate brought on by greater force from higher rotational speeds.

Fluorescence microscopy was used to evaluate nanorod distribution in $CsPbBr_3$-PS composite samples with varying spin-coating speeds (1000, 2000, or 3000 rpm) and precursor concentrations (12, 15, 20, and 30 mg mL^{-1}). A clear correlation can be drawn between adjusting either or both the spin-coating speed and the precursor concentration with the resulting nanorod size produced in the polymer matrix. By either lowing the precursor concentration or raising the speed when distribution is done through spin-coating, the length of the nanorods can be reduced (Figure 4.4).

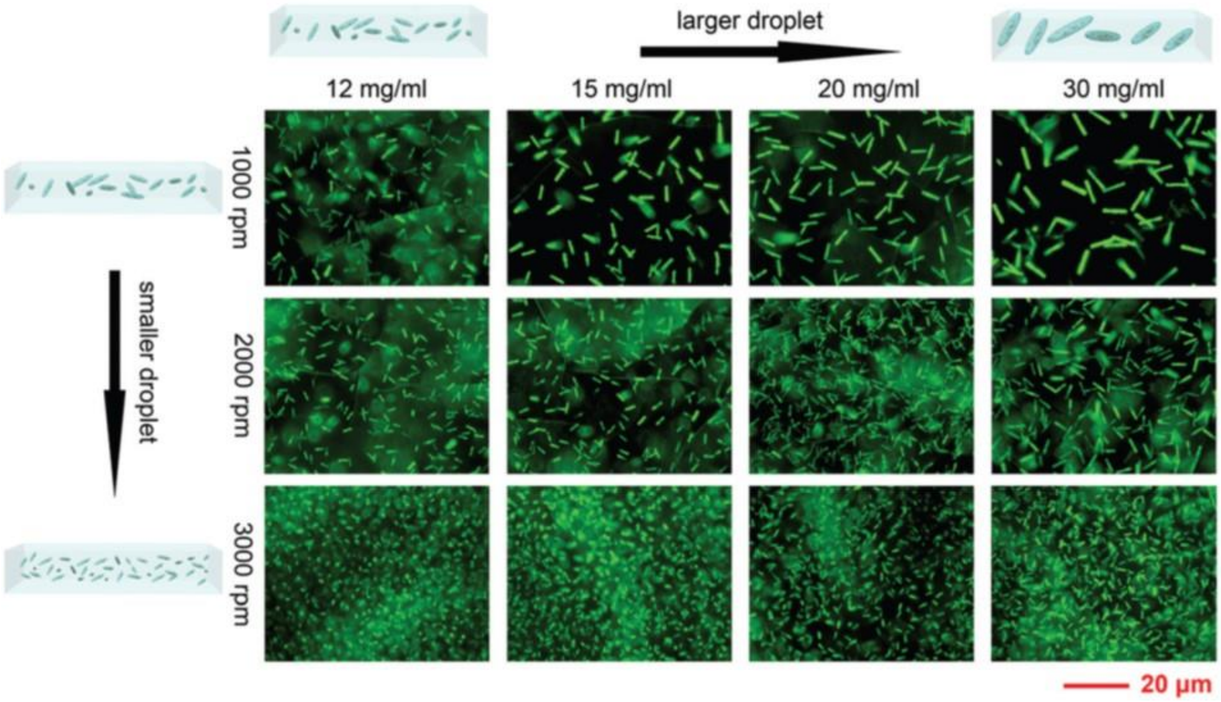

Figure 4.4: Florescence microscopy images of $CsPbBr_3$-PS composite nanorods. Precursor concentrations were varied from 12 mg/mL to 30 mg/mL and spin-coating speeds were differed from 1000 to 3000 rpm. Samples were imaged with a focal plane situated at 4-5 mm from the top surface for all samples. Reproduced from Ref. 67 with permission from The Royal Society of Chemistry.

The range of sizes made possible through varying the spin-coating and precursor concentrations was from 1.27 ± 0.16 μm to 7.15 ± 0.43 μm. The shortest nanorods (1.27 ± 0.16 μm) were made by using the lowest precursor concentration (12 mg mL^{-1}) and the highest spin-coating speed (3000 rpm). Conversely, by accessing the lowest spin-coating speed (1000 rpm) and the highest precursor concentration (30 mg mL^{-1}) available, the longest nanorods were achieved. Astonishingly, even at the most extreme ends of the spin coating speeds and precursor concentrations available, the nanorod size standard deviation peaked at 12% and for most samples stayed below 9% (Figure 4.4).This consistency in nanorod size, regardless of the set precursor concentration and spin speed for the sample, demonstrates the precision of this synthetic approach for creating uniform $CsPbBr_3$ nanorods.

While optical and photophysical characterization was carried out primarily on the $CsPbBr_3$-PS composite samples, the *in situ* nanorod microencapsulation strategy was also carried out using both polycarbonate (PC) and acrylonitrile–butadiene–styrene (ABS) polymers (Figure 4.6). This provides direct evidence of the versatility of this synthetic strategy with other polymers that will undergo a swelling-deswelling processes when brought into contact with DMF solvent. However, it should be noted the nanorod size varied with the PC and ABS polymers compared to those prepared with a PS polymer substrate. This change in nanorod size is an expected effect due to the different swelling ratios of polymers when brought into contact with DMF solvent and varying chain lengths from polymer to polymer. This is an indication that further investigation would be required for optimized spin-coating speeds and precursor concentrations when exchanging polymer substrates.

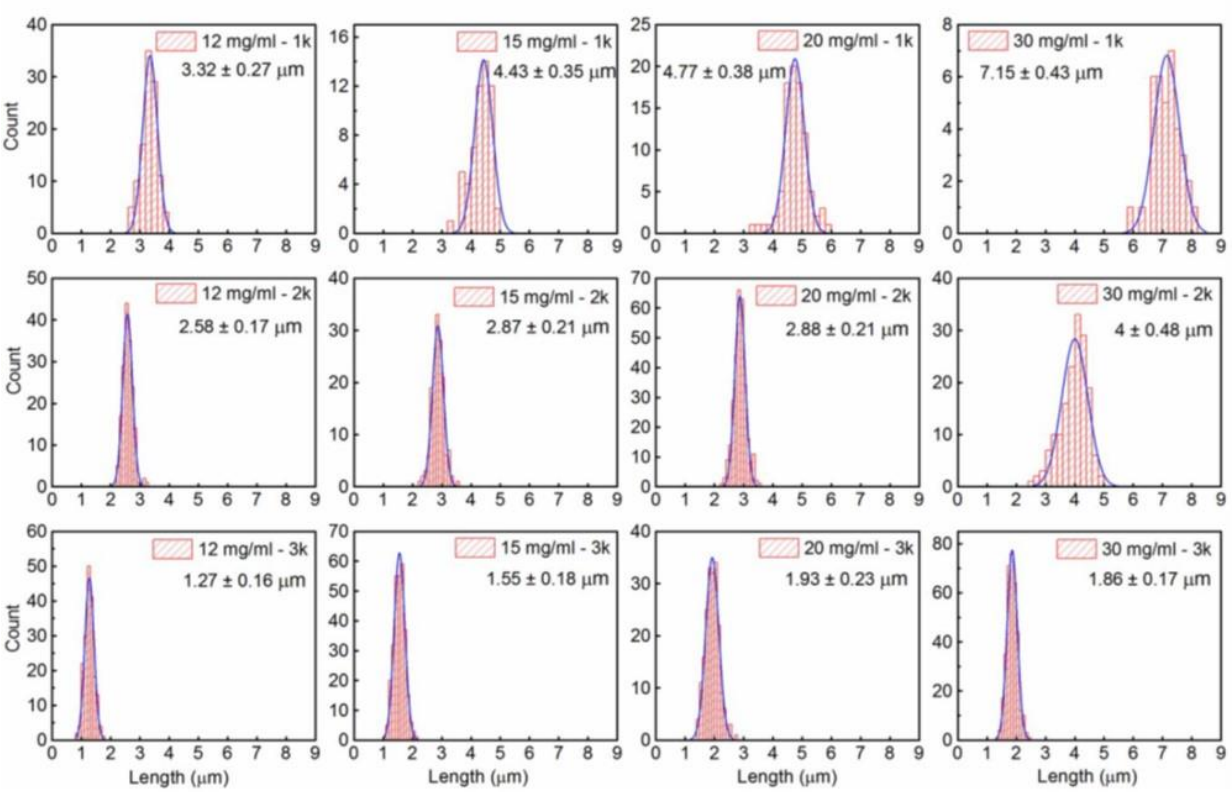

Figure 4.5: Histograms of rod length with respect to varying precursor concentrations and spin-coating speeds in $CsPbBr_3$-PS composite samples. Reproduced from Ref. 67 with permission from The Royal Society of Chemistry.

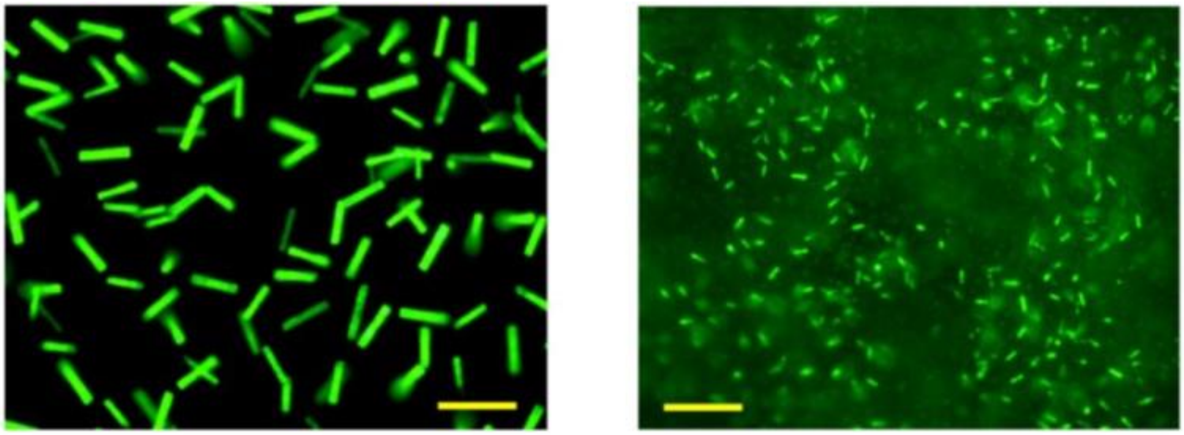

Figure 4.6: Fluorescence microscopy images of $CsPbBr_3$-PS (left) and $CsPbBr_3$-ABS (right). Both samples prepared with 30 mg mL^{-1} precursor concentrations and 1000 rpm spin-coating speed. Scale bar: 10 μm. Reproduced from Ref. [67] with permission from The Royal Society of Chemistry.

Macroscale Optical Characterization of $CsPbBr_3$-PS Composites

Macroscale UV-Vis and photoluminescence spectroscopy was carried out on $CsPbBr_3$-PS composite samples prepared under different precursor concentration and spin-coating speed conditions. UV-Vis absorption and photoluminescence spectra were acquired from $CsPbBr_3$-PS samples created by differing the spin-coating speeds (1000, 2000, and 3000 rpm) with the four varying precursor concentrations chosen for this study (12, 15, 20, and 30 mg mL^{-1}). The spectra obtained display the same characteristics: high absorption values in the UV and near UV regions, a characteristic peak ≈520 nm (a characteristic absorbance band for bromine-based perovskites) and decreased absorbance closer to the near IR region (Figure 4.7). This pronounced absorption peak originates from the band to band transition and is a segue between the strong short-wavelength and weak long-wavelength absorption observed in most semiconductor materials.

Photoluminescence spectra were obtained under the same conditions as the UV-Vis absorbance spectra, with a representative spectrum below (Figure 4.10) The data show very similar spectral characteristics from sample to sample, regardless of precursor concentration and spin-coater speed. A size insensitive and narrow FWHM (18nm) combined with a steady peak emission wavelength is a staple occurrence in perovskite materials [77]. The currently accepted theory for narrowed emission with minimal peak shifting in perovskite materials results purely from the crystal structure rather than crystal quality or dimensionality. This is due to the polar lead-halide bonds in perovskite materials inducing a Fröhlich interaction between charge carrier species and longitudinal optical (LO) phonons [77, 78]. This Fröhlich interaction results from LO phonon scattering and electron-phonon coupling, which primarily determines the linewidth of the emission spectrum [77-79]. However, from these initial spectroscopic measurements there is also a clear indication that overall nanorod size has a minimal effect on their optical properties. All PS samples had an observable peak wavelength ≈525 ± 2nm with a FWHM ≈18 nm, regardless of spin-coating speed and precursor concentration (Table 4.1). The minimal peak shifting and narrow emission peak are in agreement with the above theory that the emission peaks are determined from crystal structure rather than size or dimensionality of the perovskite material.

Photoluminescence quantum yield measurements also display minimal fluctuation with respect to spin-coating speed and precursor concentration, which was a similar observation exhibited in the UV-Vis and photoluminescence spectra. The PLQY for samples prepared with varied precursor concentrations and spin-coating speeds range from 23%-30% (Table 4.2) with lowest average values obtained from samples prepared with a precursor concentration of 30 mg mL^{-1}. There is speculation of an onset of concentration quenching occurring in these 30 mg mL^{-1} samples, though further investigation using higher precursor concentrations would be required to substantiate this claim.

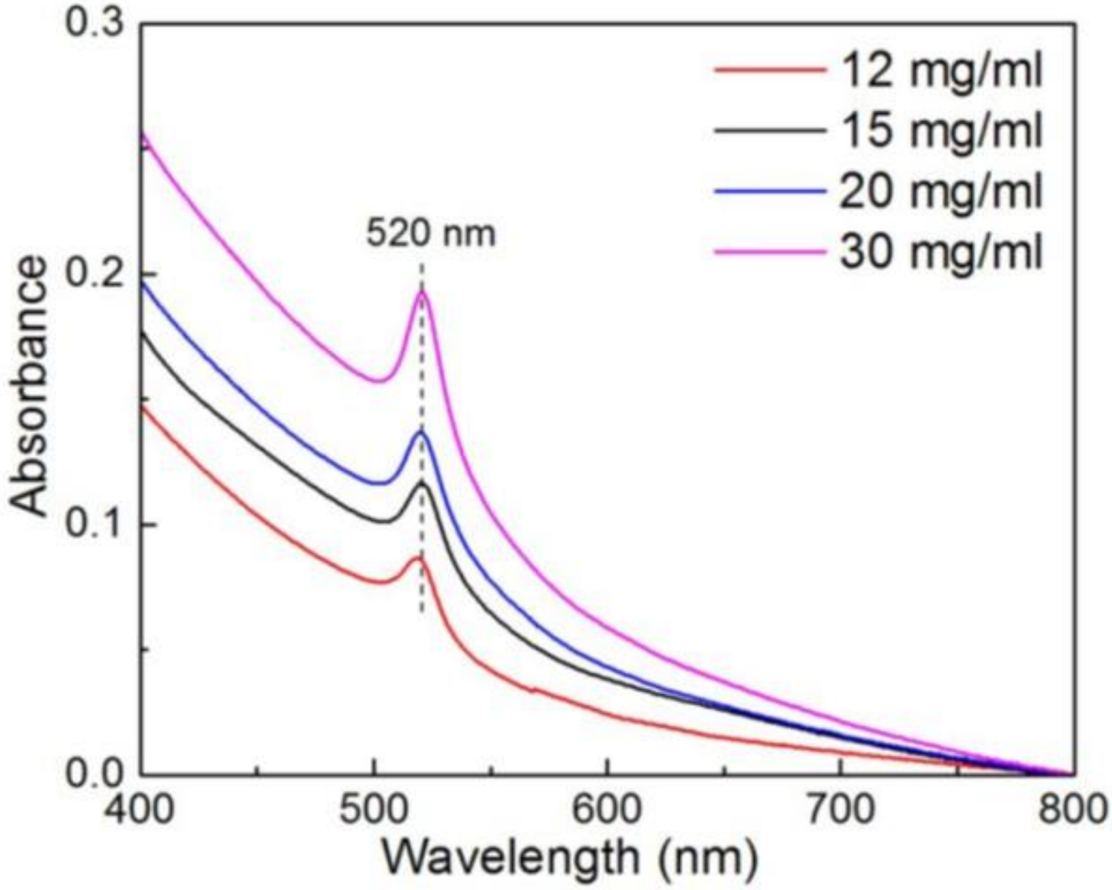

Figure 4.7: UV-Vis absorbance spectra of $CsPbBr_3$-PS composite samples at varying precursor concentrations. Reproduced from Ref. 67 with permission from The Royal Society of Chemistry.

Table 4.1: Photoluminescence spectra peak wavelengths of $CsPbBr_3$-PS composite samples prepared with varying spin-coating speeds (rpm) and precursor concentrations. Reproduced from Ref. 67 with permission from The Royal Society of Chemistry.

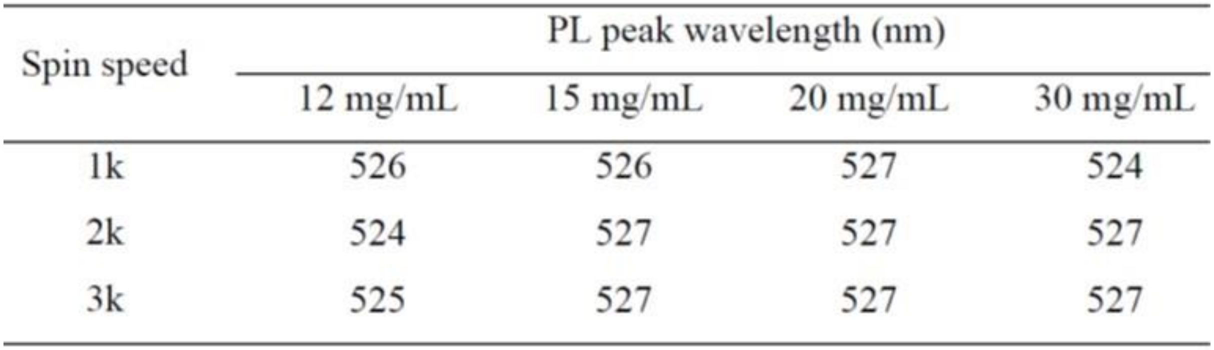

Spin speed	PL peak wavelength (nm)			
	12 mg/mL	15 mg/mL	20 mg/mL	30 mg/mL
1k	526	526	527	524
2k	524	527	527	527
3k	525	527	527	527

Table 4.2: Photoluminescence quantum yield values for $CsPbBr_3$-PS samples prepared with varying spin-coating speeds (rpm) and precursor concentrations. Reproduced from Ref. 67 with permission from The Royal Society of Chemistry.

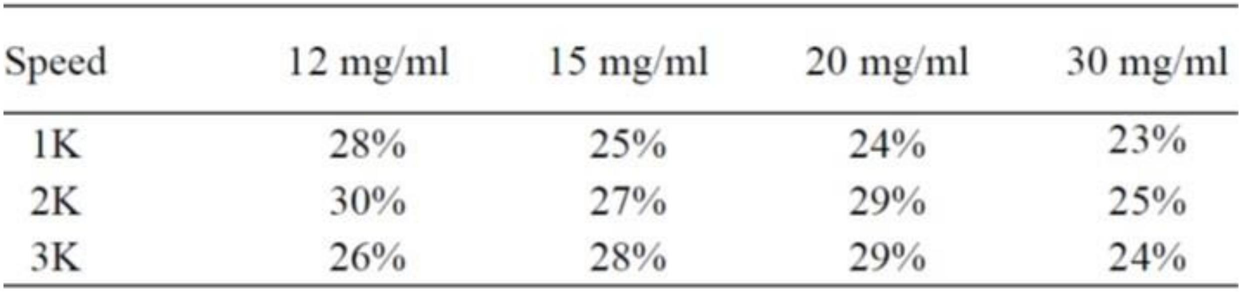

Speed	12 mg/ml	15 mg/ml	20 mg/ml	30 mg/ml
1K	28%	25%	24%	23%
2K	30%	27%	29%	25%
3K	26%	28%	29%	24%

Photoluminescence Imaging and Spectroscopy

Based on the data from steady state spectroscopies (see above section) the nanorod size has little to no impact on the optical properties of the encapsulated nanorods. Due to the lack of influence from nanorod size on optical characteristics, photoluminescence imaging was carried out for only the CsPbBr-PS composite samples prepared with a precursor concentration of 15 mg mL^{-1} and a spin coating speed of 2000 rpm. Photoluminescence imaging paints a very different picture than the macroscale fluorescence microscopy, in that there is still a rod-like structure, but it appears broken rather than one solid piece (Figure 4.9).

The area in each image is 10 x 10 μm^2, which allows for imaging of multiple nanorods in each individual image. A side by side comparison of individual nanorods shows a broken morphology unique to each nanorod. With each nanorod now discernably a different length based on their overall disjointed structure, their relative optical properties remain relatively similar as far as their absorption and photoluminescence properties. The photoluminescence imaging also allows for insight into two aspects of the nanorods: their overall level of crystallinity and the emissive states of individual nanorods.

First, the $CsPbBr_3$-PS nanorods have an overall broken appearance, which would suggest a lower order of crystallinity in individual nanorods. To further explore levels of structural order in the $CsPbBr_3$-PS nanorods, the Urbach energy can be calculated. Identical to the approach in Chapter 3, the Urbach energy can be calculated with the absorption spectrum utilizing the Urbach empirical rule as follows:

$$\alpha = \alpha_0 e^{h\nu / E_U} \tag{4.5}$$

Where α_0 is a material dependent constant and E_U denotes the energy of the band tail, which is also referred to as the Urbach energy. The Urbach energy value is weakly dependent on temperature and is often associated with the width of the band tail due to localized energy states within the energy band gap due to low crystallinity or structural disorder brought on by trap states within the semiconductor material. To determine the Urbach energy of a material, the natural log of the Urbach empirical rule equation (equation 4.5) must be taken resulting in the equation:

$$\ln \alpha = \ln \alpha_0 + ({}^{h\nu}/_{E_U}) \tag{4.6}$$

This form of the Urbach equation (equation 4.6) allows for the determination of the Urbach energy from the reciprocal of the slope of the resulting straight line by plotting ln (α) against energy (E). Because the absorption coefficient (α) is proportional to absorbance, ln (abs) is plotted against energy (E) to obtain the Urbach energy value for $CsPbBr_3$-PS.

Figure 4.8 displays the Urbach energy plot for the $CsPbBr_3$-PS nanorods, which has a slope of 2.75 and equates to an Urbach energy value of 364 meV. In an ideal semiconductor, the slope of the for an Urbach tail would be infinite and would indicate no structural disorder in the semiconductor material. However, in the case of these $CsPbBr_3$-PS nanorods the Urbach energy exhibits a higher value than most conventional semiconductors (>100 meV). The Urbach energy for these materials substantiates a claim of lower levels of crystallinity and higher levels of trap states within the $CsPbBr_3$-PS nanorods. Though even with lower orders of crystallinity, the $CsPbBr_3$-PS nanorods exhibit high levels of color purity (emission spectrum, FWHM ≈18nm) and high levels of PLQY for perovskite nanorods, which supports the earlier claim that the narrowed emission in perovskite materials results purely from the crystal structure rather than crystal quality or dimensionality.

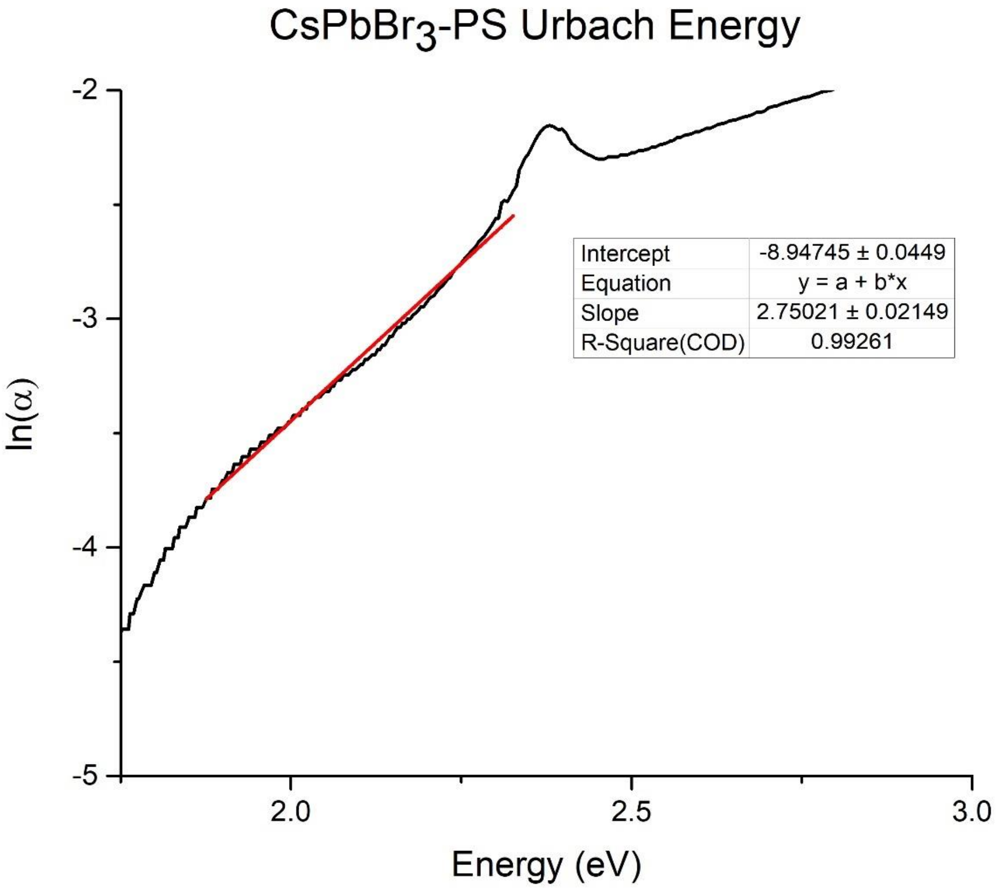

Figure 4.8: Urbach energy plot for $CsPbBr_3$-PS sample with linear fit for Urbach tail.

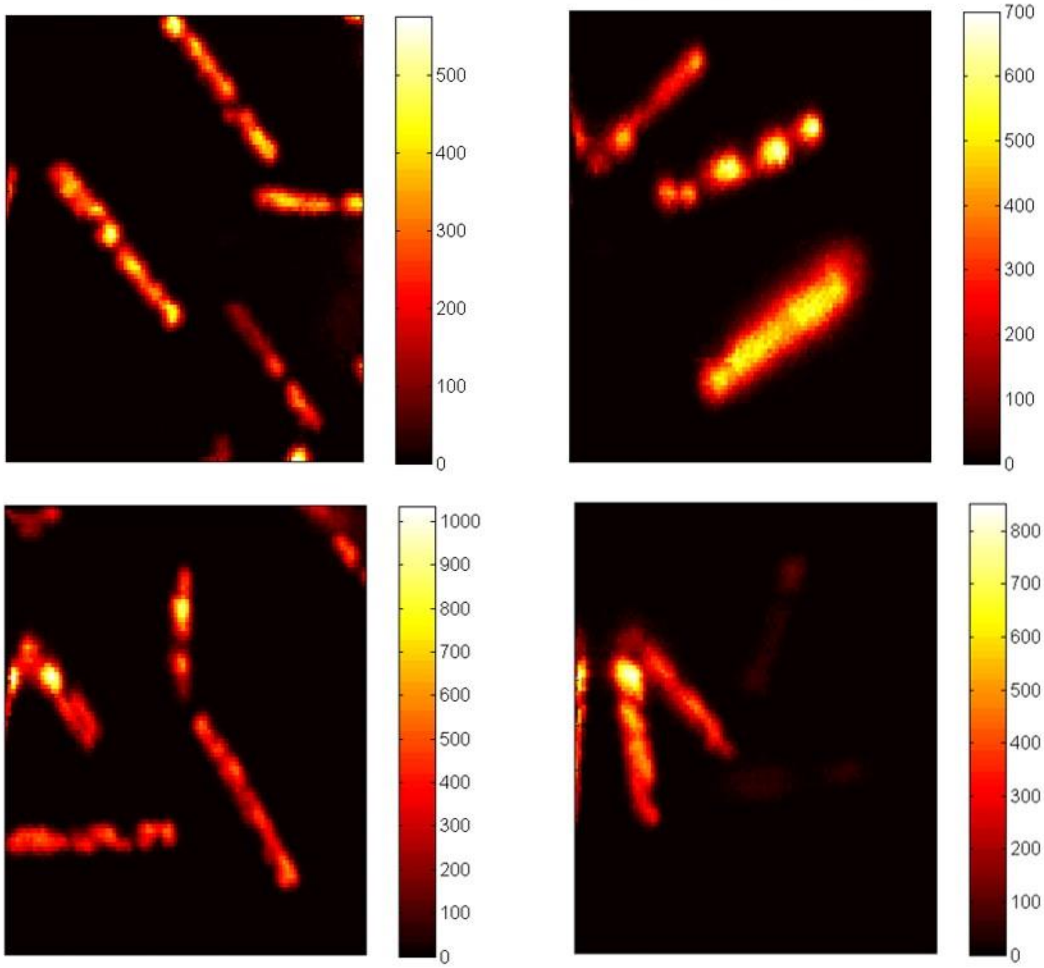

Figure 4.9: Photoluminescence images of $CsPbBr_3$-PS composite nanorods. Color bars to the right of each image indicate photoluminescence intensity in counts. Each image is 10 x 10 μm^2

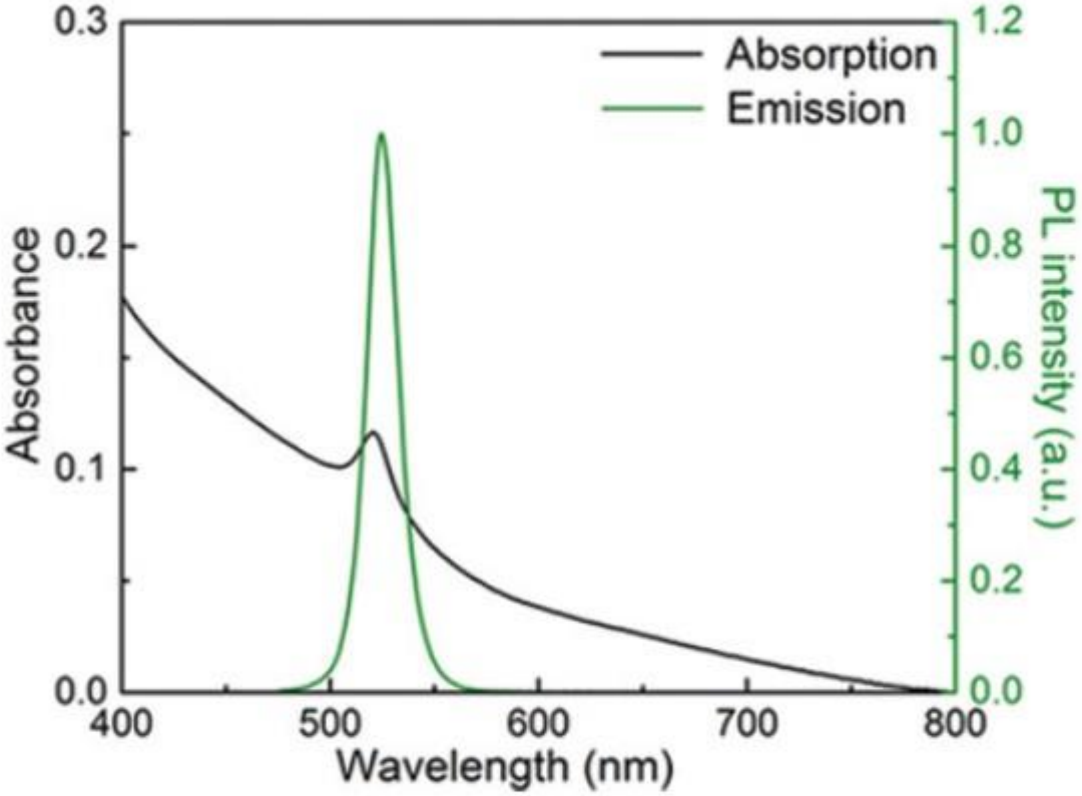

Figure 4.10: UV-Vis and photoluminescence spectra of $CsPbBr_3$-PS nanorods prepared with a precursor concentration of 15 mg mL^{-1} and spin-coating speed of 2000 rpm. Reproduced from Ref. 67 with permission from The Royal Society of Chemistry.

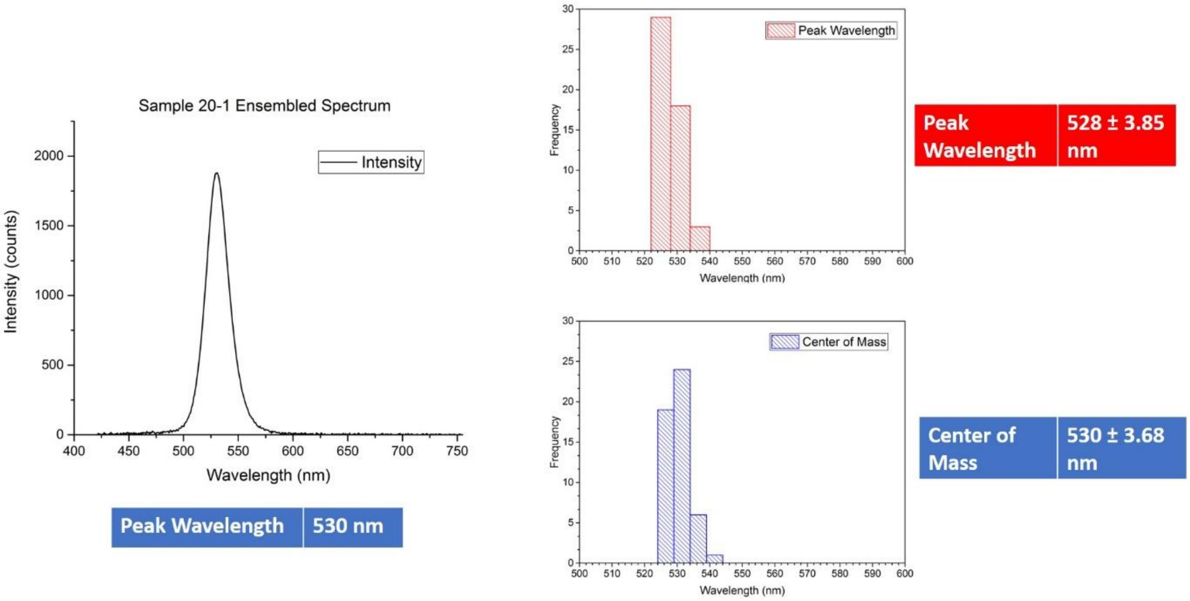

Figure 4.11: Left: Photoluminescence averaged spectra (50 averaged spectra). Right-top: Average peak wavelength for all averaged photoluminescence spectra. Right-bottom: Average center of mass for all averaged photoluminescence spectra. All spectra were taken using $CsPbBr_3$-PS composite with a precursor concentration of 15 mg mL^{-1} and a spin-coating speed of 2000 rpm.

Time Correlated Single Photon Counting (TCSPC)

Investigating the excited state dynamics behind the $CsPbBr_3$ nanorods can give valuable insight into the excited state processes occurring, especially with their seemingly broken morphology. Photoluminescence lifetimes were measured at multiple points along different nanorods, with a focus on unique structural breaks in morphology along the nanorods. Overall, the photoluminescence lifetime decay exhibited the typical biexponential decay shape expected from perovskite materials, though with much shorter decays when compared to their encapsulated methylammonium (MA) counterparts studied in chapter three [52].

The shorter lifetimes obtained from the $CsPbBr_3$-PS nanorods can be attributed to lower levels of crystallinity and an increased density of trap states within individual nanorods, which is supported by photoluminescence imaging and the calculated Urbach energy. Furthermore, by evaluating the lifetime measurements obtained from each nanorod, a distinct difference in photoluminescence decay can be discerned through variations in photoluminescence lifetimes. Basically, there exist points on each nanorod where the overall photoluminescence lifetime decay is longer and other points where the lifetime decay is much shorter (Figure 4.13).

For the $CsPbBr_3$ nanorods, 104 TCSPC measurements were taken with an average $\tau_1 \approx 34 \pm 18$ ns and an average $\tau_2 \approx 206 \pm 67$ ns and an overall contribution of $A_1 \approx 978$ counts and $A_2 \approx 38$ counts. A histogram of all photoluminescence lifetime measurements (Figure 4.12) displays a Gaussian distribution around 34 ns for the shorter lifetime component and 206 ns for the longer lifetime component. However, indicated by the standard deviation for these average values, a fluctuation in individual lifetime components on each rod exists (indicated by a wide Gaussian distribution within the histogram). This wide, Gaussian distribution of lifetime values is a good indicator of heterogeneity within the structure of the $CsPbBr_3$-PS nanorods and further supports higher densities of trap states present.

These data suggests that the overall average lifetime ($\tau_{avg} \approx 50$ ns) highly favors the shorter lifetime component, τ_1, which would also imply an overall higher abundance of trap states contributing to the photophysical processes because the shorter lifetime component has been attributed to trap assisted recombination in perovskite materials [82]. To further investigate the photophysics behind these uniquely structured perovskite nanorods, the radiative (k_r) and non-radiative (k_{nr}) rate constants were calculated using the PLQY of the perovskite nanorods synthesized at a precursor concentration of 15 mg mL^{-1} and a spin-coating speed of 2000 rpm in the following equations:

$$\tau_{avg} = \frac{1}{k_r + k_{nr}} \tag{4.7}$$

$$\phi = \frac{k_r}{k_r + k_{nr}} \tag{4.8}$$

$$k_r = \frac{\phi}{\tau_{avg}} \tag{4.9}$$

$$k_{nr} = \frac{1 - \phi}{\tau_{avg}} \tag{4.10}$$

where τ_{avg} is the average photoluminescent lifetime, ϕ is the bulk PLQY value obtained from the integrating sphere method, and k_r and k_{nr} represent the radiative and non-radiative rate constants, respectively (Table 4.3). It is assumed the bulk PLQY behaves in a similar manner for each individual nanorod due to the negligible variance in optical characteristics (absorption and steady-state photoluminescence emission) of each $CsPbBr_3$-PS sample.

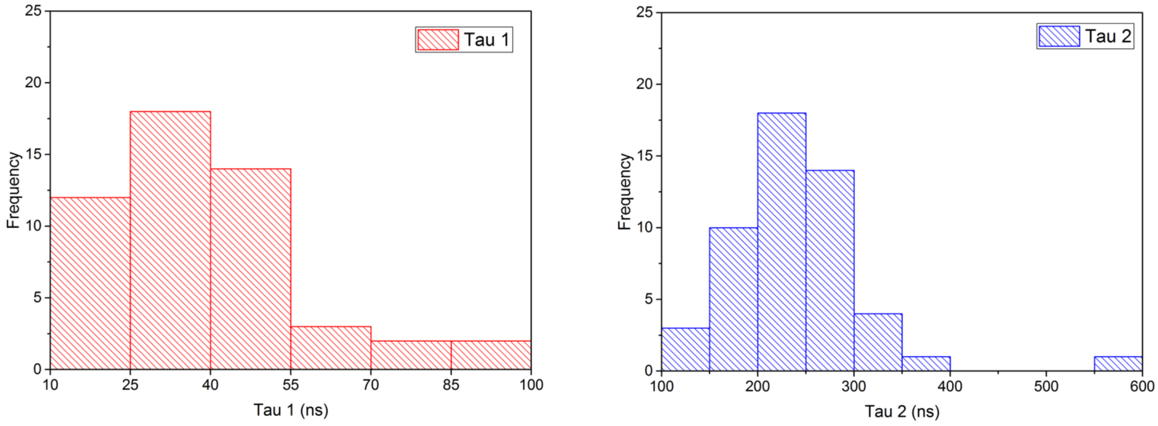

A1 (counts)	Tau 1 (ns)	A2 (counts)	Tau 2 (ns)
978	34 ± 18	38	206 ± 67

Figure 4.12: Histogram of photoluminescence lifetime measurements for $CsPbBr_3$-PS nanorods prepared with a precursor concentration of 15 mg mL^{-1} and a spin speed of 2000 rpm.

Photophysical and Charge Transfer Dynamics

Compared to the $MAPbBr_3$-PS perovskite nanoparticle sample from Chapter 3 the $CsPbBr_3$-PS perovskite nanorod sample exhibits a broader absorption spectra (Figure 4.10), lower average photoluminescence lifetime (Figure 4.12), a lower PLQY (Table 4.2), and $k_r << k_{nr}$. (Table 4.3). The broader absorption spectrum was attributed to an Urbach tail (Urbach energy = 364 meV), which is a further extension into longer wavelength excitations after the band edge peak (≈530 nm) caused by distortion or defect states in semiconductor materials [68]. These defect bands create a band tail extending from the lower end of the conduction band to areas inside the band gap, and correspondingly, the defect states close to the valance band also smear the valance band edge further into the forbidden band gap (Figure 4.13). Because of this, defect states can create intra-band states close to the valance and conduction bands for charge carriers to move, which can result in lower energy emission and an overall lower photoluminescence lifetime [80]. Bearing in mind surface defect states are the most common and abundant source of defect mediated recombination effects in perovskite materials [72-74], this could explain the lower overall average photoluminescent decay lifetime and by extension the PLQY.

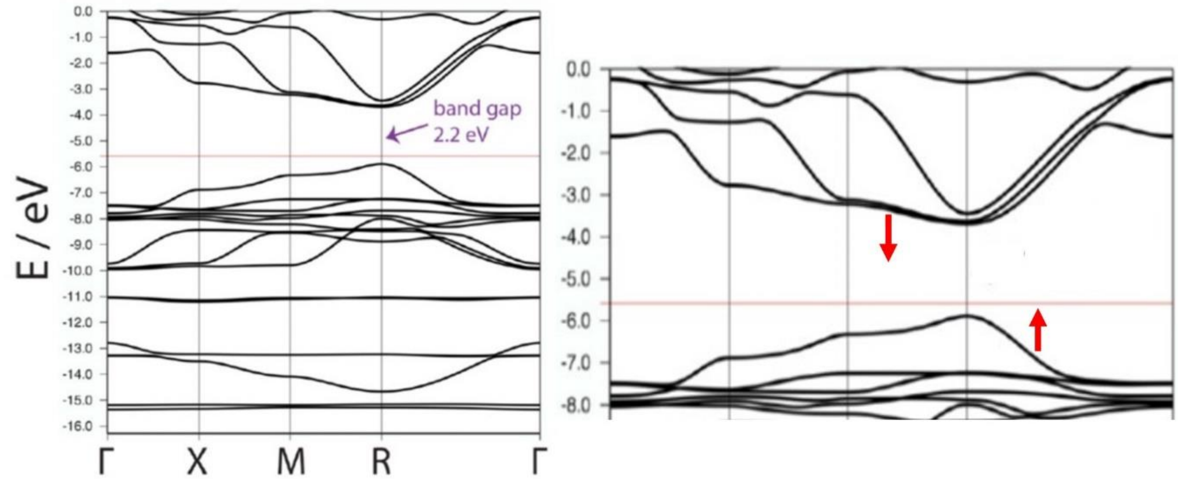

Figure 4.13: Band structure of CsPbBr$_3$, computed at SCAN/TZ2P (left) and enlarged band gap energy with arrows to show Urbach tailing effect on the band structure (right). Adapted with permission from (M. G. Goesten, R. Hoffmann, Journal of the American Chemical Society (2018) 140 (40), 12996-13010.) Copyright 2019 American Chemical Society.

To substantiate this, we examined a nanorod with an apparent photoluminescent center and an area in proximity to it within the same CsPbBr$_3$-PS sample (Figure: 4.11). The average photoluminescence lifetime at the brighter emissive center (purple) was ≈ 87 ns and the average photoluminescence lifetime for the darker emissive center (green) was ≈ 22 ns, which already insinuates more trap-state interferences present in the darker emissive center due to the higher contribution of τ_1 to τ_{avg}. Examining the radiative and nonradiative rate constants from both spots shows a much larger difference in the darker spot ($k_{nr} >> k_r$) when compared to the brighter emissive center ($k_{nr} > k_r$) showing an overall increase by a factor of four. The high contribution of τ_1 in all these samples implies the overall average photoluminescence lifetime is greatly influenced by surface defect concentrations, which are attributed mostly to Br$^-$ vacancies or exposed charged surfaces from Br^- aggregations in $CsPbBr_3$ perovskite materials [75]. If this is the case, the optical and photophysical properties will vary greatly with these trap states as these properties depend on the bonding and anti-bonding structure of Pb and Br (Figure 4.13 & Figure 4.15). Based on this assumption, the charge transfer mechanics rely heavily on the defect state of each $CsPbBr_3$ nanoparticle in the nanorod shape, where the τ_1 component results from surface defect interactions/trapping and τ_2 results from either free carrier recombination or exciton recombination from the valance to conduction band (Figure 4.16).

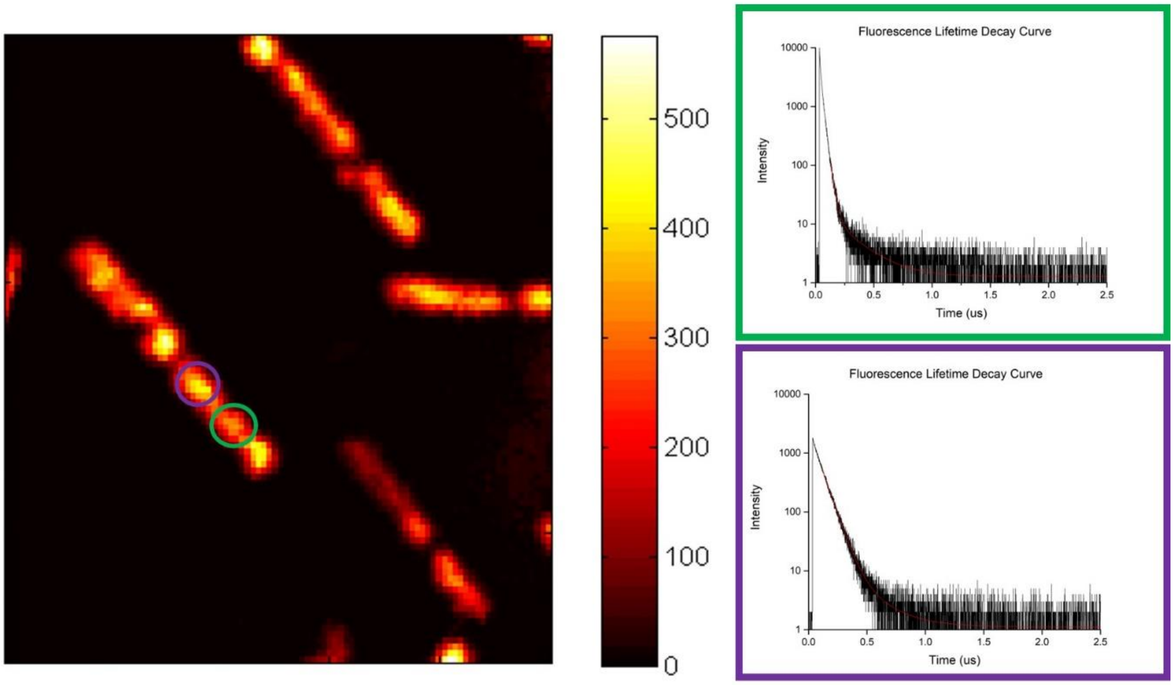

Figure 4.14: Photoluminescence image (12 x 12 μm^2) of $CsPbBr_3$-PS nanorods with corresponding photoluminescence decay curves. Green decay curve: $\tau_{avg} \approx 22$ ns, Purple decay curve: $\tau_{avg} \approx 87$ns.

Table 4.3: Photophysical data for $CsPbBr_3$-PS made with 15 mg mL^{-1} precursor concentration and 2000 rpm spin-coating speed. PS_{green} and PS_{purple} are the kinetic data derived from the highlighted areas in Figure 4.11. Bulk PLQY measurements are used for the calculations of the radiative and non-radiative rate constants.

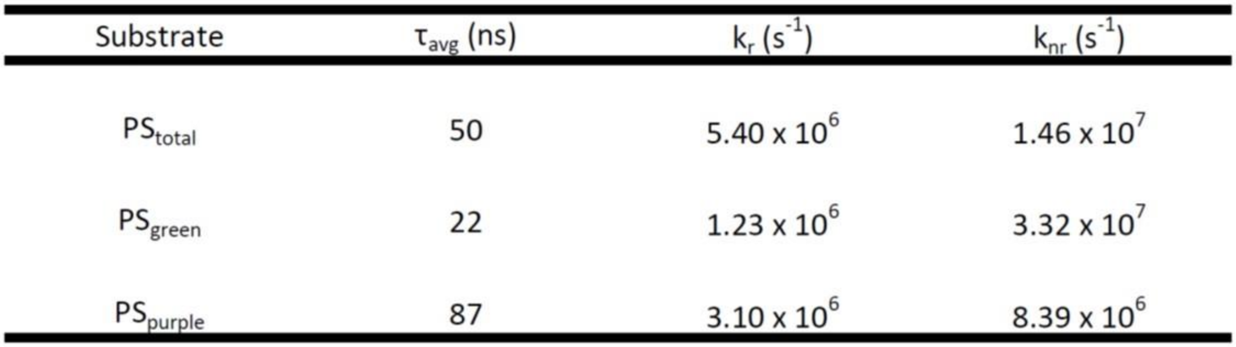

Substrate	τ_{avg} (ns)	k_r (s^{-1})	k_{nr} (s^{-1})
PS_{total}	50	5.40×10^6	1.46×10^7
PS_{green}	22	1.23×10^6	3.32×10^7
PS_{purple}	87	3.10×10^6	8.39×10^6

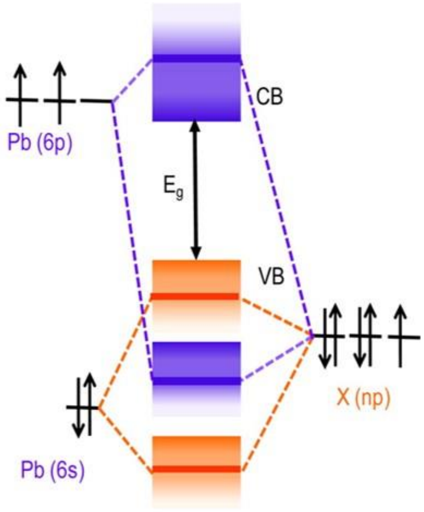

Figure 4.15: Bonding/antibonding orbitals of $APbX_3$ illustrating the formation of the valence band (VB) and conduction band (CB). Adapted with permission from Reference 76. Copyright 2016 American Chemical Society.

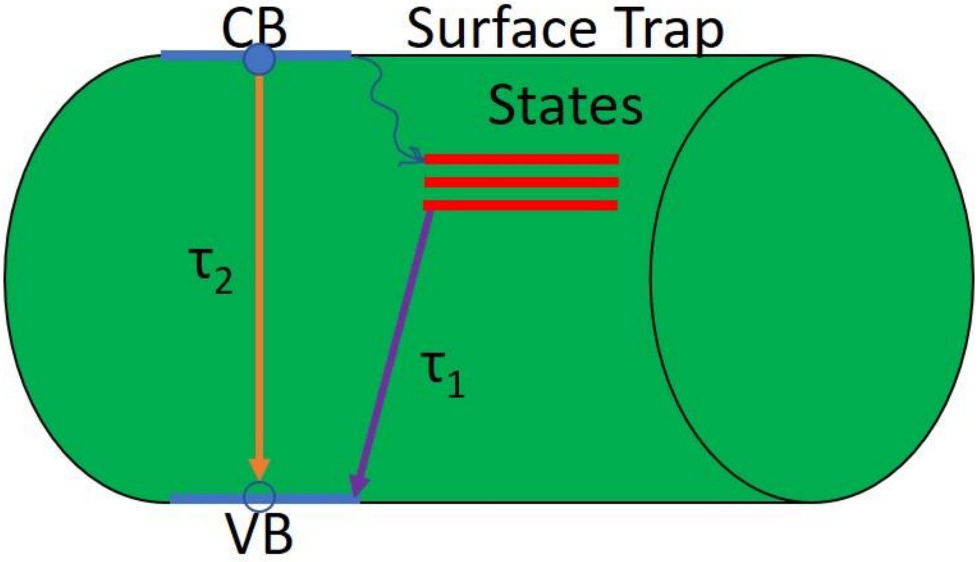

Figure 4.16: Proposed photophysical pathways. Filled circle represents an electron and open circle is a hole carrier. CB is the conduction band, VB is the valance band and τ_1 and τ_2 are the short and long lifetime components, respectively.

Individual Nanorod Photoluminescence Polarization Imaging

For 1D perovskite nanorods, their unique emissive properties as a result of their anisotropic shape gives rise to the possibility of polarized light emission. We therefore acquired individual nanorod photoluminescence polarization images of aligned nanorods in $CsPbBr_3$-PS composites. The sample was imaged over a 15 x 15 μm^2 area, with explicit interest in imaging two different nanorods with different orientations (X and Y) to observe the photoluminescence polarization influence on orthogonal nanorods and justify their macroscale alignment. The photoluminescence intensities of two perpendicular polarized signals (I_x and I_y) were collected simultaneously (Figure 4.14) and combined to obtain the resulting polarization image. The resulting pixel by pixel polarization values can then be represented using a histogram to show the distribution of polarization values for the imaged rods, which were calculated as follows:

$$P = \frac{(I_y - I_x)}{(I_y + I_x)} \tag{4.11}$$

where I_y and I_x represent the photoluminescence intensities of two perpendicular polarized signals collected simultaneously on two different SPAD detectors situated in front of a polarizing beam splitter.

For the polarization image in Figure 4.15, the upper right rod, which orients parallel along the y-axis, displays mostly positive P values. This indicates the photoluminescence emission is mostly polarized along the nanorod axis ($I_x < I_y$) Conversely, the other nanorod imaged is oriented in the nearly perpendicular direction in the lower left area of the image and displays mostly negative P values, which indicates the reverse of the other rod ($I_y < I_x$). Nanorods oriented at 45° between the detectors were avoided because at $\theta = 45°$ relative to the principle components of the image, $S (\parallel) = P (\perp)$. In this case, regardless of the magnitudes of the respective principle components, partial polarization emissions cannot be determined. From the polarization values and orientation of the nanorods imaged we can definitively discern the nanorods with orthogonal orientations with respect to one another tend to cancel the photoluminescence polarization and require macroscale alignment to circumvent the polarization cancellation effect observed here. This is validated based on nanorods orthogonal to one another exhibiting polarization values of similar magnitude but with different signs (+/-), which will in turn cancel out the polarization effects of individual nanorods (Figure 4.17 & Figure 4.18).

Polarized photoluminescence emission from $CsPbBr_3$-PS composite nanorods can be attributed to the dielectric contrast of the polymer matrix used for encapsulation and the nanorods themselves [53]. By using the known dielectric constants for both $CsPbBr_3$ (6.35) and PS (2.6), the theoretical P value for an infinitely long 1D nanostructure can be calculated as follows:

$$\frac{E_\perp}{E_\parallel} = \frac{2\varepsilon_0}{\varepsilon + \varepsilon_0} \tag{4.12}$$

$$I \propto |E|^2 \tag{4.13}$$

$$P = \frac{(I_y - I_x)}{(I_y + I_x)} = \frac{(\frac{I_\parallel}{I_\perp} - 1)}{(\frac{I_\parallel}{I_\perp} + 1)} = 0.47 \tag{4.14}$$

where P is the polarization value $E_\perp$ and $E_\parallel$ are the perpendicular or parallel electric fields $I_\perp$ and $I_\parallel$ are the resulting perpendicular and parallel intensities and ε or ε_0 is the dielectric constant of the cylindrical material or the environmental material, respectively.

This value is expected to be lower for the nanorods imaged here as they have a limited aspect ratio when compared to an infinitely long 1D nanostructure. Both the theoretical polarization value ($P = 0.47$, equations 4.12-4.14) and obtained polarization values for individual nanorods (maximum $P \approx 0.4$, equation 4.11) illustrates that modeling the nanorod as an infinite dielectric cylinder is in agreement with the polarization values obtained experimentally. It also demonstrates the polarization of the nanorods could be further improved on through two different routes: either using a different polymer with a lower dielectric constant or increase the aspect ratio of the $CsPbBr_3$-PS composite nanorods.

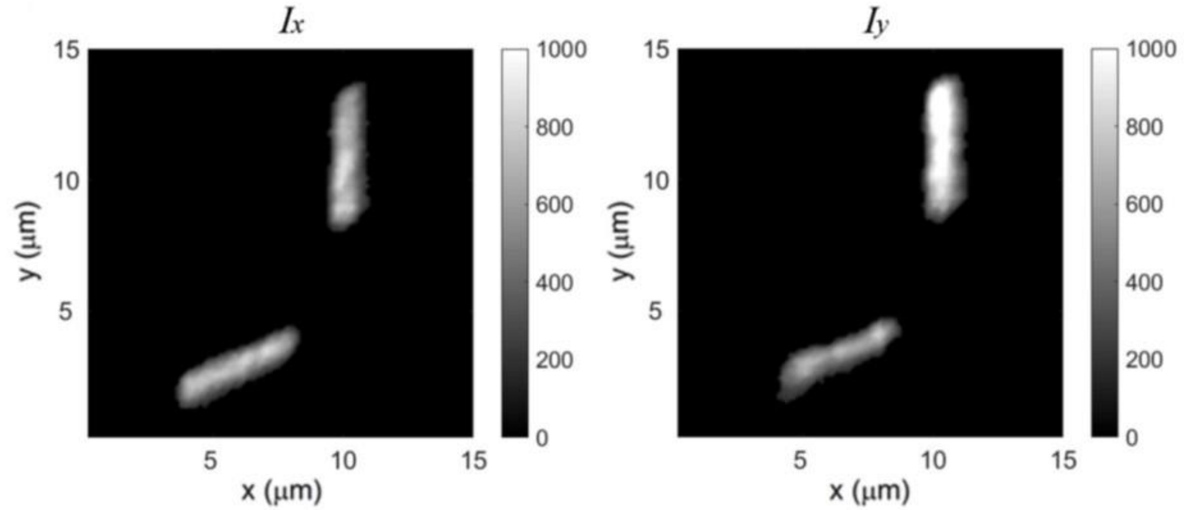

Figure 4.17: Photoluminescence images taken simultaneously of the x (left image) and y (right image) polarization for $CsPbBr_3$-PS nanorods. Sample prepared with 15 mg mL^{-1} precursor concentration and 2000 rpm spin-coating speed. Area imaged was 15 x 15 μm^2. Reproduced from Ref. 67 with permission from The Royal Society of Chemistry.

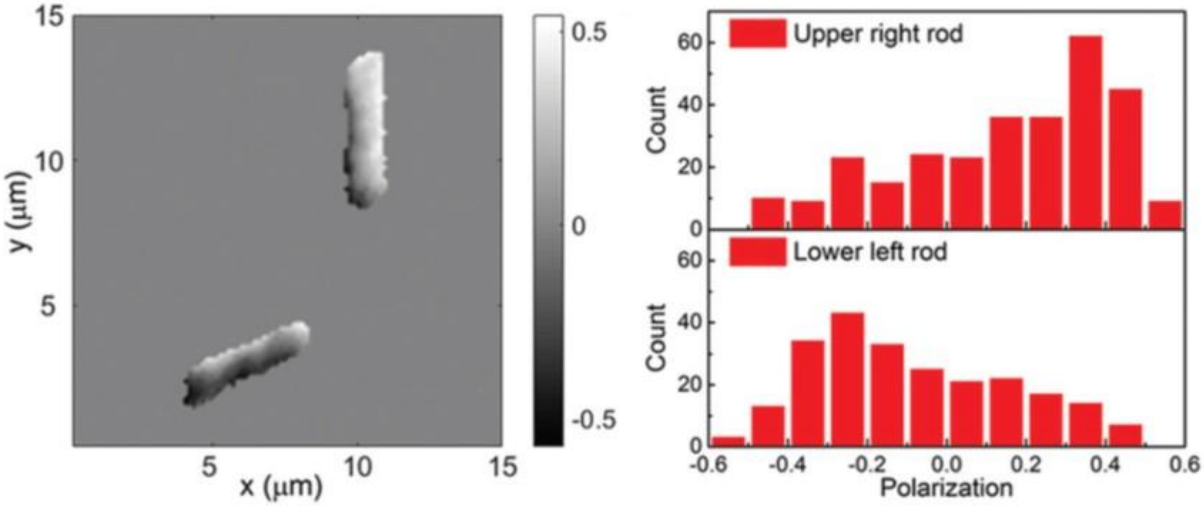

Figure 4.18: Polarization map of $CsPbBr_3$-PS nanorods (left) and histograms of *P* (polarization) values acquired from the lower left rod (bottom) upper right rod (top). Reproduced from Ref. 67 with permission from The Royal Society of Chemistry.

Conclusions

This spectroscopic study has provided valuable insight into the structural quality and photophysical processes for encapsulated $CsPbBr_3$ nanorods. The nanorods created through this process display good size control and excellent optical qualities concerning their color purity and overall brightness (PLQY). A unique segmented structure was discovered for the encapsulated $CsPbBr_3$-PS nanorods, which through photoluminescence imaging shows spots of bright emissive centers and dark states along individual nanorods. Urbach tailing was observed in the absorption spectra and the Urbach energy was calculated (364 meV), which indicated high densities of defect states and lower orders of crystallinity in the nanorods. This is further confirmed through photoluminescence lifetime imaging, which showed τ_1 as the major contributor to τ_{avg}, which is another indicator of trap assisted recombination events. Finally, Polarized emission from single nanorods along the long axis was observed from individual nanorod photoluminescence polarization imaging. Continued investigation and improvements in emission polarization could pave the way for encapsulated perovskite nanorods to become a staple building block in more efficient LCD backlight and other photonic applications.

References

[1] A. Zhang, G. Zheng and C. M. Lieber, Nanowires: Building Blocks for Nanoscience and Nanotechnology, Springer, New York, 2016.

[2] W. Lu and C. M. Lieber, Nat. Mater., 2007, 6, 841.

[3] R. Yan, D. Gargas and P. Yang, Nat. Photonics, 2009, 3, 569.

[4] Y. Li, F. Qian, J. Xiang and C. M. Lieber, Mater. Today, 2006, 9, 18.

[5] P. Yang, R. Yan and M. Fardy, Nano Lett., 2010, 10, 1529.

[6] A. P. Alivisatos, Science, 1996, 271, 933.

[7] X. Peng, L. Manna, W. Yang, J. Wickham, E. Scher, A. Kadavanich and A. P. Alivisatos, Nature, 2000, 404, 59.

[8] Y. Cui and C. M. Lieber, Science, 2001, 291, 851.

[9] X. Duan, Y. Huang, Y. Cui, J. Wang and C. M. Lieber, Nature, 2001, 409, 66.

[10] W. U. Huynh, J. J. Dittmer and A. P. Alivisatos, Science, 2002, 295, 2425.

[11] J. Hu, L. S. Li, W. Yang, L. Manna, L. W. Wang and A. P. Alivisatos, Science, 2001, 292, 2060.

[12] C. X. Shan, Z. Liu and S. K. Hark, Phys. Rev. B: Condens. Matter Mater. Phys., 2006, 74, 8.

[13] I. Hadar, G. B. Hitin, A. Sitt, A. Faust and U. Banin, J. Phys. Chem. Lett., 2013, 4, 502.

[14] A. Sitt, A. Salant, G. Menagen and U. Banin, Nano Lett., 2011, 11, 2054.

15 D. V. Talapin, R. Koeppe, S. Götzinger, A. Kornowski, J. M. Lupton, A. L. Rogach, O. Benson, J. Feldmann and H. Weller, Nano Lett., 2003, 3, 1677.

[16] I. Hadar, J. P. Philbin, Y. E. Panfil, S. Neyshtadt, I. Lieberman, H. Eshet, S. Lazar, E. Rabani and U. Banin, Nano Lett., 2017, 17, 2524.

[17] G. Yang, H. Zhong, Z. Bai, R. Liu and B. Zou, Adv. Opt. Mater., 2014, 2, 885.

[18] Y. Gao, V. D. Ta, X. Zhao, Y. Wang, R. Chen, E. Mutlugun, K. E. Fong, S. T. Tan, C. Dang, X. W. Sun, H. Sun and H. V. Demir, Nanoscale, 2015, 7, 6481.

[19] A. K. Srivastava, W. Zhang, J. Schneider, A. L. Rogach, V. G. Chigrinov and H. S. Kwok, Adv. Mater., 2017, 29, 1701091.

[20] K. Neyts, M. Mohammadimasoudi, Z. Hens and J. Beeckman, SID Symp. Dig. Tech. Papers, 2016, 47, 552.

[21] P. D. Cunningham, J. B. Souza Jr., I. Fedin, C. She, B. Lee and D. V. Talapin, ACS Nano, 2016, 10, 5769.

[22] M. Hasegawa, Y. Hirayama and S. Dertinger, SID Symp. Dig. Tech. Papers, 2015, 46, 67.

[23] M. Hasegawa and Y. Hirayama, SID Symp. Dig. Tech. Papers, 2016, 47, 241.

[24] D. Bi, W. Tress, M. I. Dar, P. Gao, J. Luo, C. Renevier, K. Schenk, A. Abate, F. Giordano, J. P. C. Baena and J. D. Decoppet, Sci. Adv., 2016, 2, e1501170.

[25] B. Luo, Y. C. Pu, S. A. Lindley, Y. Yang, L. Lu, Y. Li, X. Li and J. Z. Zhang, Angew. Chem., Int. Ed., 2016, 55, 8864.

[26] H. Cho, S. H. Jeong, M. H. Park, Y. H. Kim, C. Wolf, C. L. Lee, J. H. Heo, A. Sadhanala, N. Myoung, S. Yoo and S. H. Im, Science, 2015, 350, 1222.

[27] S. D. Stranks and H. J. Snaith, Nat. Nanotechnol., 2015, 10, 391.

[28] L. Zhang, X. Yang, Q. Jiang, P. Wang, Z. Yin, X. Zhang, H. Tan, Y. M. Yang, M. Wei, B. R. Sutherland and E. H. Sargent, Nat. Commun., 2017, 8, 15640.

[29] S. A. Veldhuis, P. P. Boix, N. Yantara, M. Li, T. C. Sum, N. Mathews and S. G. Mhaisalkar, Adv. Mater., 2016, 28, 6804.

[30] M. A. Green, A. Ho-Baillie and H. J. Snaith, Nat. Photonics, 2014, 8, 506.

[31] X. He, Y. Qiu and S. Yang, Adv. Mater., 2017, 29, 1700775.

[32] Q. Zhou, Z. Bai, W. G. Lu, Y. Wang, B. Zou and H. Zhong, Adv. Mater., 2016, 28, 9163.

[33] L. Protesescu, S. Yakunin, M. I. Bodnarchuk, F. Krieg, R. Caputo, C. H. Hendon, R. X. Yang, A. Walsh and M. V. Kovalenko, Nano Lett., 2015, 15, 3692.

[34] Y. Wang, X. Li, J. Song, L. Xiao, H. Zeng and H. Sun, Adv. Mater., 2015, 27, 7101.

[35] M. Kulbak, D. Cahen and G. Hodes, J. Phys. Chem. Lett., 2015, 6, 2452.

[36] A. Swarnkar, R. Chulliyil, V. K. Ravi, M. Irfanullah, A. Chowdhury and A. Nag, Angew. Chem., Int. Ed., 2015, 127, 15644.

[37] X. Li, Y. Wu, S. Zhang, B. Cai, Y. Gu, J. Song and H. Zeng, Adv. Funct. Mater., 2016, 231, 2435.

[38] S. N. Raja, Y. Bekenstein, M. A. Koc, S. Fischer, D. Zhang, L. Lin, R. O. Ritchie, P. Yang and A. P. Alivisatos, ACS Appl. Mater. Interfaces, 2016, 8, 35523.

[39] W. G. Lu, X. G. Wu, S. Huang, L. Wang, Q. Zhou, B. Zou, H. Zhong and Y. Wang, Adv. Opt. Mater., 2017, 5, 1700594.

[40] D. Wang, D. Wu, D. Dong, W. Chen, J. Hao, J. Qin, B. Xu, K. Wang and X. Sun, Nanoscale, 2016, 8, 11565.

[41] Y. Fu, H. Zhu, C. C. Stoumpos, Q. Ding, J. Wang, M. G. Kanatzidis, X. Zhu and S. Jin, ACS Nano, 2016, 10, 7963.

[42] H. Zhu, Y. Fu, F. Meng, X. Wu, Z. Gong, Q. Ding, M. V. Gustafsson, M. T. Trinh, S. Jin and X. Y. Zhu, Nat. Mater., 2015, 14, 636.

[43] S. W. Eaton, M. Lai, N. A. Gibson, A. B. Wong, L. Dou, J. Ma, L. W. Wang, S. R. Leone and P. Yang, Proc. Natl. Acad. Sci. U. S. A., 2016, 113, 1993.

[44] P. Zhu, S. Gu, X. Shen, N. Xu, Y. Tan, S. Zhuang, Y. Deng, Z. Lu, Z. Wang and J. Zhu, Nano Lett., 2016, 16, 871.

[45] H. Deng, D. Dong, K. Qiao, L. Bu, B. Li, D. Yang, H. E. Wang, Y. Cheng, Z. Zhao, J. Tang and H. Song, Nanoscale, 2015, 7, 4163.

[46] A. B. Wong, M. Lai, S. W. Eaton, Y. Yu, E. Lin, L. Dou, A. Fu and P. Yang, Nano Lett., 2015, 15, 5519.
[47] D. Zhang, S. W. Eaton, Y. Yu, L. Dou and P. Yang, J. Am. Chem. Soc., 2015, 137, 9230.

[48] M. J. Ashley, M. N. O'Brien, K. R. Hedderick, J. A. Mason, M. B. Ross and C. A. Mirkin, J. Am. Chem. Soc., 2016, 138, 10096.

[49] S. Sun, D. Yuan, Y. Xu, A. Wang and Z. Deng, ACS Nano, 2016, 10, 3648.

[50] L. Dou, M. Lai, C. S. Kley, Y. Yang, C. G. Bischak, D. Zhang, S. W. Eaton, N. S. Ginsberg and P. Yang, Proc. Natl. Acad. Sci. U. S. A., 2017, 114, 7216.

[51] J. Xing, X. F. Liu, Q. Zhang, S. T. Ha, Y. W. Yuan, C. Shen, T. C. Sum and Q. Xiong, Nano Lett., 2015, 15, 4571.

[52] Y. Wang, J. He, H. Chen, J. Chen, R. Zhu, P. Ma, A. Towers, Y. Lin, A. J. Gesquiere, S. T. Wu and Y. Dong, Adv. Mater., 2016, 28, 10710.

[53] J. Wang, M. S. Gudiksen, X. Duan, Y. Cui and C. M. Lieber, Science, 2001, 293, 1455.

[54] G. E. Eperon, S. N. Habisreutinger, T. Leijtens, B. J. Bruijnaers, J. J. van Franeker, D. W. deQuilettes, S. Pathak, R. J. Sutton, G. Grancini, D. S. Ginger, R. A. Janssen, A. Petrozza and H. J. Snaith, ACS Nano, 2015, 9, 9380.

[55] W. Zhou, Y. Zhao, C. Shi, H. Huang, J. Wei, R. Fu, K. Liu, D. Yu and Q. Zhao, J. Phys. Chem. C, 2016, 120, 4759.

[56] X. Gong, M. Li, X. B. Shi, H. Ma, Z. K. Wang and L. S. Liao, Adv. Funct. Mater., 2015, 25, 6671.

[57] J. You, Y. Yang, Z. Hong, T. B. Song, L. Meng, Y. Liu, C. Jiang, H. Zhou, W. H. Chang, G. Li and Y. Yang, Appl. Phys. Lett., 2014, 105, 183902.

[58] Z. Zhu, V. G. Hadjiev, Y. Rong, R. Guo, B. Cao, Z. Tang, F. Qin, Y. Li, Y. Wang, F. Hao and S. Venkatesan, Chem. Mater., 2016, 28, 7385.

[59] S. G. R. Bade, J. Li, X. Shan, Y. Ling, Y. Tian, T. Dilbeck, T. Besara, T. Geske, H. Gao, B. Ma and K. Hanson, ACS Nano, 2016, 10, 1795.

[60] X. Zhang, X. Bai, H. Wu, X. Zhang, C. Sun, Y. Zhang, W. Zhang, W. Zheng, W. W. Yu and A. L. Rogach, Angew. Chem., Int. Ed., 2018, 57, 3337.

[61] K. K. Bass, R. E. McAnally, S. Zhou, P. I. Djurovich, M. E. Thompson and B. C. Melot, Chem. Commun., 2014, 50, 15819.

[62] C.-H. Chiang, M. K. Nazeeruddin, M. Gratzel and C.-G. Wu, Energy Environ. Sci., 2017, 10, 808.

[63] R. L. Z. Hoye, M. R. Chua, K. P. Musselman, G. Li, M.-L. Lai, Z.-K. Tan, N. C. Greenham, J. L. MacManus-Driscoll, R. H. Friend and D. Credgington, Adv. Mater., 2015, 27, 1414.

[64] A. M. Leguy, Y. Hu, M. Campoy-Quiles, M. I. Alonso, O. J. Weber, P. Azarhoosh, M. Van Schilfgaarde, M. T. Weller, T. Bein, J. Nelson and P. Docampo, Chem. Mater., 2015, 27, 3397.

[65] J. M. Frost, K. T. Butler, F. Brivio, C. H. Hendon, M. Van Schilfgaarde and A. Walsh, Nano Lett., 2014, 14, 2584.

[66] J. He, Y. Wang, H. Chen, A. Towers, P. Yuan, Z. Jiang,C. Zhang, J. Chen, A. J. Gesquiere, S. T. Wu and Y. Dong. SID Symp. Dig. Tech. Papers, 2018, 49, 218.

[67] J. He, A. Towers, Y. Wang, P. Yuan, Z. Jiang, J. Chen, A. J. Gesquiere, S.-T. Wu, Y. Dong. Nanoscale 2018**,** *10* (33), 15436-15441.

[68] M. Roy Vikram, S. Banerjee, A. Mitra, A. Alam, M. Aslam, Chem. Eur. J. (2019) *25*, 9892.

[69] N. Soetan, W. R. Erwin, A. M. Tonigan, D. G Walker, R. Bardhan. The Journal of Physical Chemistry C (2017) 121 (33), 18186-18194.

[70] A. Pan, A. M Jurow, Y. Zhao, F. Qiu, Y. Liu, J. Yang, J. J. Urban, L. He, Y. Liu. Nanoscale (2017) 9 (45), 17688-17693.

[71] S. Gonzalez-Carrero, L. Bareño, E. Debroye, C. Martin, P. Bondia, C. Flors, R. E. Galian, J. Hofkens, J. Pérez-Prieto. Chemical Communications (2019) 55 (20), 2968-2971.

[72] Ananthakumar, S. Moorthy Babu, Synthetic Metals, 2018, 246, 64-95.

[73] D. M. Jang, K. Park, D. H. Kim, J. Park, F. Shojaei, H. S. Kang, J.-P. Ahn, J. W. Lee, J. K. Song, Nano Letters (2015) 15 (8), 5191-5199.

[74] M. Anaya, A. Rubino, T. C. Rojas, J. F. Galisteo-López, M. E. Calvo, H. Míguez, Advanced Optical Materials (2017) 5, 1601087.

[75] J. Kang, L.-W. Wang, The Journal of Physical Chemistry Letters 2017, 8 (2), 489-493.

[76] V. K. Ravi, G. B. Markad, A. Nag. ACS Energy Letters (2016) 1 (4), 665-671.

[77] Y.-H. Kim, H. Cho, T.-W. Lee, Proceedings of the National Academy of Sciences (2016) 113 (42), 11694.

[78] A. Wright, C. Verdi, R. Milot, et al. Nat Commun (2016) 7, 11755.

[79] G.-J. A. H. Wetzelaer, M. Scheepers, A. M. Sempere, C. Momblona, J. Ávila, and H. J. Bolink, Adv. Mater., (2015) 27: 1837-1841.

[80] B. Choudhury, M. Dey, and A. Choudhury, Int Nano Lett (2013) 3, 25.

[81] J. Liu, D. Cao, L. Zhang, The Journal of Physical Chemistry C (2008) 112 (17), 6653-6661.

[82] K. Zheng, K. K. Žídek, M. Abdellah, M. E. Messing, M. J. Al-Marri, T. Pullerits. The Journal of Physical Chemistry C (2016) 120 (5), 3077-3084.

CHAPTER 5: 2D RUDDLESDEN-POPPER HYBRID PEROVSKITES: A PRELIMINARY PHOTOPHYSICAL STUDY OF QUANTUM DOT AND NANOPLATELET VARIETIES

Introduction

Numerous strategies have been investigated for the encapsulation of perovskite materials in protective barriers encompassing polymeric materials [1,2] to inorganic, crystalline solids [3] showing promise in enhancing environmental stability. Beyond added protective layers for environmental stability, Ruddlesden-Popper 2D perovskites are gaining traction as an alternative due to their noted stability under atmospheric conditions [4]. Unlike the hydrophilic nature of MA^+ in 3D $MAPbI_3$ perovskites, the organic spacer molecules used in Ruddlesden-Popper 2D perovskites are hydrophobic, which in turn acts as a barrier to environmental hazards (moisture, air, etc.) [5, 6]. In addition to this, the exciton binding energy and band gaps of 2D perovskites can be tuned due to their unique layered structure and the ability to utilize alternative spacer molecules in their synthesis [5, 6].

As a 2D analog of hybrid organic-inorganic perovskites, Ruddlesden-Popper perovskites are comprised of repeating semiconductor layers separated by individual insulated organic layers, which are typically comprised of long-chained spacer molecules such as octyl amine and oleic acid with ammonia or carboxylic acid terminations. In contrast to the typical aggregation of inorganic layers in 3D perovskites, their 2D Ruddlesden-Popper counterparts form unique inorganic quantum well layers of perovskite material separated by a barrier layer of organic spacer molecules. However, the quantum wells exhibit a quantum confinement effect on excitons formed in the material which increases their exciton-binding energy. The already inflated exciton binding energy is further increased by the larger dielectric constant difference between the organic spacer molecules typically used in 2D perovskite materials and the inorganic well material. These large exciton-binding energies makes it difficult for excitons to form free carriers via thermal activation and lowers the carrier mobility by as much as two orders of magnitude, making understanding these excitonic species and their interactions in the material paramount to optoelectronic device implementation.

Due to the distinctive structural formation of these 2D Ruddlesden-Popper hybrid perovskites, facilitated changes to the material's optical properties and by extension their photophysical properties can be achieved by simple modification of the number of perovskite layers present and their distance from one another via the organic spacer layer [7]. In addition, the confinement effects exhibited on charge carriers due to the small individual and separated layers enable stable excitons with large Bohr radii and enhanced binding energies [4]. These excitonic properties have been further linked to the dielectric differences between the perovskite materials and organic spacer molecules, which would suggest that quantum confinement isn't the sole factor driving these unique excitonic transport properties [4].

Very little photophysical information is currently available on 2D Ruddlesden-Popper perovskite quantum dots and nanoplatelets, with the most current publication of their synthesis published in 2018 [8]. The biggest drawback to studying 2D perovskite structures in general was the lack of consistent synthetic method, which has led to a case by case study of these valuable materials. With the successful synthesis of 2D Ruddlesden-Popper variety of perovskite materials, a more reliable method now exists to synthesize consistent 2D perovskite structures, making growth in the understanding of 2D perovskite materials immanent.

With the wide wavelength range and bright emissive properties coupled with enhanced stability and unique charge transport properties, 2D Ruddlesden-Popper perovskite quantum dots and nanoplatelets serve as strong candidates for white light emission [9], nanostructured solar cell materials [10], small cavity lasing [11], and photodetectors [12]. Growth and development of 2D Ruddlesden-Popper perovskites will provide a platform for precise synthesis of 2D perovskite structures, which will help to build a thorough understanding of the fundamental and photophysical transport properties in these materials.

Here we report the spectroscopic study of 2D Ruddlesden-Popper perovskite quantum dots and nanoplatelets of $(CH_3(CH_2)_3NH_3)_2(CH_3NH_3)_{n-1}$ Pb_nI_{3n+1} where n = 1, 2, 3, etc. expresses the layers of perovskite material present in the sample. The synthesis is accomplished through three separate synthetic methods: A top-down (TD), bottom-up (BU), and nanoplatelet (NP) method combining reflux and sonication techniques. The TD and BU approaches generated quantum dots of similar sizes (≈ 4.5 – 10 nm) along with similar absorption properties while the NP method created nanoplatelets with ≈5 nm thickness and ≈50 nm lateral dimensions.

These materials were further characterized using steady-state UV-Vis absorption and photoluminescence spectroscopy as well as TCSPC to measure photoluminescence lifetimes. The steady-state absorbance and photoluminescence spectra as well as photoluminescence lifetime measurements indicate a mixed layer system with n = 2 & 3 and strong lattice vibration effects arising from quantum confinement in the mixed layer system. From these observations, exciton-polaron effects greatly influence the photophysical pathways available for light emission in 2D-Ruddlesden-Popper quantum dots and nanoplatelets.

Experimental

Materials

Hydroiodic acid (HI, aqueous, 57% w/w), hypophosphorous acid (H_3PO_2), lead II oxide (PbO), methylammonium iodide (MAI), N-butylamine, toluene, sodium hydroxide pellets, and dimethylformamide (DMF) all purchased from Sigma Aldrich. Syringe, syringe filter (0.22 μm PTFE), and HPLC grade acetone (omnisolv) were purchased from VWR international. Coverslips (22x22-1) were purchased from Fisher Scientific (Catalog No. 12-544-10). All chemicals were used as is with no further modifications.

Synthesis of 2D Ruddlesden-Popper Perovskite (n = 2)

The PbO powder (2232 mg, 10mmol) was dissolved in a two-component mixture of 57% w/w HI solution (10mL, 76 mmol) and 50% aqueous H_3PO_2 (1.72 mL, 15.5 mmol) by heating to a boil under constant magnetic stirring for five minutes. MAI (338 mg, 5 mmol) was then added to the resulting hot yellow solution, which resulted in the formation of a black precipitate and its almost immediate redissolution into a clear yellow solution. In a separate vial, N-butylamine (248 uL, 7mmol) was added to 57% w/w HI solution (5 mL, 38mmol) and allowed to cool on an ice bath. The n-$CH_3(CH_2)_3NH_3I$ solution was then added dropwise to the hot PbI_2 solution, which resulted in a bright yellow solution and was allowed to cool to room temperature after five additional minutes of stirring. The formation of cherry red crystals occurred after cooling to room temperature and they were subsequently separated by vacuum filtration and dried under reduced pressure.

Synthesis Scheme: Top-Down Method

The previously synthesized Ruddlesden-Popper perovskite crystals were dispersed in toluene and underwent probe sonication for fifteen minutes. The red crystals dispersed well in the toluene and larger crystal formations settled to the bottom of the vial five minutes after sonication was ceased. The resulting supernatant solution was then filtered through a syringe filter (0.22μm, PTFE membrane), which resulted in a clear dispersion of 2D Ruddlesden-Popper perovskites containing a faint red-orange hue (Figure 4.1, top).

Synthesis Scheme: Bottom-Up Method

The cherry red Ruddlesden-Popper perovskites from the above method were slowly added to toluene at room temperature and the resulting mixture exhibited at clear bi-layer separation. The bottom layer of the resulting solution was bright yellow, and the top layer of the solution contained the red perovskite crystals suspended in toluene. A syringe and syringe filter (0.22 μm, PTFE membrane) was used to separate and filter the top layer of the solution (Figure 4.1 middle).

Synthesis Scheme: Nanoplatelet Method

The resulting Ruddlesden-Popper crystals are treated using the method in the “Synthesis Scheme: Top-Down Method.” The filtered supernatant is then refluxed for thirty minutes under vigorous stirring and cooled to room temperature. Finally, the cooled toluene suspension is ultra-sonicated for five minutes (Figure 4.1, bottom).

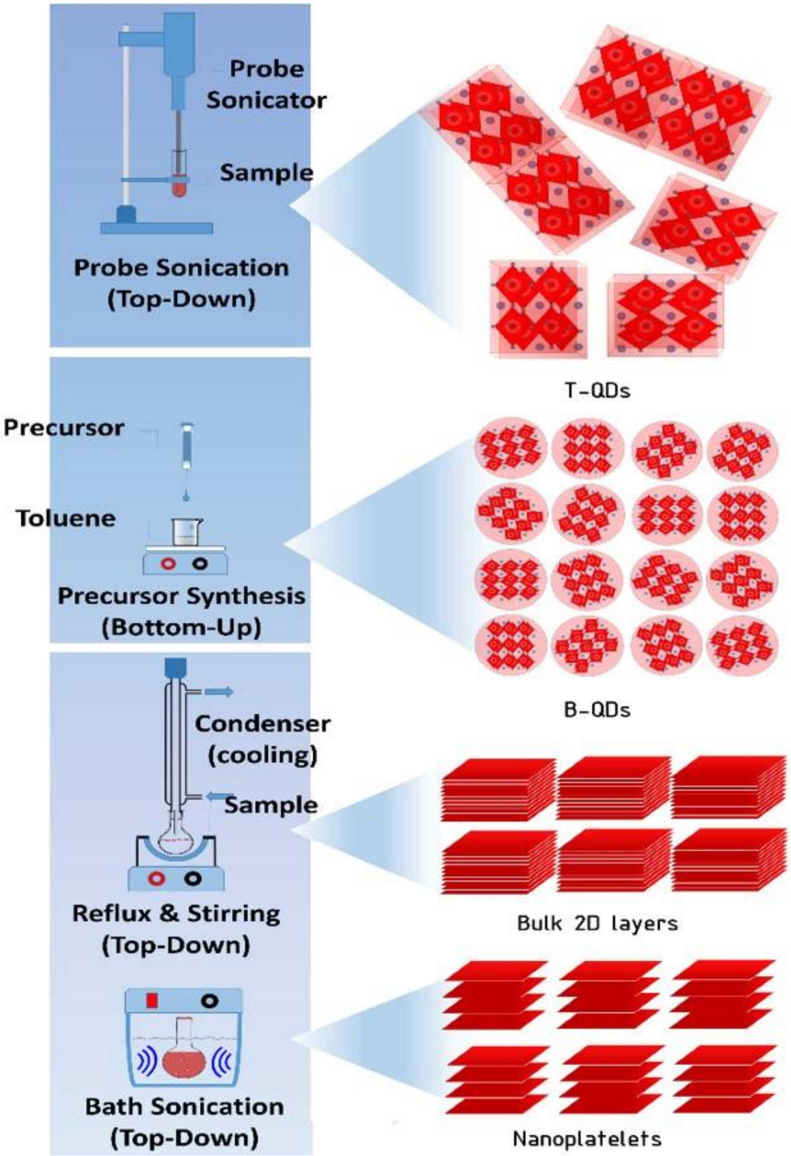

Figure 5.1: Synthetic scheme for 2D Ruddlesden-Popper perovskite top-down (top image) and bottom-up (middle image) quantum dots. Synthetic scheme for 2D Ruddlesden-Popper perovskite nanoplatelets (bottom image). Figure courtesy of Dr. Sreekanth Varma [32].

Transmission Electron Microscopy (TEM)

One drop of the appropriate filtered 2D Ruddlesden-Popper suspension was applied onto a 400-mesh carbon coated gold TEM grid and samples were imaged as is. HRTEM images were taken by a FEI Tecnai F30 operating at 190 kV.

X-Ray Diffraction (XRD)

Structural analysis was accomplished through XRD measurements using PANanalytical Empyrean with 1.8 KW Copper X-ray tube. Sample preparation involved drop casting each sample in the middle of a glass substrate and allowing it to dry, samples were run as is.

UV-Vis Absorption Spectroscopy

Absorption spectra were obtained using an Agilent Cary 300 spectrometer. Samples were suspended in toluene and absorption spectral was collected using quartz cuvettes.

Photoluminescence Spectroscopy

Emission spectra was obtained using a Horiba Nanolog (SPEX, Jobin Yvon Horiba) with an excitation wavelength of 285 nm and a 2.0 ND filter to keep count levels below the saturation threshold. Samples were suspended in toluene and emission spectra was collected using quartz cuvettes.

Coverslip Cleaning and Preparation for TCSPC Measurements

The coverslips (22 x 22-1) are used for samples in the custom-built sample holder used for microscope stage. The coverslips are first rinsed with nanopure water and sonicated in HPLC grade acetone (Omnisolv) for twenty minutes. The coverslips are then rinsed with nanopure water and sonicated in a 10 %wt sodium hydroxide solution for twenty minutes. Finally, the coverslips are rinsed with nanopure water and put through two more rounds of sonication in nanopure water for twenty minutes each time. After the subsequent washes, the coverslips are dried with N_2 and processed in a UV-Ozone chamber for 15 minutes.

Photoluminescence Imaging

photoluminescence images were acquired using a home-built sample-scanning confocal microscope. A 373 nm pulsed laser was used as the excitation source (Picoquant LDH-P-C-375) for all 2D Ruddlesden-Popper perovskite samples. The excitation side before the sample includes the following filters and optical elements: A gradient ND filter, 2.0 ND filter, 375/5 IF, and a dichroic mirror for 375 nm. The emission side after the sample includes the following optical elements: 400 nm LP filter, and an achromatic lens (FL = 75 mm). The laser was focused down to a spot size of ~300nm using a Zeiss 100x Fluar objective lens (NA 1.3, WD 0.17mm). To create a photoluminescence image of the scanned area, the 2D Ruddlesden-Popper perovskite samples were raster scanned across the focused laser beam using a Mad City Labs piezoelectric stage (Nano-LP100). Photoluminescence from single particles was collected using a fast, single photon counting detector (Picoquant, Micro Photon Devices, PDM series). Images were collected using the following scan parameters: dwell time of 5 ms, a laser repetition rate of 500 kHz, a scanning range of 10 x 10 μm^2 – 100 x 100 μm^2, and a laser power registering <1nW.

Time Correlated Single Photon Counting

Using the same set-up as described above, TCSPC excited state lifetime studies were completed by parking an area of interest of the samples over the focused pulsed laser beam (Picoquant LDH-P-C-375) and collecting photons with a fast, single photon counting detector (Picoquant, Micro Photon Devices, PDM series). The photon timing was measured using a pulsed laser driver (PDL 800-D), which provided the timing signal to a PicoHarp 300 TCSPC module in combination with a detector router (PHR 800), all from Picoquant. The following parameters were used in each decay curve acquisition: 500kHz repetition rate, 512ps resolution, 60 second collection time, laser power intensity >1nw for excitation, and counts recorded kept at ~3000 cts for all samples.

Results and Discussion

2D Ruddlesden-Popper Material Design

Top-down and Bottom-up approaches are common for designing materials with specific nanostructures where the top-down method typically begins with a larger scale starting material that is broken down into the desired product and he bottom-up method takes the opposite approach by building up to the desired product from an atomic or molecular level. In this case the top-down method uses sonication to break down nanocomposite substrates to achieve quantum dots of 2D perovskite materials. For the bottom-up approach, synthesized perovskite crystals are redistributed in a solvent (toluene) where they can be collected and filtered out. Finally, further modification of the top-down quantum dots is achieved through reflux to create compressed 2D structures which are then redistributed and broken up into nanoplatelets through ultra-sonication (Figure 5.1).

Currently, 2D films of $(CH_3(CH_2)_3NH_3)_2(CH_3NH_3)_{n-1}$ Pb_nI_{3n+1} are formed as a film in a self-assembly fashion and display growth in a perpendicular manner to their substrate. They can be grown with multiple layers up to n = 5 and are shown to be stable in ambient conditions. However, structural analysis on the crystallographic orientation of these materials shows unique situations involving the rotation axis as the layers grow beyond n = 1 [4]. This is due to the competition between the MA and BA cations attempting to satisfy the stereochemical demands of the 2D lattice, which results in a net distortion in the intermediate 2D structure (mainly the Pb-I bond). Using the our top-down, bottom-up, and nanoplatelet approaches should preserve the 2D structural characteristics described above but alter the confinement effects exhibited by 2D perovskites by creating quantum dots and nanoplatelets out of the 2D material. By taking the 2D material from a film to either a quantum dot or nanoplatelet we hypothesize an overall increase in quantum confinement effects, which should be pronounced through spectral characteristics (broadening, additional peaks, etc.) in both absorption and emission spectroscopies.

Structural and Morphological Characterization

TEM images were taken of each synthesized 2D Ruddlesden-Popper perovskite sample: Top-down, bottom-up, and nanoplatelet approach (Figure 5.1). Successful formation of perovskite quantum dot structures is seen in TEM images, though with some slight size variations: the quantum dots manufactured by the top-down method are slightly larger (≈5-10 nm) than the quantum dots quantum dots manufactured by the bottom-up method (≈4.5-5 nm). Fast Fourier Transform of the TEM images verifies the presence of the crystal faces typically seen in 2D perovskite samples (020 and 111) [15]. The nanoplatelet structure can be clearly observed in the TEM image (lateral dimension ≈50 nm, thickness ≈5 nm), which demonstrates the top-down nanoparticles as viable candidates for further structural modifications.

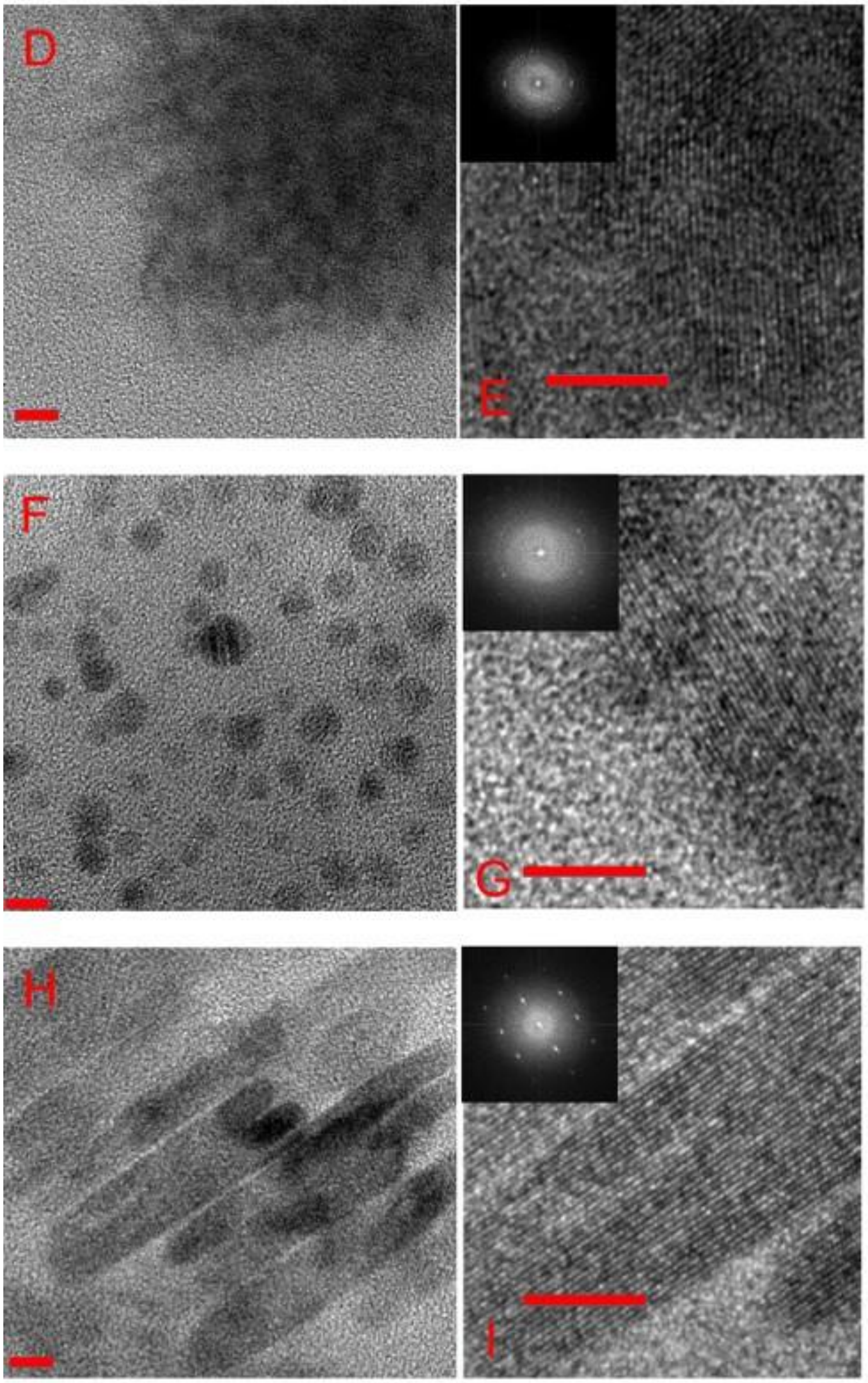

Figure 5.2: TEM images of 2D Ruddlesden-Popper perovskite nanostructures: Top-down quantum dots (D,E), Bottom-up quantum dots (F,G), and nanoplatelets (H,I). Scale bar in each image is 5 nm and insets are FFT images. Data collection and figure courtesy of Dr. Sreekanth Varma and Jitesh Kumar [32].

XRD spectra were taken from a 2D Ruddlesden-Popper perovskite film, 2D Ruddlesden-Popper perovskite nanoparticles (Top-down), and 2D Ruddlesden-Popper perovskite nanoplatelets (Figure 5.3). Using the 2D Ruddlesden-Popper perovskite film as a reference, nanoplatelet samples display a slight broadening and shifting of prominent peaks in their corresponding XRD spectra. This is an expected phenomenon that is due to the confinement effects increasing in the nanoplatelets because of structural changes that initiate a relaxation and distortion of the crystal lattice, which indicates a material with stronger quantum confinement effects than traditionally 2D perovskite films. [20, 28]. Specifically, XRD spectra for the nanoplatelets and quantum dots supports the claim of lattice relaxation, as those prepared with reflux methods show shifted peaks to lower 2θ values. Beyond this, the peaks for the 2D Ruddlesden-Popper quantum dots show depreciation in peak resolution, intensity, as well as shifting in position to lower 2θ values. Contemplating these XRD spectral results brings about a clear indication of increased confinement effects from the decrease in dimensionality brought on by lower ordered nanostructures compared to a solid film.

The presence of the 111 reflection rather than the typical 110 reflection seen in 3D perovskite materials indicates a 2D layered structure [4]. The proposed structure then becomes similar to 3D perovskites but rather the layers consist of tilted, corner-sharing $[PbI_6]^{4-}$ octahedra that propagate in two directions. In the third dimension (which would make for typical bulk materials), the 2D octahedra sheets are physically disconnected by intercalated organic bilayers [4]. Additionally, XRD peaks of the nanoplatelets and quantum dots also suggest an onset of perovskite layers beyond n = 2. Characteristically, the addition of low angle reflections ($2\theta < 4$) signals an incremental increase in the number of layers present [4]. This indicates the possibility of a mix layered system where both n = 2 and n = 3 layers are present, which can be further investigated through spectroscopic means.

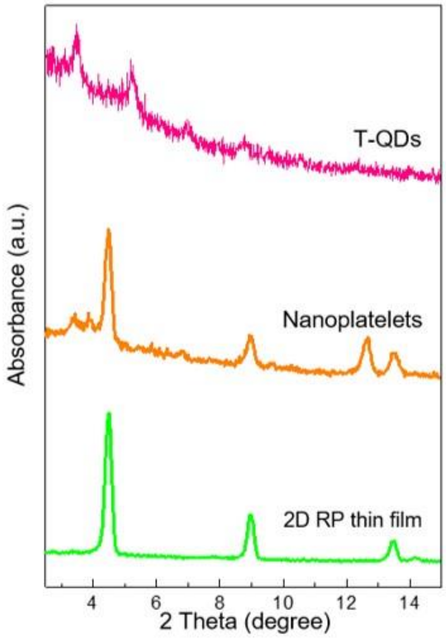

Figure 5.3: XRD spectra of 2D Ruddlesden-Popper perovskite thin film, nanoplatelets, and top-down quantum dots. Data collection and figure courtesy of Dr. Sreekanth Varma and Jitesh Kumar [32].

Optical and Photophysical Characterization

Absorption spectroscopy was accomplished through the use of a UV-Vis spectrometer (Agilent Cary 300) for all three synthetic variations. The 2D Ruddlesden-Popper perovskite quantum dots and nanoplatelets obtained from the top-down, bottom-up, and reflux synthetic methods all demonstrate a strong molecular absorption band centered at 300 nm and a weak and broad absorption band centered at 500 nm (Figure 5.4). The peak characteristics in the absorption band for 2D Ruddlesden-Popper perovskite films differ from those of the reduced quantum dot or nanoplatelet dimensionality in that the films display a broad range of absorptions [15,21]. This is an expected outcome of the 2D Ruddlesden-Popper perovskite quantum dots and nanoplatelets as these nanostructures are known for narrower emission and absorption bands [22].

While little has been done to characterize the deep UV absorption of 2D Ruddlesden-Popper perovskites (typically broad with little peak definition), the absorption band at 500 nm is common among layered structures [21,23]. The strong absorption band observed in each material obtained from all three synthetic strategy display multiple shoulders, which is common in 2D perovskite materials as their optical properties are heavily influenced by quantum confinement effects determined by the number of layers (n) present [21]. The increase in the presence of shoulders in the absorption band could also substantiate the claim of a mixed layer system, where these shoulders represent an aggregation of peaks resulting from other layers exhibiting different confinement effects [13]. Furthermore, the defined, yet broad absorption peak at a higher energy (≈ 300 nm) is indicative of strong electron-hole interactions arising from dielectric confinement, which further supports an increase in confinement effects and lattice conformation changes in the form of distorted octahedra [4]. This peak is also further blue shifted than typically reported for 2D Ruddlesden-Popper perovskites, which could also indicate the smaller size of nanoplatelets, and quantum dots is also contributing to the higher energy peak [4,13].

Steady state photoluminescence spectra were obtained with a fluorescence spectrometer (SPEX, Jobin Yvon Horiba) for the materials obtained from each of the synthetic methods. Samples were excited at 300 nm, which produced emission spectra with strong peaks in the UV region. The top-down synthesized quantum dots displayed the most exotic spectra of the three methods analyzed through photoluminescence spectroscopy with the onset of a doublet peak forming in the UV region with peak wavelengths at 350 nm and 375 nm (Figure 5.4). These observations indicate the top-down synthetic route introduces a higher concentration of defect states and this could be a result of an exciton bound to higher-lying defect state [14]. In this instance there are two possible explanations for this: a formation of layers beyond n = 2 (n = 3) [24] and/or lattice vibrations creating spatial potential fluctuations, resulting in phonon replicas at ≈350 nm and ≈375nm [9, 14]. Considering the absorption spectra obtained and the widening of the photoluminescence peaks, the likely case arises from a combination of different layers (n = 2 or 3) and lattice vibrations.

Lattice vibrations can create two different types of potential fluctuations in semiconductor materials: spatial and temporal, which are both observable in spectroscopic measurements. Spatial potential fluctuations cause a scattering effect with excitons in semiconductors, which can be observed in optical spectroscopies through broadening of excitonic peaks and temporal potential fluctuations are what imparts the fine structure to spectra referred to as the Frank-Condon shape [16, 17]. In conjunction with these potential fluctuations, moving excitons are able to create vibrational effects around their immediate vicinity, which induces lattice distortions that result in changes to optical properties such as: peak broadening, blue and red shifting, and the appearance of additional vibrational modes [16, 17]. Additional peaks or shoulders in the photoluminescence spectrum can also indicate multiple layers (n = 2 or

3) present as each layer has different confinement effects depending on the thickness of the active material layer. The photoluminescence spectra obtained for all three samples has instances of pronounced shoulders, especially in the QD samples, and further supports a mixed layered system and instances of exciton-phonon coupling.

The shoulders produced from the absorption spectrum, and the doublet formation in the photoluminescence spectrum photoluminescence spectra generated from materials manufactured using the bottom-up synthetic approach show a single yet broader peak when compared to the top-down materials. The peak also contains shoulders at ≈330 nm and ≈360 nm, which again suggest the mixed layer system and lattice vibrational effects due to the unique quantum and dielectric confinement phenomenon in 2D Ruddlesden-Popper perovskite materials. Reflux-synthesized nanoplatelets demonstrate a single peak wavelength ≈ 355 nm with no apparent shoulder structures (Figure 5.4), indicating out of the three synthetic methods, the reflux technique produces the most consistent n = 2 layered structure. However, the appearance of additional peaks on the XRD when compared to the 2D Ruddlesden-Popper film suggests there are still instances of formation of n = 3 layers. In addition to this, the broad emission peak produced through steady-state photoluminescence measurements indicate there are still lattice vibrational effects felt by the nanoplatelets.

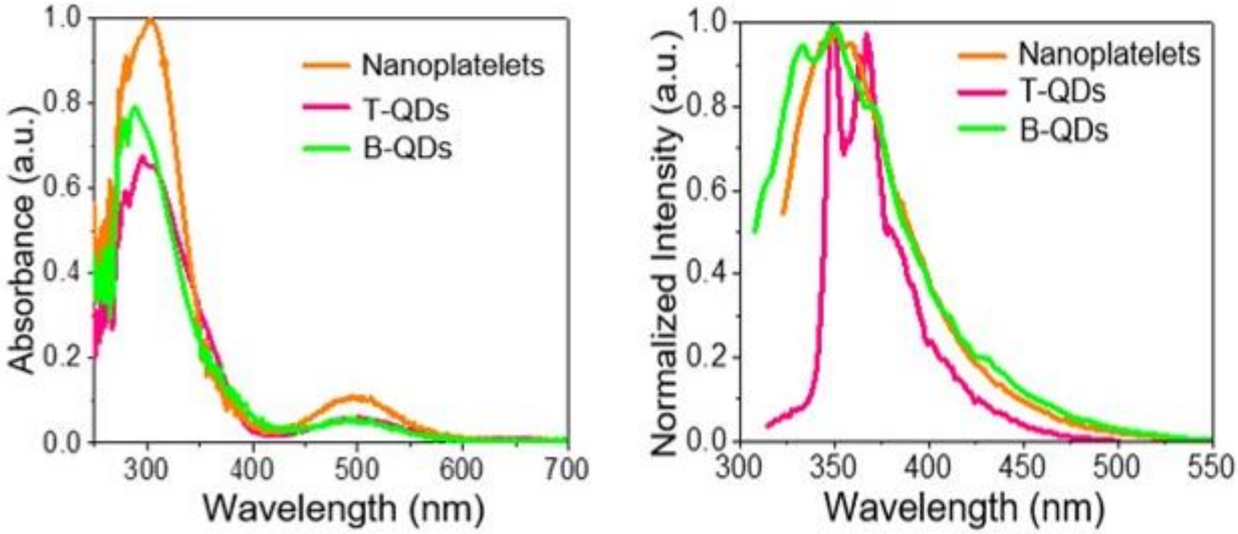

Figure 5.4: Absorption (top) and emission (bottom) spectra of 2D Ruddlesden-Popper perovskite quantum dots (top-down, bottom-up) and nanoplatelets. Data collection and figure courtesy of Dr. Sreekanth Varma and Jitesh Kumar [32].

Photoluminescence imaging was completed for all 2D Ruddlesden-Popper samples to map out photoluminescence intensities in preparation for time correlated single photon counting (TCSPC) measurements. Each sample was prepared by drop casting 10 μL onto an ultra-clean glass coverslip and allowed to dry in atmospheric conditions for five minutes before imaging. For photoluminescence imaging and TCSPC measurements three different samples were used: the top-down (Figure 5.5) and bottom-up (Figure 5.6) 2D Ruddlesden-Popper perovskite quantum dots, and the 2D Ruddlesden-Popper nanoplatelets Figure 5.7).

The photoluminescence images for the 2D Ruddlesden-Popper perovskites show similar morphology and similar photoluminescence intensity with respect to laser power used (≈ 100 nW) and counts recorded (≈ 300-500 counts/sec). Similar photoluminescence decay properties were observed for all three different sample variations (Table 5.1). The photoluminescence decay for all three samples show a τ_1 = 2-3 ns and a τ_2 = 9-11 ns with low standard deviation values for both components. The average photoluminescence lifetime for both the bottom-up quantum dots and nanoplatelets was 6 ns and the average photoluminescence lifetime for the top-down quantum dots was 7 ns. Consistencies between all three samples with regards to their photoluminescence decay indicate similar photophysical and charge transfer mechanics at play though with different moieties as evident with their absorption and emission profiles.

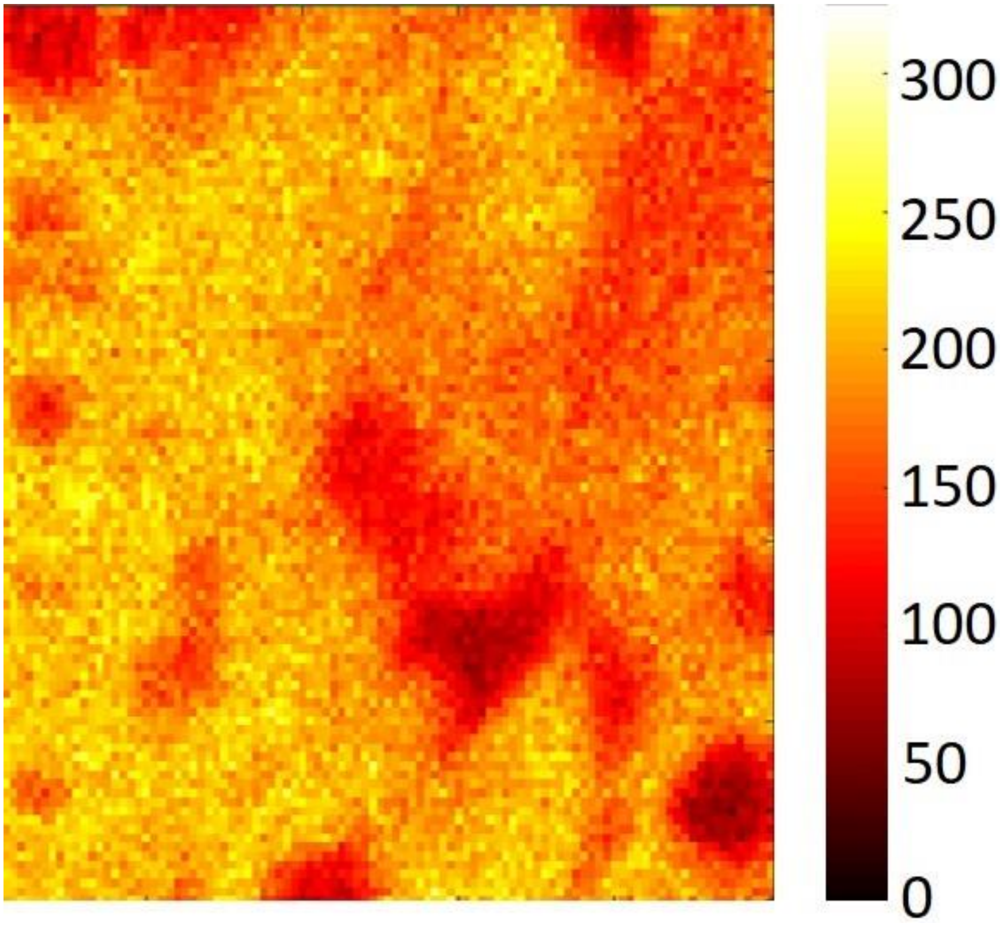

Figure 5.5: Photoluminescence image (10 x 10 μm^2) of top-down 2D Ruddlesden-Popper perovskite quantum dots.

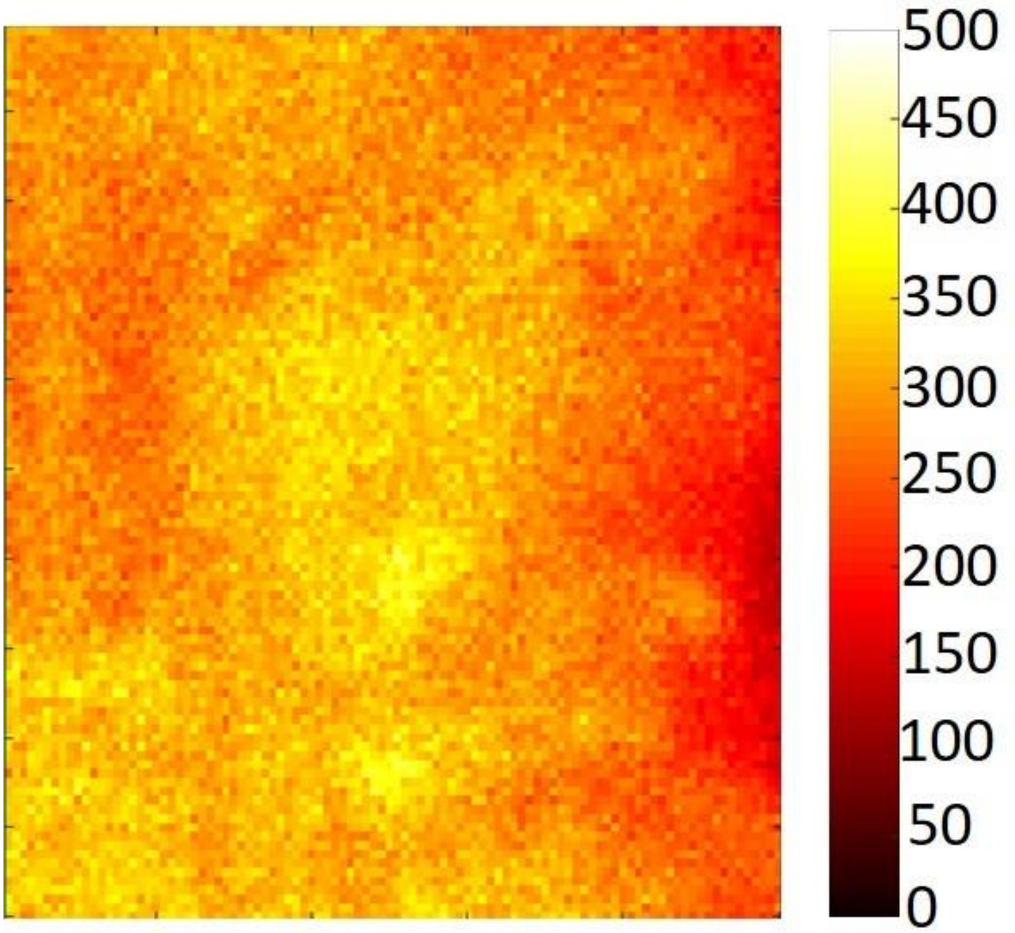

Figure 5.6: Photoluminescence image (10 x 10 μm^2) of bottom-up 2D Ruddlesden-Popper perovskite quantum dots.

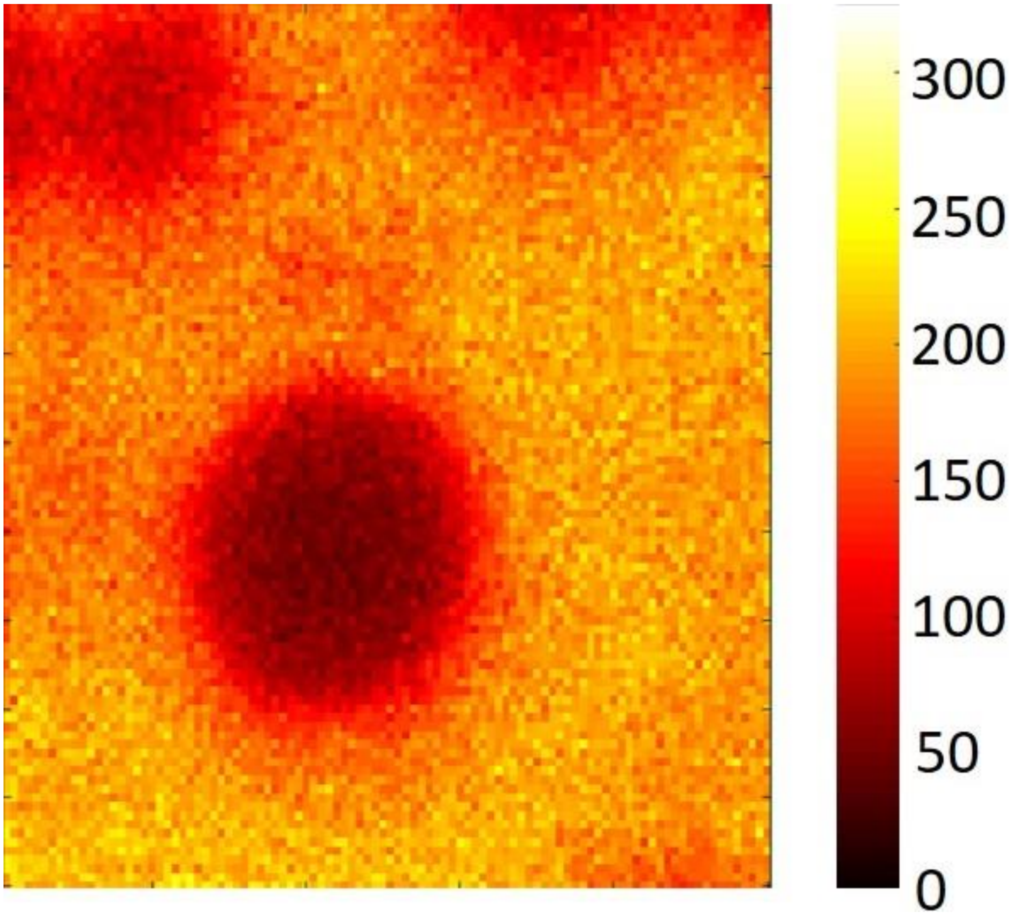

Figure 5.7: Photoluminescence image (10 x 10 μm^2) of refluxed 2D Ruddlesden-Popper perovskite nanoplatelets.

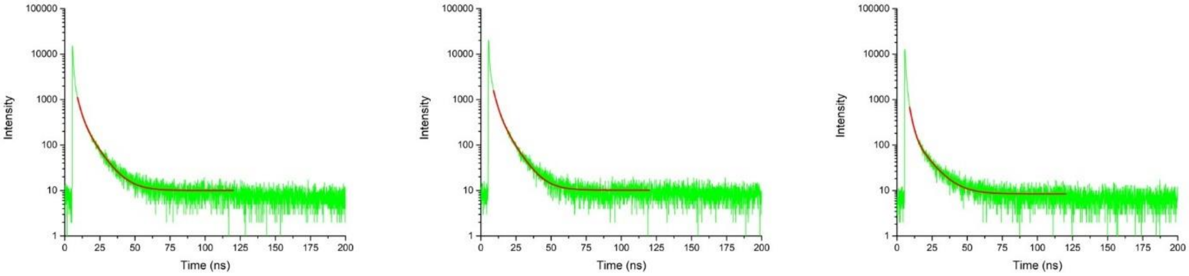

Figure 5.8: Photoluminescence decays for 2D Ruddlesden-Popper perovskite quantum dots (top-down: left, bottom-up: middle) and nanoplatelets (right)

Table 5.1: Photoluminescence decay and photophysical constants for 2D Ruddlesden-Popper perovskite quantum dots (top-down and bottom up) and nanoplatelets (refluxed).

Synthetic Method	τ_1 (ns)	A_1 (counts)	τ_2 (ns)	A_2 (counts)	τ_{avg} (ns)	k_{nr} (s^{-1})	k_r (s^{-1})
Top-down	2.00 ± 0.48	892 ± 213	11.00 ± 1.09	225 ± 74	7.23 ± 1.41	2.76×10^7	1.10×10^8
Bottom-up	2.00 ± 0.48	810 ± 179	9.00 ± 0.51	239 ± 97	6.00 ± 0.49	3.33×10^7	1.33×10^8
Refluxed	3.00 ± 0.20	1044 ± 236	9.00 ± 0.33	317 ± 155	5.86 ± 0.15	3.41×10^7	1.36×10^8

Photophysical and excited state mechanisms are vastly more complicated for 2D perovskite materials when compared to their 3D counterparts due to the quantum and dielectric confinement effects unique to 2D perovskites. The typical charge transfer dynamics in 3D perovskites are attributed to: (A) defect trapping, (B) free electron/hole recombination, and (C) Auger recombination, expressed in the following equation:

$$-\frac{dn}{dt} = k_1 n + k_2 n^2 + k_3 n^3 \tag{5.1}$$

where n represents the carrier density, k_1 is the defect trapping rate constant, k_2 is the free zcarrier/exciton recombination constant, and k_3 is the Auger non-radiative rate constant. As of writing no adapted model for 2D perovskite materials has been proposed and all speculations will be made using the 3D model listed above. At low fluences of power, such as measurements carried out in TCSPC, contribution from Auger recombination is negligible and we will consider two major pathways for excited state decay: trap assisted and bimolecular recombination.

Examining the excited state dynamics through photoluminescence decay can provide insight into the radiative and non-radiative pathways utilized in the material. The average photoluminescence lifetime (τ_{avg}) can be described through the following equation:

$$\tau_{avg} = \frac{1}{k_r + k_{nr}} \tag{5.2}$$

where k_r and k_{nr} represent the rate constants for radiative and non-radiative decay, respectively. The radiative and non-radiative contributions can be further described based on a material's quantum yield (ϕ) through the following equations:

$$\phi = \frac{k_r}{k_r + k_{nr}} \tag{5.3}$$

$$k_r = \frac{\phi}{\tau_{avg}} \tag{5.4}$$

$$k_{nr} = \frac{1-\phi}{\tau_{avg}} \tag{5.5}$$

While the photoluminescence quantum yield hasn't been measured for these materials as of writing, estimations and suggestions to the contributions of k_r and k_{nr} can be made based on recently published PLQY values for 2D Ruddlesden-Popper perovskite quantum dots [13]. A study by Yang, *et.al* found the PLQY of 2D Ruddlesden-Popper perovskite quantum dots with the formula $(BA)_2(MA)_{n-1}Pb_nX_{3n+1}$ (n = 2 and X = I) to be ≈ 20% [13]. Assuming 20% is the highest PLQY obtainable by 2D Ruddlesden-Popper perovskite quantum dots, the overall contributions from both the radiative and non-radiative rate constant can be calculated using the above equations (Table 5.1).

In all three 2D Ruddlesden-Popper samples $k_r > k_{nr}$ (10^8 vs 10^7 s^{-1}), which indicates for these samples, radiative processes are slightly out competing the radiative processes. However, due to the complexity of 2D perovskite systems (quantum and dielectric confinement) exciton-phonon coupling has been recognized as a major contributor to increased non-radiative pathways in 2D perovskite structures through lattice distortions caused by increased vibrational modes. [27]. The lattice vibrations are also able to cause broadening in emission spectra [28], which can be observed in all three methods of preparation for 2D-Ruddlesden-Popper perovskites. In addition to this, electron-phonon coupling also enables the creation of self-trap states, which can lead to free exciton trapping [28] or self-trapping of excitons [30]. These phenomena drastically affect both the PLQY (decrease) and rate of nonradiative decay times (increase) [29]. Finally, the effects of free exciton trapping, or self-trapping are fostered by the presence of defect states within the material, which provide an anchor for the exciton within the distorted lattice [31].

Strong evidence of exciton-phonon self-trapped excitons is present in the optical and photophysical characterization data for all synthesized 2D Ruddlesden-Popper perovskites in this study. The first instance where this is observed is in the broad photoluminescence spectra obtained for all 2D Ruddlesden-Popper perovskite samples. The second observable trait indicating self-trapping of excitons is the red shifting of emission peak over a wider range of wavelengths due to the decreased energy of the self-trapped exciton [16]. Finally, the shorter photoluminescence lifetimes provide evidence of self-trapped excitons as the lifetime of electrons bound in this state is shorter due to inelastic collisions (carrier-carrier or exciton-exciton scattering) [9, 16].

The presence of both free and self-trapped excitons allows for more than one luminescence pathway due to the difference in activation energy (E_g) to achieve either of these pathways along with high exciton binding energies (E_b) (Figure 5.9) intrinsic to 2D perovskite materials [9, 19]. These pathways specifically are the recombination event of a free exciton, the recombination of an intrinsically self-trapped exciton (exciton-polaron interaction), and the recombination of a defect trapped exciton [9, 19]. Due to the defect tolerant nature of perovskite materials, it is assumed the trap-states formed in the material are shallow in nature which would lead to an eventual radiative recombination event occurring. This is due to the low binding energy of shallow trapped excitons, which allows for radiative recombination though from the trapper level [16, 18]. The calculated band structure for 2D-Ruddlesden-Popper perovskites shows an increase in the density of states as the value of the active layer material increased (n = 1, 2, 3, etc.) (Figure 5.10). The band gap energy is also observed to be decreasing as more layers are added to the material, which would indicate the shallow defect sites located at the valance band maximum and conduction band minimum are able to be further incorporated into the band structure, which would further support the self-trapped and defect trapped exciton photoluminescence decay pathways. This is due to distortion effects caused by exciton-polaron interactions and shallow defect states being more readily available at similar energy levels where free excitons exist [26].

Little variation in the photoluminescence lifetimes also signal that changes to the morphology (quantum dots vs nanoplatelets) do not affect the photophysical pathways available for radiative emission. To further probe the actual E_g and E_b required for these transitions, low temperature optical measurements need to be carried out in order to minimize vibrational distortions caused by exciton-phonon interactions in these materials [9].

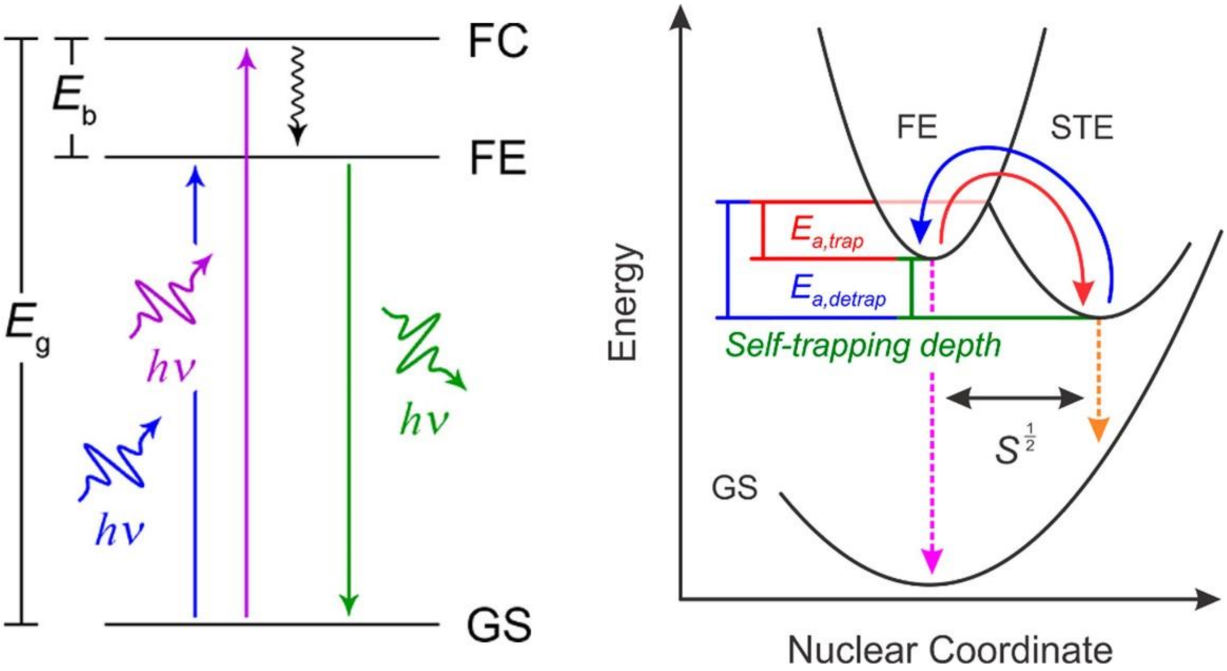

Figure 5.9: Typical band-to-band and excitonic transitions observed in 2D lead-halide perovskites (left). Band energy diagram depicts the ground state (GS), free carriers (FC) and free excitons (FE). Colored arrows represent absorption or photoluminescence processes, and the black arrow denotes nonradiative relaxation. Self-trapping (blue) and detrapping (red) excitonic processes in 2D perovskite materials displayed via nuclear coordinated diagram (right). Energy levels displayed are the ground state (GS), the self-trapped exciton states (STE), and the free exciton state (FE). Energy requirements are represented as activation energy for detrapping ($E_{\mathrm{a,detrap}}$) and activation energy for self-trapping ($E_{\mathrm{a,trap}}$) displayed with the Huang-Rhys parameter (S). The orange and pink arrows illustrate STE and FE photoluminescence, respectively. Adapted from ref [9] with permission from the Royal Society of Chemistry.

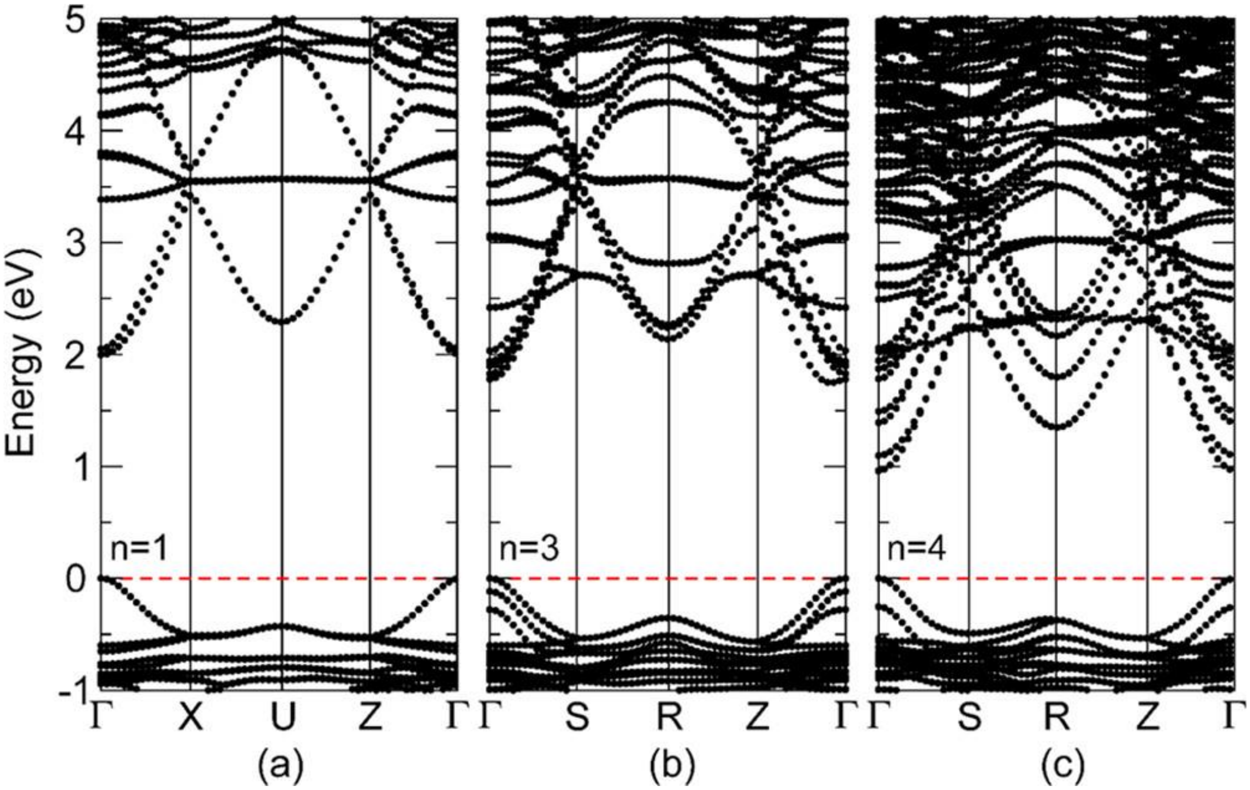

Figure 5.10: Electronic band structure of the polar configurations of selected $(BA)_2(MA)_{n-1}Pb_nI_{3n+1}$ perovskites. (a) $(BA)_2PbI_4$ ($n = 1$), (b) $(BA)_2(MA)_2Pb_3I_{10}$ ($n = 3$), and (c) $(BA)_2(MA)_3Pb_4I_{13}$ ($n = 4$) along the Γ(0,0,0)-X/S(1/2,0,0)-U/R(1/2,0,1/2)-Z(0,0,1/2)-Γ(0,0,0) path (solid vertical lines) throughout the Brillouin zone. The Fermi level is set to 0 eV and indicated by the horizontal broken red line. Reproduced with permission from Reference [4]. https://pubs.acs.org/doi/full/10.1021/acs.chemmater.6b00847. This is an unofficial adaptation of an article that appeared in an ACS publication. ACS has not endorsed the content of this adaptation or the context of its use. Further permissions related to the material excerpted should be directed to the ACS

Conclusions

We have spectroscopically investigated the products of three separate methods to synthesize 2D Ruddlesden-Popper perovskite nanostructures in the form of quantum dots and nanoplatelets with the general formula $(BA)_2(MA)_{n-1}Pb_nX_{3n+1}$ ($n = 2$ and $X = I$).

Both the morphology and optical properties for each sample are greatly influenced by the method chosen for synthesis of the final 2D Ruddlesden-Popper perovskite structure. The 2D Ruddlesden-Popper perovskite quantum dots and nanoplatelets show strong absorption and emission in the UV region as well as short average photoluminescence decay lifetimes. The outcome of these optical properties can be attributed to the strong quantum and dielectric confinement brought on by the unique quantum well structure adopted by 2D perovskite materials, specifically lattice vibration effects (exciton-polaron interactions) and a mixed layered material ($n = 2$ or 3). Finally, the photophysical properties of these materials were explored and elaborated on by determining the overall contributions of k_r and k_{nr} ($k_r > k_{nr}$) to the average photoluminescence lifetime. From the rate constants determined for each of the samples and their optical characteristics, strong indications of electron-phonon coupling can be seen in these samples. As a result of this, three radiative pathways were proposed as possible mechanistic emissive processes in these 2D Ruddlesden-Popper perovskites: free exciton, intrinsically trapped, and defect trapped recombination. Further photophysical characterization through low-temperature, transient spectroscopies is required to flush out exact charge carrier mechanisms for these materials and their overall contributions to the photophysical pathways in the 2D Ruddlesden-Popper perovskite quantum dots and nanoplatelets.

References

[1] J. He, A. Towers, Y. Wang, P. Yuan, Z. Jiang, J. Chen, A. J. Gesquiere, S.-T. Wu, Y. Dong. Nanoscale (2018) 10 (33), 15436-15441.

[2] Y. Wang, J. He, H. Chen, J. Chen, R. Zhu, P. Ma, A. Towers, Y. Lin, A. J. Gesquiere, S. Wu, Y. Dong. (2016) Adv. Mater., 28: 10710-10717.

[3] M. Mei, Z. Han, P. Liu, F. Fang, W. Chen, J. Hao, D. Wu, R. Pan, W. Cao, K. Wang. Nanotechnology (2019) 30 (39), 395702.

[4] C. C. Stoumpos, D. H. Cao, D. J. Clark, J. Young, J. M. Rondinelli, J. I. Jang, J. T. Hupp, M. G. Kanatzidis. Chemistry of Materials (2016) 28 (8), 2852-2867.

[5] Y. Zheng, T. Niu, X. Ran, J. Qiu, B. Li, Y. Xia, Y. Chen, W. Huang, Journal of Materials Chemistry A (2019) 7 (23), 13860-13872.

[6] Y. Chen, Y. Sun, J. Peng, J. Tang, K. Zheng, Z. Liang, Adv. Mater. (2018) 30, 1703487.

[7] J. C. Blancon, H. Tsai, W. Nie, C. C. Stoumpos, L. Pedesseau, C. Katan, M. Kepenekian, C. M. M. Soe, K Appavoo, M. Y. Sfeir, S. Tretiak, P. M. Ajayan, M. G. Kanatzidis, J. Even, J. J. Crochet, A. D. Mohite. Science (2017) 355 (6331), 1288.

[8] Y.-H. Chang, J.-C Lin, Y.-C. Chen, T.-R. Kuo, D.-Y. Wang. Nanoscale Research Letters (2018) 13 (1), 247.

[9] M. D. Smith, H. I. Karunadasa. Accounts of Chemical Research (2018) 51 (3), 619-627.

[10] H. Tsai, W. Nie, J.-C. Blancon, C. C. Stoumpos, R. Asadpour, B. Harutyunyan, A. J. Neukirch, R. Verduzco, J. J. Crochet, S. Tretiak, L. Pedesseau, J. Even, M. A. Alam, G. Gupta, J. Lou, P. M. Ajayan, M. J. Bedzyk, M. G. Kanatzidis, A. D. Mohite, Nature (2016) 536, 312.

[11] H. Zhang, Q. Liao, Y. Wu, Z. Zhang, Q. Gao, P Liu, M. Li, J. Yao, H. Fu. Adv. Mater. (2018) 30, 1706186.

[12] Z. Tan, Y. Wu, H. Hong, J. Yin, J. Zhang, L. Lin, M. Wang, X. Sun, L. Sun, Y. Huang, K. Liu, Z. Liu, H. Peng. Journal of the American Chemical Society (2016) 138 (51), 16612-16615.

[13] Y. Chen, Y. Sun, J. Peng, J. Tang, K. Zheng, Z. Liang. Adv. Mater. (2018) 30, 1703487.

[14] M. Sebastian, J. A. Peters, C. C. Stoumpos, J. Im, S. S. Kostina, Z. Liu, M. G. Kanatzidis, A. J. Freeman, B. W. Wessels, Physical Review B 2015, 92 (23), 235210.

[15] D. H. Cao, C. C. Stoumpos, O. K. Farha, J. T. Hupp, M. G. Kanatzidis. Journal of the American Chemical Society 2015, 137 (24), 7843-7850.

[16] Y. Lekina, Z. X. Shen. Journal of Science: Advanced Materials and Devices (2019) 4 (2), 189-200.

[17] M. Ueta, H. Kanzaki, K. Kobayashi, Y. Toyozawa, E. Hanamura, ExcitonicProcesses in Solids, Springer Berlin Heidelberg, Berlin, Heidelberg, 1986 pgs 200-216.

[18] T. Ishihara, J Takahashi, T Goto, Physical Review B (1990) 42 (17), 11099-11107.

[19] M. D. Smith, A. Jaffe, E. R. Dohner, A. M. Lindenberg, H. I. Karunadasa. Chemical Science (2017) 8 (6), 4497-4504.

[20] L. Dou, A. B. Wong, Y. Yu, M. Lai, N. Kornienko, S. W. Eaton, A. Fu, C. G. Bischak, J. Ma, T. Ding, N. S. Ginsberg, L.-W. Wang, A. P. Alivisatos, P. Yang. Science (2015) 349, 6255, 1518.

[21] N. Wang, L. Cheng, R. Ge, S. Zhang, Y. Miao, W. Zou, C. Yi, Y. Sun, Y. Cao, R. Yang, Y. Wei, Q. Guo, Y. Ke, M. Yu, Y. Jin, Y. Liu, Q. Ding, D. Di, L. Yang, G. Xing, H. Tian, C. Jin, F. Gao, R. H. Friend, J. Wang, W. Huang. Nature Photonics (2016) 10, 699.

[22] T. R. Pisanic Ii, Y. Zhang, T. H. Wang. Analyst (2014) 139 (12), 2968-2981.

[23] X. Hong, T. Ishihara, A. V. Nurmikko. Physical Review B (1992) 45 (12), 6961-6964.

[24] J. Cho, Y.-H. Choi, T. E. O’Loughlin, L. De Jesus, S. Banerjee. Chemistry of Materials (2016) 28 (19), 6909-6916.

[25] S. Kumar, J. Jagielski, S. Yakunin, P. Rice, Y.-C. Chiu, M. Wang, G. Nedelcu, Y. Kim, S. Lin, E. J. G. Santos, M. V. Kovalenko, C.-J. Shih. ACS Nano (2016) 10 (10), 9720-9729.

[26] W. Peng, J. Yin, K.T. Ho, O. Ouellette, M. De Bastiani, B. Murali, O. El Tall,C. Shen, X. Miao, J. Pan, E. Alarousu, J.H. He, B.S. Ooi, O.F. Mohammed,E. Sargent, O.M. Bakr, Nano Lett. 17 (2017) 4759e4767.

[27] M. Ueta, H. Kanzaki, K. Kobayashi, Y. Toyozawa, E. Hanamura, ExcitonicProcesses in Solids, Springer Berlin Heidelberg, Berlin, Heidelberg, 1986.

[28] K. Gauthron, J-S. Lauret, L. Doyennette, G. Lanty, A. Al Choueiry, S.J. Zhang, A. Brehier, L. Largeau, O. Mauguin, J. Bloch, and E. Deleporte, Opt. Express (2010)18, 5912-5919.

[29] X. Gong, O. Voznyy, A. Jain, W. Liu, R. Sabatini, Z. Piontkowski, G. Walters,G. Bappi, S. Nokhrin, O. Bushuyev, M. Yuan, R. Comin, D. McCamant,S.O. Kelley, E.H. Sargent. Nat. Mater. (2018) 17 550-556.

[30] Z. Guo, X. Wu, T. Zhu, X. Zhu, L. Huang. ACS Nano (2016) 10 9992-9998

[31] I. Pelant, J. Valenta: Lumin. Spectrosc. Semi-cond., (2012) 161-204.

[32] J. Cherusseri, V. J. Varma, B. Pradhan, J. Li, J. Kumar, E. Barrios, Z. A. Mohammad, A. Towers, A. J. Gesquiere, J. Thomas. Nanoscale (2020) Submitted.

CHAPTER 6: CONCLUSIONS

The goal of this dissertation was to spectroscopically investigate the optical and photophysical properties resulting from synthetic modifications made to perovskite materials. The synthetic modifications explored in this dissertation resulted in changes to the dimensionality of perovskite materials (3D → 2D →1D), alterations in material composition (cationic and halide substitutions), and the addition of protective casing (polymer encapsulation). Encapsulation was accomplished through a swelling-deswelling method using DMF as a "good" solvent and driving it out through baking, while dimensionality changes were brought on through precursor spin-coating alongside the swelling-deswelling strategy or through the addition of organic spacer molecules, and compositional changes were done by substitution of either cationic or halogen species in the original reaction scheme.

After each synthetic modification, optical and photophysical characterization was accomplished through: steady-state absorption and photoluminescence spectroscopies and TCSPC to investigate the role synthesis and processing plays on the overall photophysical properties in perovskite materials. Until recently there hadn't been a push to delve into the photophysics behind the absorptive and luminescent properties as research groups moved from one modification to the next with incremental increases to PLQY and emissive qualities. However, even with the push to unravel the charge transfer mechanics and photophysical pathways in these materials, limitations in the reproducibility of synthetic techniques as well as their overall shelf lifetime make it difficult to study perovskite materials.

Initially, the encapsulation of 3D $MAPbBr_3$ perovskite nanoparticles in a polymer substrate was meant to simply increase the overall stability in the perovskite nanoparticle by protecting them from undesirable atmospheric interactions. Interestingly, the study produced six unique perovskite polymer composite samples displaying varying levels of PLQY (14% – 47%) and photoluminescence lifetime decay depending on the polymer used (PS, PC, PVC, ABS, CA, and PMMA). Optical and photophysical characterization revealed differences in charge transport properties depending on the polymer substrate used to create the $MAPbBr_3$-polymer composite. By further examining the photophysical kinetic properties through probing the radiative and non-radiative pathways available it was discovered that the polymer substrates played a role in defect passivation depending on their ability to interact with defect sites and their overall moisture permeability. The $MAPbBr_3$-polymer composite sample's photophysics are driven by trap state dynamics, which can lead to increased PLQY and stability depending on the polymer's ability to interact with prevalent surface defect states. The understanding of photophysical processes in these samples allows for optimization of optical properties and protection from degradation pathways prevalent in perovskite materials, making this a good candidate for eventual optoelectronic applications.

To further improve on material stability, the MA^+ was exchanged for Cs^+ due to the higher intrinsic stability afforded by all inorganic perovskite materials. In addition to this, various precursor and spin-coating speeds were used to achieve a 1D nanorod structure. Macroscale measurements showed uniform nanorods with a lower PLQY than their MA^+ counterparts along with a broader absorption band. Photoluminescence imaging elucidated a more detailed structure of individual nanorods, revealing the nanorods displayed a disjointed morphology unique to each nanorod. Urbach tailing was observed in the absorption spectra and the Urbach energy was calculated (364 meV), which indicated high densities of defect states and lower orders of crystallinity in the nanorods. Radiative and non-radiative kinetic constants coupled with optical spectroscopy determined the nanorods displayed more trap assisted photophysical processes based on lower τ_{avg} and $k_{nr} > k_r$ rate constants. Beyond the photophysical measurements, polarization imaging performed on mechanically aligned $CsPbBr_3$-PS nanocomposites ascertained when aligned the nanorods are able to emit polarized light. Again, this study reveals the value of photophysical and optical characterization of these materials as this specific $CsPbBr_3$-PS perovskite composite could be eventually used for enhancing backlight emission in LCD displays.

The final study focused on investigating the optical properties and photophysics of 2D Ruddlesden-Popper perovskite quantum dots and nanoplatelets. 2D Ruddlesden-Popper perovskites represent a method to increase the reproducibility in synthesizing 2D perovskite materials, which would help alleviate the case-by-case photophysical studies on 2D perovskite materials. This study focused on materials produced from three different synthetic routes, a top-down and bottom-up method for 2D Ruddlesden-Popper perovskite quantum dots and a reflux method for 2D Ruddlesden-Popper nanoplatelets. Each method produced a 2D-Ruddlesden-Popper perovskite nanostructure with different structural moieties evident through optical spectroscopy but with very similar photophysical process. Due to the extreme quantum confinement in these materials, it was discovered through analysis of the radiative and nonradiative constants the 2D Ruddlesden-Popper nanostructures display strong indications of electron-phonon coupling. This phenomenon leads to self-trapped exciton states, which induces photoluminescence band broadening while raising the photoluminescence lifetime decay rate. This study provides some of the first evidence of photophysical processes occurring in quantum dots and nanoplatelets of 2D Ruddlesden-Popper perovskite materials, which are already being coveted as upcoming replacements for more stable solar cell active layer materials.

The study of photophysical processes in perovskite materials is important to the future of these materials for eventual commercial applications. Any review article published about specific types of perovskite materials always has a statement in the outlook section at the end of the article that states, “Further understanding of the fundamental photophysical processes of X perovskite material is required for future optimization of Y and Z processes.[1-3]” Understanding the underlying photophysical processes in a semiconductor material will promote smart synthetic and processing optimization and allow growth of the material. This is especially true with semiconductor materials as most of them are susceptible to varying defect states, which interfere with charge transfer and photophysical processes responsible for luminescence and absorption.

Due to the versatility and defect tolerance of perovskite materials, there is a cornucopia of uses for them in: solar cell, display, photodetector, lasing, and many other applications [4-9]. Because of this, synthetic methods for perovskite materials are constantly changing to alter them for specific uses or to create desired characteristics [10]. In order to keep up with this, photophysical analysis is required to understand the consequences of the modifications made to perovskite materials. Ultra-fast spectroscopies are one of the most valuable tools in this armory of techniques to analyze these fast processes occurring perovskite materials and will be a necessity in order to truly understand the rapid photophysical processes that drive these materials [11-13].

In conclusion, we have derived a clear correlation between the synthetic strategies employed to create perovskite materials and the photophysical processes that drive them. We have demonstrated optical spectroscopy and TCSPC as viable techniques to elucidate photophysical processes occurring in perovskite materials. These techniques coupled with further structural and ultra-fast spectroscopies are the future of understanding the fundamental processes in perovskite materials.

References

[1] H. Lin, C. Zhou, Y. Tian, T. Siegrist, B. Ma. ACS Energy Letters (2018) 3 (1), 54-62

[2] M. Liu, H. Zhang, D. Gedamu, P. Fourmont, H. Rekola, A. Hiltunen, S. G. Cloutier, R. Nechache, A. Priimagi, P. Vivo. Small (2019) 15, 1900801.

[3] Y. Chen, Y. Sun, J. Peng, J. Tang, K. Zheng, Z. Liang. Adv. Mater. (2018) 30, 1703487.

[4] Y. Ling, Z. Yuan, Y. Tian, X. Wang, J. C. Wang, Y. Xin, K. Hanson, B. Ma, H. Gao., Adv Mater (2016) 28, 305-311.

[5] Z.-K. Tan, R. S. Moghaddam, M. L. Lai, P. Docampo, R. Higler, F. Deschler, M. Price, A. Sadhanala, L. M. Pazos, D. Credgington, F. Hanusch, T. Bein, H. J. Snaith, R. H. Friend. Nat Nanotechnol (2014) 9, 687-692.

[6] X. Hu, X. Zhang, L. Liang, J. Bao, S. Li W. Yang, Y. Xie. Adv Funct Mater (2014) 24, 7373-7380.

[7] H. Yu, K. Ren, Q. Wu, J. Wang, J. Lin, Z. Wang, J. Xu, R. F. Oulton, S. Qu, P. Jin. Nanoscale (2016) 8, 19536-19540.

[8] R. Zhang, J. Fan, X. Zhang, H. Yu, H. Zhang, Y. Mai, T, Xu, J. Wang, H. J. Snaith. ACS Photonics (2016) 3, 371-377.

[9] H.-S. Kim, C.-R. Lee, J.-H. Im, K.-B. Lee, T. Moehl, A. Marchioro, S.-J. Moon, R. Humphry-Baker, J.-H. Yum, J. E. Moser, M. Grätzel, N.-G. Park, Sci. Rep. (2012) 2, 591.

[10] Y. Chen, Y. Sun, J. Peng, J. Tang, K. Zheng, Z. Liang. Adv. Mater. (2018) 30, 1703487.

[11] S. D. Stranks, R. L. Z. Hoye, D. Di, R. H. Friend, F. Deschler. Adv. Mater.(2018) 1803336.

[12] M. D. Smith, H. I. Karunadasa. Accounts of Chemical Research 2018, 51 (3), 619-627.

[13] X. Gong, O. Voznyy, A. Jain, W. Liu, R. Sabatini, Z. Piontkowski, G. Walters, G. Bappi, S. Nokhrin, O. Bushuyev, M. Yuan, R. Comin, D. McCamant, S. O. Kelley, E. H. Sargent, Nature Materials 2018, 17 (6), 550-556.

APPENDIX: COPYRIGHT PERMISSION

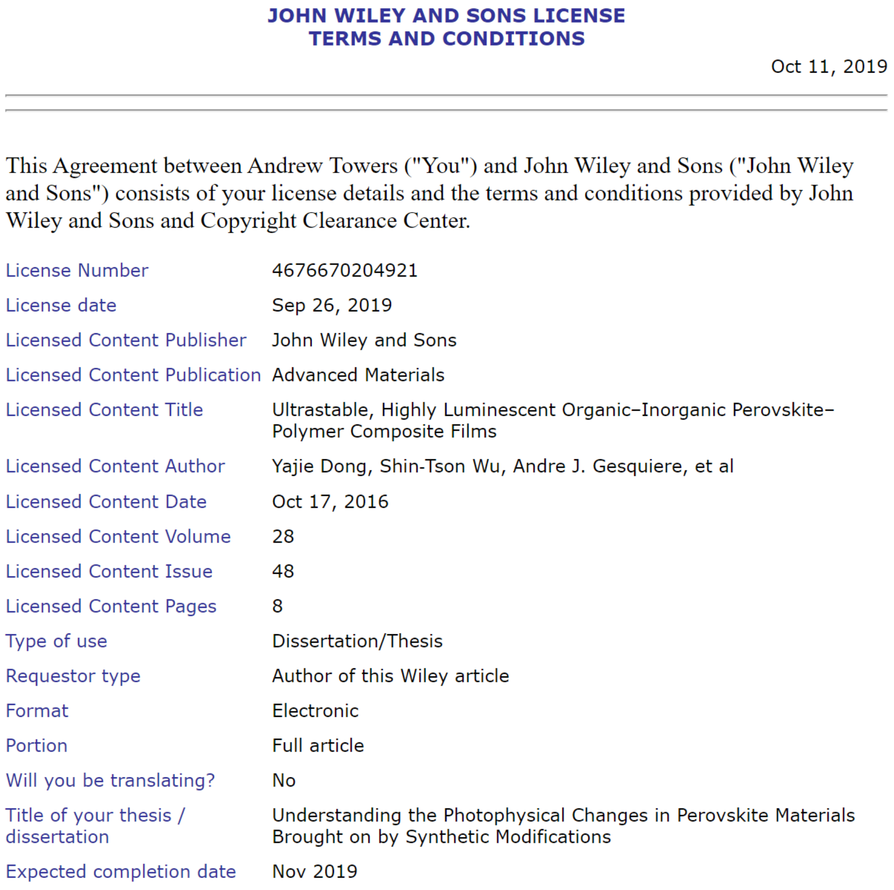

JOHN WILEY AND SONS LICENSE
TERMS AND CONDITIONS

Oct 11, 2019

This Agreement between Andrew Towers ("You") and John Wiley and Sons ("John Wiley and Sons") consists of your license details and the terms and conditions provided by John Wiley and Sons and Copyright Clearance Center.

License Number	4676670204921
License date	Sep 26, 2019
Licensed Content Publisher	John Wiley and Sons
Licensed Content Publication	Advanced Materials
Licensed Content Title	Ultrastable, Highly Luminescent Organic–Inorganic Perovskite–Polymer Composite Films
Licensed Content Author	Yajie Dong, Shin-Tson Wu, Andre J. Gesquiere, et al
Licensed Content Date	Oct 17, 2016
Licensed Content Volume	28
Licensed Content Issue	48
Licensed Content Pages	8
Type of use	Dissertation/Thesis
Requestor type	Author of this Wiley article
Format	Electronic
Portion	Full article
Will you be translating?	No
Title of your thesis / dissertation	Understanding the Photophysical Changes in Perovskite Materials Brought on by Synthetic Modifications
Expected completion date	Nov 2019

Chapter 2 of this thesis is based on the paper:

In situ synthesis and macroscale alignment of $CsPbBr_3$ perovskite nanorods in a polymer matrix

As a co-author of this publication, the following copyright restrictions apply to it’s reuse in this thesis:

Authors contributing to RSC publications (journal articles, books or book chapters) do not need to formally request permission to reproduce material contained in this article provided that the correct acknowledgement is given with the reproduced material.

Reproduced material should be attributed as follows:

- For reproduction of material from NJC:
  Reproduced from Ref. XX with permission from the Centre National de la Recherche Scientifique (CNRS) and The Royal Society of Chemistry.

- For reproduction of material from PCCP:
  Reproduced from Ref. XX with permission from the PCCP Owner Societies.
- For reproduction of material from PPS:
  Reproduced from Ref. XX with permission from the European Society for Photobiology, the European Photochemistry Association, and The Royal Society of Chemistry.
- For reproduction of material from all other RSC journals and books:
  Reproduced from Ref. XX with permission from The Royal Society of Chemistry.

If the material has been adapted instead of reproduced from the original RSC publication "Reproduced from" can be substituted with "Adapted from".

In all cases the Ref. XX is the XXth reference in the list of references.

If you are the author of this article you do not need to formally request permission to reproduce figures, diagrams etc. contained in this article in third party publications or in a thesis or dissertation provided that the correct acknowledgement is given with the reproduced material.

Reproduced material should be attributed as follows:

- For reproduction of material from NJC:
  [Original citation] - Reproduced by permission of The Royal Society of Chemistry (RSC) on behalf of the Centre National de la Recherche Scientifique (CNRS) and the RSC
- For reproduction of material from PCCP:
  [Original citation] - Reproduced by permission of the PCCP Owner Societies
- For reproduction of material from PPS:
  [Original citation] - Reproduced by permission of The Royal Society of Chemistry (RSC) on behalf of the European Society for Photobiology, the European Photochemistry Association, and RSC
- For reproduction of material from all other RSC journals:
  [Original citation] - Reproduced by permission of The Royal Society of Chemistry

If you are the author of this article you still need to obtain permission to reproduce the whole article in a third party publication with the exception of reproduction of the whole article in a thesis or dissertation.

Title: High Defect Tolerance in Lead Halide Perovskite CsPbBr3
Author: Jun Kang, Lin-Wang Wang
Publication: Journal of Physical Chemistry Letters
Publisher: American Chemical Society
Date: Jan 1, 2017
Copyright © 2017, American Chemical Society

Logged in as:
Andrew Towers
Account #:
3001524759

PERMISSION/LICENSE IS GRANTED FOR YOUR ORDER AT NO CHARGE

This type of permission/license, instead of the standard Terms & Conditions, is sent to you because no fee is being charged for your order. Please note the following:

- Permission is granted for your request in both print and electronic formats, and translations.
- If figures and/or tables were requested, they may be adapted or used in part.
- Please print this page for your records and send a copy of it to your publisher/graduate school.
- Appropriate credit for the requested material should be given as follows: "Reprinted (adapted) with permission from (COMPLETE REFERENCE CITATION). Copyright (YEAR) American Chemical Society." Insert appropriate information in place of the capitalized words.
- One-time permission is granted only for the use specified in your request. No additional uses are granted (such as derivative works or other editions). For any other uses, please submit a new request.

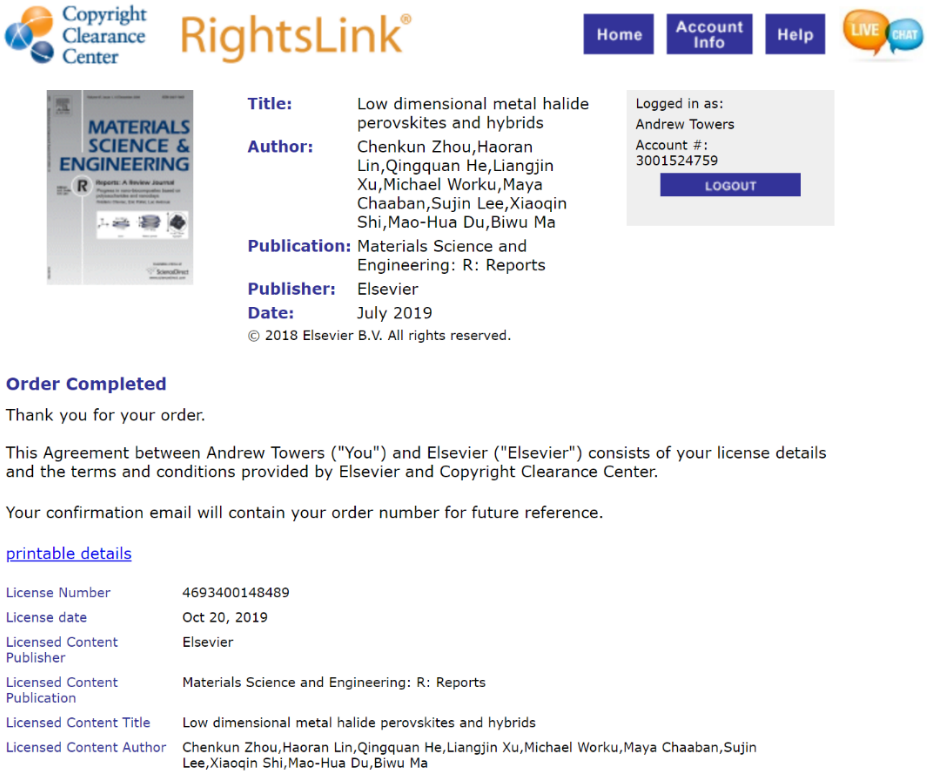

Title: Low dimensional metal halide perovskites and hybrids
Author: Chenkun Zhou,Haoran Lin,Qingquan He,Liangjin Xu,Michael Worku,Maya Chaaban,Sujin Lee,Xiaoqin Shi,Mao-Hua Du,Biwu Ma
Publication: Materials Science and Engineering: R: Reports
Publisher: Elsevier
Date: July 2019
© 2018 Elsevier B.V. All rights reserved.

Logged in as:
Andrew Towers
Account #:
3001524759

Order Completed

Thank you for your order.

This Agreement between Andrew Towers ("You") and Elsevier ("Elsevier") consists of your license details and the terms and conditions provided by Elsevier and Copyright Clearance Center.

Your confirmation email will contain your order number for future reference.

printable details

License Number	4693400148489
License date	Oct 20, 2019
Licensed Content Publisher	Elsevier
Licensed Content Publication	Materials Science and Engineering: R: Reports
Licensed Content Title	Low dimensional metal halide perovskites and hybrids
Licensed Content Author	Chenkun Zhou,Haoran Lin,Qingquan He,Liangjin Xu,Michael Worku,Maya Chaaban,Sujin Lee,Xiaoqin Shi,Mao-Hua Du,Biwu Ma

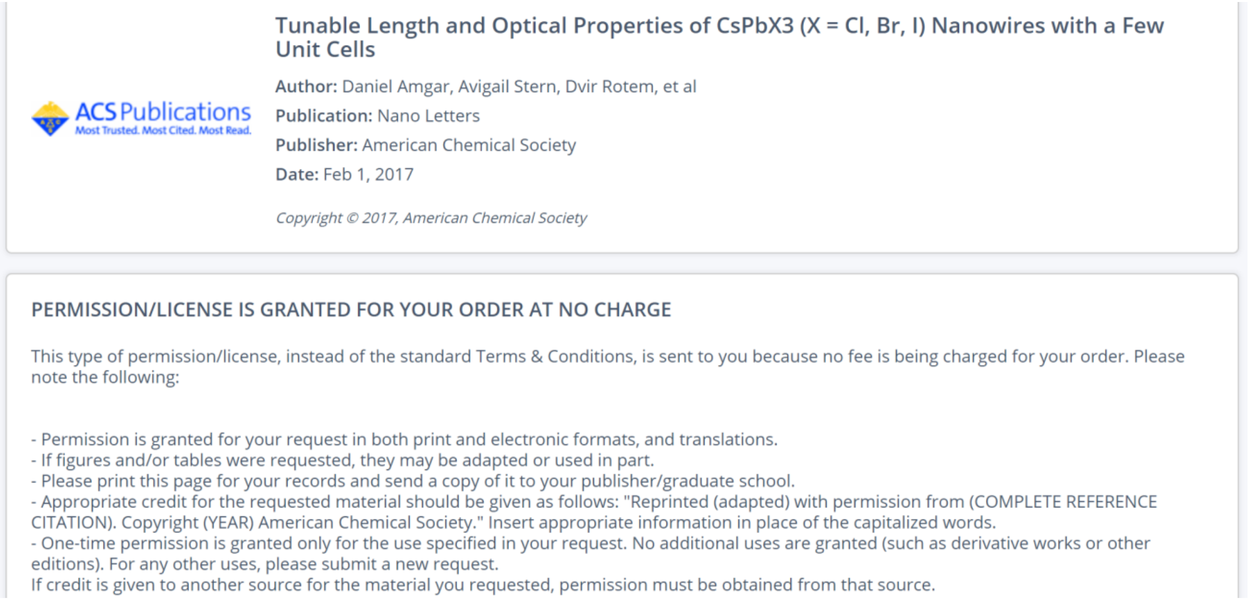

Tunable Length and Optical Properties of CsPbX3 (X = Cl, Br, I) Nanowires with a Few Unit Cells

Author: Daniel Amgar, Avigail Stern, Dvir Rotem, et al

Publication: Nano Letters

Publisher: American Chemical Society

Date: Feb 1, 2017

PERMISSION/LICENSE IS GRANTED FOR YOUR ORDER AT NO CHARGE

This type of permission/license, instead of the standard Terms & Conditions, is sent to you because no fee is being charged for your order. Please note the following:

- Permission is granted for your request in both print and electronic formats, and translations.
- If figures and/or tables were requested, they may be adapted or used in part.
- Please print this page for your records and send a copy of it to your publisher/graduate school.
- Appropriate credit for the requested material should be given as follows: "Reprinted (adapted) with permission from (COMPLETE REFERENCE CITATION). Copyright (YEAR) American Chemical Society." Insert appropriate information in place of the capitalized words.
- One-time permission is granted only for the use specified in your request. No additional uses are granted (such as derivative works or other editions). For any other uses, please submit a new request.

If credit is given to another source for the material you requested, permission must be obtained from that source.

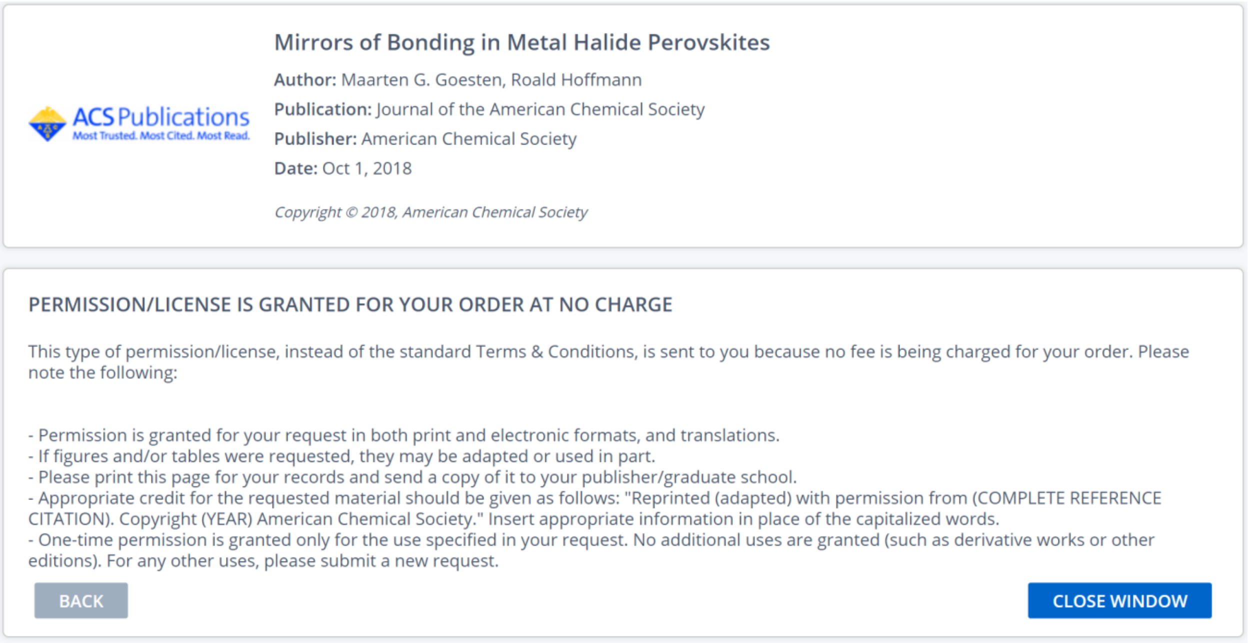

Mirrors of Bonding in Metal Halide Perovskites

Author: Maarten G. Goesten, Roald Hoffmann

Publication: Journal of the American Chemical Society

Publisher: American Chemical Society

Date: Oct 1, 2018

PERMISSION/LICENSE IS GRANTED FOR YOUR ORDER AT NO CHARGE

This type of permission/license, instead of the standard Terms & Conditions, is sent to you because no fee is being charged for your order. Please note the following:

- Permission is granted for your request in both print and electronic formats, and translations.
- If figures and/or tables were requested, they may be adapted or used in part.
- Please print this page for your records and send a copy of it to your publisher/graduate school.
- Appropriate credit for the requested material should be given as follows: "Reprinted (adapted) with permission from (COMPLETE REFERENCE CITATION). Copyright (YEAR) American Chemical Society." Insert appropriate information in place of the capitalized words.
- One-time permission is granted only for the use specified in your request. No additional uses are granted (such as derivative works or other editions). For any other uses, please submit a new request.

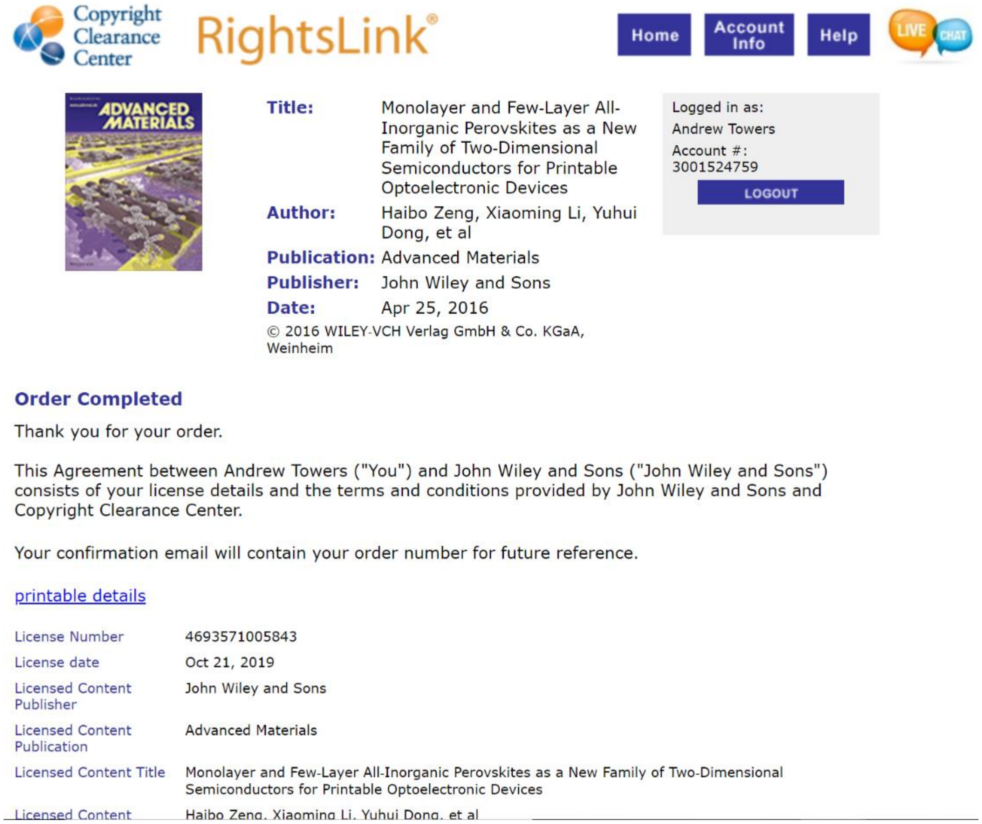

Title: Monolayer and Few-Layer All-Inorganic Perovskites as a New Family of Two-Dimensional Semiconductors for Printable Optoelectronic Devices

Author: Haibo Zeng, Xiaoming Li, Yuhui Dong, et al

Publication: Advanced Materials

Publisher: John Wiley and Sons

Date: Apr 25, 2016

© 2016 WILEY-VCH Verlag GmbH & Co. KGaA, Weinheim

Logged in as:
Andrew Towers
Account #:
3001524759

Order Completed

Thank you for your order.

This Agreement between Andrew Towers ("You") and John Wiley and Sons ("John Wiley and Sons") consists of your license details and the terms and conditions provided by John Wiley and Sons and Copyright Clearance Center.

Your confirmation email will contain your order number for future reference.

printable details

License Number	4693571005843
License date	Oct 21, 2019
Licensed Content Publisher	John Wiley and Sons
Licensed Content Publication	Advanced Materials
Licensed Content Title	Monolayer and Few-Layer All-Inorganic Perovskites as a New Family of Two-Dimensional Semiconductors for Printable Optoelectronic Devices
Licensed Content	Haibo Zeng, Xiaoming Li, Yuhui Dong, et al

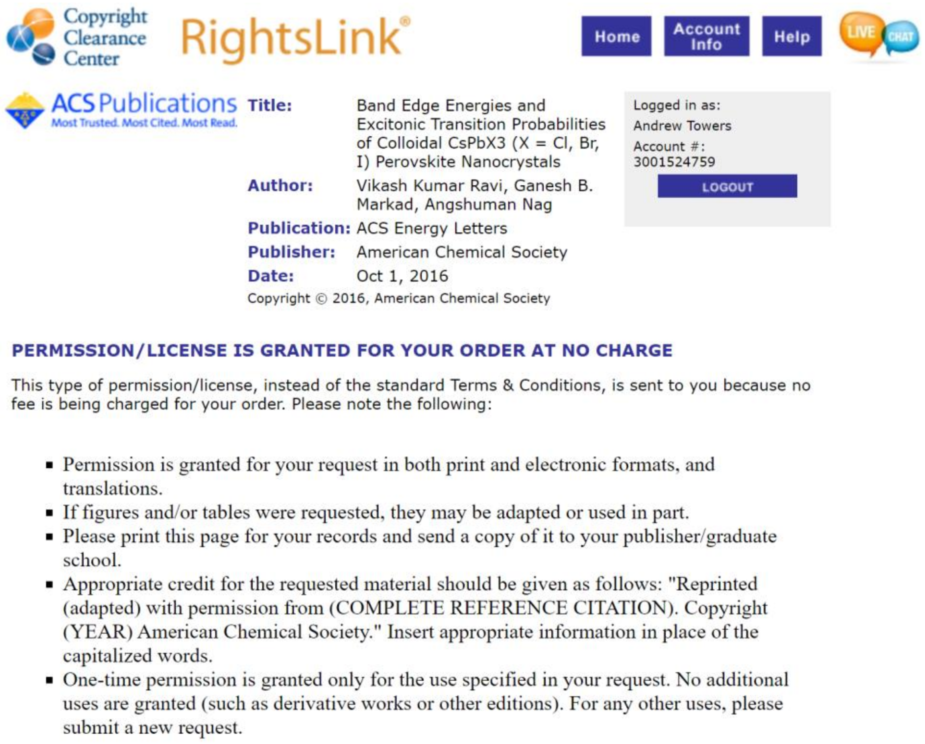

Title: Band Edge Energies and Excitonic Transition Probabilities of Colloidal CsPbX3 (X = Cl, Br, I) Perovskite Nanocrystals

Author: Vikash Kumar Ravi, Ganesh B. Markad, Angshuman Nag

Publication: ACS Energy Letters

Publisher: American Chemical Society

Date: Oct 1, 2016

Copyright © 2016, American Chemical Society

Logged in as:
Andrew Towers
Account #:
3001524759

PERMISSION/LICENSE IS GRANTED FOR YOUR ORDER AT NO CHARGE

This type of permission/license, instead of the standard Terms & Conditions, is sent to you because no fee is being charged for your order. Please note the following:

- Permission is granted for your request in both print and electronic formats, and translations.
- If figures and/or tables were requested, they may be adapted or used in part.
- Please print this page for your records and send a copy of it to your publisher/graduate school.
- Appropriate credit for the requested material should be given as follows: "Reprinted (adapted) with permission from (COMPLETE REFERENCE CITATION). Copyright (YEAR) American Chemical Society." Insert appropriate information in place of the capitalized words.
- One-time permission is granted only for the use specified in your request. No additional uses are granted (such as derivative works or other editions). For any other uses, please submit a new request.

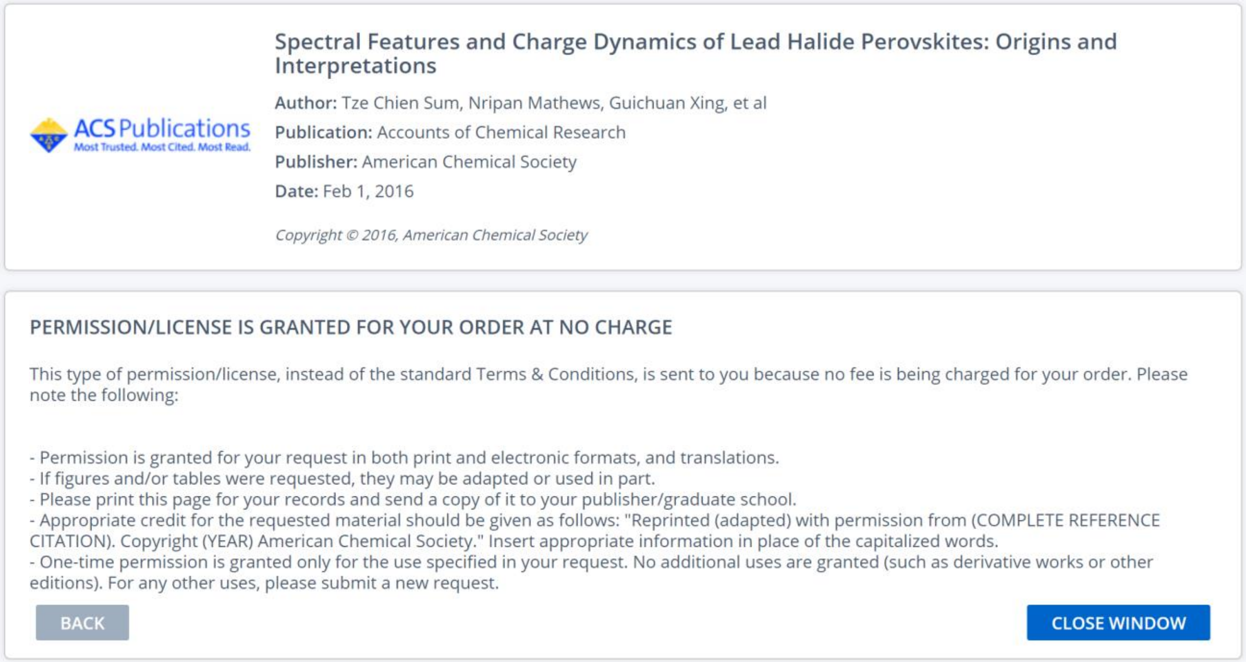

Spectral Features and Charge Dynamics of Lead Halide Perovskites: Origins and Interpretations

Author: Tze Chien Sum, Nripan Mathews, Guichuan Xing, et al
Publication: Accounts of Chemical Research
Publisher: American Chemical Society
Date: Feb 1, 2016

Copyright © 2016, American Chemical Society

PERMISSION/LICENSE IS GRANTED FOR YOUR ORDER AT NO CHARGE

This type of permission/license, instead of the standard Terms & Conditions, is sent to you because no fee is being charged for your order. Please note the following:

- Permission is granted for your request in both print and electronic formats, and translations.
- If figures and/or tables were requested, they may be adapted or used in part.
- Please print this page for your records and send a copy of it to your publisher/graduate school.
- Appropriate credit for the requested material should be given as follows: "Reprinted (adapted) with permission from (COMPLETE REFERENCE CITATION). Copyright (YEAR) American Chemical Society." Insert appropriate information in place of the capitalized words.
- One-time permission is granted only for the use specified in your request. No additional uses are granted (such as derivative works or other editions). For any other uses, please submit a new request.

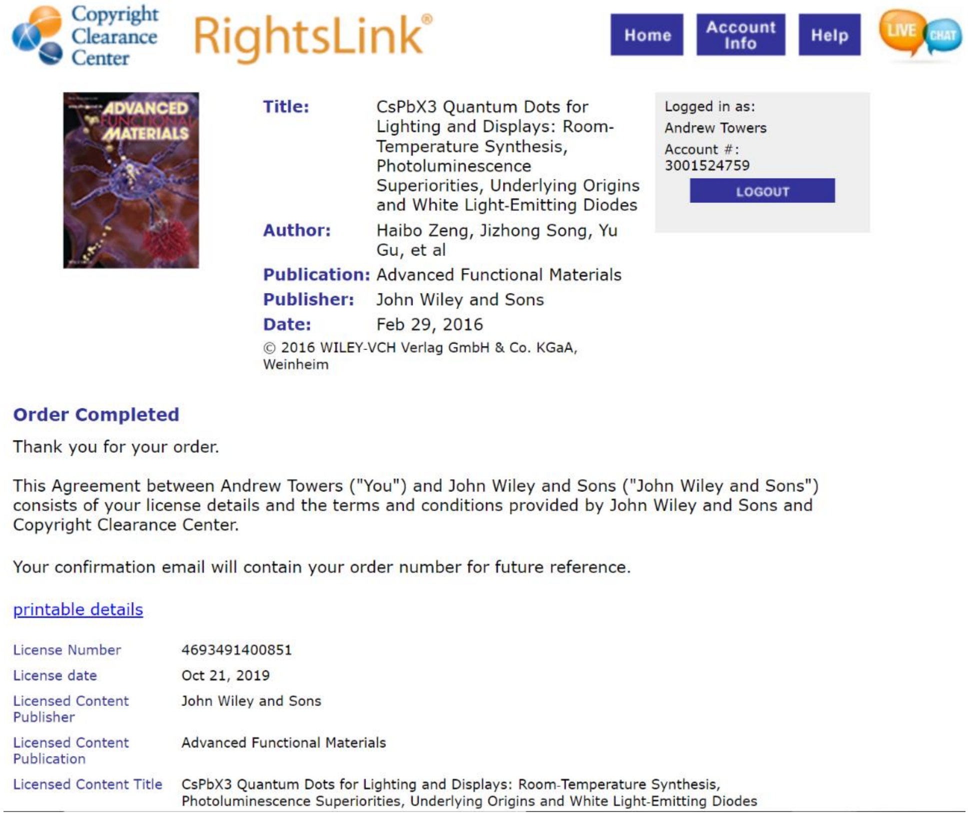

Title:	CsPbX3 Quantum Dots for Lighting and Displays: Room-Temperature Synthesis, Photoluminescence Superiorities, Underlying Origins and White Light-Emitting Diodes
Author:	Haibo Zeng, Jizhong Song, Yu Gu, et al
Publication:	Advanced Functional Materials
Publisher:	John Wiley and Sons
Date:	Feb 29, 2016

© 2016 WILEY-VCH Verlag GmbH & Co. KGaA, Weinheim

Logged in as:
Andrew Towers
Account #:
3001524759

Order Completed

Thank you for your order.

This Agreement between Andrew Towers ("You") and John Wiley and Sons ("John Wiley and Sons") consists of your license details and the terms and conditions provided by John Wiley and Sons and Copyright Clearance Center.

Your confirmation email will contain your order number for future reference.

printable details

License Number	4693491400851
License date	Oct 21, 2019
Licensed Content Publisher	John Wiley and Sons
Licensed Content Publication	Advanced Functional Materials
Licensed Content Title	CsPbX3 Quantum Dots for Lighting and Displays: Room-Temperature Synthesis, Photoluminescence Superiorities, Underlying Origins and White Light-Emitting Diodes

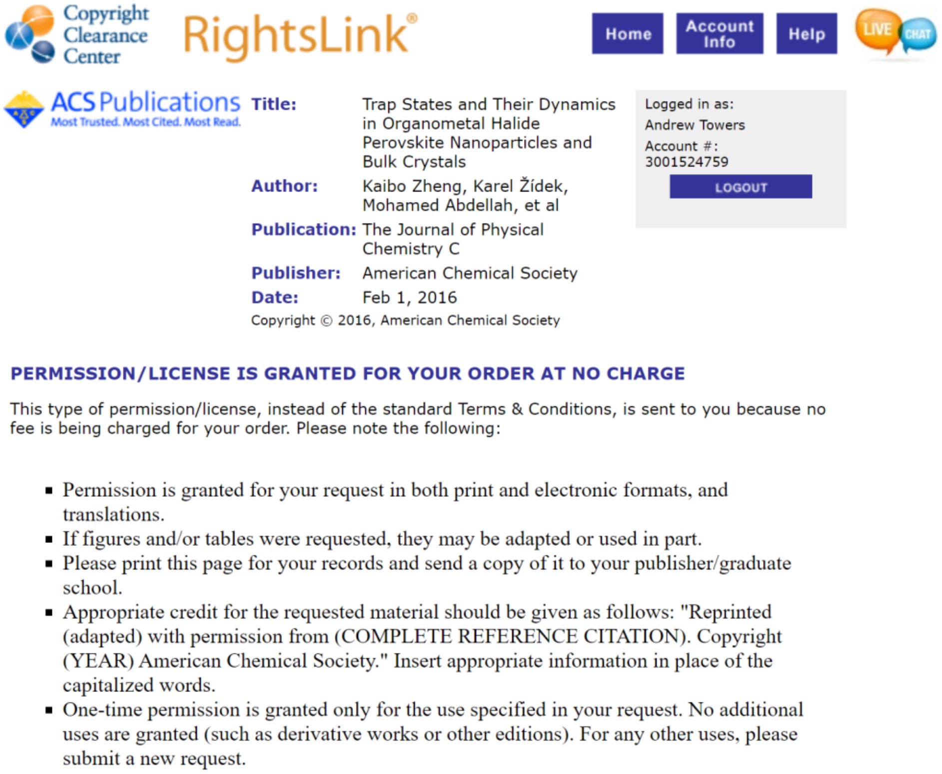

Title:	Trap States and Their Dynamics in Organometal Halide Perovskite Nanoparticles and Bulk Crystals
Author:	Kaibo Zheng, Karel Žídek, Mohamed Abdellah, et al
Publication:	The Journal of Physical Chemistry C
Publisher:	American Chemical Society
Date:	Feb 1, 2016

Copyright © 2016, American Chemical Society

Logged in as:
Andrew Towers
Account #:
3001524759

PERMISSION/LICENSE IS GRANTED FOR YOUR ORDER AT NO CHARGE

This type of permission/license, instead of the standard Terms & Conditions, is sent to you because no fee is being charged for your order. Please note the following:

- Permission is granted for your request in both print and electronic formats, and translations.
- If figures and/or tables were requested, they may be adapted or used in part.
- Please print this page for your records and send a copy of it to your publisher/graduate school.
- Appropriate credit for the requested material should be given as follows: "Reprinted (adapted) with permission from (COMPLETE REFERENCE CITATION). Copyright (YEAR) American Chemical Society." Insert appropriate information in place of the capitalized words.
- One-time permission is granted only for the use specified in your request. No additional uses are granted (such as derivative works or other editions). For any other uses, please submit a new request.

Title:	White-Light Emission from Layered Halide Perovskites
Author:	Matthew D. Smith, Hemamala I. Karunadasa
Publication:	Accounts of Chemical Research
Publisher:	American Chemical Society
Date:	Mar 1, 2018

Copyright © 2018, American Chemical Society

Logged in as:
Andrew Towers
Account #:
3001524759

PERMISSION/LICENSE IS GRANTED FOR YOUR ORDER AT NO CHARGE

This type of permission/license, instead of the standard Terms & Conditions, is sent to you because no fee is being charged for your order. Please note the following:

- Permission is granted for your request in both print and electronic formats, and translations.
- If figures and/or tables were requested, they may be adapted or used in part.
- Please print this page for your records and send a copy of it to your publisher/graduate school.
- Appropriate credit for the requested material should be given as follows: "Reprinted (adapted) with permission from (COMPLETE REFERENCE CITATION). Copyright (YEAR) American Chemical Society." Insert appropriate information in place of the capitalized words.
- One-time permission is granted only for the use specified in your request. No additional uses are granted (such as derivative works or other editions). For any other uses, please submit a new request.

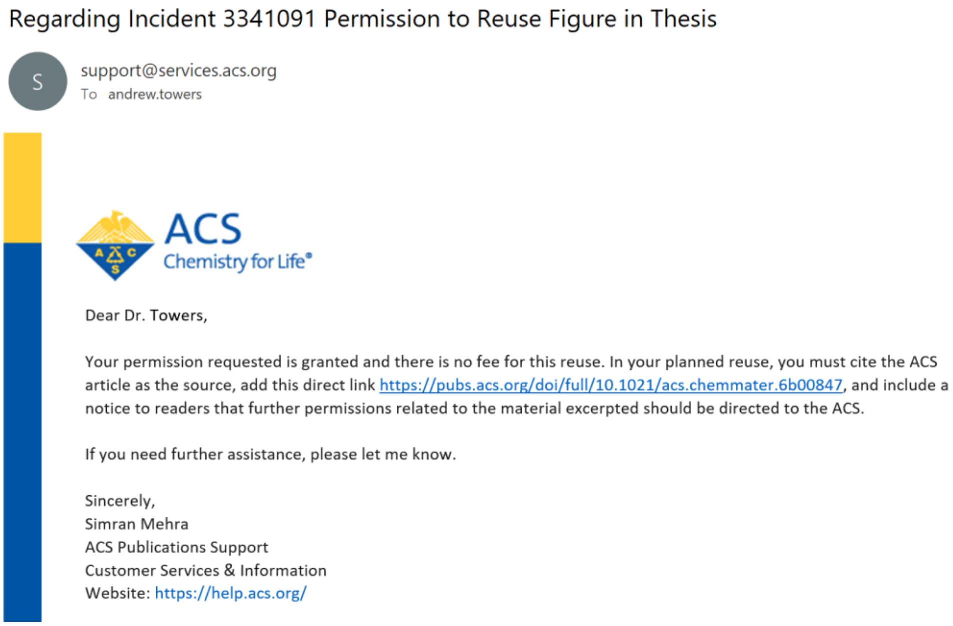

Regarding Incident 3341091 Permission to Reuse Figure in Thesis

support@services.acs.org
To andrew.towers

Dear Dr. Towers,

Your permission requested is granted and there is no fee for this reuse. In your planned reuse, you must cite the ACS article as the source, add this direct link https://pubs.acs.org/doi/full/10.1021/acs.chemmater.6b00847, and include a notice to readers that further permissions related to the material excerpted should be directed to the ACS.

If you need further assistance, please let me know.

Sincerely,
Simran Mehra
ACS Publications Support
Customer Services & Information
Website: https://help.acs.org/

This is an open access article published under an ACS AuthorChoice License, which permits copying and redistribution of the article or any adaptations for non-commercial purposes.

1. SCOPE OF GRANT

ACS grants You non-exclusive and nontransferable permission to access and use this ACS article subject to the terms and conditions set forth in this Agreement.

2. PERMITTED USES

a. For non-commercial research and education purposes only, You may access, download, copy, display and redistribute articles as well as adapt, translate, text and data mine content contained in articles, subject to the following conditions:

i. The authors' moral right to the integrity of their work under the Berne Convention (Article 6bis) is not compromised.

ii. Where content in the article is identified as belonging to a third party, it is your responsibility to ensure that any reuse complies with copyright policies of the owner.

iii. Copyright notices or the display of unique Digital Object Identifiers (DOI’s), ACS or journal logos, bibliographic (e.g. authors, journal, article title, volume, issue, page numbers) or other references to ACS journal titles, web links, and any other journal-specific “branding” or notices that are included in the article or that are provided by the ACS with instructions that such should accompany its display, should not be removed or tampered with in any way. The display of *ACS AuthorChoice* or *ACS Editors’ Choice* articles on non-ACS websites must be accompanied by prominently displayed links to the definitive published versions of those articles on the ACS website.

iv. Any adaptations for non-commercial purposes must prominently link to the definitive published version on the ACS website and prominently display the statement: “This is an unofficial adaptation of an article that appeared in an ACS publication. ACS has not endorsed the content of this adaptation or the context of its use.”

v. Any translations for non-commercial purposes, for which a prior translation agreement with ACS has not been established, must prominently link to the definitive published version on the ACS website and prominently display the statement: “This is an unofficial translation of an article that appeared in an ACS publication. ACS has not endorsed the content of this translation or the context of its use.”

b. Each time You distribute this ACS article or an adaptation, ACS offers to the recipient a license to this ACS article on the same terms and conditions as the license granted to You under this License.

c. For permission to use ACS copyrighted articles beyond that permitted here,
visit: http://pubs.acs.org/copyright/permissions.html

3. PROHIBITED USES

a. Use of this ACS article for commercial purposes is prohibited. Examples of such prohibited commercial purposes include but are not limited to:

i. Copying or downloading of articles, or linking to such postings, for further distribution, sale or licensing, for a fee;

ii. Copying, downloading or posting by a site or service that incorporates advertising with such content;

iii. The inclusion or incorporation of article content in other works or services (other than normal quotations with an appropriate citation) that is then available for sale or licensing, for a fee;

iv. Use of articles or article content (other than normal quotations with appropriate citation) by a for-profit organizations for promotional purposes, whether for a fee or otherwise;

v. Sale of translated versions of the article that have not been authorized by license or other permission from the ACS

4. TERMINATION

ACS reserves the right to limit, suspend, or terminate your access to and use of the ACS Publications Division website and/or all ACS articles immediately upon detecting a breach of this License.

5. COPYRIGHTS; OTHER INTELLECTUAL PROPERTY RIGHTS

Except as otherwise specifically noted, ACS is the owner of all right, title and interest in the content of this ACS article, including, without limitations, graphs, charts, tables illustrations, and copyrightable supporting information. This ACS article is protected under the Copyright Laws of the United States Codified in Title 17 of the U.S. Code and subject to the Universal Copyright Convention and the Berne Copyright Convention. You agree not to remove or obscure copyright notices. You acknowledge that You have no claim to ownership of any part of this ACS article or other proprietary information accessed under this Agreement.

The names “American Chemical Society,” “ACS” and the titles of the journals and other ACS products are trademarks of ACS.

6. DISCLAIMER OF WARRANTIES; LIMITATION OF LIABILITY

ACS warrants that it is entitled to grant this Agreement.

EXCEPT AS SET FORTH IN THE PRECEDING SENTENCE, ACS MAKES NO WARRANTY OR REPRESENTATION OF ANY KIND, EXPRESS OR IMPLIED, WITH RESPECT TO THIS ACS ARTICLE INCLUDING, BUT NOT LIMITED TO WARRANTIES AS TO THE ACCURACY OR COMPLETENESS OF THE ACS ARTICLE, ITS QUALITY, ORIGINALITY, SUITABILITY, SEARCHABILITY, OPERATION, PERFORMANCE, COMPLIANCE WITH ANY COMPUTATIONAL PROCESS, MERCHANTABILITY OR FITNESS FOR A PARTICULAR PURPOSE.

ACS SHALL NOT BE LIABLE FOR: EXEMPLARY, SPECIAL, INDIRECT, INCIDENTAL, CONSEQUENTIAL OR OTHER DAMAGES ARISING OUT OF OR IN CONNECTION WITH THE AGREEMENT GRANTED HEREUNDER, THE USE OR INABILITY TO USE ANY ACS PRODUCT, ACS’S PERFORMANCE UNDER THIS AGREEMENT, TERMINATION OF THIS AGREEMENT BY ACS OR THE LOSS OF DATA, BUSINESS OR GOODWILL EVEN IF ACS IS ADVISED OR AWARE OF THE POSSIBILITY OF SUCH DAMAGES. IN NO EVENT SHALL THE TOTAL AGGREGATE LIABILITY OF ACS OUT OF ANY BREACH OR TERMINATION OF THIS AGREEMENT EXCEED THE TOTAL AMOUNT PAID BY YOU TO ACS FOR ACCESS TO THIS ACS ARTICLE FOR THE CURRENT YEAR IN WHICH SUCH CLAIM, LOSS OR DAMAGE OCCURRED, WHETHER IN CONTRACT, TORT OR OTHERWISE, INCLUDING, WITHOUT LIMITATION, DUE TO NEGLIGENCE.

The foregoing limitations and exclusions of certain damages shall apply regardless of the success or effectiveness of other remedies. No claim may be made against ACS unless suit is filed within one (1) year after the event giving rise to the claim.

7. GENERAL

This Agreement sets forth the entire understanding of the Parties. The validity, construction and performance of this Agreement shall be governed by and construed in accordance with the laws of the District of Columbia, USA without reference to its conflicts of laws principles. You acknowledge that the delivery of the ACS article will occur in the District of Columbia, USA.

You shall pay any taxes lawfully due from it, other than taxes on ACS's net income, arising out of your use of this ACS article and/or other rights granted under this Agreement. You may not assign or transfer its rights under this Agreement without the express written consent of ACS.

8. ACCEPTANCE

You warrant that You have read, understand, and accept the terms and conditions of this Agreement. ACS reserves the right to modify this Agreement at any time by posting the modified terms and conditions on the ACS Publications Web site. Any use of this ACS article after such posting shall constitute acceptance of the terms and conditions as modified.